FIELD EFFECT FLOW CONTROL OF ELECTRO-OSMOTIC FLOW IN MICROFLUIDIC NETWORKS

Egbert van der Wouden

The research described in this thesis was carried out at the BIOS Lab-on-a-Chip Group of the MESA$^+$ Institute for Nanotechnology of the University of Twente, Enschede, The Netherlands. The project was financially supported by the Dutch Technology Foundation (STW – project number TMM. 5384)

Promotiecommissie:

Voorzitter	Prof.dr.ir. A.J. Mouthaan	
Secretaris	Prof.dr.ir. A.J. Mouthaan	University of Twente
Promotor	Prof. dr. ir. A. van den Berg	University of Twente
Co-promotor	Prof. dr. J.G.E. Gardeniers	University of Twente
Leden	Prof.dr.ing. M. Wessling	University of Twente
	Prof.dr. D. Lohse	University of Twente
	Prof.dr. J.G. Santiago	Stanford University
	Dr. M.P.B. van Bruggen	Philips Research
	Dr.ir. J.H. Nieuwenhuis	Philips Research
	Prof.dr.ir. J. Westerweel	Technical University Delft

Van der Wouden, Egbert

Field Effect Flow Control of Electro-osmotic Flow in Microfluidic Networks

PhD thesis University of Twente, Enschede, The Netherlands

ISBN: 90-365-2453-9
Publisher: Wöhrmann Print Service, Zutphen, The Netherlands
Cover design: Egbert van der Wouden

FIELD EFFECT FLOW CONTROL OF ELECTRO-OSMOTIC FLOW IN MICROFLUIDIC NETWORKS

PROEFSCHRIFT

ter verkrijging van
de graad van doctor aan de Universiteit Twente,
op gezag van de rector magnificus,
prof. dr. W.H.M. Zijm,
volgens het besluit van het College voor Promoties
in het openbaar te verdedigen
op vrijdag 15 december 2006 om 13.15 uur

door

Egbert van der Wouden

geboren op 29 september 1979
te Heerenveen, Nederland

Dit proefschrift is goedgekeurd door:

Promotor:	Prof. dr. ir. A. van den Berg
Co-promotor:	Prof. dr. J.G.E. Gardeniers

1

Introduction

1 Abstract

This chapter will give an overview of the project goal and an introduction to the use of Electro Osmotic Flow (EOF) in lab on a chip systems, and the potential of Field Effect Flow Control (FEFC) in medication delivery systems. Furthermore an overview of the thesis content is provided.

2 Project goal

The goal of this project is to develop and test a new principle for a normally closed valve, primarily but not exclusively for implantable medication infusion systems. The drug flow through the valve in the open state should be electronically controllable and adjustable within a specified flow range. The valve, with all its control parts, should fulfill specified safety regulations and lifetime requirements. Since for the main application the valve should be integrated in an (existing or future) implantable infusion system, its size or volume should be limited to ca. 1 cm^3. The fabrication of such a small device, with its tiny fluidic and electronic parts, can only be achieved with the aid of modern micromachining and thin film techniques, similar to the fabrication methods well-known in micro-electronic circuit fabrication.
The basic idea of the valve is that, by an appropriate choice of dimensions and shape of fluidic channels, a flow restriction will be constructed with a very high hydraulic resistance, so that the specifications for the leakage rate in the "normally closed" state are met for the pressure delivered by a liquid-vapour pressure source, that is conventional in implantable infusion systems. In the "open" state, the desired drug flow rate will be forced through the flow restriction by controlled electroosmotic flow. Several new principles will be used and studied in the project, like external electrical fields (so-called FEFC principle), both DC and AC, and surface modification for control of electroosmotic flow. The specifications of the valve to be developed are given bellow in table 1.1.

Parameter	Minimum value	Maximum value
Leakage in closed state	d.n.a.*	1 µl / day
Flow range	10 µl / day	500 µl / day
Allowable flow variation	d.n.a.	10 %
Lifetime / durability	10 years	d.n.a.
Size / volume	d.n.a.	2 cc
Electrical current	d.n.a.	10 µA at max. flow
Electrical voltage	d.n.a.	3 Volts
Pressure source[#]	d.n.a.	300 mbar

Table 1.1: *Summary of the valve specifications to be constructed.*
*d.n.a.: does not apply

3 Miniaturized systems

Recently, the introduction of chip-based technologies and the corresponding design strategies has given an enormous impetus to progress in the field of fluidic devices, mainly for the analytical sciences. An increasing number of new companies, mainly based in the USA, are penetrating the market with different kinds of pocket-size chemistry equipment, including high-throughput drug-screening systems, portable environmental screening devices, miniature DNA analysers, etc.[1, 2]. These chips are frequently being referred to as "microfluidics", in analogy with the more familiar "microelectronics" chips. A similar revolutionary impact is expected of these so-called "labs-on-a-chip", with probably numerous new applications. At present these miniaturised chemical labs owe most of their appeal to the much lower costs (because of batch fabrication), with respect to their much larger, but similarly performing counterparts.

In the field of medication delivery a similar trend towards miniaturisation and chip-like technologies is becoming apparent, for obvious reasons. In this project we focus on one component of existing medication infusion systems, viz. a micro-valve. Medication infusion systems or pumps are generally used to deliver a selected medication or drug in a scheduled or pre-programmed way. In recent years, such infusion systems have been developed in compact form adapted for direct implantation into the body of a patient, to deliver a specific medication to the patient in discrete doses over an extended period of time. An implanted infusion pump of this general type (e.g. the Medtronic SynchroMed Infusion System [3]) includes an internal chamber for receiving (e.g. through an inlet port that permits percutaneous

refilling via a hypodermic needle) and storing a supply of the medication in liquid form, with the medication being subjected to a predetermined storage pressure, e.g. by a fluorocarbon propellant pump, to ensure accurate and repeatable delivery conditions, through the use of e.g. a micropump and associated programmed control means. For reasons of safety and energy consumption reduction, state-of-the-art infusion systems utilise a normally-closed valve which is opened in a programmed way to release the drug, which is delivered because of the driving force of the described fluorocarbon pump. It is the goal of this project to develop such a normally closed microvalve, with dimensions that are smaller than the existing types, therewith allowing further miniaturisation of existing infusion systems.

4 Electro Osmotic Flow control in micro fluidic systems

In classical EOF systems potentials of several hundred volts are required to satisfy the requirements listed in table 1. These voltages are too high for practical use of the proposed valve type, especially in an implantable device. A way has to be found to reduce these voltages to acceptable values, say a few tens of Volts.

We think that this may be achieved by the introduction of the "FlowFET" principle [4, 5]. A flowFET, or also named Field Effect Flow Control (FEFC) device [6], consists of a liquid channel, through which the electrokinetic flow is controlled by application of an external electric field across the channel walls, which affects the so called Zeta potential, with which the flow is proportional. The Flow-FET or FEFC principle, although not named as such, was demonstrated already in the beginning of the nineties [7]. In these early studies, fused silica capillaries were used, and the purpose of that work was the enhancement of electrophoretic separation efficiency, rather than flow control. Because of the thickness of the capillary walls, relatively high voltages (several kilo Volts) were required to establish sufficiently high radial electrical fields. Since modern microfabrication and thin film deposition techniques allow the fabrication of capillaries with extremely thin channel walls, the required radial electrical fields can now be achieved with more acceptable voltages, like a few tens of Volts, as was demonstrated in more recent work [4].

5 Thesis outline

The content of the remaining chapters is as follows:

Chapter 2: Characterization of operating parameters of Field Effect Flow Control of Electro-Osmotic Flow.
Here an introduction is provided to electrical double layer, EOF and FEFC. Furthermore characterization methods for EOF are discussed and several coatings are characterized for their application in tuning of EOF.

Chapter 3: Design aspects and fabrication of Field Effect Flow Control systems.
In this chapter the various considerations and requirements in the fabrication of a Field Effect Flow Control (FEFC) structure are discussed.
The applications of a meandering channel structure with high hydraulic resistance, is introduced for pumping at low actuation potentials.

Chapter 4: Fabrication of microfluidic networks with integrated electrodes.
In this chapter the process for fabrication of FEFC structures is described.
The reduction of surface roughness and surface topography with the aid of Chemical Mechanical Polishing (CMP) is analyzed. CMP is required for the bonding of wafers with embedded electrodes.

Chapter 5: Simulation of Field Effect Flow Control of Electro-Osmotic Flow.
In this chapter velocity profiles and the influence of surface of the gate electrode in FEFC are modeled and analyzed. The potential of flow directioning in FEFC arrays is analyzed with finite element simulations. Furthermore an electrical equivalent model of a FEFC structure is used to predict the transient charging behaviour.

Chapter 6: Field effect control of electro-osmotic flow in microfluidic networks.
This chapter presents a characterization of fabricated FEFC structures. The gate zeta potential as a function of the zeta potential is analyzed and the dependency on the pH is measured with the aid of the current monitoring method.

Chapter 7: Directional flow induced by synchronized longitudinal and zeta-potential controlling AC-electrical fields.

In this chapter the control of EOF with the synchronized AC-switching of the gate and channel potentials is presented. Furthermore, an analysis of the charging dynamics is provided and the role of the surface buffer pH is discussed.

Chapter 8: Particle image velocimetry and particle tracking for electrokinetic flow in microchannels
In this chapter, Particle Tracking Velocimetry (PTV) and Particle Image Velocimetry (PIV) measurements are presented in Field Effect Flow Control (FEFC) systems with a floating gate electrode.

Chapter 9: Conclusions
In this chapter an overview of the conclusions and discussion that were presented in the different chapters of this thesis is provided.

6 References

1. Burns, M.A., et al., *An integrated nanoliter DNA analysis device.* Science, 1998. **282**(5388): p. 484-487.
2. Service, R.F., *Future chips - Labs on a chip - Coming soon: The pocket DNA sequencer.* Science, 1998. **282**(5388): p. 399-401.
3. *http://www.medtronic.com.*
4. Schasfoort, R.B.M., S. Schlautmann, L. Hendrikse and A. van den Berg, *Field-effect flow control for microfabricated fluidic networks.* Science, 1999. **286**(5441): p. 942-945.
5. van den Berg, A., *Inrichting voor het besturen van een vloeistofstroom.* Dutch patent application nr. NL-1010327, 1998, 1998.
6. Sniadecki, N.J., C.S. Lee, P. Sivanesan and D.L. DeVoe, *Induced pressure pumping in polymer microchannels via field-effect flow control.* Analytical Chemistry, 2004. **76**(7): p. 1942-1947.
7. Lee, C.S., W.C. Blanchard and C.T. Wu, *Direct Control of the Electroosmosis in Capillary Zone Electrophoresis by Using an External Electric-Field.* Analytical Chemistry, 1990. **62**(14): p. 1550-1552.

2

Characterization of operating parameters of Field Effect Flow Control of Electro-Osmotic Flow

1 Abstract

In this chapter an overview is given of the different aspects that are involved in flow control in microfluidic systems by the use of radial electrical fields. In section 2 a general introduction in electrical double layers at the solid/liquid interface will be given followed by a description of the formation of charge at different types of surfaces. In section 3 the concept of Electro Osmotic Flow (EOF) will be introduced and the different parameters involved will be discussed. Furthermore different techniques to characterize the EOF will be reviewed and the possibility to influence the surface charge by the application of surface coatings is discussed. In section 4 the influence and nature of the surface charge on flow profiles will be analyzed as well as the response of the surface charge on an external radial field.

2 Electrical double layers and electrokinetics

A solid surface in contact with an electrolyte will develop a surface charge depending on the characteristics of both the solid and the liquid. This surface charge will influence the ion distribution in the liquid near the surface due to electrostatic interactions. Ions charged oppositely to the surface, so-called counterions, are attracted towards the wall, while coions having the same charge as the surface are repelled from the surface [1]. The local region near the surface with a net charge associated to it is referred to as the Electrical Double Layer (EDL).

The first concept of the electrical double layer was developed by Helmholtz who looked at the solid liquid interface as a thin capacitor where the surface charge was screened by a fixed layer of counterions.

Later on Gouy and Chapman further developed the electrical model and described the diffuse charge model where a charge on the surface is screened by an equal amount of counter charge in the so called diffuse double layer. They showed that the concentration of counter ions in the EDL is described by the Boltzmann equation. (Eq. 2.1) An overview of the symbols and their units is provided in appendix A.

$$n = n_0 \exp\left(\frac{ze\Psi}{\kappa T}\right) \qquad \text{(Eq. 2.1)}$$

The total charge density in a volume i in the EDL is given by equation 2.2

$$\rho_i = \Sigma z_i e n_i \qquad \text{(Eq. 2.2)}$$

The interaction between ions in the double layer can be expressed by the Poison equation (Eq. 2.3), so by combining equations 2.1-3 the charge density can be written as a function of the potential gradient as shown in equation 2.4 and is also referred to as the Poisson-Boltzmann equation.

$$\frac{d^2\Psi}{dx^2} = -\frac{\rho}{\varepsilon_0 \varepsilon_r} \qquad \text{(Eq. 2.3)}$$

$$\frac{d^2\Psi}{dx^2} = -\frac{1}{\varepsilon_0 \varepsilon_r} \Sigma n_i z_i e \exp\left(\frac{z_i e \Psi}{\kappa T}\right) \qquad \text{(Eq. 2.4)}$$

Under the condition that the electrostatic interaction is small compared to the thermal energy ($|z_i e\Psi| < \kappa T$) which corresponds to low surface potentials equation 2.4 can be simplified to equation 2.5

$$\frac{d^2\Psi}{dx^2} = \left(\frac{\Sigma z^2 e^2 n^2}{\varepsilon_0 \varepsilon_r \kappa T}\right)\Psi \qquad \text{(Eq. 2.5)}$$

The term between brackets has the dimension of length^{-2} and is also used to indicate the thickness of the EDL by the Debye-Hückel parameter also indicated as the Debye length. This is roughly the point where the potential in the double layer is Ψ_0/e and is given by equation 2.6.

$$\frac{1}{\lambda} = \left(\frac{\varepsilon_0 \varepsilon_r \kappa T}{e^2 \Sigma z^2 n}\right)^{\frac{1}{2}} \qquad \text{(Eq. 2.6)}$$

The distribution of counter and coions and the resulting potential in the case of a positive surface is illustrated in Fig. 2.1 a) shows the excess of counter ions in the EDL up to the bulk of the solution where the potential decays to zero and there is a balance in co- and counterions b) shows the associated potential decay.

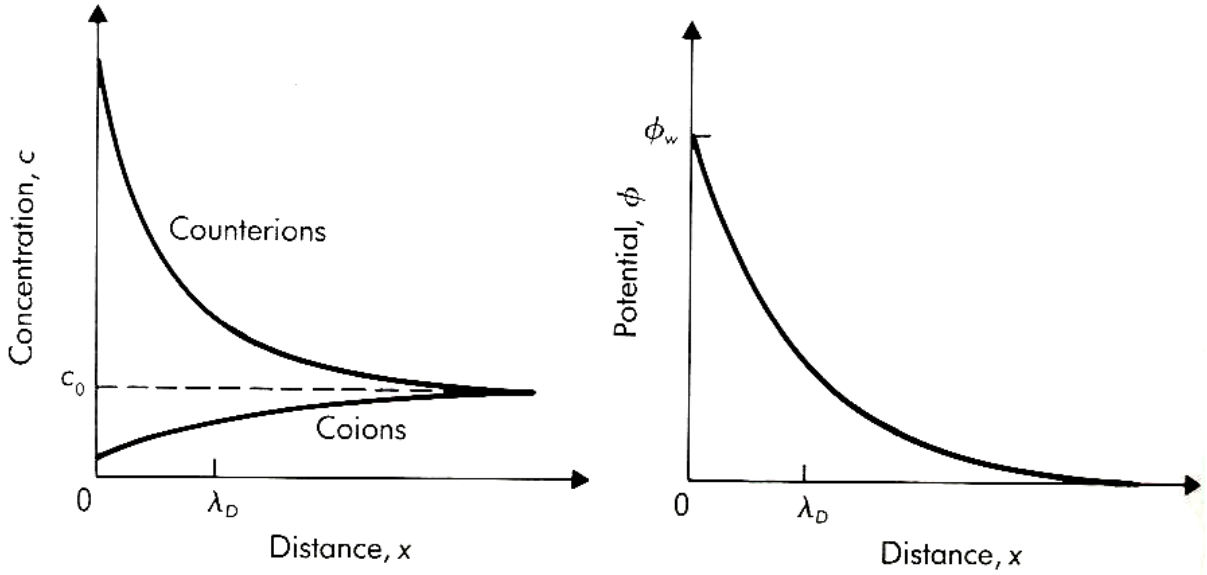

Fig. 2.1: *Schematic illustration of the ion distribution and potential decay in the EDL*.

The above description of the diffuse double layer is referred to as the Gouy-Chapman model. The model gives a good description of the ion distribution inside the EDL however it is assumed that the ions can be considered as point charges and can thus approach the surface infinitely close, while in practice the distance of the center of an ion to the surface is limited by its radius.
Stern adapted the model of Gouy-Chapman and expanded it with a thin layer in which no charge is present due to the radius of the ions.
This layer is generally referred to as the Stern layer and can be subdivided in the Inner Helmholtz Plane (IHP) and the Outer Helmholtz Plane (OHP) where the former is composed of dehydrated and the latter of hydrated ions.
The potential at the interface between the Stern layer and the diffuse double layer is referred to as the zeta potential, which is an important parameter in several electrokinetic phenomena.
The different relevant potentials and their position in the EDL are indicated in figure 2.2.

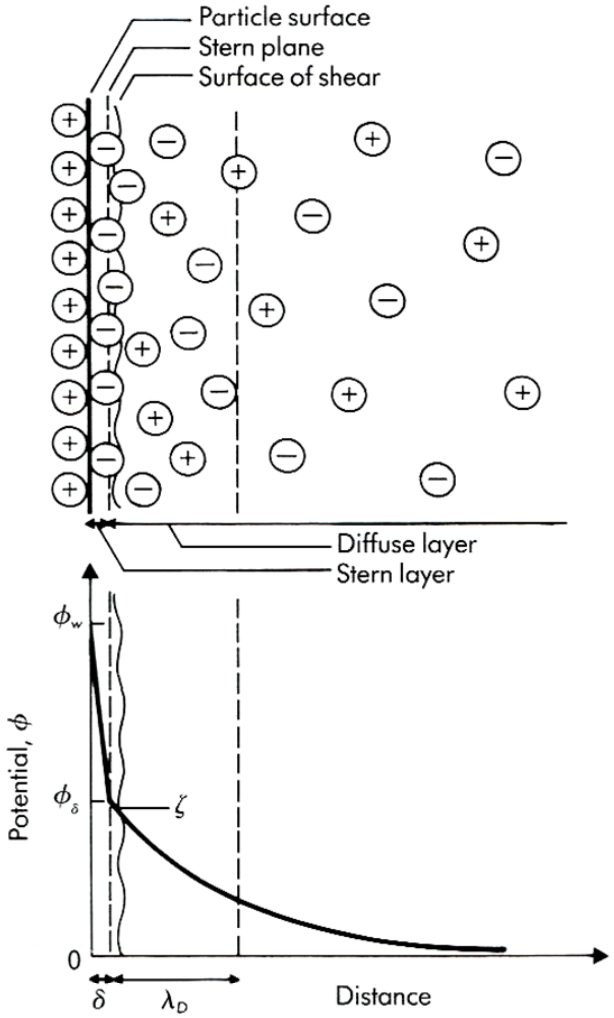

Fig. 2.2: *Charge and potential distribution in the electric double layer*

Electrokinetic phenomena, such as EOF, occur when the mobile portion of the diffuse double layer and an external electric field interact with the viscous shear layer near the surface.
If an electric field is applied tangentially along a microchannel the charged molecules of the fluid will be influenced by an electrical force. In the bulk of the fluid, where the concentration of both, co- and counterions is equal no net movement will be induced. However near the solid surface a net charge is present so also a net movement will be generated in this region. Due to viscous interaction the ions in the EDL will drag the nearby fluid and in this way create a fluid flow that is referred to as Electro Osmotic Flow.

2.1 Surface charge at solid liquid interfaces

When a solid surface is brought into contact with a liquid, most materials will develop a surface charge. Mechanisms for surface charge generation can be subdivided based on the properties of the solid surface. Generally a distinction can be made for surfaces that undergo Nernstian and non-Nernstian behavior, in which the latter can be subdivided based on the dissociation behavior of the functional surface groups.
In case of Nerstian surfaces the formation of a surface charge will primarily be due to an imbalance in cations and anions in the crystal lattice. For non-Nerstian materials the main reasons for surface charge generation are impurities on the solid surface, adsorption of ions from the solution, crystal lattice defects and pH dependent surface charge [2].

The EDL properties for Nernstian surfaces have extensively been studied especially in the case of silver iodide (AgI) and mercury [2, 3].
The generation of a surface charge on a Nernstian surface is caused by a difference in cation and anion concentration on the solid surface.
This mechanism is only present on ionic crystals and originates at the dissolution of surface groups and consequent preferential absorption of potential determining ions from the liquid.

$$AgI \xleftrightarrow{K_a} Ag^+ + I^- \qquad \text{(Eq. 2.7)}$$

For the example of silver iodide the dissolution of surface groups is shown in equation 2.7. The surface will be at the point of zero charge (p.z.c.) in case as many positive as negative ions are present at the surface. However this does not correspond to equal concentration of Ag^+ and I^- in the solution since Iodide has a higher affinity for adsorption on the solid surface.
The surface charge can thus be tuned by changing the concentration of the ions in solution, for example dissolving $AgNO_3$. Since the surface charge will depend on the concentration of Iodide and Silver in the solution these ions are referred to as potential determining ions.
When Silver is added to the solution the surface potential can be expressed by equation 2.8. Here ($Ag^+/Ag^+_{p.z.c.}$) is the ration between the actual silver concentration and the silver concentration at the p.z.c.

$$\psi_0 = 0.059 \log_{10}\left[\frac{Ag^+}{Ag^+_{p.z.c.}}\right] \qquad \text{(Eq. 2.8)}$$

Equation 2.8 can be rewritten to yield equation 2.9, the solution shows that a 10 times increase in concentration of Ag leads to a surface potential change of 60 mV. This slope of the potential as a function of the concentration is referred to as ideal Nernstian behaviour.
This expression is not limited to the case of AgI but is a general solution for Nerstian surfaces so Ag can be replaced with the potential determining ion for that specific case.

$$\psi_0 = 0.059\left(\mathrm{pAg}_{\mathrm{p.z.c.}} - pAg\right) \qquad \text{(Eq. 2.9)}$$

The mechanism of surface charge generation for Non-Nernstian surfaces is primarily pH dependent association or dissociation of surface groups[1, 4, 5].
The properties of surface functional groups can generally be subdivided in two categories:
1) Single site dissociation
2) Two site dissociation

In case of single site dissociation the surface contains only one type of ionizable surface group that acts either as an acid or a base. In case of an acid like for instance carboxyl groups that are often present at polymeric surfaces, the surface charge will be zero at a sufficiently low pH and will become more negative with an increase in pH.
The dissociation reaction can be illustrated by equation 2.10

$$AH \xleftrightarrow{K_a} A^- + H^+ \qquad \text{(Eq. 2.10)}$$

Here AH is the surface group, A^- the conjugated base and K_a the dissociation constant that is given by equation 2.11.
In equation 2.11 $a(H^+)_s$ is the proton activity expressed with the Boltzmann equation that is given by equation 2.12, where $a(H^+)_b$ is the proton activity in the bulk of the solution, e is the elementary charge, Ψ_0 the surface potential, κ the Boltzmann constant and T the temperature.

$$K_a = \frac{\left[A^-\right]a(H^+)_s}{\left[AH\right]} \qquad \text{(Eq. 2.11)}$$

$$a(H^+)_s = a(H^+)_b e^{\frac{-e\psi_0}{\kappa T}} \qquad \text{(Eq. 2.12)}$$

In the case of single site dissociation, the total number of surface sites N_s is the sum of the conjugated base and the neutral surface groups:

$$N_s = [AH] + [A^-] \qquad \text{(Eq. 2.13)}$$

Since the neutral surface sites do not contribute to the net charge the surface charge can be expressed by equation 2.14.

$$\sigma_0 = -e[A^-] \qquad \text{(Eq. 2.14)}$$

By combining the equations 2.11-2.14 the surface charge can be written as:

$$\sigma_0 = \frac{eN_s}{1 + \left(\frac{a_b}{K_a}\right) e^{\left(\frac{-e\psi_0}{\kappa T}\right)}} \qquad \text{(Eq. 2.15)}$$

Healy and White [6] introduced the parameter ξ which represents a characteristic value for a system that includes site density and electrolyte effects and is given by:

$$\xi = 10^3 N_s \frac{\kappa}{4 N_a c} \qquad \text{(Eq. 2.16)}$$

When it is assumed that all counter charge is present in the diffuse part of the electrical double layer ($\sigma_0 = -\sigma_d$), the surface potential as a function of the pH of the electrolyte can be written as equation 2.17 for Ψ_0 in mV and T= 298 K:

$$\psi_0 = 59.5\left(pK_a - pH\right) - 59.8\log\left(\frac{-\xi}{\sinh\left(0.0195\psi_0\right)} - 1\right) \qquad \text{(Eq. 2.17)}$$

It can be seen that the first part of equation 2.17 is equal to the Nernst equation and represents the ideal deprotonation of the surface groups. The second term represents the non-ideal behaviour of the surface due to the influence of the electrical double layer.
Due to the assumption that $\sigma_0 = -\sigma_d$ and thus that the surface potential equals the zeta potential the model can show some deviations from experimental values, especially at high ionic concentrations [1, 2, 4, 7].

Surfaces which show two-sites dissociation can be subdivided in different categories 3 different categories can be distinguished:
1- The surface can have two different surface groups of the same type so either two base or two acid groups.
2- The surface consists of both an acid and base dissociable group. This type of surface is also indicated as a zwitterionic surface.
3- The surface has a single amphoteric group that can act both as an acid and as a base.

The first two types might be an intrinsic property of the surface, but it can also be formed when a surface is coated and no complete surface coverage is achieved. For instance, if a glass surface is coated with an incomplete APS (aminopropylsiloxane) monolayer coating, both silanol and amino groups will be present on the surface of which the first acts as an acid and the latter as a base so that a zwitterionic surface is formed.

The relation between pH and surface charge for oxide surfaces can be described by the site binding model that was originally develop by Yates *et al.*[8] and later modified by Bousse et al. [9] for use in FET based systems.
In case of oxide surface like silica the functional groups will show amphoteric behavior. This originates in the presence of hydroxyl groups on the surface which can act both as an acid and as a base as is shown in equation 2.18 a/b with the equilibrium constants K_a and K_b.

$$ROH \xleftrightarrow{Ka} RO^- + H^+ \qquad Ka = \frac{\left[RO^-\right]\left[H^+\right]_s}{\left[ROH\right]} \qquad \text{(Eq. 2.18a)}$$

$$ROH_2^+ \xleftrightarrow{Kb} ROH + H^+ \qquad Kb = \frac{[ROH][H^+]_s}{[ROH_2^+]} \qquad \text{(Eq. 2.18b)}$$

In case of an amphoteric surface the density in surface groups is equal to the density in both acidic and basic surface groups [10], so the point of zero charge is determined by the average of both equilibrium constants K_a and K_b as shown in equation 2.19.

$$pH_{p.z.c.} = \frac{pK_a + pK_b}{2} \qquad \text{(Eq. 2.19)}$$

The total amount of charge at the surface σ_0, is given by the summation of the number of positive and negative surface groups times the elementary charge e, as shown in equation 2.20.

$$\sigma_0 = -e[B] = -e\left([SiO^-] - [SiOH_2^+]\right) \qquad \text{(Eq. 2.20)}$$

In section 2.1 it was explained that the formation of surface charge will be screened in the EDL with an equal amount of charge but with opposite sign. Since both layers have an equal potential and charge associated with them they can be modeled as a capacitor C_{EDL} (Eq. 2.21)

$$-\frac{d\sigma_0}{d\psi_0} = \frac{d\sigma_{EDL}}{d\psi_0} = -C_{EDL} \qquad \text{(Eq. 2.21)}$$

The change in surface charge as a function of the change in pH can be written as:

$$\frac{d\sigma_0}{dpH_s} = -e\frac{d[B]}{dpH_s} = -q\beta_{\text{int}} \qquad \text{(Eq. 2.22)}$$

Here pH_s is the surface pH which can be related to bulk pH with the use of the Boltzmann equation (equation 2.23) and β_{int} is the intrinsic buffer capacity of the surface. This parameter was introduced to explain the pH

dependent sensitivity of ISFETS [11-13] and acts to keep the surface pH constant upon a change in bulk pH by acting as a source or sink for protons.

$$pH_s = pH_b + \frac{ze\Psi_0}{2.3\kappa T} \qquad \text{(Eq. 2.23)}$$

By a combination of equations 2.21 and 2.22 a relation between the surface potential and the surface pH can be obtained (equation 2.24). This relation is especially useful in FET based structures where surface potential measurements are used to measure for instance solution pH. In these cases a large response of the surface is needed which requires a large ratio between β_{int} and C_{EDL} as can be seen from equation 2.24. However when a Field Effect Flow Control (FEFC) structure is used to control the zeta potential the opposite is the case and the ratio between β_{int} and C_{EDL} should be as low as possible as will be discussed in section 4.1.1.

$$\frac{d\Psi_0}{dpH_s} = \frac{d\Psi_0}{d\sigma_0}\frac{d\sigma_0}{dpH_s} = \frac{-e\beta_{\text{int}}}{C_{EDL}} \qquad \text{(Eq.2.24)}$$

The buffering capacity of the oxide surface groups depends on the ability of the surface to either donate or adsorb protons. The value for the buffer capacitance can thus be calculated as a function of the association and dissociation constant of the surface silanol groups K_a and K_b as well as the surface site density N_s as shown in equation 2.25.

$$\beta = N_s \frac{K_b a_{H_S^+}^2 + 4K_a K_b + K_a K_{b+}^2}{(K_a K_b + K_b a_{H_S^+} a_{H_S^+}^2)^2} 2.3 a_{H_S^+} \qquad \text{(Eq. 2.25)}$$

The relation between pH dependent surface charge generation of silica and the electrokinetic phenomena that occur at the silica/liquid interface are known to be unusually small compared to different solid surfaces [1]. Possible explanations for this that are suggested in literature are the formation of a gel-like structure at the solid liquid interface [14, 15] or the adsorption of indifferent counterions on the solid surface [16-18].

3 Characteristics of Electro Osmotic Flow

Electro Osmotic Flow (EOF) refers to the bulk movement of an aqueous solution past a stationary solid surface due to an externally applied electric field. EOF belongs to the electrokinetic phenomena occurring as a result of the presence of an electric double layer. The electric double layer forms because of an interaction of ionized solution with static charges on dielectric surfaces. In pressure-driven systems parabolic flow profiles arise as shown in Fig. 2.3b. The frictional forces of the mobile phase interacting at the wall of the microchannel result in radial velocity gradients throughout the microchannel. As a result, the fluid velocity is the greatest in the middle of the microchannel and a substantial pressure drop along the microchannel is formed.

a)

b)

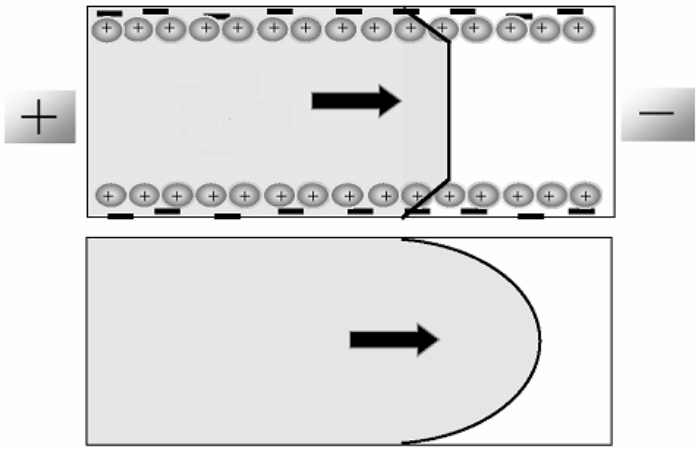

Fig. 2.3: Comparison of velocity profiles of a) EOF b) hydrodynamic flow

In contrast to this, electroosmotically-driven systems, where the double layer thickness is very small compared to the width of the capillary, do not provide a parabolic flow profile as the pressure-driven systems do. EOF is generated uniformly along the length of the microchannel as illustrated in Fig. 2.3a. there is no pressure drop in the microchannel. All of the solute molecules experience the same velocity component caused by EOF regardless of their cross-sectional position in the microchannel. Therefore, a plug-like flow is generated. This can be used to transport fluid, with minimal hydrodynamic force in the microfluidic devices.

The velocity v_{EOF} of the EOF is described by the Helmholtz-Smochulowski equation:

$$v_{EOF} = \frac{\varepsilon_0 \varepsilon_r \varsigma}{\eta} E_x \qquad \text{(Eq. 2.26)}$$

In equation 2.26, η is the dynamic viscosity, ζ the zeta potential and E_x the electric field gradient along the channel.
The electroosmotic mobility μ_{EOF} is given as follows:

$$\mu_{EOF} = \frac{\varepsilon_0 \varepsilon_r \varsigma}{\eta} \qquad \text{(Eq. 2.27)}$$

so that the electroosmotic volume flow q_{EOF} through the channel is defined as:

$$q_{EOF} = \frac{\varepsilon_0 \varepsilon_r \varsigma}{\eta} \frac{A}{L} U \qquad \text{(Eq. 2.28)}$$

Here A is the cross-sectional area of the channel, L its length, and U the potential difference along the channel length.
These equations show that the EOF is strongly dependent on the zeta potential. It has to be taken into account that this potential is not constant and it is influenced by several factors. The zeta potential is determined mainly by the surface charge of the walls, which is pH-dependent. As a consequence of this pH-dependence, the electroosmotic volume flow q_{EOF} also depends on the pH. For instance, the charge on the wall of glass capillaries that contain a simple aqueous electrolyte solution arises from the dissociation of the silanol groups (-SiOH) or the preferential adsorption of OH^- ions. For glass, which mainly contains silicon dioxide (SiO_2), the sign of the ζ-potential is invariably negative if the pH of the electrolyte is higher than the point of zero charge which is known to be around pH 2 [19]. In addition, the ζ-potential is influenced by the ionic strength of the electrolyte solution since a higher ionic strength leads to a compression of the electric double layer. As a result of this compression the ζ-potential will be reduced. Besides, a chemical modification of the capillary wall, the material of the capillary wall, the addition of surface-active species or organic modifiers to the buffer and an applied external voltage are parameters influencing the ζ-potential. The influence and the usage of an external gate voltage will be discussed in the following sections.

3.1. Measurement of zeta potentials

The zeta potential is an important parameter in microfluidic systems. Electrokinetic processes like EOF scale with the magnitude of this potential. Therefore its important to be able to influence and characterize this potential. For application in microfluidic systems, a technique that is able to measure with both a high spatial and time resolution without the need of an elaborate measurement setup would be ideal.
In the next section some commonly applied techniques will be reviewed and the possibility for application in microfluidic systems will be discussed.

3.1.1 Streaming Potential and Streaming Current

For the determination of the zeta potential at the solid liquid interface both Streaming Potential (SP) and Streaming Current (SC) are extensively studied and applied techniques. In both cases a pressure difference is applied over a channel or capillary which results in the movement of the diffuse part of the EDL due to viscous drag. When SP is used, measurements are performed at high input impedance so that no external current is running and ions accumulate upstream of the channel which results in a potential difference that can be measured and directly related to the zeta potential. When SC is applied measurements are performed at low input impedance so a current can be measured that relates to the zeta potential.
The process of SP is schematically illustrated in Figure 2.4

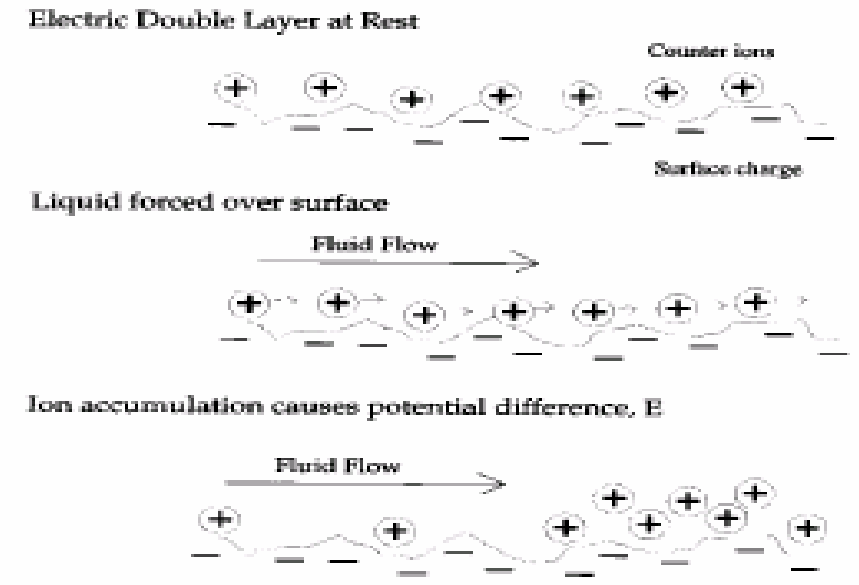

Fig. 2.4: *Schematic overview Streaming Current measurement.*

When a pressure difference is applied over a channel, this will result in flow with a hyperbolic flow profile given by the Poiseuille equation.
Due to viscous drag forces the diffuse part of the EDL will be carried downstream of the fluidic channel. The convection of the net charge in the EDL results in a streaming current that is proportional to the pressure gradient applied over the channel and the cross sectional area of the channel. When the streaming current is measured the zeta potential can be solved with equation 2.28. The equation however is limited to the case of a homogeneous distribution of the surface charge over the complete channel surface and the assumption of a linear decay in the velocity of the pressure driven flow over the electrical double layer. These assumptions limit the application of the equation to round capillaries or parallel plates or porous plugs in case the double layer thickness is small compared to the pore diameter. At more complex geometries the aforementioned assumptions are no longer valid due to the influence of corner surfaces. Electrokinetic flow through more complex geometries has been studied in case of elliptical [20] and square channels [21, 22] and has been shown to be dependent on the aspect ratio and dimensions.

In equation 2.29 ε_0 and ε_r are respectively the dielectric constant of vacuum and of air, A is the cross section area, L is the length of the channel, ΔP the applied pressure difference between the inlet and outlet of the channel and I_s the measured streaming current. Figure 2.5 shows the measurement conditions for determination of the SC or SP.

$$\varsigma(I_s) = \frac{I_s}{A} * \frac{\eta}{\varepsilon * \varepsilon_0} * \frac{L}{\Delta P} \qquad \text{(Eq. 2.29)}$$

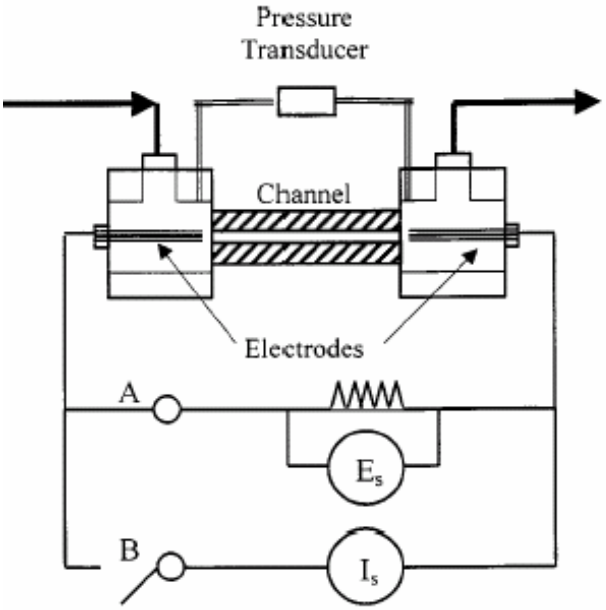

Measurement	I_s	V_s
A	Open	Closed
B	Closed	Open

Fig. 2.5: *Measurement setup for the determination of streaming current and streaming potential .*

When SP is used, measurements are performed at high input impedance so that no current is running through the measurement setup. The ion flux due to the SC thus accumulates downstream of the channel and leads to the build up of a potential which in turn leads to a counter conduction current through the channel electrolyte until an equilibrium is set according to equation 2.30. Here I_s and I_c are respectively the streaming current and counter conduction current.

$$I_s + I_c = 0 \qquad \text{(Eq. 2.30)}$$

The equilibrium between the induced streaming current and the counter conduction current is called the streaming potential and can be related to the zeta potential according to equation 2.31. In this equation K is the conductivity of the channel electrolyte.

$$\xi(V_s) = \frac{V_s \eta}{\mathrm{K} \varepsilon \varepsilon_0 \Delta P} \qquad \text{(Eq. 2.31)}$$

The counter conduction current I_c can attribute to errors in the determined zeta potential in several ways.
The streaming potential build up can lead to a counter EOF which leads to a higher apparent viscosity of the solution and thus an increased hydraulic resistance of the fluidic channel. This effect increases with a decrease of the channel dimensions and can lead to deviation in the derived zeta potential.
An other major effect that should be taken into account when SP is used to characterize surfaces is the influence of surface conduction on the counter conduction current. This effect also starts to become more dominant at smaller channel dimensions as well as higher channel resistances.

Surface conduction can be defined as an increased conductivity at the solid liquid interface compared to the conductivity of the bulk electrolyte.
This can be attributed to an increased conduction through the electrical double layer due to the excess of charge carriers near the surface or conduction through the solid surface itself. The latter can also be the case when the solid surface itself is not conducting, but if there is charge transfer between the solid and the liquid or if the solid surface is porous.
The effect of surface conduction leads to a higher counter conduction current and thus in a shift in the equilibrium with the streaming current towards lower values. This in turn results in lower deduced values for the zeta potential if surface conduction is unaccounted for.
The influence of the surface conduction can be included in equation 2.31 by including the surface conduction in the channel resistance.
Since the surface conduction and the bulk electrolyte conduction are in parallel, both contributions can be added up to yield the net conductivity.
The channel resistance is then given by equation 2.32.

$$R_{tot} = \frac{1}{\frac{K_b * A}{L} + \frac{K_s * C}{L}} \qquad \text{(Eq. 2.32)}$$

The first and second terms in the denominator of equation 2.31 are respectively the contribution of the bulk and surface conduction. In the equation L, is the channel length, A the cross section area, C the circumference of the channel and K_b and K_s are respectively the bulk and surface conductivities.
With the use of equation 2.32 the attribution of the surface conductivity can be determined by measuring the channel resistance and determination of the electrolyte conductivity in a bulk solution. From the measured conductivity the channel resistance can be calculated if the geometry is known.
When equation 2.31 is now multiplied by the ratio between the calculated and the measured resistances, the zeta potential can be determined without the influence of the enhanced channel conductivity.
A drawback of the latter procedure is that the dimensions and shape of the channel have to be known precisely; if this is not the case other methods are available to determine the value for K_s.
Werner et al. [23, 24] developed a procedure where the height of the channel was varied by a spacer between two parallel plates; the conductivity was then measured as a function of the height. If the conductivity is then extrapolated to h=0 the surface conduction can be found.
A similar approach can be used where the surface conduction is determined by measuring at different ionic strength and thus at different ratios between K_s and K_b when extrapolating to an ionic strength of zero the value for K_s can be found. However these procedures have disadvantages associated with them as well. In the first case either the height or width of the channel should be variable which limits the application to parallel plates. In the second case the assumption is made that the contribution of the surface conduction is independent of the ionic strength, which is questionable in the case that the enhanced conduction takes place through the diffuse part of the electrical double layer.
When SP and SC are compared the determination of SC will be less elaborate because of the absence of the influence of surface conduction. A drawback is however that the currents that should be measured are in the range of approximately 1 nA per kPa pressure difference, while for SP the

signal is about 100 mV per kPa pressure which will be easier to detect. However both methods lack spatial resolution in the measurement of the zeta potential so in the case of heterogeneous surface charge only average values can be determined.

3.1.2 Current monitoring in Electro Osmotic Flow

In this method for the determination of the zeta potential a channel is filled with an electrolyte solution. Subsequently the solution at the inlet of the channel is removed and replaced by a solution of the same composition but with a different ionic concentration. When an electrical field is applied over the channel the solution at the inlet reservoir will replace the solution in the channel due to the EOF [25, 26]. The procedure is schematically illustrated in figure 2.6. In the figure the first current plateau represents the current at an EOF with the first electrolyte solution, at the start of the slope the solution with a higher conductivity is applied at the inlet of the channel. At the second plateau the solution has completely replaced the initial electrolyte in the channel by the EOF. The time between the two plateaus gives the time for the EOF to cover the length of the channel.

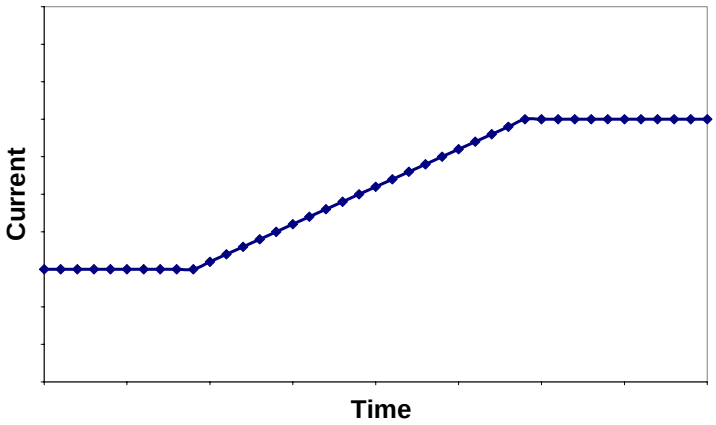

Fig. 2.6: *Schematic illustration of the current monitoring method.*

While this replacement occurs, the length of the mixing zone and the lengths of the two sections having the initial concentrations c_1 and c_2 of the two electrolytes change with time. The electrical resistance of the liquid during substitution is defined as follows:

$$R = \sum_{i=1}^{n} R_i \qquad \text{(Eq. 2.33)}$$

with

$$R_i = \frac{L_i}{c_i \cdot \lambda_i \cdot A} \qquad \text{(Eq. 2.34)}$$

Where L_i is the length of section i, c_i is the concentration of the *i*th section, and λ_i is the molar conductivity of section i. So, the electrical resistance R_i of the liquid in the capillary will change with time during electroosmosis since the overall liquid conductivity in the capillary is changed, resulting in a change in the electrical current flow. When the second solution has completely replaced the first one, the current through the capillary reaches a plateau. The concentrations c_1 and c_2 should not differ too much to assure a constant and uniform zeta potential and ionic distributions, resulting in temporally constant EOF. The average EOF velocity v_{EOF} can be calculated by the following equation

$$v_{eof} = \frac{L}{\Delta t} \qquad \text{(Eq. 2.35)}$$

In equation 2.35 v_{EOF} is the average electroosmotic velocity, L the total length of the capillary and Δt the time required for completion of the replacement that is determined by the current record.
When the average flow velocity is determined the zeta potential can be determined by modifying the Smoluchowski equation (2.36)

$$\zeta = \frac{\eta * v_{eof}}{\varepsilon_0 \varepsilon_r * E} \qquad \text{(Eq. 2.36)}$$

Since the zeta potential is roughly proportional to the square root of the ionic concentration, the concentrations for the 2 solutions should be chosen such that the influence on the zeta potential is minimal and will be constant in each segment of the channel with concentration c_i. Furthermore it has to be considered that the electric field strength will be proportional to the electrical resistance of each plug. Since the resistance will thus not be constant along the length of the channel also the EOF velocity will vary with the longitudinal

direction [27]. Figure 2.7 gives a typical measurement with a simulated curve based on the previous assumptions. The accuracy of this technique is given by the resolution of the current-time response, which is governed by the nature of the solutions employed. For very low EOF one has to take into account that the two zones of different ionic concentration inter-diffuse, leading to a smoothened current curve, with no clear points to identify the start and end of the conductivity transition. For example a 10 % error would occur if the transition time is of the order of $10*L^2/D$.
The main advantage of this measurement method is its simplicity. The technique can be integrated in a measurement set up with very little infrastructure and takes little time. The method however includes the drawback that it only gives a time average zeta potential with no spatial resolution.

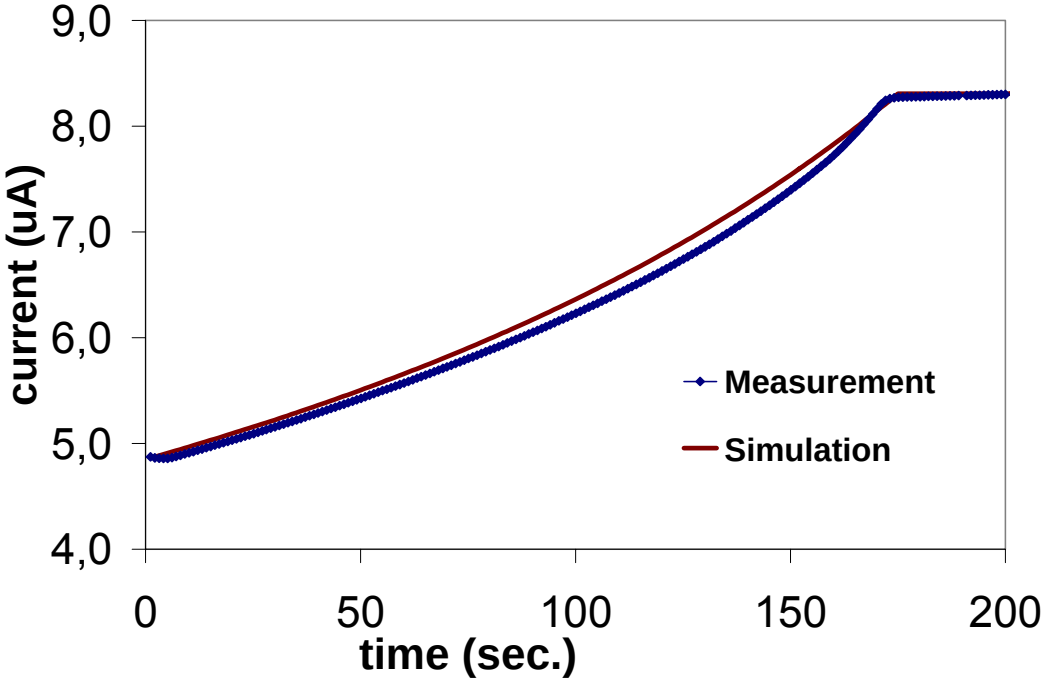

Fig. 2.7: *Current vs. time measurement with a simulation of the current–time relation based on measured conductivity values of 0.4 and 0.7 mS/cm and a constant flow rate.*

3.1.3 Fluorescent dye imaging

A commonly used technique for flow visualization is the use of fluorescent dyes. By tracking the movement of a plug injected into a channel information about local flow fields can be obtained.

However, diffusion limits the resolution of the technique due to distortion of the sample plug. In case of a uniform EOF the dye plug will be distorted due to diffusion to a thickness δ that is given by equation 2.37, where D is the diffusion coefficient and t the time.

$$\delta \approx \sqrt{(2Dt)} \qquad \text{(Eq. 2.37)}$$

However, in case of linear gradients in zeta potential extra dispersion will occur due to differences in flow velocity. Datta and Kotamarthi [28] calculated dispersion rates in this case.
In case a heterogeneous surface charge is present in a system the velocity profile will consist of an EOF component and a pressure driven flow that will lead to extra dispersion of the plug due to differences in flow rate.
Taylor *et al.* [29, 30] derived equation 2.38 that gives the dispersion rate due to the hydrodynamic component.

$$\sigma^2 = 2Dt + 2\left(\frac{r_0^2 \bar{v}_{pres}}{48D}\right)t \qquad \text{(Eq. 2.38)}$$

The influence of dispersion limits the use of fluorescent dyes to yield flow velocity information to the time just after injection of the fluorescent plug.
However, this drawback can be reduced by exciting a dye at a specific location inside a microchannel. Lempert et al. [31] introduced the use of caged dyes that can be introduced homogenously into the system and subsequently be excited into a specific location by use of a laser, so that complex plug injection systems become redundant and dispersion due to diffusion is minimized. The technique was later modified for the use in microsystems by Paul *et al.* [32] and further develop for use in large scale flows [33, 34].
A significant drawback of fluorescent imaging is however the influence of the electrophoretic component of the velocity field. Dependent on the pH of the solution dyes will be charged and thus move in the electric field with a velocity proportional to its charge and the electrical field.

3.1.4 Particle tracking velocimetry and particle image velocimetry

In contrast to the flow monitoring methods discussed previously, both Particle Tracking Velocimetry (PTV) and Particle Image Velocimetry (PIV) can be used to resolve velocity profiles as well as average flow in micro channels.
In both methods tracer particles are added to a solution, by monitoring the velocity and trajectory of the particles, information about the flow profile can be extracted.
With PTV low densities of tracer particles are used so that individual particles can be tracked, while in PIV higher densities are used and velocity profiles are extracted by analyzing the movement of ensembles of particles.
PTV has the advantage that it is relatively easy to use. With the use of a simple digital camera the position of a single bead can be determined at different time frames.
With the use of equation 2.39 the average flow velocity can then be determined. In the equation Δx is the displacement and Δt the time difference.

$$v = \frac{\Delta x}{\Delta t} \qquad \text{(Eq. 2.39)}$$

A drawback of PTV is the limited information that can be extracted since low tracer densities are used. So the method only gives useful information if the local gradients in velocity are limited, like in a uniform EOF profile, where only average values are of interest.

If more information about local flow fields is desired, PIV is a more suitable technique. PIV was developed In the early 90's [35-39] and images were initially acquired analogue. Later on the theory was developed for digital imaging [40, 41] and introduced for the use in microfluidics [42, 43].
In PIV the fluid motion is deduced by monitoring the motion of ensembles of tracer particles, these particles are considered ideal tracer particles if they fulfill the properties that [44]:
- The particles exactly follow the fluid motion.
- They do not influence the fluid motion.
- The particles do not interact with each other.

For a PIV measurement initially two timeframes are captured with a short time interval Δt, subsequently sub-regions are defined in the image and cross correlated to yield the average displacement. Alternatively two time frames can be captured in a single image by double exposing within the time frame of the single image so that autocorrelation of the image can be used to determine the displacement. A drawback of the latter method however, is that there is no information about the direction of the displacement acquired. This artifact is generally solved by exposing an image three times with asymmetric time intervals.
In figure 2.8 the principle of PIV is schematically illustrated for two recorded images. The initial recording is shown which is subdivided into smaller Interrogation Region (IR). In the figure the IR of the first image is indicated by S_1 and the image recorded after a time interval Δt as S_2.

.

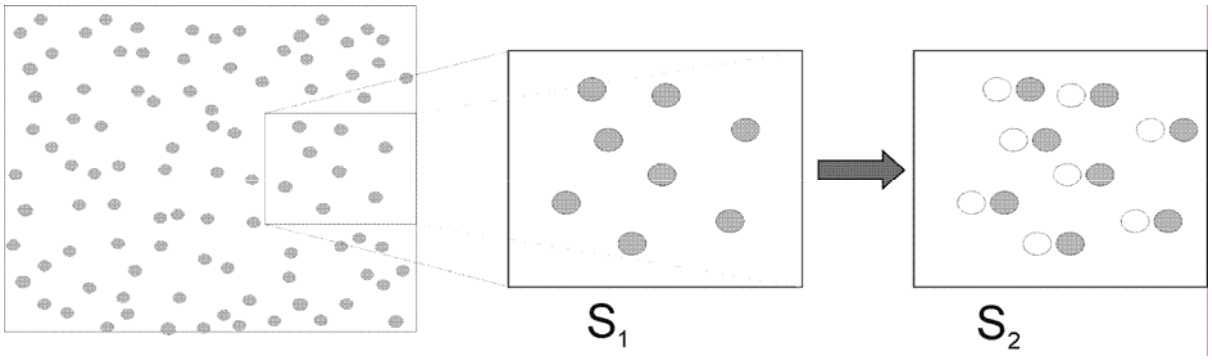

Fig. 2.8: *Schematic illustration of the principle of Particle Image velocimetry.*

The displacement in an IR is generally obtained by cross-correlating of the first image with the second image [45].

In figure 2.9 a typical correlation peak is plotted as a function of the position. The peak in the correlation indicates the displacement of second image compared to the first one and thus the average displacement of the beads in the IR window. With the aid of equation 2.37, now the average velocity can be determined. The PTV and PIV techniques will be discussed in more detail in chapter 8.

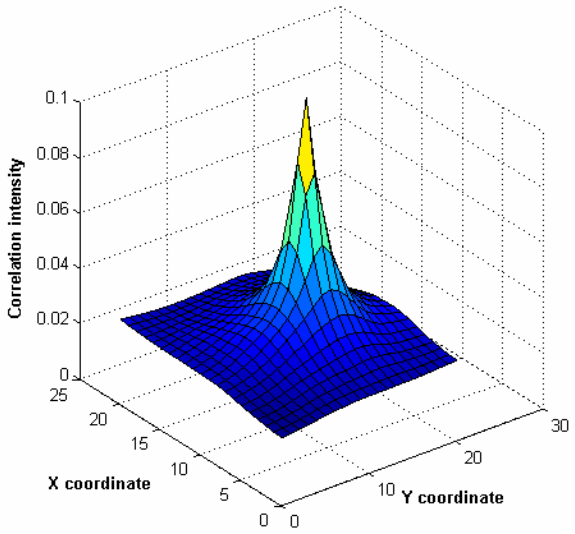

Fig. 2.9: Cross correlation peak for the determination of the displacement

3.2 Concentration dependence of Electro Osmotic Flow

In section 2.1 the relation between the diffuse double layer potential and the electrolyte concentration was expressed by equation 2.5 which showed a decrease in zeta potential with the square root of the concentration. As more counterions are available to screen the surface charge the EDL thickness will decrease which leads to a lower zeta potential.
This implies that the EOF will also depend on the electrolyte concentration.
Figure 2.10 shows the relation between the zeta potential for sodium acetate/acetic acid buffers of pH 7 for different concentrations in glass chips. It can be seen that the zeta potential increases with a decrease in concentration as expected. Furthermore, the plot shows that the measurement uncertainty increases at lower concentrations. This is due to the measurement method. The zeta potentials were measured with the current monitoring method. At lower concentrations, lower absolute differences in concentration were applied to avoid an influence of the concentration on the zeta potential. However, at lower absolute differences also the resolution of the measurement decreases which results in a lower accuracy.

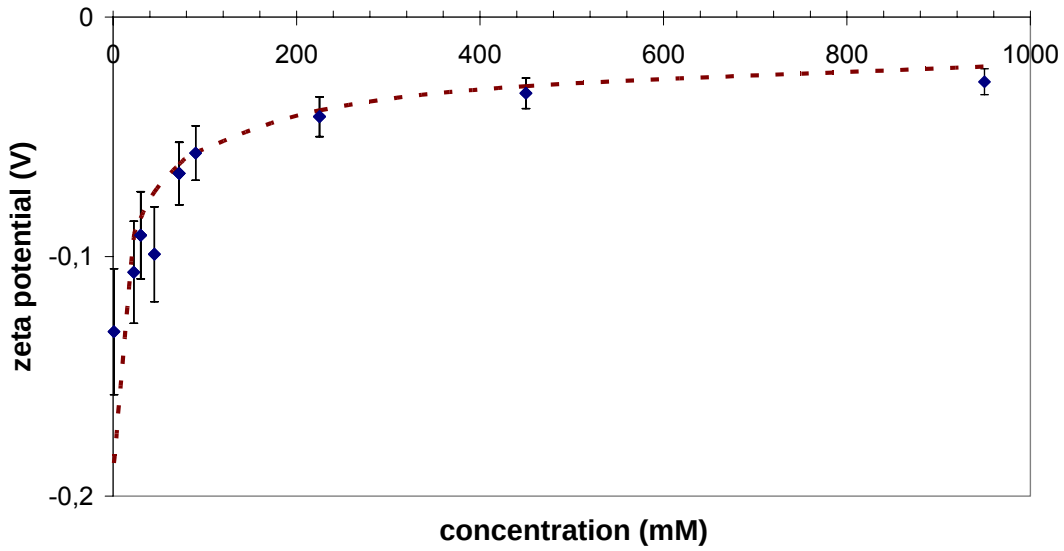

Fig. 2.10: *Relation between the zeta potential and concentration for glass chips as a function for sodium acetate buffers of pH 7 (dots) and the theoretical expected trend (dotted line).*

The course of decay in zeta potential with an increase in concentration can be explained with a simple electrical model as shown in figure 2.11. As explained in section 2.1, the zeta potential is defined as the potential at the interface of the Stern and diffuse double layer which can both be modeled as capacitors.
The Stern layer is generally concentration independent with a magnitude of 20 μF/cm^2 while the diffuse capacitance is given by equation 2.41.

$$C_d = \left(\frac{2z^2 q^2 \varepsilon_o \varepsilon_r n_o}{\kappa T} \right)^{0.5} A\, COSh\left(\frac{zq}{2\kappa T} \zeta_0 \right) \qquad \text{(Eq.2.41)}$$

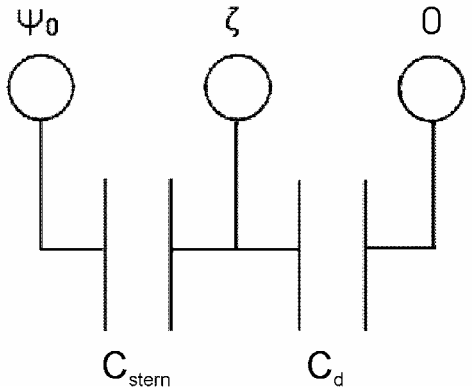

Fig. 2.11: *Electrical model for the determination of the relation between the zeta potential and electrolyte concentration.*

It can be seen from the above model and equation 2.41 that the potential distribution will change as the diffuse capacitance will change as a function of the concentration. The zeta potential as a function of the diffuse capacitance can be expressed by equation 2.42 at a constant surface potential.

$$\varsigma = \frac{C_{st}}{C_{st} + C_{dif}} \Psi_0 \qquad \text{(Eq. 2.42)}$$

Based on the previous equation, the theoretical curve of the zeta potential as a function of the electrolyte concentration was plotted in figure 2.10, indicated by the dashed line. The surface potential was determined to be -0.25 V by a least squares difference method applied to the measurements results.

3.3 Electro Osmotic Flow in organic solvents

The zeta potential of Pyrex glass in different organic solvent has been determined with the current monitoring method. The use of organic solvents in stead of aqueous electrolytes can have several advantages in EOF systems; especially for application in electrophoretic separation the use of organic solvents has gained attention. The effect of different acid-base behavior, increased effect of hydrophilic interactions or reduced adsorption on the solid walls offers advantages over conventional aqueous solvents [46-48]. Furthermore, when EOF is used for instance in drug delivery the

choice of the solvent may depend on the solubility of the specific drug to be delivered. Also, in case of external control of EOF by radial electrical fields the effect of the external field on the flow scales inversely proportional to the dielectric constant of the solution. Since this value is high in the case of water (78.5), a different choice of solvent can be favorable.
Figure 2.13 shows the measured zeta potentials for methanol/water mixtures at different mixture ratios. Since the current monitoring method was applied in the measurements, the determined zeta potentials were corrected for the influence of the mixing ratio on the viscosity. It can be seen that the zeta potential is strongly dependent on the mixture ratio. The course of the curve can be explained by two competing processes. First of all, the dielectric constant of the medium is a function of the mixture ratio. The dielectric constant of water and methanol are respectively 33 and 78.5 so the value for the mixture will be the average of the two times the mixture ratio. The effect of the dielectric constant acts on the Debye length as can be seen from equation 2.9 and with this on the zeta potential. In a less polarizable medium, the Debye length will become larger and thus also the zeta potential will increase in case of a constant surface potential. As the methanol concentration increases the zeta potential decreases to more negative values after a minimum around a concentration of 40 %. This decrease is caused by the influence of methanol on the solution pH. Most acids show a lager pKa value in organic solvents than in water due to the poor solubility of anion in most non- aqueous solvents [48]. This effect will cause a higher apparent pH and with this a more negative surface- and zeta-potential as the methanol concentration increases.

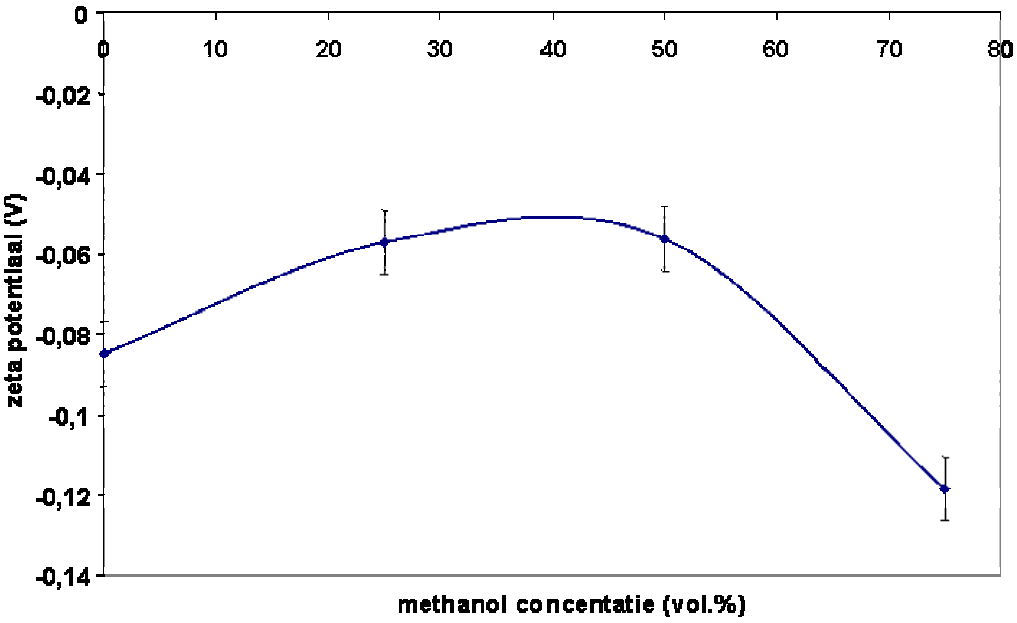

Fig.2.13: *Zeta potential as a function of the water/methanol ratio for 40-50 mM sodium acetate buffers of pH 7.*

3.4 Modification of Electro Osmotic Flow

The EOF in a microchannel is directly related to the surface charge at the solid /liquid interface as was discussed in section 2. This surface charge is mainly dependent on the pH and exhibits rather high values at neutral or basic pH. However, for control of the zeta potential, especially in silica, a low offset value for the zeta potential and thus the surface charge is mandatory (chapter 7) which limits the applicable buffers to the acidic pH range in case of silica. Furthermore, if biocompatible surfaces are needed, or adsorption of analytes from the solution has to be avoided, the surface properties of silica are not favorable.

The aforementioned drawbacks can be overcome by a surface modification of the silica surface by either dynamic or fixed coatings. For use in a FEFC structure a coating should exhibit ideally a low offset in zeta potential over a wide pH range and exhibit hydrophilic surface properties.

In case of silica surfaces coatings have especially been investigated for application in electrophoretic separation techniques to control or stabilize the EOF mobility [49-51]. The suppression of EOF has been demonstrated by either reduction of the surface charge [52-54] or by coating with a viscous layer like polyacrylamide to diminish the EOF [55-57]. The latter however is poorly applicable in FEFC since modification of the zeta potential

will no longer alter the flow. Compared to fixed surface coatings the addition of a dynamic coating to the background electrolyte is much easier to apply. In general a surface active species is added to the buffer [58-60] and subsequently absorbed to the solid surface. A drawback however is that in some application contamination of the buffer with surface active species is unwanted.

3.4.1 Zeta potential of silica

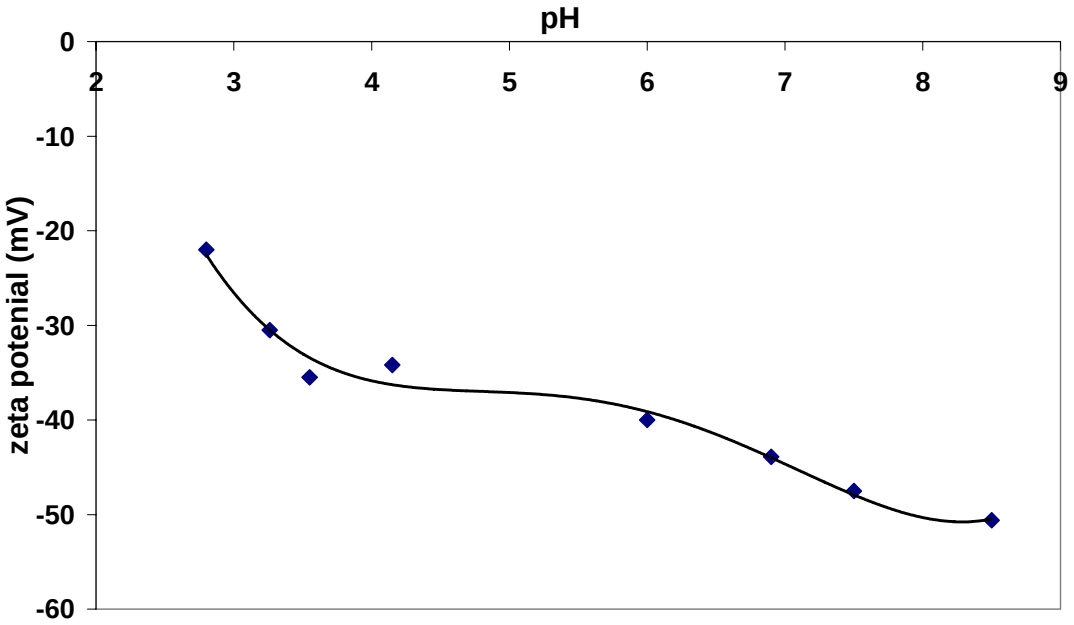

Fig.2.14: *zeta potential of PECVD silica as a function of the electrolyte pH.*

The zeta potential of PECVD silica films was measured with the current monitoring method. Sodium acetate buffers were used up to pH 6, from pH 7 on sodium acetate buffers were utilized. Silica acts as an amphoteric surface since the surface silanol groups can act both as an acid and as a base. The surface reactions can be described by equations 2.18a/b with R replaced by Si. The resulting equilibrium constants, K_a and $K_{b,}$ are respectively 6 and -2 [61], so that the expected p.z.c. is around 2 as can be seen from equation 2.19. The trend in figure 2.14 shows a plateau in the zeta potential around pH 6 which corresponds to the pK_a value of reaction 2.18a. Towards lower pH the zeta potential becomes less negative towards the p.z.c. around pH 2. With an increase in pH, the zeta potential becomes increasingly negative due to the increased level of negatively charged SiO^- groups at the surface.

3.4.2 Dynamic and fixed surface coatings

3.4.2.1. Poly Ethylene Glycol

Poly Ethylene Glycol (PEG) coatings can be applied to control the EOF [62, 63] and leads to hydrophilic surface properties which makes it very suitable for use in microfluidic systems.
The electrokinetic properties are known to strongly depend on the solvent plus type and concentration of ions in the solution [64, 65]. Especially in organic solvents, the EOF can be significantly reduced or reversed. For aqueous solutions, a strong reduction in EOF has been reported [62]. The nature of the ion dependent EOF is due to cation adsorption onto the solid. Surface hydroxy groups form structures that adsorb cations in a similar way as cation complexation occurs by crown ethers [65, 66]. This causes a surface charge that depends on the size and concentration of cations in the solution. The zeta potential of PEG coated chips has been measured with the current monitoring method. Chips have been coated with PEG by placing a chip overnight in a solution of toluene with 0.1 vol. % poly (ethylene glycol)-silane.
The coated chips show a near constant zeta potential over almost the entire pH range. This is probably due to the counterions dependence of the surface charge. However, the large magnitude of the zeta potential makes PEG a less suitable candidate for application in FEFC structures.

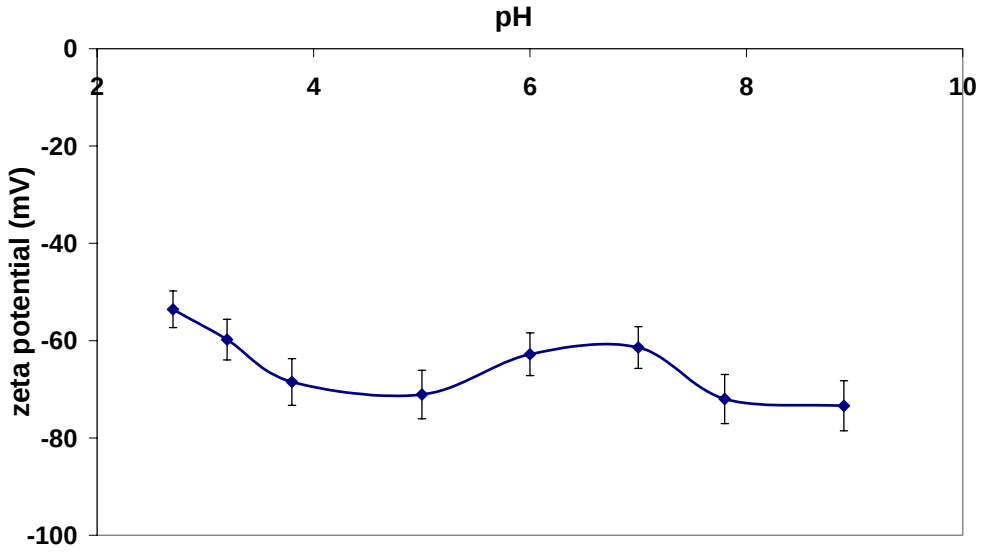

Fig 2.15: *zeta potential of PEG coated channels as a function of the pH*

3.4.2.2. Amino Propyl Siloxane

Amino Propyl Siloxane (APS) coatings have been applied with two different procedures. Initially chips were placed in a solution of ethanol and 0.3 vol. % 3-(triethoxisilyol) propylamine for 1 hour at 60 ^{0}C. In a second approach, chips were placed overnight in the same solution at room temperature.
Figure 2.16 gives the zeta potentials measured with the current monitoring method for glass chips coated with APS as a function of pH. Series 1 is measured after coating for 1 hour at 60 ^{0}C, series 2 was measured after coating overnight at room temperature.

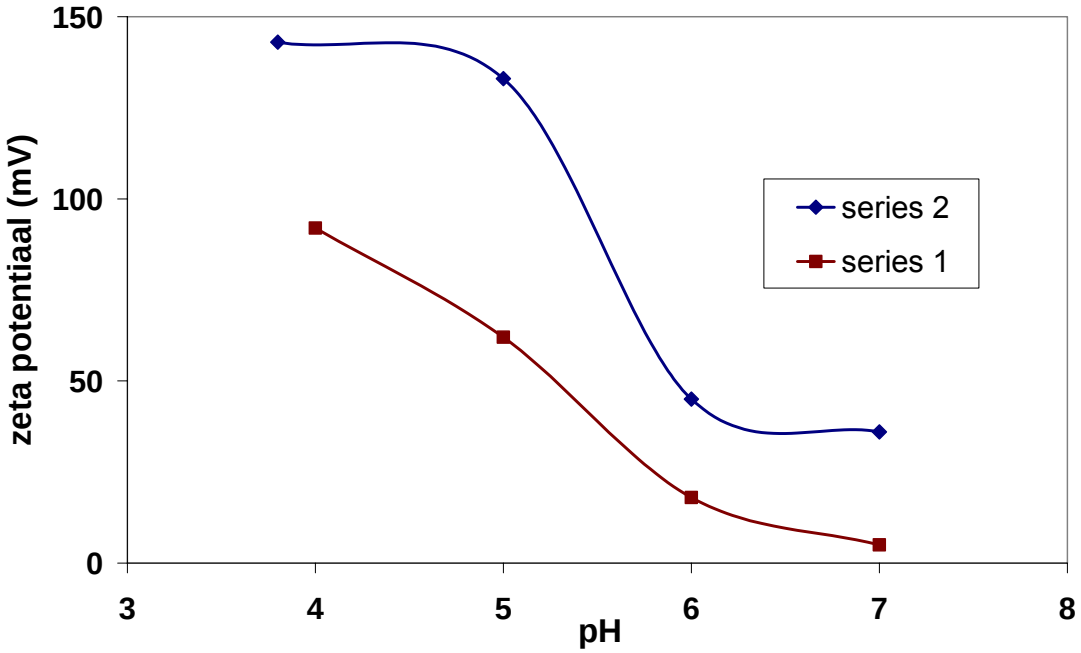

Fig.2.16: *zeta potential as a function of pH for two different coating procedures.*

The measured values for the zeta potential show a reversal of the surface charge for both coating procedures over the entire measured pH range. This is caused by deprotonation of amino groups of the APS.
When measurements were performed in the high pH range an EOF in the direction of the cathode was measured with a zeta potential that corresponds to the natural zeta potential of silica. This indicates that the monolayer coating is unstable at basic pH and is etched away.
It is clear from figure 2.16 that both coating procedures result in different values for the zeta potential. In comparison to series 2, the overall zeta

potential of series 1 is smaller. Also the change in zeta potential around the pKa value of the amino groups is less pronounced.
This can be explained by a difference in surface coverage for both coating procedures. In the case of series 1 a lower surface coverage of the APS coating was achieved, so the surface charge of the solid liquid interface has two components, a negative contribution of deprotonation of unbound silica surface groups and a positive contribution of amino surface groups.

3.4.2.3 Hexa Methyl Di Silazane

Chips have been coated with Hexa Methyl Di Silazane (HMDS) by placing a chip overnight in a solution of toluene with 0.1 vol. % Hexamethyldisilazane.
The zeta potential has been measured with the current monitoring method; the values are plotted in figure 2.17 as a function of the pH. Sodium acetate buffers have been used until pH 7. At higher pH values sodium phosphate has been used as a buffer. HMDS has functional methyl groups which have no expected pH response in the measured pH regime. From the measurements it can be seen that the p.z.c. is around pH 2.5 which is close to p.z.c. of silica. From this it can be concluded that in this pH regime silanol groups are responsible for the pH dependent surface charge due to an incomplete surface coverage of the coating. However, above pH 5 the zeta potential is lager than that measured for bare silica so that the extra component should be due to the HMDS itself. This can be attributed to HMDS molecules that did not covalently bound to the silanol groups so that the functional NH group that should bind with the surface, is available to contribute to the surface charge.

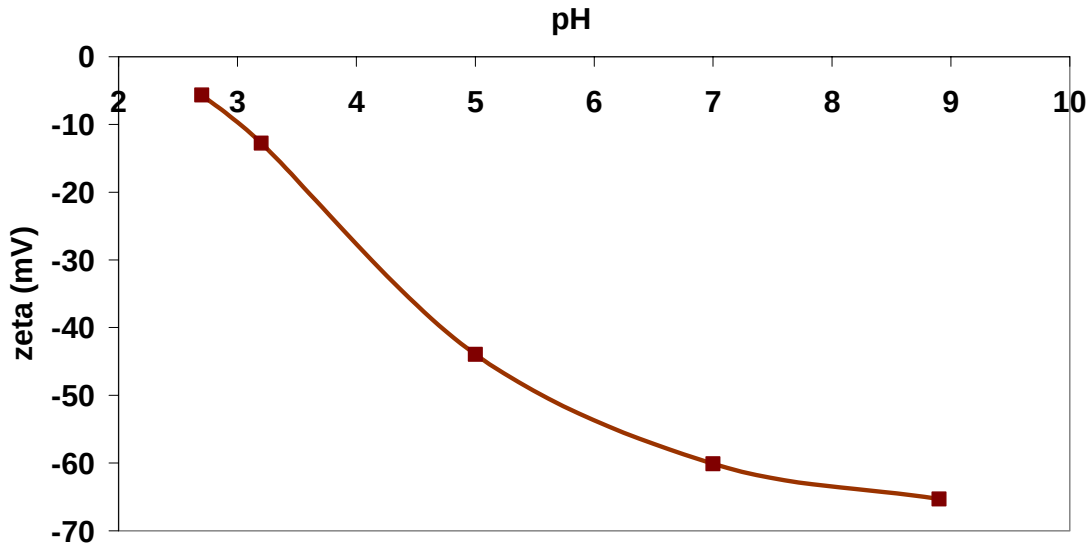

Fig. 2.17: *zeta potential of HMDS coated glass chips as a function of the pH*

3.4.3.2 Dynamic coatings

3.4.2.4 Cetyl Tri Ammonium Bromide

The zeta potential of silica was measured with Cetyl Trimethyl Ammonium Bromide (CTAB) added to the buffer as a dynamic coating.
Zeta potential measurements were performed with the current monitoring method with 2.5 and 5 mM sodium phosphate buffers of pH 7.
The addition of CTAB to the running buffer leads to the formation of micelles on the channel surface, which results in a local positive surface charge.
In this way the point of zero charge can be shifted towards higher pH values [67]. The shift in surface charge that is achieved depends on the surface coverage of the CTAB and with this the surface- and zeta-potential are concentration dependent [68, 69].
In figure 2.18 the average zeta potential is plotted as a function of the CTAB concentration. The figure shows that around 30 μM the zeta potential is reversed.

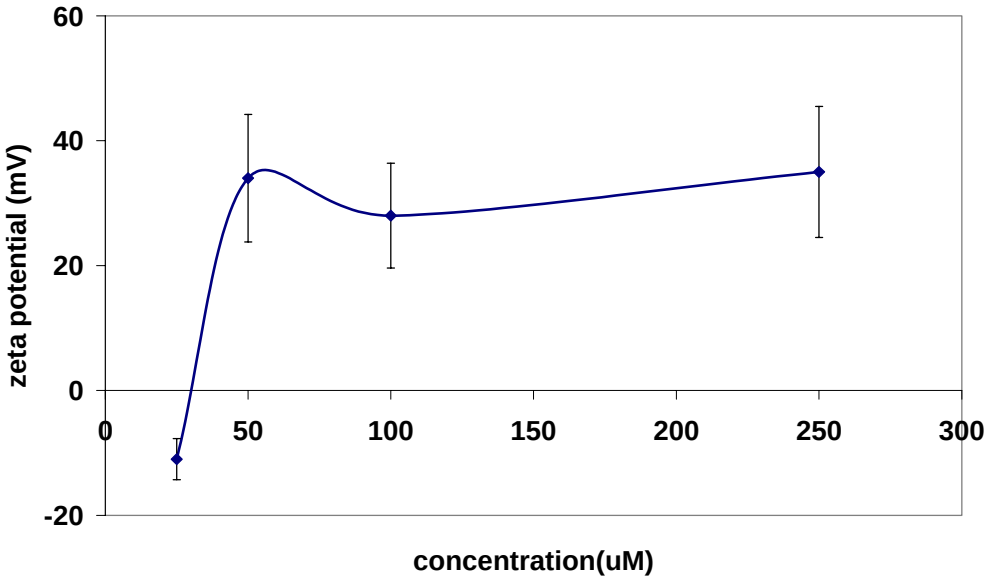

Fig. 2.18: Zeta potential as a function of the CTAB concentration for pH 7 sodium phosphate buffer 2.5→5 mM.

Figure 2.19 shows a characteristic current vs. time curve when the solution in the channel is replaced by EOF with a solution of higher conductivity. The curve shows a clear change in slope. This indicates that the EOF is not stable; this is probably caused due to an inhomogeneous surface coverage over the channel length. This results in a zeta potential gradient over the channel length and thus differences in EOF velocities. The poor uniformity in zeta potential as well as the need to add the CTAB into the running buffer of the systems makes CTAB a less suitable method for reduction of the zeta potential in lab on a chip systems.

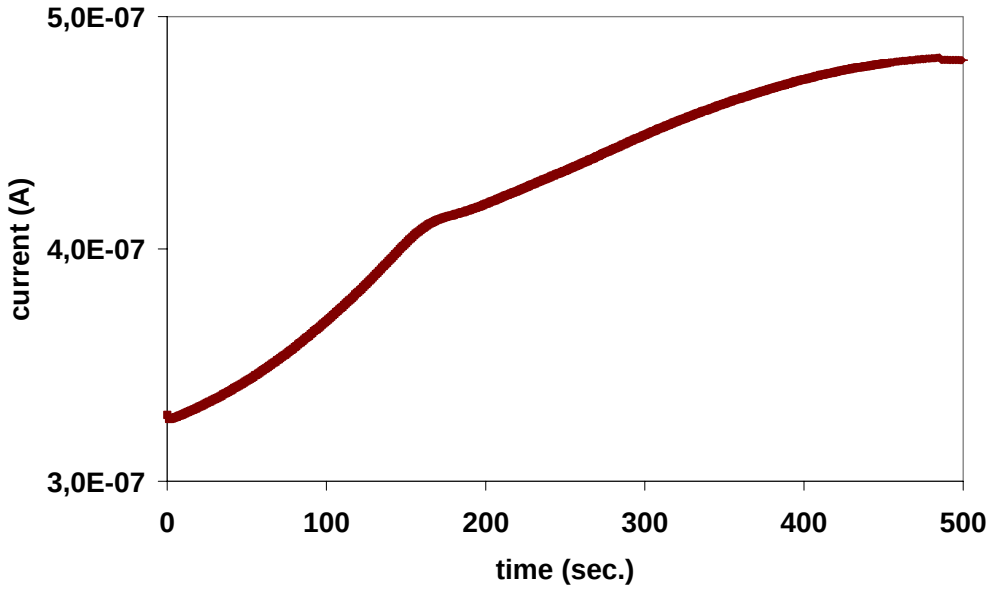

Fig. 2.19: *Current as a function of the time 2.5→5mM sodium phosphate buffer pH7 + 100 µM CTAB.*

4 Characteristics of Field Effect Flow Control

4.1. Three capacitor model

In equation 2.26 it was shown that the EOF can be controlled with the longitudinal field E_x. However, in complex microfluidic networks this can lead to leakage in side branches due to resistive coupling of the electrical fields [70, 71]. A more sophisticated way of flow control can be achieved with the use of integrated gate electrodes for control over the zeta potential.

In Section 3 it was shown that the electroosmotic velocity u_{EOF} depends linearly on the ζ-potential (Eq. 2.26). Hence, if the ζ-potential is influenced by a perpendicular electric field between the gate electrode and the bulk of the fluid, a local change of u_{EOF} independent of the electric field over the channel can be created. The control of EOF can be based on the interaction of the longitudinal electric field E combined with the switching of ζ-controlling elements in the microfluidic circuitry.

In order to control the zeta potential at the solid/liquid interface and in this way the EOF, structures have been developed and studied since the early 90's [72-85] which made use of round capillaries with an external electrode to control the zeta potential. In these cases the principle was generally referred to as External Voltage Control (EVC).

Later, with the use of micro technology more sophisticated structures could be fabricated which have been referred to as flowFET[67] or FEFC [86] and have been studied for various channel geometries and gate insulation materials [87-93]. These names results from the working principle that is comparable to that of the solid-state field-effect transistor (FET) in integrated circuits, where an electric current is manipulated by a perpendicular field generated by a third electrode or gate electrode. In this setup, the ends of a channel play a role that is similar to the source and drain contacts of a FET, while the gate controls the flow rate through the channel. The theory behind the principle of EVC was first proposed by Lee *et al.* [78] and Hayes and Ewing [73]. Their approach was based on the electrostatic interaction of an external electric field on the diffuse double layer charge. The analogue electrical equivalent circuit they presented consisted of a complex network of resistances and capacitances.
Later, Poppe *et al.* [85] proposed an alternative theory based on a Gaussian model and showed that the equivalent circuit can be represented by a much simpler equivalent network. The main difference between the two approaches is that in the first one for the calculation of the diffuse double layer capacitance the Debye-Hückel approximation of the Gouy-Chapman model [94] was used. This assumption leads to a deviation from the latter theory at high offset values for the zeta potential due to the non-linear increase in the diffuse double layer capacitance with the zeta potential. A schematic overview of the analogue electrical circuit is shown in Figure 2.20

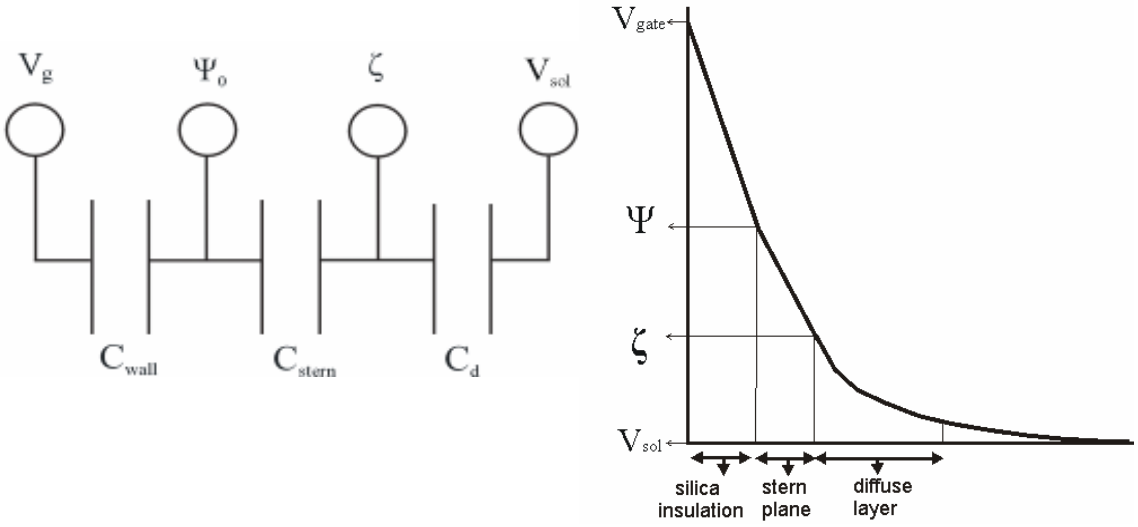

Fig. 2.20: *Equivalent electrical circuit of a FEFC structure (left) and an overview of the potential decay (not to scale).*

In the above scheme the indicated potentials in figure 2.20b correspond to the ones in figure 2.20a. V_g represents the applied gate potential,Ψ_0 is the surface potential, ζ the zeta potential at the solid liquid interface and V_0 the local channel potential. $C_{wall,}$ C_{stern} and C_d indicate respectively the capacitances of the gate insulation layer which also acts as the wall material, the stern layer and the diffuse double layer.
At moderate and low ionic strength, the Stern capacitance is generally much larger than the diffuse double layer capacitance, so that as can be seen in figure 2.20 the potential drop over the Stern layer will be very small.
Based on the latter the influence of the gate potential on the local zeta potential is determined by the ratio between C_{wall} and C_d as is illustrated in equation 2.43.

$$\Delta\varsigma = \frac{C_{wall}}{C_d}\left(V_g - V_{sol}\right) \qquad \text{(Eq.2.43)}$$

The capacitance of the gate insulation is given by equation 2.44. Here A is the surface area, d the thickness of the insulation and ε_0 and ε_r are respectively the dielectric constant of vacuum and of the solution in the channel.

$$C_{wall} = \frac{\varepsilon_0 \varepsilon_r \mathrm{A}}{d_{ox}} \qquad \text{(Eq.2.44)}$$

The diffuse double layer capacitance is given by equation 2.41, in case of monovalent electrolyte at room temperature with a dielectric constant of 78.5. This equation can be simplified to equation 2.45.

$$C_d = 228Az\sqrt{c}COSH(19.5z\varsigma) \qquad \text{(Eq.2.45)}$$

In Figure 2.21 the operating principle of a FEFC is schematically illustrated. At a constant longitudinal electric field, the flow direction and magnitude can be controlled by the application of an appropriate gate potential to modify the local zeta potential. In figure 2.21, case a) reflects the situation without any gate voltage. The EOF in this case is proportional to the natural zeta potential. In case b), the negative ζ-potential is enhanced by an external

negative gate voltage V_g. In case c), a positive gate potential is applied which reverses the charge in the double layer and thus also the EOF.

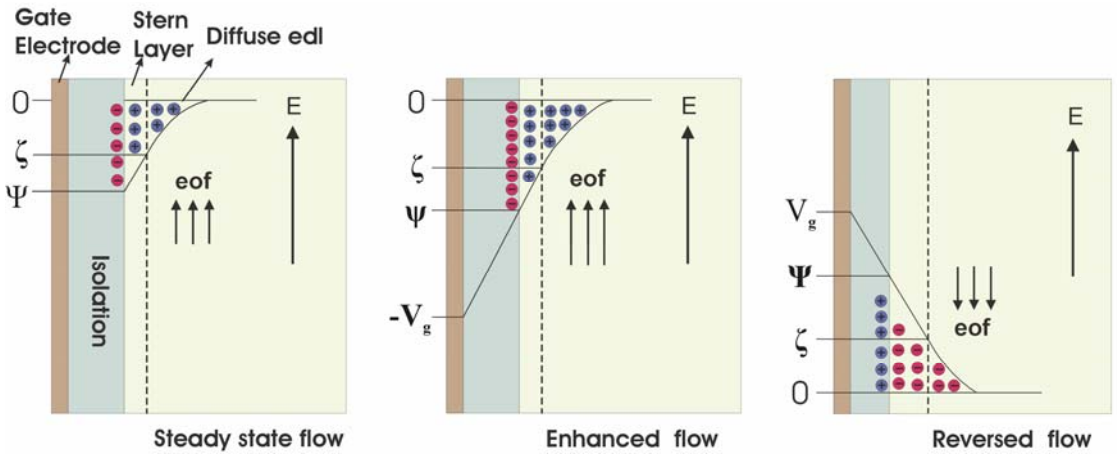

Fig. 2.21: *Schematic illustration of the operating principle of a FEFC structure, see text for details.*

4.2 EOF with AC potentials

The schematic of a FEFC structure can also be applied for use in AC-operation. The use of oscillating potentials offers the advantage that electrolysis at the open channel electrode can be suppressed or even completely eliminated [95]. The application of AC potentials or current at open electrodes to create a net flow has been studied especially in the case of open asymmetric electrodes arrays [96-110].
When an AC potential is applied over a microchannel the resulting EOF will oscillate with the frequency of the electric field (Eq. 2.46), when the time for EOF to develop is much smaller than frequency period, and thus not show a net component.

$$v_{EOF} = \frac{\varepsilon_0 \varepsilon_r \zeta}{\eta} E_x \sin(\omega t) \qquad \text{(Eq.2.46)}$$

When the zeta potential in the gate region is also modified with the same frequency and in phase with the channel potential, a net flow can be generated. The change in zeta potential for an AC potential is given by equation 2.47 in case the gate and channel potential have the same frequency ω with a phase difference φ [89].

$$\Delta\varsigma = \frac{C_{wall}}{C_d}\left(V_g \sin(\varpi t) - V_{sol} \sin(\varpi t + \varphi)\right) \qquad \text{(Eq.2.47)}$$

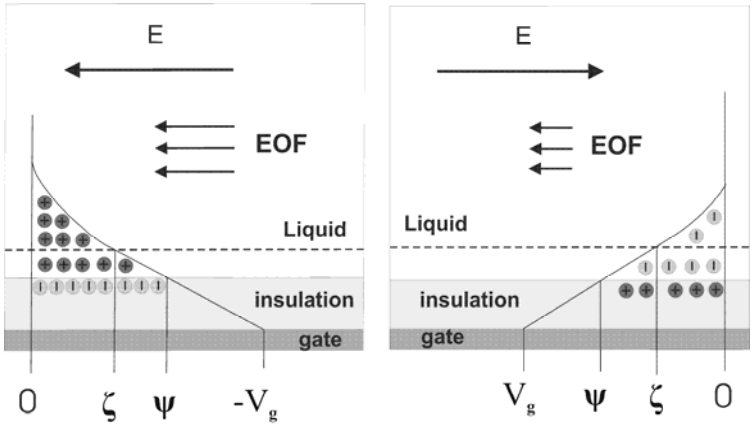

Fig.2.22: *Schematic overview of directional AC-pumping.*

Figure 2.22 shows a schematic overview of the concept of a net flow generation with zero average AC potentials. The first drawing shows the situation where both channel and gate potential are negative.
The negative gate will lead to a more negative zeta potential and thus an enhanced flow in the direction of the anode. The second image shows the situation for both, a positive gate and channel potential. The positive gate potential will lead to a reversal of the zeta potential; since also the channel potential is reversed, the EOF will maintain the same direction. This synchronized switching scheme is analog to the concept of AC magnetohydrodynamic pumping where both the current and magnetic field are synchronized to create a unidirectional Lorentz force on the ions in a microchannel [95, 111].
The maximum operating frequency that can be achieved depends on the charging dynamics of the EDL and the time needed for the EOF to establish. The time τ_{EOF} for the EOF to develop in a microchannel with diameter d filled with a liquid with density ρ is given by equation 2.48 [112]:

$$\tau_{EOF} = \frac{d^2}{\eta/\rho} \qquad \text{(Eq. 2.48)}$$

From equation 2.48 it can be seen that for water based solutions in microchannels (d ~ 10 µm) the time needed for the EOF to develop will be in the sub millisecond range [113].
The charging of the EDL upon application of a gate potential is limited by the current, which depends on the series impedances of the gate insulation capacitance and the channel electrolyte resistance [114].
The current as a function of the time in a RC network is given by equation 2.49, where I_0 is the current at time 0 and t is the time.

$$I(t) = I_0 e^{-\frac{t}{RC}} \qquad \text{(Eq. 2.49)}$$

The electrolyte resistance of a microchannel is given by equation 2.50, when the influence of surface conduction can be neglected and in the case of a channel shape that resembles a half ellipse.

$$R = \frac{L}{\mathrm{K}\pi wh} \qquad \text{(Eq. 2.50)}$$

The capacitance is given by equation 2.44, when the time constant is defined as the point where the current has dropped to 10 % of the initial value, the charging time can be defined as a function of the geometry:

$$\tau_{EDL} = 2.3\frac{L^2\varepsilon_0\varepsilon_r}{2\mathrm{K}\pi hd_{ox}} \qquad \text{(Eq. 2.51)}$$

4.3 Zeta potential as a function of the gate potential

In section 4.1 it was illustrated that the change in zeta potential that can be induced depends on the ratio between the capacitances of the gate insulation and of the diffuse double layer. Equation 2.45 shows that the diffuse double layer capacitance is proportional to the square root of the ion

concentration. This means that at larger electrolyte concentrations the effective potential drop over the diffuse EDL will decrease and with this the influence on the zeta potential. Figure 2.23 shows the calculated change in zeta potential as a function of the gate potential for insulating silica of 200 nm thicknesses with a dielectric constant of 4.
The curves show a decreasing change in zeta potential for an increase in concentration. Close to V=0, a linear relation between the gate potential and the zeta potential exists. At larger gate potential a decrease in the slope can be observed. This is caused by the hyperbolic cosine dependency of the diffuse EDL capacitance on the zeta potential as shown in equation 2.45. At increasing zeta potential the ratio between C_{wall} and C_d decreases, which leads to a smaller slope as can be seen from equation 2.43.

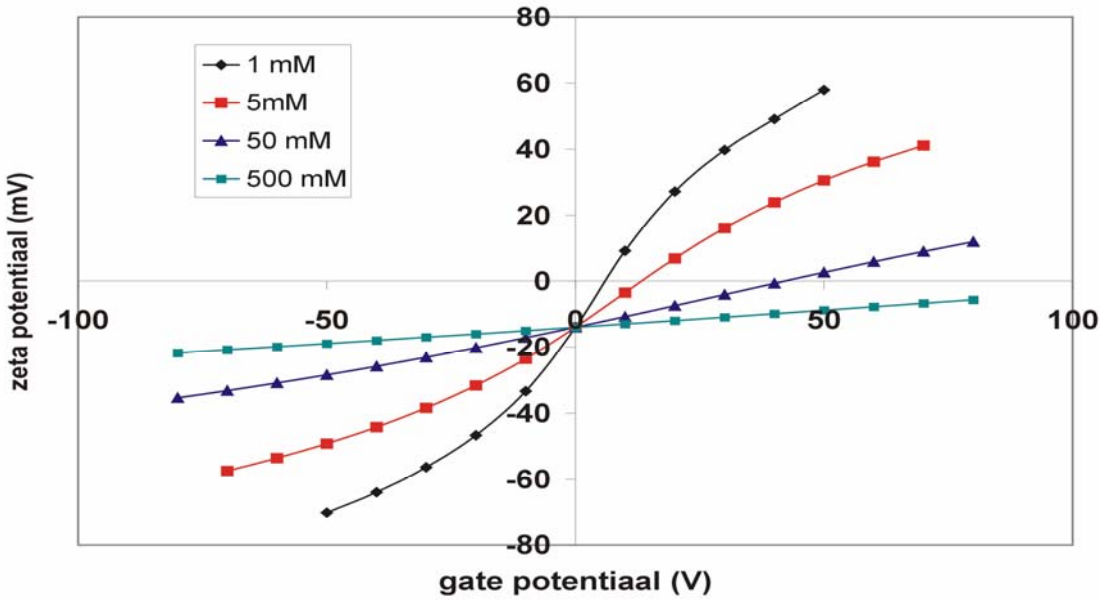

Fig. 2.23: *Change in zeta potential as a function of the gate potential for different buffer concentrations.*

4.3.1 Influence of the buffer capacitance

In section 2.2 it was illustrated that the influence of the bulk pH on the surface potential depends on both the buffer capacitance of the silica surface and on the EDL capacitance as was expressed in equation 2.25.

At a change in electrolyte pH, the buffer capacitance of the silica will act to keep the surface pH constant by dissociation or association of silanol groups. The reverse reaction also occurs; when a gate potential is applied, the resulting change in surface potential will lead to a shift in surface pH that involves a change in surface charge that counteracts the induced surface potential modification.
The induced counter potential scales with the magnitude of the buffer capacitance. For larger values of $C_{buf,}$ the effective change in the zeta potential as a function of the gate potential is reduced. This implies that the three capacitor model as discussed in section 4.1 is only valid in case the buffer capacitance is low, which is the case when the electrolyte pH is close to the p.z.c. of silica. The magnitude of the buffer capacitance for oxide surfaces as discussed in section 2.1 was given by equation 2.25 in case of silica. For practical pH range only the association and dissociation of silanol surface groups needs to be taken into account. Under this assumption equation 2.25 can be approximated by equation 2.52.

$$\beta = N_s \frac{a_{H_S^+} K_a}{(K_a + a_{H_S^+})^2} 2.3 a_{H_S^+} \qquad \text{(Eq.2.52)}$$

When the buffer pH is unequal to the electrolyte pH, the three capacitor model as discussed before should be expanded to account for the surface charge response to an applied gate potential. The influence of the buffer capacitance acts in parallel to the diffuse EDL capacitance and is limited by diffusion of protons through the EDL. Diffusion processes can be modelled by a series of a diffusion capacitance and a diffusion resistance [115] where the product forms the time constant given by κ^2/D, where κ is the Debye length and D the diffusion constant of a proton in the EDL.
When this process is included in the three capacitor model an equivalent circuit as depicted in figure 2.24 can be composed. The impact of the buffer capacitance on the operation of a FEFC structure will be discussed in further detail in chapter 7.

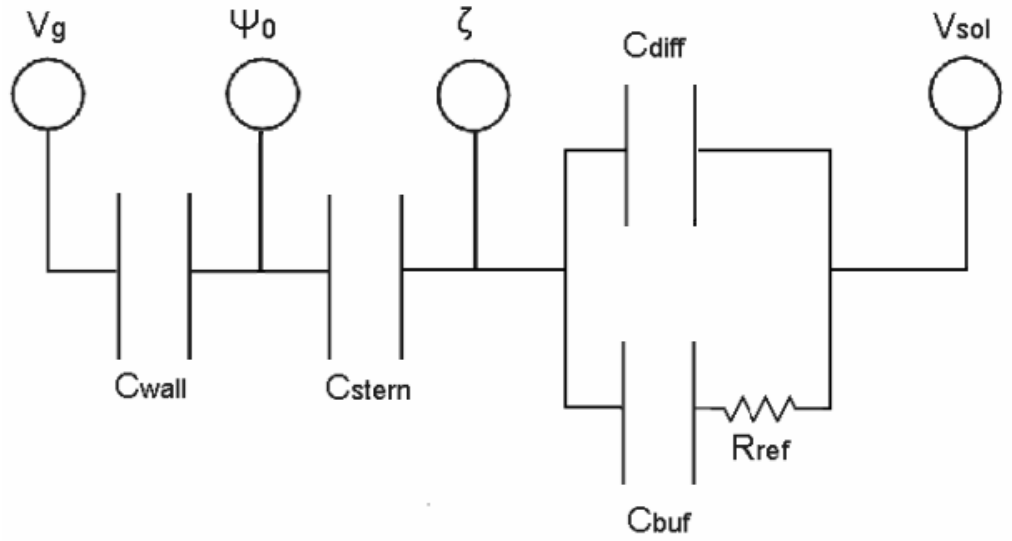

Fig 2.24: *Schematic illustration of the operating principle of a FEFC structure.*

4.4 Zeta potential gradients

When a longitudinal potential is applied over a microfluidic channel to create an EOF, the potential in the channel will show a gradient, so the electric potential will be a function of the position in the channel.
When subsequently a potential is applied at the gate electrode, the influence in the local zeta potential will be a function of the gate potential with respect to the local channel potential as was discussed in section 4.1. Since the gate electrode consists of a conducting metal, this potential will be independent of the position so that the gate potential with respect to the channel potential will show a gradient. This gradient will be equal to the channel potential difference between the beginning and end of the gate electrode.
To achieve a stable flow situation either several gate electrodes or a resistive gate electrode can be created to match the gradient in the channel potential. This effect of the zeta potential distribution will be further discussed in chapter 8.

4.5 Heterogeneous surface charge

As illustrated in the previous paragraphs, the application of a gate potential in a flowFET structure will lead to heterogeneous distribution in the zeta

potential. At the interface between a normal wall and a part with a gate electrode located underneath, a discrete step in the zeta potential will be present. Figure 2.25 illustrates the situation of a stationary EOF with a step change in zeta potential present. In the situation of figure 2.25, ζ_1 is smaller than ζ_2, consequently the EOF in region 2 will be proportionally larger and in this way pull the solution in region 1 [116] so that a constant flow in each cross section of the channel is maintained [117]. The pressure difference that emerges is known to be confined to a small region at the interface [118]. When the small region near the discontinuity is ignored the flow field in each section of the channel is composed of the summation of the stationary EOF and a pressure driven component. The velocity profiles under these conditions have been extensively investigated [119-122] and will be described in more detail in chapter 5.
Herr *et al.* derived an expression for the velocity as a function of the radial position for each section of the channel. Their analysis was based on the work of Rice and Whitehead [123] who theoretically investigated the EOF in capillaries with an additional pressure difference applied.

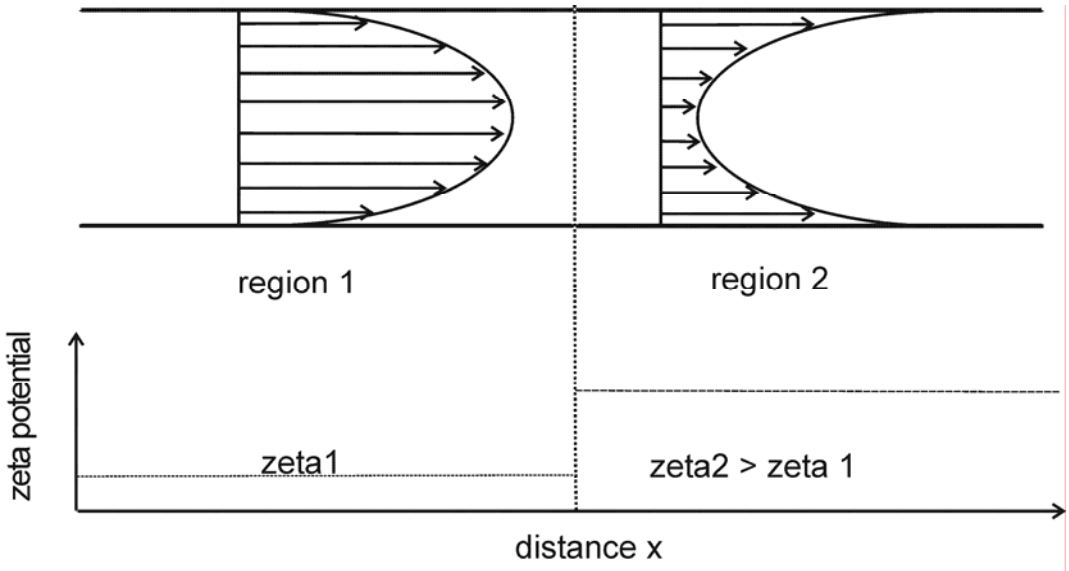

Fig. 2.25: *Schematic overview of the influence of a heterogeneous zeta potential on the velocity profile.*

The expression of Herr *et al.* was valid in the case of round capillaries. The fabrication process used in the scope of this thesis leads to geometry that resembles a half ellipse (chapter 3) as is illustrated in figure 2.26. The velocity profile for an ellipse at an applied pressure difference is given by

the second part of expression 2.53 [124]. The first part is the velocity contribution of the EOF and is equal to equation 2.2, which is in case of a uniform zeta potential at the different surfaces constant through the entire cross section. Thus, the variation of the net velocity with the position is only attributed to the pressure driven flow. In equation 2.53 is, a half the width, b the height of the channel, x and y respectively the horizontal and vertical position.

$\left(\frac{dP}{dx}\right)_i$ and ζ_i are respectively the pressure gradient and the zeta potential in each section *i* of the channel.

The summation of the velocity profiles of the pressure driven flow and EOF gives the velocity as a function of the horizontal and vertical position for each section of the channel as illustrated in figure 2.26.

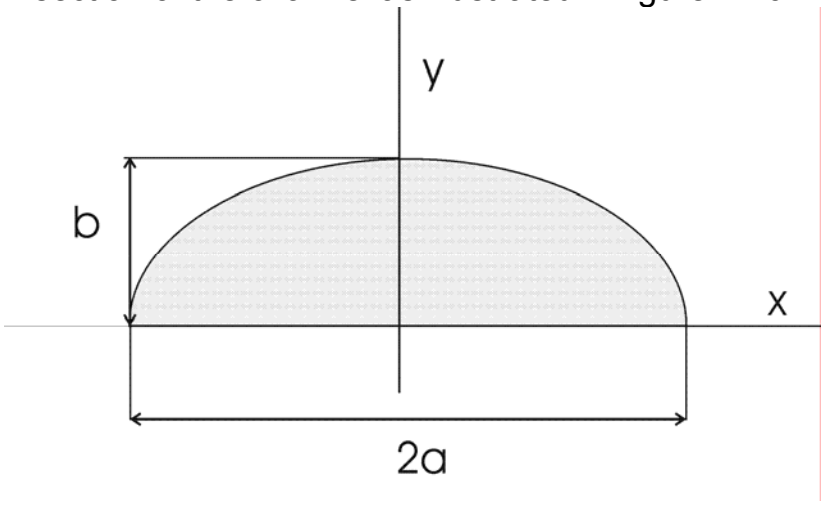

Fig. 2.26: *Schematic overview of the channel geometry, 2a is the width, b the height of the channel, y the vertical and x the horizontal position.*

$$v(x,y)=\frac{-\varepsilon_0\varepsilon_r\zeta_i}{\eta}E_x-\left(\frac{dP}{dx}\right)_i\frac{3}{2\eta}\left(\frac{a^2y}{3a^2+b^2}\right)\left(y-\frac{b}{a}\sqrt{a^2-x^2}\right) \quad \text{(Eq. 2.53)}$$

It has to be mentioned that the flowFET structures as described in chapter 3 and 4, only influence the zeta potential at the bottom channel wall. The velocity component of the EOF through the channel will thus not be uniform as is assumed in 2.53, but will also be a function of the position. The equation needed to accurately describe the position dependent velocity

should take this into account and is thus a more complex function of the position than equation 2.53 suggests. This effect was studied in case of different wall materials, which leads to different local zeta potential [125-127].

The general equation for an ellipse is given in by equation 2.54

$$\frac{x^2}{a^2}+\frac{y^2}{b^2}=1 \qquad \text{(Eq. 2.54)}$$

When the terms in the latter equation are rearranged the radial position as a function of the lateral position is given by equation 2.55

$$x=\left(1-\frac{y^2}{b^2}\right)^2 a^2 \qquad \text{(Eq. 2.55)}$$

Under the assumption that the EOF in the gate area as a function of the height decays linearly from the gate EOF to the natural EOF, the velocity as a function of the height of the channel is given by equation 2.56

$$v(x,y)=\frac{-\varepsilon_0\varepsilon_r\left(\varsigma_g-\frac{y\left(\varsigma_g-\varsigma_0\right)}{\left(\left(1-\frac{x^2}{a^2}\right)b^2\right)^{\frac{1}{2}}}\right)}{\eta}E_x-\left(\frac{dP}{dx}\right)_i\frac{3}{2\eta}\left(\frac{a^2y}{3a^2+b^2}\right)\left(y-\frac{b}{a}\sqrt{a^2-x^2}\right) \qquad \text{(Eq. 2.56)}$$

4.6 Influence of gate area coverage

As was shown in the work of Herr *et al.*[117], integration of the velocity distribution over the channel cross section yields the flow rate in the channel section. At the boundary conditions of atmospheric pressure at the inlet and outlet of the channel, fully developed flow and a continuous and linear

pressure in each channel section the pressure gradients in each section can be calculated.
Based on this procedure the velocity profile of equation 2.53 can be integrated to yield the volume flow Q, through each cross-section of the channel (Eq. 2.57)

$$Q = \frac{\pi a b \varepsilon_0 \varepsilon_r \varsigma_i}{2\eta} E_x - \left(\frac{dP}{dx}\right)_i \frac{\pi}{32\eta}\left(\frac{3a^3 b^3}{3a^2 + b^2}\right) \qquad \text{(Eq. 2.57)}$$

At the conditions mentioned before the pressure gradient that develops due to differences in EOF rate in sections with different zeta potential can be calculated by equation 2.58. Here $\bar{\varsigma}$ is the average zeta potential over the entire channel length and is given by equation 2.59. Here L is the total channel length; L_i is the length of a section with zeta potential ζ_i.

$$\left(\frac{dP}{dx}\right)_i = \frac{16\varepsilon_0 \varepsilon_r E_x}{3}\left(\bar{\varsigma} - \varsigma_i\right)\frac{3a^2 + b^2}{a^2 b^2} \qquad \text{(Eq. 2.58)}$$

$$\bar{\varsigma} = \frac{1}{L}\Sigma L_i \varsigma_i \qquad \text{(Eq. 2.59)}$$

Combining equations 2.53 and 2.58 gives the velocity profile as a function of the position for every section of the channel with a zeta potential ζ_i (Eq. 2.60). Combination of the equations for the flow rate and pressure gradient shows that the average velocity and thus also the flow rate through a channel with a heterogeneous surface charge is determined by the average zeta potential (equation 2.61).

$$v(x,y) = \frac{\varepsilon_0 \varepsilon_r \varsigma_i E_x}{\eta} - \frac{8\varepsilon_0 \varepsilon_r E_x}{\eta}\left(\bar{\varsigma} - \varsigma_i\right)\frac{a^2 y}{a^2 + b^2}\left(y - \frac{b}{a}\sqrt{a^2 - b^2}\right) \qquad \text{(Eq. 2.60)}$$

$$\bar{v} = \frac{\varepsilon_0 \varepsilon_r \bar{\varsigma}}{\eta} E_x \qquad \text{(Eq. 2.61)}$$

Based on the previous equations it is clear that the average zeta potential is the flow controlling parameter. In order to be able to control the flow in a large window also the average zeta potential should be controllable. It follows from equation 2.59 that in order to obtain this, both the offset value for the natural zeta potential should be kept low and the gate area coverage should be as high as possible.

4.6.1 Influence of surface conduction on the local zeta potential in the gate region

In the previous analyses it was assumed that the influence of the applied gate potential was limited to the gate electrode area. However, it has been suggested that the influence of the gate area might extend further due to the influence of surface conduction [76, 89].
The influence of surface conduction is recognized especially in the field of streaming potential and is known to have a field strength variance [128]. Surface conduction in Streaming Potential originates manly from conduction in the EDL. In FEFC the influence of surface conduction might be due to the strong gradients in local charge that develop at the transition between an influenced gate region and a non-influenced region. Depending on the applied potential a strong difference in counter charge concentration in the longitudinal direction can occur, where in some cases even the charge of counterions can be opposite. Diffusion of counter charge to compensate for the resulting strong concentration differences can cause a spreading of the induced change in zeta potential to the parts of the wall where no gate electrode is present.
Alternative models have been proposed that include a linear decay in zeta potential. Sniadecki *et al* [89] showed results in PDMS/Parylene microchannels where the induced flow was dependent on the position of the gate electrode. They explained their observations by an influence of the gate potential outside of the gate region. This effect was shown before by Hayes *et al.* [76] in capillaries with 50 μm inner diameter, which were only partially influenced by a radial voltage. Their experimental results showed significant deviation from the classical theory where a discrete change in zeta potential in the gate region is assumed. To account for the influence of surface conduction they composed a more elaborate electrical equivalent model of a FEFC structure where the zeta potential in the non-influenced region was coupled to the gate zeta potential by a resistance parallel to the

bulk electrolyte resistance. This model was able to give a better quantitative and qualitative result compared to the classical theory.
Figure 2.27 gives a schematic overview of the linear decaying zeta potential model. In the gate region the zeta potential is assumed to be constant. At the edge of the gate region the zeta potential starts to decay linearly to the offset value at the beginning and end of channel.

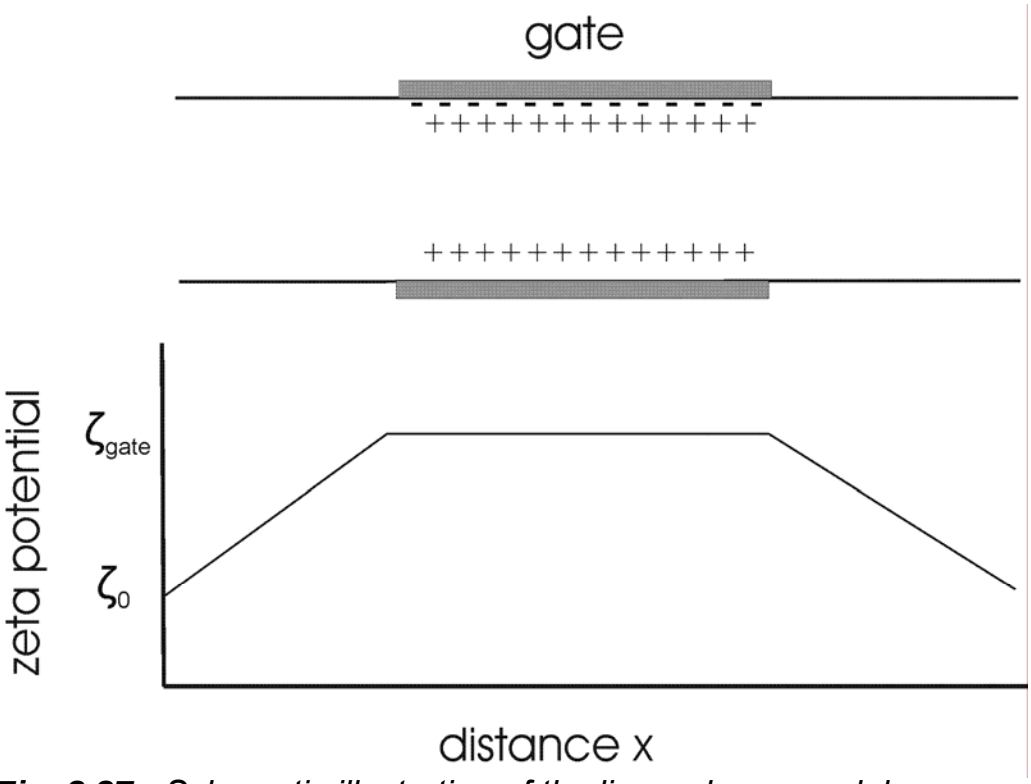

Fig. 2.27: *Schematic illustration of the linear decay model.*

5 Discussion and conclusions

An overview of various detection and characterization techniques for EOF are summarized and discussed. For flow characterization of FEFC PIV seems to offer the best characteristics since it couples the ability to obtain local flow information with high accuracy. However, the method requires an elaborate and extensive setup. So when only information of the EOF velocity is required the current monitoring technique is a more suitable one,

since it allows fast and easy measurement without the need of an elaborate setup.
The zeta potential of bare silica is measured with the current monitoring. For efficient manipulation the flow with FEFC low offset in zeta potential are required. It is shown that with bare silica low buffer pH's are necessary to obtain such a low offset. To allow efficient actuation at neutral pH, which is required in biomedical applications several dynamic and fixed coatings have been applied. Best results are obtained for APS coatings when coated at 60 ˚C for 1 hour, an offset value for the zeta potential of 5 mV is found at pH 7.
Furthermore, the three capacitor model is discussed that is classically used in FEFC. It is shown that in order to account for the response of active surface groups the influence of the surface buffer capacitance should be included in the model.

6 References

1. Hunter, R.J., Zeta Potential in Colloid Science: Principles and Applications. Academic Press, London, 1981.
2. Hunter, R.J., Foundations of Colloid Science. Oxford university press., 2001.
3. Lyklema, J., Fundamentals of Interface and colloid Science: Volume II: solid-liquid interfaces. Academic Press, London, 1995.
4. Healy, T.W. and L.R. White, Adv. Colloid Interface Sci, 1978. **9**(303): p. 45.
5. James, R.O. and G.A. Parks, Characterization of aqueous colloids by their double layer and intrinsic surface. In surface and colloid science. Vol. 12 Plenum, New York, 1982.
6. Healy, T.W. and L.R. White, Ionizable surface group models of aqueous interfaces. Advances in Colloid Interface Science, 1978. **9**: p. 303-345.
7. Ottewill, R.H. and J.N. Shaw, Discuss. Faraday Soc., 1966(42): p. 154.
8. Yates, D.E., S. Levine and T.W. Healy, Site-binding model of the electrical double layer at the oxide/water interface. J. Chem. Soc. Faraday Trans, 1974. **70**: p. 1807-1818.
9. Bousse, L., The chemical Sensitivity of Electrolyte/Insulator/Silicon Structures: Fundamentals of ISFET Operation. PhD thesis, University of Twente (Enschede), 1982.
10. Levine, S. and A.L. Smith, Discuss. Faraday Soc., 1971. **52**: p. 290.

11. Vanhal, R.E.G., J.C.T. Eijkel and P. Bergveld, A Novel Description of Isfet Sensitivity with the Buffer Capacity and Double-Layer Capacitance as Key Parameters. Sensors and Actuators B-Chemical, 1995. **24**(1-3): p. 201-205.
12. vanHal, R.E.G., J.C.T. Eijkel and P. Bergveld, A general model to describe the electrostatic potential at electrolyte oxide interfaces. Advances in Colloid and Interface Science, 1996. **69**: p. 31-62.
13. Vankerkhof, J.C., J.C.T. Eijkel and P. Bergveld, Isfet Responses on a Stepwise Change in Electrolyte Concentration at Constant Ph. Sensors and Actuators B-Chemical, 1994. **18**(1-3): p. 56-59.
14. Lyklema, J., J.Electroanal.Chem, 1968. **18**(341).
15. Lier, J.A.v., P.L.d. Bruyn and J.T.G. Overbeek, J. Phys. Chem., 1960. **64**: p. 1675.
16. Bousse, L. and P. Bergveld, The role of buried OH-sites in the response mechanism of inorganic-gate-pH-sensitive ISFETS Sensors and Actuators, 1984. **6**: p. 65.
17. Yates, D.E., S.L. S and T.W. Healy, Site-binding model of the electrical double layer at the oxide/water interface. Trans. Faraday Soc., 1974. **70**: p. 1807.
18. Davis, J.A., R.O. James and J.O. Leckie, J. Colloid Interface Sci., 1978. **69**: p. 480.
19. Bousse, L.J., N.F.d. Rooij and P. Bergveld, IEEE Trans. Electron Devices, 1983. ED-30: p. 1263.
20. Hsu, J.P., C.Y. Kao, S. Tseng and C.J. Chen, Electrokinetic flow through an elliptical microchannel: Effects of aspect ratio and electrical boundary conditions. Journal of Colloid and Interface Science, 2002. **248**(1): p. 176-184.
21. Yang, C. and D.Q. Li, Electrokinetic effects on pressure-driven liquid flows in rectangular microchannels. Journal of Colloid and Interface Science, 1997. **194**(1): p. 95-107.
22. Yang, C. and D.Q. Li, Analysis of electrokinetic effects on the liquid flow in rectangular microchannels. Colloids and Surfaces a-Physicochemical and Engineering Aspects, 1998. **143**(2-3): p. 339-353.
23. Werner, C., R. Zimmermann and T. Kratzmuller, Streaming potential and streaming current measurements at planar solid/liquid interfaces for simultaneous determination of zeta potential and surface conductivity. Colloids and Surfaces a-Physicochemical and Engineering Aspects, 2001. **192**(1-3): p. 205-213.

24. Werner, C., H. Korber, R. Zimmermann, S. Dukhin and H.J. Jacobasch, Extended electrokinetic characterization of flat solid surfaces. Journal of Colloid and Interface Science, 1998. **208**(1): p. 329-346.
25. Huang, X.H., M.J. Gordon and R.N. Zare, Current-Monitoring Method for Measuring the Electroosmotic Flow-Rate in Capillary Zone Electrophoresis. Analytical Chemistry, 1988. **60**(17): p. 1837-1838.
26. Arulanandam, S. and D.Q. Li, Determining zeta potential and surface conductance by monitoring the current in electro-osmotic flow. Journal of Colloid and Interface Science, 2000. **225**(2): p. 421-428.
27. Chien, R.L. and J.C. Helmer, Electroosmotic Properties and Peak Broadening in Field-Amplified Capillary Electrophoresis. Analytical Chemistry, 1991. **63**(14): p. 1354-1361.
28. Datta, R. and V.R. Kotamarthi, Electrokinetic Dispersion in Capillary Electrophoresis. Aiche Journal, 1990. **36**(6): p. 916-926.
29. Taylor, G.I., Dispersion of soluble matter in solvent flowing slowly through a tube Proceedings of the Royal Society of London series A-Mathematical and Physical Sciences, 1953. **219**: p. 186-203.
30. Aris, R., On the dispersion of a solute in a fluid flowing through a tube Proceedings of the Royal Society of London Series A-Mathematical and Physical Sciences 1956.
31. Lempert, W.R., K. Magee, P. Ronney, K.R. Gee and R.P. Haugland, Flow Tagging Velocimetry in Incompressible-Flow Using Photo-Activated Nonintrusive Tracking of Molecular-Motion (Phantomm). Experiments in Fluids, 1995. **18**(4): p. 249-257.
32. Paul, P.H., M.G. Garguilo and D.J. Rakestraw, Imaging of pressure- and electrokinetically driven flows through open capillaries. Analytical Chemistry, 1998. **70**(13): p. 2459-2467.
33. Gendrich, C.P. and M.M. Koochesfahani, A spatial correlation technique for estimating velocity fields using molecular tagging velocimetry (MTV). Experiments in Fluids, 1996. **22**(1): p. 67-77.
34. Gendrich, C.P., M.M. Koochesfahani and D.G. Nocera, Molecular tagging velocimetry and other novel applications of a new phosphorescent supramolecule. Experiments in Fluids, 1997. **23**(5): p. 361-372.
35. Adrian, R.J., Scattering particle characteristics and their effect on pulsed laser measurements of fluid-flow-speckle velocimetry vs. Particle Image Velcimetry Applied Optics, 1984. **23**: p. 1690.

36. Adrian, R.J., Double Exposure, Multiple-Field Particle Image Velocimetry for Turbulent Probability Density. Optics and Lasers in Engineering, 1988. **9**(3-4): p. 211-228.
37. Adrian, R.J., Review of Particle Image Velocimetry Research Presented at the Symposium on Optical Methods in Flow and Particle Diagnostics, 6th International-Congress on Applications of Lasers and Electro-Optics, 8-12 November 1987, San-Diego, California, USA. Optics and Lasers in Engineering, 1988. **9**(3-4): p. 317-319.
38. Adrian, R.J., Dynamic ranges of velocity and spatial resolution of particle image velocimetry. Measurement Science & Technology, 1997. **8**(12): p. 1393-1398.
39. Adrian, R.J., Experiments in Fluids - Experimental methods and their applications to fluid flow - Third International Workshop on Particle Image Velocimetry, Santa Barbara, CA, September 16-18, 1999 - Preface. Experiments in Fluids, 2000. **29**: p. S1-S1.
40. Westerweel, J., Digital Particle Image Velocimetry. Delft: University Press, 1993.
41. Willert, C.E. and M. Gharib, Digital Particle Image Velocimetry. Experiments in Fluids, 1991. **10**(4): p. 181-193.
42. Santiago, J.G., S.T. Wereley, C.D. Meinhart, D.J. Beebe and R.J. Adrian, A particle image velocimetry system for microfluidics. Experiments in Fluids, 1998. **25**(4): p. 316-319.
43. Meinhart, C.D., S.T. Wereley and J.G. Santiago, PIV measurements of a microchannel flow. Experiments in Fluids, 1999. **27**(5): p. 414-419.
44. Westerweel, J., Fundamentals of digital particle image velocimetry. Measurement Science & Technology, 1997. **8**(12): p. 1379-1392.
45. Keane, R.D. and R.J. Adrian, Theory of Cross-Correlation Analysis of Piv Images. Applied Scientific Research, 1992. **49**(3): p. 191-215.
46. Riekkola, M.L., M. Jussila, S.P. Porras and I.E. Valko, Non-aqueous capillary electrophoresis. Journal of Chromatography A, 2000. **892**(1-2): p. 155-170.
47. Steiner, F. and M. Hassel, Nonaqueous capillary electrophoresis: A versatile completion of electrophoretic separation techniques. Electrophoresis, 2000. **21**(18): p. 3994-4016.
48. Riekkola, M.L., Paper symposium - Nonaqueous capillary electrophoresis. Electrophoresis, 2002. **23**(3): p. -.
49. Belder, D. and M. Ludwig, Surface modification in microchip electrophoresis. Electrophoresis, 2003. **24**(21): p. 3595-3606.

50. Dolnik, V., Wall coating for capillary electrophoresis on microchips. Electrophoresis, 2004. **25**(21-22): p. 3589-3601.
51. Pallandre, A., B. de Lambert, R. Attia, A.M. Jonas and J.L. Viovy, Surface treatment and characterization: Perspectives to electrophoresis and lab-on-chips. Electrophoresis, 2006. **27**(3): p. 584-610.
52. Hayes, M.A., Extension of external voltage control of electroosmosis to high-pH buffers. Analytical Chemistry, 1999. **71**(17): p. 3793-3798.
53. Munro, N.J., A.F.R. Huhmer and J.P. Landers, Robust polymeric microchannel coatings for microchip-based analysis of neat PCR products. Analytical Chemistry, 2001. **73**(8): p. 1784-1794.
54. Srinivasan, K., G. Pohl and N. Avdalovic, Cross-linked polymer coatings for capillary electrophoresis and application to analysis of basic proteins, acidic proteins, and inorganic ions. Analytical Chemistry, 1997. **69**(14): p. 2798-2805.
55. McKnight, T.E., C.T. Culbertson, S.C. Jacobson and J.M. Ramsey, Electroosmotically induced hydraulic pumping with integrated electrodes on microfluidic devices. Analytical Chemistry, 2001. **73**(16): p. 4045-4049.
56. Yezek, L.P. and H.P. van Leeuwen, An electrokinetic characterization of low charge density cross-linked polyacrylamide gels. Journal of Colloid and Interface Science, 2004. **278**(1): p. 243-250.
57. Hjerten, S., High-performance electrophoresis - elimination of electroendosmosis and solute adsorption. Journal of chromatography, 1985. **347**: p. 191-198.
58. F.M. Everaerts, F.M., J.L. J.L. Beckers and T.P.E.M. Verheggen, Isotachophoresis – Theory, Instrumentation and Applications, Journal of Chromatography Library,. Journal of Chromatography Library, Elsevier, Amsterdam., 1976.
59. Lindner, H., W. Helliger, A. Dirschlmayer, M. Jaquemar and B. Puschendorf, High-Performance Capillary Electrophoresis of Core Histones and Their Acetylated Modified Derivatives. Biochemical Journal, 1992. **283**: p. 467-471.
60. Tian, H.J. and J.P. Landers, Hydroxyethylcellulose as an effective polymer network for DNA analysis in uncoated glass microchips: optimization and application to mutation detection via heteroduplex analysis. Analytical Biochemistry, 2002. **309**(2): p. 212-223.
61. Bousse, L.J., N.F. de Rooij and P. Bergveld, Operation of chemically sensitive field-effect sensors as a function of the insulattor-electrolyte interface. IEEE Transactions on Electron Devices, 1983. **30**: p. 1263.

62. Belder, D. and J. Warnke, Electrokinetic effects in poly(ethylene glycol)-coated capillaries induced by specific adsorption of cations. Langmuir, 2001. **17**(16): p. 4962-4966.
63. Belder, D., H. Husmann and J. Warnke, Directed control of electroosmotic flow in nonaqueous electrolytes using poly(ethylene glycol) coated capillaries. Electrophoresis, 2001. **22**(4): p. 666-672.
64. Wright, P.B., A.S. Lister and J.G. Dorsey, Behavior and use of nonaqueous media without supporting electrolyte in capillary electrophoresis and capillary electrochromatography. Analytical Chemistry, 1997. **69**(16): p. 3251-3259.
65. Banka, P.A., J.C. Selser, B. Wang, D.K. Shenoy and R. Martin, Nonionic polymer-salt interactions in dilute solution: The poly(ethylene oxide)/LiClO4/methanol system. Macromolecules, 1996. **29**(11): p. 3956-3959.
66. Okada, T., Polyethers in inorganic capillary electrophoresis. Journal of Chromatography A, 1999. **834**(1-2): p. 73-87.
67. Schasfoort, R.B.M., S. Schlautmann, L. Hendrikse and A. van den Berg, Field-effect flow control for microfabricated fluidic networks. Science, 1999. **286**(5441): p. 942-945.
68. Galli, V. and C. Barbas, Optimization in sample stacking for the measurement of short chain organic acids in serum of natural rubber latex by capillary electrophoresis. Analytica Chimica Acta, 2003. **482**(1): p. 37-45.
69. Paruchuri, V.K., A.V. Nguyen and J.D. Miller, Zeta-potentials of self-assembled surface micelles of ionic surfactants adsorbed at hydrophobic graphite surfaces. Colloids and Surfaces a-Physicochemical and Engineering Aspects, 2004. **250**(1-3): p. 519-526.
70. Harrison, D.J., K. Fluri, K. Seiler, Z.H. Fan, C.S. Effenhauser and A. Manz, Micromachining a Miniaturized Capillary Electrophoresis-Based Chemical-Analysis System on a Chip. Science, 1993. **261**(5123): p. 895-897.
71. Harrison, D.J., A. Manz, Z.H. Fan, H. Ludi and H.M. Widmer, Capillary Electrophoresis and Sample Injection Systems Integrated on a Planar Glass Chip. Analytical Chemistry, 1992. **64**(17): p. 1926-1932.
72. Ghowsi, K. and R.J. Gale, Field-Effect Electroosmosis. Journal of Chromatography, 1991. **559**(1-2): p. 95-101.

73. Hayes, M.A. and A.G. Ewing, Electroosmotic Flow-Control and Monitoring with an Applied Radial Voltage for Capillary Zone Electrophoresis. Analytical Chemistry, 1992. **64**(5): p. 512-516.
74. Hayes, M.A. and A.G. Ewing, Electroosmotic Flow-Control and Monitoring with an Applied Radial Voltage for Capillary Zone Electrophoresis (Vol 64, Pg 512, 1992). Analytical Chemistry, 1993. **65**(17): p. 2407-2407.
75. Lee, C.S., W.C. Blanchard and C.T. Wu, Direct Control of the Electroosmosis in Capillary Zone Electrophoresis by Using an External Electric-Field. Analytical Chemistry, 1990. **62**(14): p. 1550-1552.
76. Hayes, M.A., I. Kheterpal and A.G. Ewing, Electroosmotic Flow-Control and Surface Conductance in Capillary Zone Electrophoresis. Analytical Chemistry, 1993. **65**(15): p. 2010-2013.
77. Wu, C.T., T. Lopes, B. Patel and C.S. Lee, Effect of Direct Control of Electroosmosis on Peptide and Protein Separations in Capillary Electrophoresis. Analytical Chemistry, 1992. **64**(8): p. 886-891.
78. Lee, C.S., D. Mcmanigill, C.T. Wu and B. Patel, Factors Affecting Direct Control of Electroosmosis Using an External Electric-Field in Capillary Electrophoresis. Analytical Chemistry, 1991. **63**(15): p. 1519-1523.
79. Lee, C.S., C.T. Wu, T. Lopes and B. Patel, Analysis of Separation Efficiency in Capillary Electrophoresis with Direct Control of Electroosmosis by Using an External Electric-Field. Journal of Chromatography, 1991. **559**(1-2): p. 133-140.
80. Wu, C.T., T.L. Huang and C.S. Lee, Leakage Current Consideration of Capillary Electrophoresis under Electroosmotic Control. Journal of Chromatography A, 1993. **652**(1): p. 277-281.
81. Wu, C.T., T.L. Huang, C.S. Lee and C.J. Miller, Dispersion Studies of Capillary Electrophoresis with Direct Control of Electroosmosis. Analytical Chemistry, 1993. **65**(5): p. 568-571.
82. Wu, C.T., C.S. Lee and C.J. Miller, Ionized Air for Applying Radial Potential Gradient in Capillary Electrophoresis. Analytical Chemistry, 1992. **64**(19): p. 2310-2311.
83. Huang, T.L., P. Tsai, C.T. Wu and C.S. Lee, Mechanistic Studies of Electroosmotic Control at the Capillary Solution Interface. Analytical Chemistry, 1993. **65**(20): p. 2887-2893.
84. Bello, M.S., L. Capelli and P.G. Righetti, Dependence of the Electroosmotic Mobility on the Applied Electric-Field and Its

Reproducibility in Capillary Electrophoresis. Journal of Chromatography A, 1994. **684**(2): p. 311-322.
85. Poppe, H., A. Cifuentes and W.T. Kok, Theoretical description of the influence of external radial fields on the electroosmotic flow in capillary electrophoresis. Analytical Chemistry, 1996. **68**(5): p. 888-893.
86. Sniadecki, N.J., C.S. Lee, P. Sivanesan and D.L. DeVoe, Induced pressure pumping in polymer microchannels via field-effect flow control. Analytical Chemistry, 2004. **76**(7): p. 1942-1947.
87. Lee, C.Y., C.H. Lin and L.M. Fu, Band spreading control in electrophoresis microchips by localized zeta-potential variation using field-effect. Analyst, 2004. **129**(10): p. 931-937.
88. Lee, G.B., L.M. Fu, C.H. Lin, C.Y. Lee and R.J. Yang, Dispersion control in microfluidic chips by localized zeta potential variation using the field effect. Electrophoresis, 2004. **25**(12): p. 1879-1887.
89. Sniadecki, N.J., R. Chang, M. Beamesderfer, C.S. LEe and D.L. Devoe, Field Effect Flow Control in a polymer T-intersection microfluidic networkI. Proceedings 7th lnternational Conference on Miniaturized Chemical and Blochemlcal Analysts Systems, 2003
90. Buch, J.S., P.C. Wang, D.L. DeVoe and C.S. Lee, Field-effect flow control in a polydimethylsiloxane-based microfluidic system. Electrophoresis, 2001. **22**(18): p. 3902-3907.
91. S. Mutlu, F.S., C.H. Mastrangelo, J.M.J. Fr´echet, Y.B. Gianchandani,, Enhanced Electro-Osmotic pumping with liquid bridge and Field Effect Flow rectification. Proceedings of the IEEE Workshop on MEMS, January 25–29,Maastricht, The Netherlands, 2004.
92. Hartley, N.K. and M.A. Hayes, Examination of theoretical models in external voltage control of capillary electrophoresis. Analytical Chemistry, 2002. **74**(6): p. 1249-1255.
93. van der Wouden, E.J., T. Heuser, D.C. Hermes, R.E. Oosterbroek, J.G.E. Gardeniers and A. van den Berg, Field-effect control of electro-osmotic flow in microfluidic networks. Colloids and Surfaces a-Physicochemical and Engineering Aspects, 2005. **267**(1-3): p. 110-116.
94. Bard, A.J. and L.R. Raulkner, Electrochemical Methods, Fundamentals and Applications. J. Wiley & Sons: New York, 1980; Chapter 12, 1980.
95. Lemoff, A.V. and A.P. Lee, An AC magnetohydrodynamic micropump. Sensors and Actuators B-Chemical, 2000. **63**(3): p. 178-185.

96. Gonzalez, A., A. Ramos, N.G. Green, A. Castellanos and H. Morgan, Fluid flow induced by nonuniform ac electric fields in electrolytes on microelectrodes. II. A linear double-layer analysis. Physical Review E, 2000. **61**(4): p. 4019-4028.
97. Green, N.G., A. Ramos, A. Gonzalez, H. Morgan and A. Castellanos, Fluid flow induced by nonuniform ac electric fields in electrolytes on microelectrodes. I. Experimental measurements. Physical Review E, 2000. **61**(4): p. 4011-4018.
98. Green, N.G., A. Ramos, A. Gonzalez, H. Morgan and A. Castellanos, Fluid flow induced by nonuniform ac electric fields in electrolytes on microelectrodes. III. Observation of streamlines and numerical simulation. Physical Review E, 2002. **66**(2): p. 026305
99. Ramos, A., A. Gonzalez, A. Castellanos, N.G. Green and H. Morgan, Pumping of liquids with ac voltages applied to asymmetric pairs of microelectrodes. Physical Review E, 2003. **67**(5): p. 056302.
100. Ramos, A., H. Morgan, N.G. Green and A. Castellanos, Ac electrokinetics: a review of forces in microelectrode structures. Journal of Physics D-Applied Physics, 1998. **31**(18): p. 2338-2353.
101. Ramos, A., H. Morgan, N.G. Green and A. Castellanos, AC electric-field-induced fluid flow in microelectrodes. Journal of Colloid and Interface Science, 1999. **217**(2): p. 420-422.
102. Ramos, A., H. Morgan, N.G. Green, A. Gonzalez and A. Castellanos, Pumping of liquids with traveling-wave electroosmosis. Journal of Applied Physics, 2005. **97**(8): p. 84906.
103. Ajdari, A., Pumping liquids using asymmetric electrode arrays. Physical Review E, 2000. **61**(1): p. 45-48.
104. Brown, A.B.D., C.G. Smith and A.R. Rennie, Pumping of water with ac electric fields applied to asymmetric pairs of microelectrodes. Physical Review E, 2001. **6302**(2): p. 016305.
105. Studer, V., A. Pepin, Y. Chen and A. Ajdari, Fabrication of microfluidic devices for AC electrokinetic fluid pumping. Microelectronic Engineering, 2002. **61**-2: p. 915-920.
106. Studer, V., A. Pepin, Y. Chen and A. Ajdari, An integrated AC electrokinetic pump in a microfluidic loop for fast and tunable flow control. Analyst, 2004. **129**(10): p. 944-949.
107. Cahill, B.P., L.J. Heyderman, J. Gobrecht and A. Stemmer, Electro-osmotic pumping on application of phase-shifted signals to interdigitated electrodes. Sensors and Actuators B-Chemical, 2005. **110**(1): p. 157-163.

108. Mpholo, M., C.G. Smith and A.B.D. Brown, Low voltage plug flow pumping using anisotropic electrode arrays. Sensors and Actuators B-Chemical, 2003. **92**(3): p. 262-268.
109. Nadal, F., F. Argoul, P. Kestener, B. Pouligny, C. Ybert and A. Ajdari, Electrically induced flows in the vicinity of a dielectric stripe on a conducting plane. European Physical Journal E, 2002. **9**(4): p. 387-399.
110. Brown, A.B.D., C.G. Smith and A.R. Rennie, Pumping of water with ac electric fields applied to asymmetric pairs of microelectrodes. Physical Review E, 2001. **6302**(2): p. 056302.
111. Eijkel, J.C.T., C. Dalton, C.J. Hayden, J.P. Burt and A. Manz, A circular ac magnetohydrodynamic micropump for chromatographic applications. Sensors and Actuators B-Chemical, 2003. **92**(1-2): p. 215-221.
112. Dose, E.V. and G. Guiochon, Timescales of Transient Processes in Capillary Electrophoresis. Journal of Chromatography A, 1993. **652**(1): p. 263-275.
113. Yan, D., N.T. Hguyen, C. Yang and X. Huang, Visualizing the transient electroosmotic flow and measuring the zeta potential of microchannels with a micro-PIV technique. Journal of Chemical physics, 2006. **124**: p. 021103.
114. Gajar, S.A. and M.W. Geis, An Ionic Liquid-Channel Field-Effect Transistor. Journal of the Electrochemical Society, 1992. **139**(10): p. 2833-2840.
115. Conway, B.E., Transition from Supercapacitor to Battery Behavior in Electrochemical Energy-Storage. Journal of the Electrochemical Society, 1991. **138**(6): p. 1539-1548.
116. Anderson, J.L. and W.K. Idol, Electroosmosis through pores with nonuniformly charged walls,. Chem. Eng. Commun., 1985. **28**: p. 93-106.
117. Herr, A.E., J.I. Molho, J.G. Santiago, M.G. Mungal, T.W. Kenny and M.G. Garguilo, Electroosmotic capillary flow with nonuniform zeta potential. Analytical Chemistry, 2000. **72**(5): p. 1053-1057.
118. Long, D., H.A. Stone and A. Ajdari, Electroosmotic flows created by surface defects in capillary electrophoresis. Journal of Colloid and Interface Science, 1999. **212**(2): p. 338-349.
119. Ajdari, A., Elctroosmosis on Inhomogeneously Charged Surfaces. Physical Review Letters, 1995. **75**(4): p. 755-758.

120. Ajdari, A., Transverse electrokinetic and microfluidic effects in micropatterned channels: Lubrication analysis for slab geometries. Physical Review E, 2002. **65**(1).
121. Erickson, D. and D.Q. Li, Three-dimensional structure of electroosmotic flow over heterogeneous surfaces. Journal of Physical Chemistry B, 2003. **107**(44): p. 12212-12220.
122. Stroock, A.D., M. Weck, D.T. Chiu, W.T.S. Huck, P.J.A. Kenis, R.F. Ismagilov and G.M. Whitesides, Patterning electro-osmotic flow with patterned surface charge. Physical Review Letters, 2000. **84**(15): p. 3314-3317.
123. Rice, C.L. and R.J. Whitehead, Electrokinetic Flow in a Narrow Cylindrical Capillary. Phys. Chem., 1965. **69**: p. 4017-4023.
124. Oosterbroek, R.E., Modeling, design and realization of microfluidic components. Ph.D. Thesis,University of Twente, The Netherlands, 1999.
125. Devasenathipathy, S., J.G. Santiago and K. Takehara, Particle tracking techniques for electrokinetic microchannel flows. Analytical Chemistry, 2002. **74**(15): p. 3704-3713.
126. Bianchi, F., A. Ferrigno and H.H. Girault, Finite element simulation of an electroosmotic-driven flow division at a T-junction of microscale dimensions. Analytical Chemistry, 2000. **72**(9): p. 1987-1993.
127. Bianchi, F., F. Wagner, P. Hoffmann and H.H. Girault, Electroosmotic flow in composite microchannels and implications in microcapillary electrophoresis systems. Analytical Chemistry, 2001. 73(4): p. 829-836.
128. Vandegoor, A.A.A.M., B.J. Wanders and F.M. Everaerts, Modified Methods for Off-Line and Online Determination of Electroosmosis in Capillary Electrophoretic Separations. Journal of Chromatography, 1989. **470**(1): p. 95-104.

Appendix list of symbols

Symbol	Parameter	Unit
n	Ion concentration	Mol/m^3
n_0	Bulk ion concentration	Mol/m^3
z	Ion valence	Unit less integer
e	Elementary charge	C
Ψ_0	Surface potential	V
Ψ	Potential	V
κ	Boltzmann constant	J/K
T	Temperature	K
N_a	Avogadro number	1/mol
ρ	Charge density	
ε_0	Dielectric constant vacuum	F/m
ε_r	Dielectric constant medium	Unit less
λ	Debye length	meter
K_a	Reaction Equilibrium constant	
K_b	Reaction Equilibrium constant	
AH	Surface group	
A^-	Conjugated base	
H^+	Proton	
$a(H^+)_s$	Surface proton activity	
$a(H^+)_b$	Bulk proton activity	
σ_0	Surface charge	q/m^2
N_s	Site density	m^{-2}
c	Concentration	M
ξ	System parameter	
$pH_{p.z.c.}$	pH at the point of zero charge	
B	Number of charged surface sites	
Σ_{EDL}	Electrical double layer charge	
C_{EDL}	Electrical double layer capacitance	F/cm^2
C_{stern}	Stern layer capacitance	F/cm^2

C_d	Diffuse double layer capacitance	F/cm^2
C_{wall}	Gate insulation capacitance	F/cm^2
pH_s	pH at the surface	
pH_b	pH in the bulk solution	
B_{int}	Intrinsic buffer capacitance of the surface	F/cm^2
$_{EOF}$	Electro Osmotic Flow	
v_{EOF}	EOF velocity	m/sec
η	Viscosity	Pa*sec
E_x	Electric field strength	V/m
μ_{EOF}	EOF mobility	$m^2/Vsec$
q_{EOF}	Volume flow EOF	m^3/sec
A	Cross-section area	m^2
L	Length	m
U	Potential	V
I_s	Streaming current	A
P	Pressure	Pa
I_c	Conduction current	A
K	conductivity	S/m
C	Circumference	M
K_{bulk}	Bulk conductivity	S/m
K^s	Surface conductivity	S/m
w	width	m
R	Resistance	Ω
λ	Molar conductivity	$m^2/ \Omega mol$
δ	Diffusion length	m
D	Diffusion coefficient	m^2/sec
t	Time	sec
σ^2_d	Dispersion rate	
r_0	Hydraulic resistance	$Pasec/m^3$
$\bar{v}$	Average velocity	m/s
C	Correlation	
V_g	Gate electrode potential	V
V_{sol}	Solution potential	V
d_{ox}	Thickness insulating layer	m
ω	Angular frequency	Rad/sec
φ	Phase difference	Rad.

ρ	Density	Kg/m^3
C	Capacitance	F/cm^2
d	Channel diameter	m
τ_{EOF}	Time constant development EOF	seconds
τ_{EDL}	Time constant EDL charging	seconds
I	Current	A
I_0	current at time zero	A
a	Half channel width	m
b	Channel height	m
$\bar{\zeta}$	average zeta potential	V
ζ	Zeta potential	V
ζ_g	Gate area zeta potential	V
ζ_0	Natural zeta potential	V

3

Design aspects and fabrication of Field Effect Flow Control systems

1 Abstract

In this chapter the various considerations and requirements in the fabrication of a Field Effect Flow Control (FEFC) structure are discussed. A device that consists of a meandering channel structure with high hydraulic resistance is discussed for its application as a microvalve in which low potentials are needed for actuation. The possible applicable technologies are discussed and the optimal design dimensions are analyzed. It is shown that with an appropriate choice of materials and technology, a meandering channel structure can be fabricated with a high hydraulic resistance in which with low potentials a flow can be generated. Silica PECVD films have been optimized to obtain high dielectric breakdown strength towards both, positive and negative polarization. Best results are obtained for deposition at high frequency at elevated temperatures. Fabrication of FEFC structures in glass is chosen, to obtain a uniform surface charge at the solid walls. To allow bonding between the PECVD silica insulating layer and a second glass substrate with etched channels a Chemical Mechanical Polishing (CMP) process has been developed. It is shown that step height resulting form the electrodes during PECVD deposition can be removed sufficiently to obtain a high bond strength during annealing of the two glass substrates.

2 Design requirements

In chapter 2.2 the operating principle of a FEFC device was discussed. For the design and fabrication of such devices several requirements and demands must be considered. The principle layout of a FEFC device is shown in figure 3.1. The structure consists of a bottom substrate on which insulated gate electrodes for control of the zeta potential and open channel electrodes to supply the longitudinal electrical field are deposited. On top of this, a second substrate should be attached which facilitates the microfluidic channels, inlet and outlet connections and fluid reservoirs.

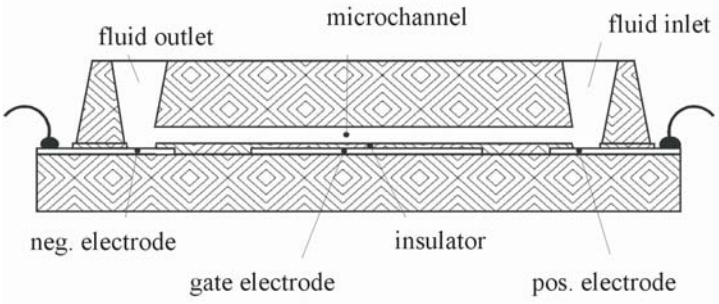

Fig 3.1: Schematic drawing of a flow-FET structure.

For the development of a FEFC device in which the fundamentals of flow control can be studied, some requirements have to be taken into account which puts restrictions on the possible applicable technologies, processes and materials. These issues will be discussed in the following sections.

2.1. Gate insulating layer

In chapter 2.4 it was illustrated that the change in zeta potential that is obtained is determined by the gate potential times the ratio between the capacitances of the gate insulating layer and the diffuse electrical double layer (Eq.2.43). Both, the double layer and the insulating layer capacitance scale with the surface area, so at a fixed double layer capacitance the maximum change in zeta potential is determined by the breakdown potential and the dielectric constant of the insulating layer. This implies that for a large as possible flow control, the insulating material should exhibit both, an as high as possible dielectric constant as well as an as high as possible dielectric breakdown value.

2.2. Optical transparency

For flow quantification and especially flow profile characterization optically transparent materials are desired, since many flow visualization techniques, like PIV or fluorescent dye monitoring, require visual inspection of the fluidic channel. So at least the top or bottom substrate should be transparent. However, it is favorable to use the same material for all channel walls so that a uniform zeta potential is present for all channel surfaces and to guarantee a uniform surface coverage in case a surface coating is applied.
In case gate electrodes are applied at both the top and bottom of the channel, also at least on one side transparent electrodes, like ITO (Indium Tin Oxide), should be used to allow visual inspection of the channel.

2.3. Leakage

The prevention of leakage is crucial for fluidic microsystems, since leakage will give rise to cross-talk between adjacent fluidic conduits.
Furthermore, if a short circuit will be present between the gate electrode and the fluidic channel, electrolysis and consequently bubble formation will take place that leads to blocking of the channel and disconnection of the electrical circuit formed by the two electrodes that supply the longitudinal field. In order to prevent leakage a high bond strength should be obtained.

2.4. Electrochemical resistivity of electrode materials

The electrodes which supply the longitudinal electrical field can either be placed as wires in the fluid reservoirs after fabrication or they can be directly integrated in the FEFC device as shown in figure 3.1. In both cases the electrodes should be corrosion resistant, so no degradation over time occurs which can affect the performance over time. In case noble metal electrodes are integrated in the device, a possible adhesion layer for the electrodes should either not dissolve in the solutions to be pumped, or direct contact with the solution should be avoided in the design.

2.5. Surface chemistry

For the choice of the wall material the functional groups of the surface should be considered. For flow control over a wide window a small offset in zeta potential is required [1]. Furthermore, the surface should exhibit a low ability to donate or adsorb protons since a high buffer capacitance leads to a reduced control over the zeta potential as explained in chapter 2 (section 4.3.1). Generally both the zeta potential and the buffer capacitance are a function of the pH of the solution. For application of a FEFC structure in a biomedical environment its operation is restricted to the near neutral pH range. So either the material properties should be such that around pH 7 the surface exhibits favorable properties, or it should be possible to apply a surface coating to shift the offset value of the zeta potential and the buffer capacitance.

3 Layout and design aspects of FEFC systems

The design that was illustrated in figure 3.1 for a FEFC system offers good opportunities for the principle investigation of its operation. However, for its application in a drug delivery system some additional conditions are required. In chapter 1 it was illustrated that for biomedical application a leakage rate of maximum 1 µl/day was specified. This requires a high hydraulic resistance and thus small dimension of the fluidic channel. However, an additional requirement is an as large as possible flow rate at an as low as possible potential, which requires a large surface area. To meet the conflicting demands, a system can be developed in which multiple FEFC structures are connected electrically in parallel and hydraulically in series. Figure 3.2 gives a schematic overview of the concept. The structure consists of a meandering channel structure in which the same potential is applied at the subsequent branches of the channel. In this way opposite electrical field gradients are created in each branch which normally results

in average zero flow. However, by using the FEFC principle the sign and magnitude of the zeta potential can be adapted to create a uniform EOF flow rate in each subsequent channel section. The latter principle requires the application of open electrodes inside the fluidic channel, which will result in electrolysis and possible bubble formation, which can lead to blocking of the channel. To avoid this, a potential scheme can be applied in which both the gate and channel potentials are switched at an AC-potential. It has been shown that a frequency of several hundred hertz should be sufficient to avoid bubble formation [2].

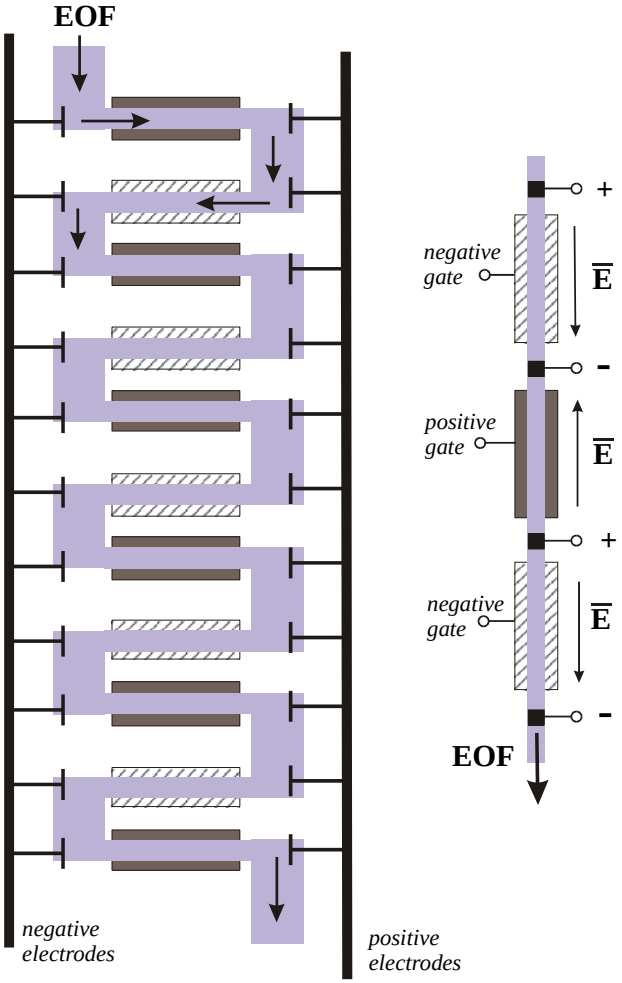

Fig.3.2: *Proposed design for a flow restriction opened by electroosmotic flow control. The basic principle is shown on the right: positively and negatively charged electrodes ensure alternating electrical fields, which give rise to EOF in the same direction, if corresponding gates have a positive or negative voltage. The right figure is a compact version of this principle.*

In chapter 2 it was shown that in the AC-control of EOF two time constances play a role, which can both be expressed as a function of the diameter of the channel (Eq. 2.48/2.51). By plotting both functions versus the diameter, the height at which a maximum frequency can be applied can be determined. It is assumed that the electrolyte consists of an acetate buffer of 5 mM and pH 3 with a conductivity of 0.02 S/m. and that the total channel is covered with the gate electrode for a channel length of 0.5 cm with 500 nm gate insulation material with a dielectric constant of 4.

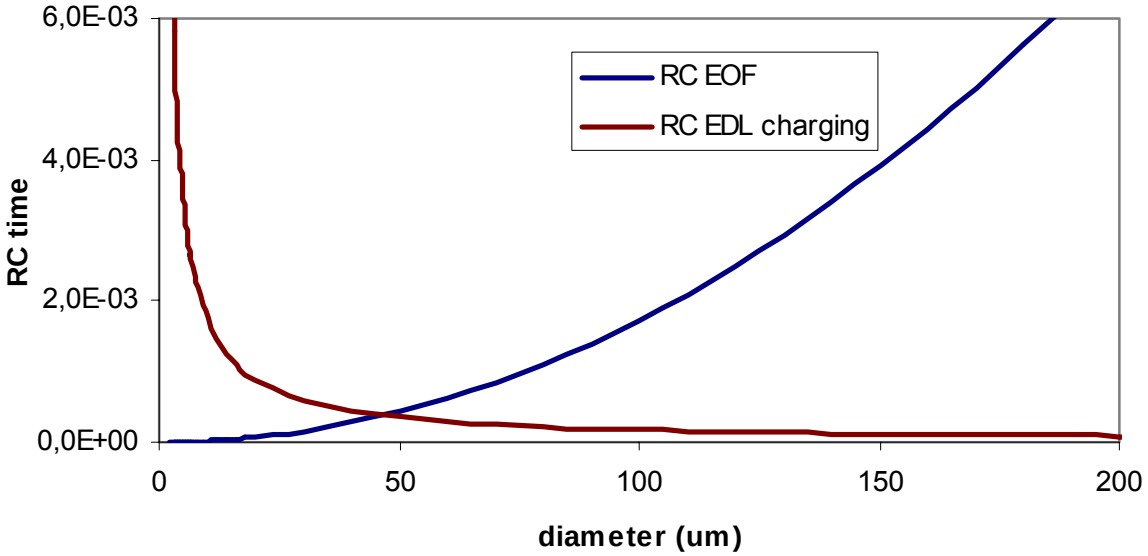

Fig.3.3: *Time constants for the double layer charging and build up of EOF as a function of the channel diameter.*

In figure 3.3 it can be seen that the optimum channel height for a minimum time constant is at 46 µm. At this point both time constants are less than 1 msec. Based on the criteria mentioned in section 3.2 glass is a suitable material for use as a substrate for the microfluidic channels, since it is optically transparent, chemically inert and allows the application of various coatings for surface property modification. In this case, etching of the channels with buffered HF is a suitable technique which will lead to half ellipsoidally shaped channels with a width that is at least two times the height due to under etching. However, under these conditions, a channel length of 5 meters would be required, which is practically unrealistic and indicates that smaller dimensions are required.
If a minimum applicable frequency of 200 Hz is assumed, which corresponds to a time constant of 5 msec the minimum allowed height is

less than 5 µm. In order to guarantee a possible maximum volume flow of 500 µl/day a width of 3 mm is chosen.
Based on the latter dimensions, the minimum length for the channel can be calculated to provide a hydraulic flow resistance that meets the maximum leakage requirements. Provided that, the maximum length of the chip is 2 cm, this gives also the maximum height difference between the reservoirs. In case of water as the solution, this amounts to a maximum leakage pressure of 200 Pa. For a maximum leakage rate of 1 µl/day a maximum flow rate of 12 pl/sec is allowed. From this a minimum hydraulic resistance of 1.7 *10^{16} Pa*sec can be determined.

$$R_{hyd} = \frac{32\eta l}{\pi}\frac{3a^2 + b^2}{3a^3b^3} \qquad \text{(Eq. 3.1)}$$

Equation 3.1 gives the hydraulic resistance for a half ellipse with η the viscosity, l the channel length, a half the width and b the height of the channel. Since the minimum resistance, the width and height are known, a minimum length for the meandering channel of 31 cm can be calculated.

4 Applicable technologies

4.1 Deposition and etch-back technique

This is a technique where the oxide that embeds the electrodes is covered with a thick resist or polymer layer. This functions as a planarization layer as shown in Fig. 3.4

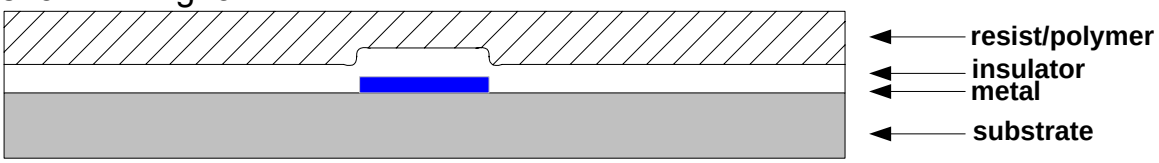

Fig. 3.4: *Schematic drawing of deposition and etch-back technique.*

Then, the resist and the insulator are etched-back with a process that has equal etch rates for the insulator and the resist/polymer. The etching is stopped when the entire resist is removed and only a complete insulating layer is remaining. Optionally this planarized insulating layer can be covered with an additional layer of the same insulating material in order to decrease the surface roughness that has been affected by the etching.

The main advantage of the deposition and etch-back technique is that it only consists of standard processes as lithography, deposition and etching. Its drawback is that a combination of insulator, resist/polymer and etchant has to be found that facilitates an equal etching rate.

4.2 Spin-on-glass

Spin-on-Glass is a material that also has interesting intermetal dielectric properties, which are comparable to SiO_2 ($\varepsilon_{r\ SOG}$ = 3,1; $\varepsilon_{r\ SiO2}$ = 3,9). Moreover, Spin-On-Glass is able to planarize a surface. It is directly spinned on the substrate in a liquid form and it has the capability to fill narrow gaps. It either fills the upper metal areas or the lower substrate areas to planarize the surface. Spin-On-Glass materials are silicates, phosphosilicates or siloxanes.
Spin-On-Glass is a technology which is easy applicable and has good insulating properties, but it is also acquainted to have a poor adhesion to metal layers. Beyond that, when curing at higher temperature the solvent in the Spin-On-Glass evaporates and can cause cracks in the remaining layer. Particularly this temperature cycling is known to be a very critical step. Furthermore the spinning settings require optimization, since it strongly depends on the design in terms of the ratio of lower and upper areas.

4.3 Intermediate layer

This approach implies the embedding of the metal electrodes by a dielectric layer that has the ability to flow at high temperatures. Such layers are SU-8 or boron-doped glass. For instance, glass doped with 3-4 % wt of boron has the property to flow at temperatures above 850 °C. This would eliminate a portion of topography. This application is limited on the one hand by the height of the metal electrodes, and on the other hand by the melting point of the metal. Boron-doped glass is also not applicable in combination with the glass substrates because the glass substrates already start melting before a curing temperature of 850 °C is reached. Another crucial step might be the blocking of the microchannels while bonding. Those intermediate layers are directly bonded to the channel wafer. The bonding occurs by melting the intermediate layer in the liquid phase, so that the channels might be blocked.

4.4 Evaporation

This method basically includes the deposition and the patterning of an insulating layer on a substrate. A contact mask for the evaporation process is used that matches to the structure of the insulating layer. The patterns are filled with evaporated metal and lastly another insulating layer is deposited to cover and planarize the metal/insulator surface.
This technique is used for coarser dimensions than used here. During evaporation shadow effects may occur. Besides, the first insulating layer could be totally covered with a metal layer leading to short circuits. Additionally, a second insulating layer might poorly adhere to the metal or the first insulating layer, or unwanted interface effects, like the accumulation of particles causing voids, might occur.

4.5 Polyimide

Polyimides are polymers that have a high thermal stability and good mechanical and dielectric properties (ε_r = 3,3; ρ = 10^{16} Ωcm). Typically they are dispensed in liquid form and then they are cured at temperatures up to 350 °C. There are two main kinds of polyimides, photosensitive and non-photosensitive ones. Only the photosensitive one could find application for the fabrication of the electrode wafer, because this kind of polyimides provides the option to include the channels on the electrode wafer. That means that the polyimide is spinned on the substrate, which contains the electrodes, and afterwards is patterned with a lithography step. To end with, a second wafer is bonded on top. This second wafer functions as a lid of the channel. Leakage might appear after bonding because the solvent in the polyimide evaporates while annealing. Therefore, voids might be generated. Also the cycle of the temperature might cause the same problems as already discussed for Spin-On-Glass in section 4.2

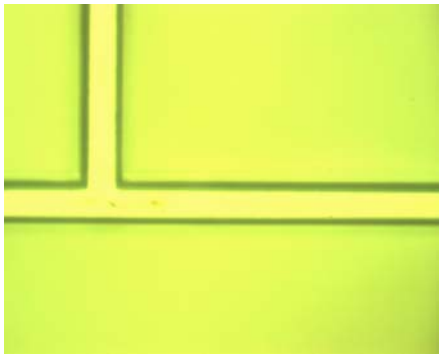

Fig.3.5: *Example of* fabricated *polyimide channels, channel width and height respectively 50 and 15 µm.*

4.6 PDMS

The combination of high temperature steps and integrated electrodes in microfluidic steps can cause several problems like hillock formation or compressive stress. Since the bonding of a glass wafer with microfluidic channels to the electrode wafers requires temperatures of more than 500 ˚C, alternative methods can be favorable. PDMS offers several of the favorable properties of glass without the need of a high anneal step during bonding with a glass substrate. Furthermore, with the use of PDMS, rapid and cheap fabrication of microfluidic components can be achieved [3, 4]. Figure 3.6 gives a schematic overview of the fabrication process. In a), the bottom wafer is shown to which the PDMS channel has to be bonded. Initially a PDMS mold is fabricated in Silicon and coated with a hydrophobic Teflon coating to mediate the removal of a PDMS slab after curing. Subsequently, a monomer PDMS solution is casted on the mold, degassed under vacuum and cured at 60 ˚C for 1 hour. After curing, both the PDMS slab and the glass substrate are placed in an oxygen plasma for 30 seconds to form surface silanol groups and create a hydrophilic PDMS surface [4]. In a last step, the glass substrate and the PDMS are bonded at 60 ˚C for 1 hour by covalent bonding between the surface silanol groups. Before contacting both substrates the glass is covered with methanol so that the PDMS slab can be aligned.

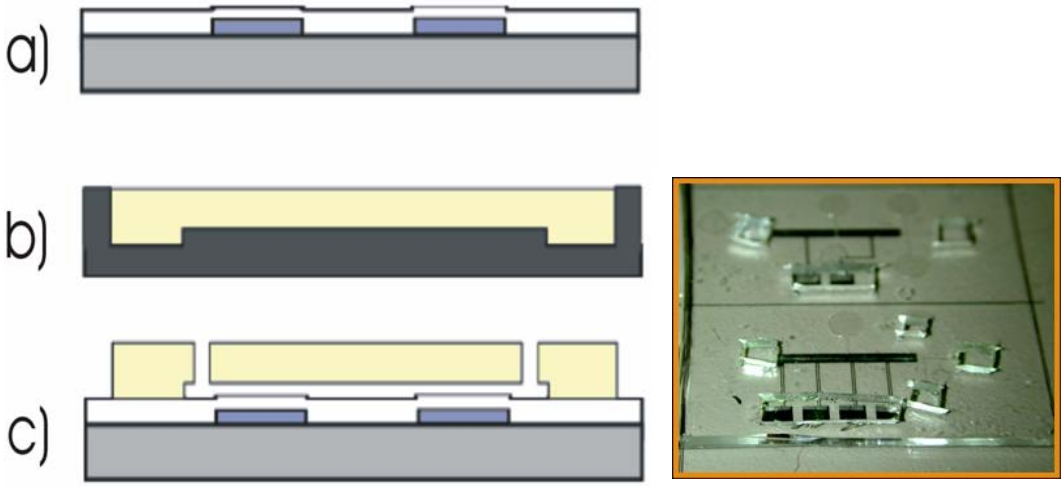

Fig.3.6: *a) Schematic overview fabrication* FEFC *structures with PDMS fluidic channels b) an example of PDMS fabricated structures.*

A potential drawback of PDMS is its hydrophobic nature that originates from the presence of the surface $-O-Si(CH_3)_2$-groups.

After treatment with oxygen plasma the surface exhibits hydrophilic properties. However, in air the PDMS will recover to its original hydrophobic state within 30 minutes [5]. This drawback can be circumvented by storing the PDMS emerged in water to retain its hydrophilic properties. This can offer some disadvantages for practical operation of a microfluidic chip. Modification of the functional PDMS surface groups can alter the surface properties to a permanent hydrophilic state. For instance grafting the surface with HEMA [6] or PEG [7] has been shown to lead to a stable modification of the PDMS surface.

4.7 Recess deposition

If a uniform thin film is applied to cover the electrodes with an insulating layer, a step height will be present at the insulating layer due to the thickness of the electrodes. Such a step height can lead to a limited bond quality and consequent leakage at the interface. The step height can be reduced by recess deposition of the gate electrodes. The recess approach is a quite simple technique. As opposed to a deposition of the electrodes on top of the metal, holes are etched into the substrate and afterwards filled with metal. If the deposition rate of the metals is very accurately defined, so that the filling of the holes can be controlled, it is advantageous that the final remaining step will be much lower compared to the direct deposition on the substrate. In contrast, there are also critical issues that have to be taken into consideration. The etching of the glass is not very well defined, so that a strong under-etch could occur. This under-etch will not be filled by metal deposition because it is still protected by resist as exposed below.

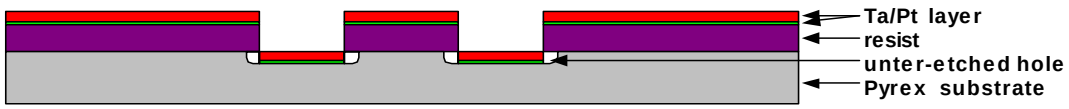

Fig. 3.7: *Illustration of under-etched holes, which are expected for the glass etching in* the *recess process.*

These under-etched areas have to be closed up with the insulating material to avoid leakage. However, this under-etch might also be useful as it is does

not create a sharp transition between metal and glass. It will bring a more slightly rising slope until the upper glass level is reached. Although the step height after dielectric layer deposition can be reduced by the recess technique, both etching and deposition parameters have to be accurately known to completely match the height of the electrodes with the glass surface. This makes recess deposition a technique more suitable for reduction of the step heights than to completely eliminate it. For complete planarization of the surface topography and reduction of the surface roughness Chemical Mechanical Polishing (CMP) is a more suitable technique, which will be discussed in section 6.4.

5 Critical processing steps

5.1 Stress in PECVD-deposited SiO_2-layers

A residual stress is remaining in nearly all films due to a mismatch in the thermal expansion coefficient, non-uniform plastic deformation, lattice mismatch, impurities or growth processes [8]. The stress-causing factors are characterized as either extrinsic or intrinsic. Extrinsic stresses develop by intended external factors such as temperature gradients, while intrinsic stresses come up during film nucleation. Therefore, it is necessary to determine the intrinsic stress of the PECVD-deposited SiO_2 layer, because the stress could lead to a deformation causing further problems for processing, like hillock formation [9] or reduced bonding. The influence and characterization of stress will be further discussed in Chapter 4.2

5.2 Step coverage of surface features

CVD-films have the function to passivate or insulate underlying surface features against subsequent layers or the atmosphere. The insulating SiO_2 layer must fulfill the same function. Therefore it has to be ensured that the electrodes are completely covered, to avoid the formation of short-circuits between the liquid and electrodes. An important property of those films is its ability to cover pits and edges. As illustrated in Fig: 3.8. three cases of the coverage of pits and edges can be distinguished.

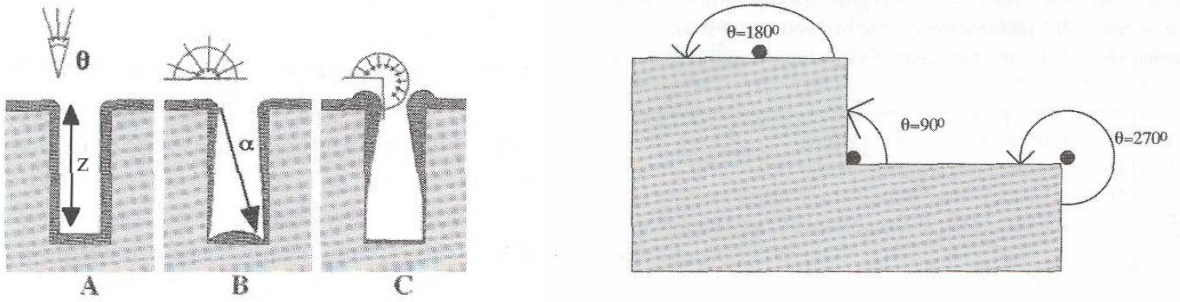

Fig: 3.8: *left) Three cases of step coverage of deposited films; right) different arrival angles in two dimensions.*

Case **A** reflects the ideal formation of a dense and uniform coating. This occurs when the reactants, after first hitting the surface, have enough energy left for surface migration before a bond with the underlying substrate is established. Without any surface migration the reactants stick to the position where firstly contacted the surface. The more perpendicular the particle hits the surface, the more likely is a reaction with the surface. The angle of arrival is given as follows:

$$\Theta = \arctan\frac{b}{t} \qquad \text{(Eq. 3.2.)}$$

where b is the width of the opening and t the distance from the surface.

Case **B** shows the result of missing surface migration but a mean free path in the gas of the reactants that is much higher than the dimensions of the opening. At the upper edge of the opening the particles can arrive under an angle of maximum 180°. In case **C,** the mean free path is assumed to be smaller than the width of the opening. The edge can be covered from an angle up to 270°. An enhanced deposition occurs at the edge that leads to shadow effects of the lower parts. In this work the surface coverage of the metal gate electrodes was evaluated with SEM pictures after cleaving the sample. To avoid peeling of the metal due to its higher elastic properties compared to glass and SiO_2,, the samples were cleaved in a cooled liquid nitrogen environment. Two different fabrication methods were evaluated. In the first case, electrodes were deposited and covered with PECVD silica and subsequently planarized with CMP. In the second method, electrodes were deposited with the recess technique and covered with PECVD silica.

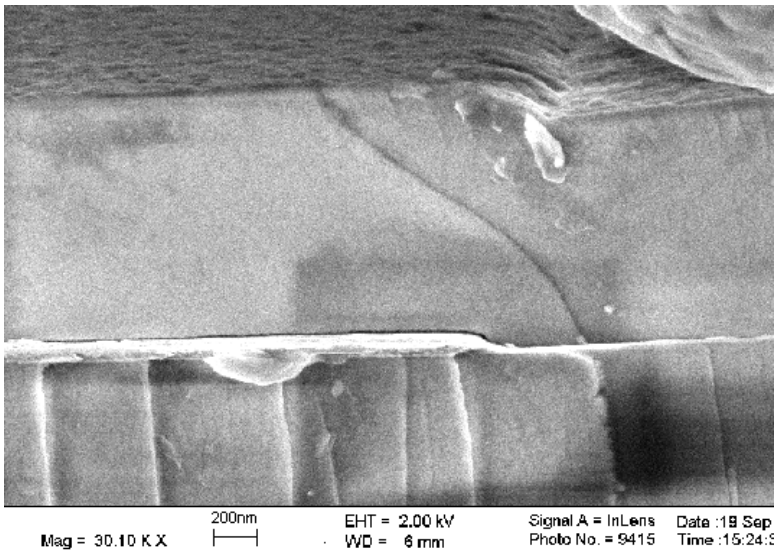

Fig. 3.9: *SEM picture showing a detailed view of the step coverage of the conventionally processed wafer.*

Figure 3.9 show a SEM picture of a sample treated with CMP; it indicates that the metal step is completely covered. The picture shows a detailed view of the metal step-coverage. Any cracks or irregularities of the oxide cannot be noticed. Further on, it seems that the oxide was deposited very homogeneously because the surface of the oxide is quite smooth. The covered step is not as sharp as before oxide deposition.

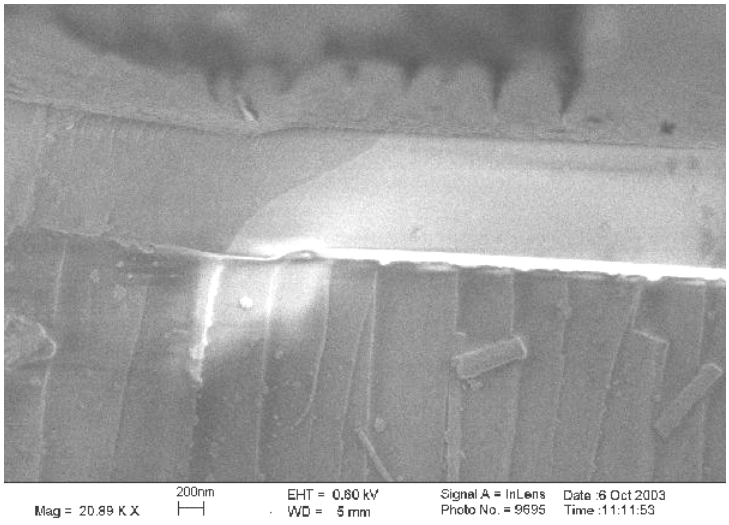

Fig. 3.10: *SEM picture showing a cross-section of the wafer processed with recess technique.*

Figure 3.10 highlights a detailed cross-section view of the wafer processed with recess technique. There is still a little step at the point where the metal is located, although the metal should be fully integrated into the Pyrex. It is believed that an under-etch occurred while etching the glass. The negative slope of either the SiO_2 or the Pyrex from the left merge of the picture to the point where the metal is situated also explains the assumption of the under-etch. It can be concluded that all pictures show a uniform and homogeneous SiO_2 layer composition, which is not categorically expected for PECVD depositions. All metal steps seem to be sufficiently covered without any cracks, which indicate that the PECVD deposition of silica will lead to a sufficient surface coverage for application in FEFC structures.

5.3 Requirements for direct wafer bonding

Direct wafer bonding does not make use of any outside force such as an externally applied electrostatic field. It refers to surface forces determining the adhesion of solid bodies. The attraction mechanism during the direct bonding is attributed to the Van-der-Waals interaction or the hydrogen bonding. Van-der-Waals interactions exist almost between all kinds of substances when they are in intimate contact [10]. Hence, room temperature direct wafer bonding is in principle applicable for nearly all material if their surfaces fulfill specific bonding conditions, such as contamination, roughness, flatness and bow [11]. If the surfaces are smooth enough, pre-bonds will be formed at contact. These pre-bonds follow from hydrogen bonds between silanol groups on the surface, which are developed when water reacts with residual valences of free SiO_2 on the surface. Afterwards, the pre-bonded wafers are annealed, so that atomic bonds can be formed [12].

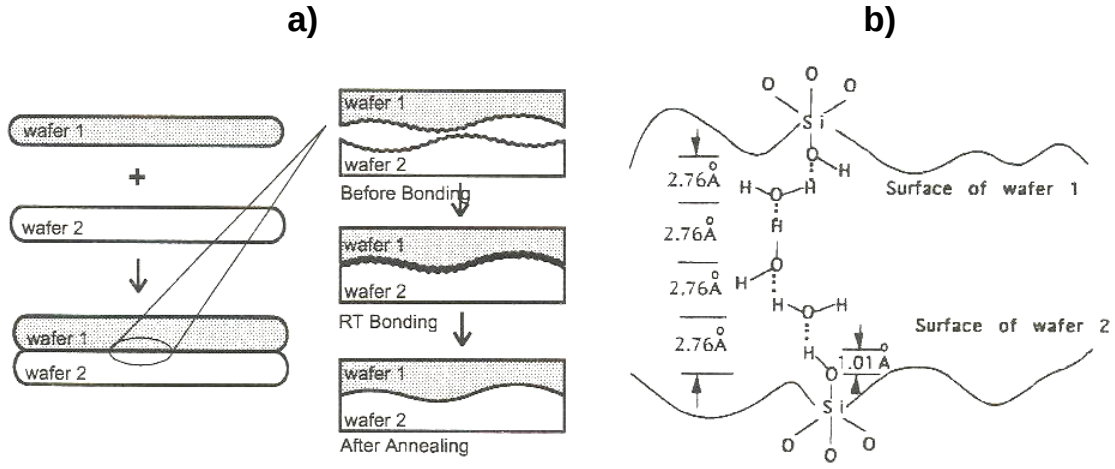

Fig3.11: a) *Illustration of the direct wafer bonding process;* ***b)*** *schematic illustration of a linkage of three water molecules between hydrophilic mating surfaces to bridge a gap between wafers at room temperature.*

5.3.1 Contamination

In order to achieve a successful bonding, the mating surfaces must be sufficiently clean because surface contamination, caused by e.g. particles, organic or metallic residuals, can significantly reduce the surface reactivity and lower the bonding energy. However, particles cause the main bonding problems. They act as spacers and lower or prevent a complete contact between the surfaces. A particle of about 1 µm diameter leads to a bubble about 5000 times larger for typical 4'' wafers with a thickness of 525 µm [11, 13].

5.3.2 Roughness

Due to the fact that wafer bonding is determined by inter-molecular and inter-atomic forces, the wafer surface smoothness becomes one of the most critical parameters in this process. The roughness is a measure category. Commonly two parameters, the root mean roughness (R_q) and the mean roughness (R_a) are used to evaluate the roughness. They are defined as follows:

$$R_q = \sqrt{\frac{1}{l}\int_0^l Z^2(x)dx} \qquad \text{(Eq. 3.3)}$$

and

$$R_a = \frac{1}{l}\int_0^l \left|Z(x)dx\right| \qquad \text{(Eq. 3.4)}$$

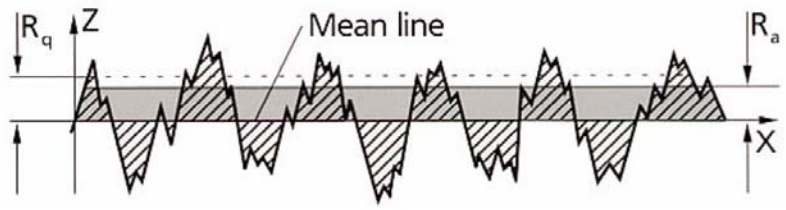

Fig3.12: Illustration of R_q and R_a.

The higher the surface roughness is, the smaller the area of contact gets which causes the formation of voids. For direct wafer bonding, stricter surface conditions are required compared to the anodic bonding process, the mean roughness R_a must be in the sub-nanometer range, ideally less than 0,5 nm [14].

5.3.3 Flatness and bow

Wafer surfaces are in practice never completely flat. This means that the macroscopic flatness non-uniformity of the surfaces leads to a gap at the interface when two such surfaces are contacted. The flatness non-uniformity is generally given by the maximal Total Thickness Variation (TTV), which describes the difference between the minimal and maximal thickness of the wafer. The condition for closing a gap during pre-bonding depends on the ratio of the gap radius (r) compared to the thickness of the wafer (t).

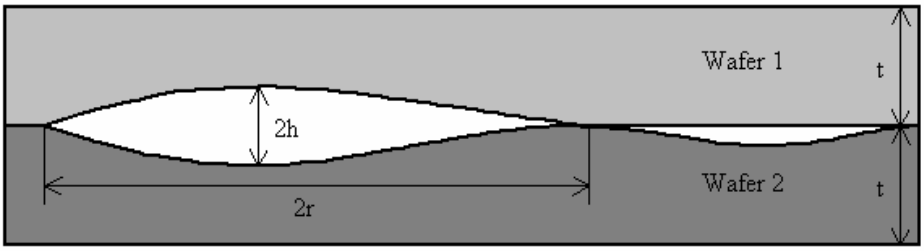

Fig. 3.13: Schematic *drawing of a gap caused by flatness non-uniformity.*

If r < 2*t, the maximum gap height is given by the following equation:

$$h < \frac{r^2}{\sqrt{\frac{2 \cdot E^* \cdot t^3}{3 \cdot \gamma}}} \qquad \text{(Eq. 3.5)}$$

Here E* = E/ (1- ν), E being Young's modulus, ν Poisson's ratio and γ the surface energy between the contacted surfaces.
The bow of a wafer is defined as the curvature of the wafer without thickness variations. The wafer bow does not hamper the bonding procedure due to its large lateral extension [11].

5.4 Chemical Mechanical Polishing of silica

Chemical Mechanical Polishing (CMP) is a process that is used to minimize the surface topography and surface roughness. In this particular approach for fabrication of FEFC structures, the CMP process has the task to provide on the one hand surface properties and minimum step heights that enable bonding. But on the other hand, the CMP has to be controllable in a way that the amount of SiO_2 remaining on the steps and the substrate can be regulated. CMP refers to a material removal that is achieved by a combination of chemical and mechanical interaction. A substrate is pressed against a polishing pad, while chemically active, abrasive slurry is present. The slurry contains sub-micron abrasive particles that get trapped between the substrate and the polishing pad and due to the movement of the pad creates stress fields in the silica surface. Chemical reactions are mediated by the appearance of these stress fields. The water entry into the glass is accelerated by compressive stress imposed into the surface by the abrasive particles, and the solubility increases as a result of compressive stress and hydrostatic pressure. The material removal due to the dissolution is highest just in front of the moving abrasive particle. As a result of this reaction, nanogrooved shaped volumes are removed from the work piece.
The chemical reaction is not fully understood but it is known that the presence of water, which still is the essential part of the slurry, plays an important role in the glass polishing process.
Water weakens the Si-O bond in a SiO_2 film, which most glass is composed of. Ahead, water softens the surface as it becomes hydrated with Si-OH bonds. Hence, the removal mechanism is enhanced. This effect can be described by Eq. (3.6) that was proposed by Cook:

$$Si - O - Si + H_2O \rightarrow 2SiOH \qquad \text{(Eq.3.6)}$$

A schematic overview of a CMP process is illustrated in figure 3.14.

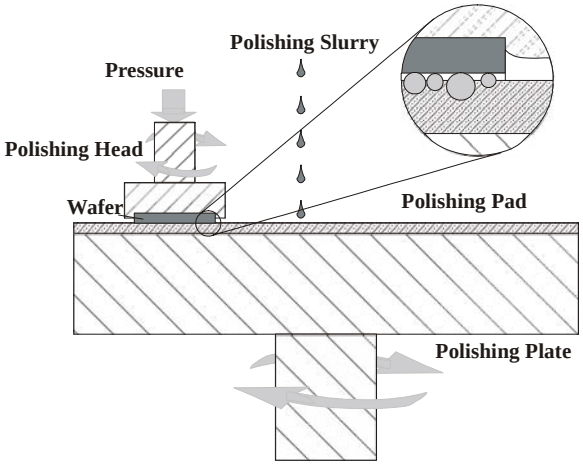

Fig 3.14: *Schematic drawing of the CMP process.*

5.4.1 Removal rate of silica

The reduction of the surface topography with the aid of CMP was measured with silica structures of 200 nm covered with a second PECVD silica layer of 800 nm. Figure 3.15 gives the surface profile before CMP as measured with a dektak scan and after CMP at different time intervals measured with an ellipsometer.

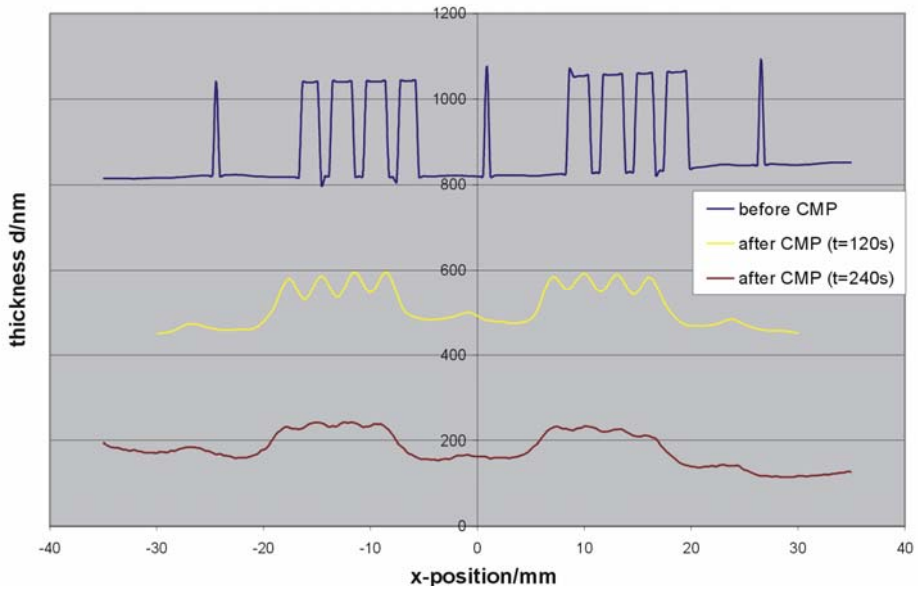

Fig. 3.15: *Dektak scan (before CMP) and ellipsometer measurements of the surface topography (after CMP).*

The rounded curves after 2 and 4 minutes of CMP are caused by the limited resolution of the ellipsometer. The measured profile shows that a reduction of the surface topography is obtained after polishing. However, with increasing polishing time, nearby structures join together to a whole, which results in a reduced reduction of the step height as the polishing time increases. This effect is caused by the elasticity of the polishing pad.
With a decrease in step height the polishing path gets distorted and a more uniform pressure will be present on top and next of the structures.
Due to this effect, the removal rates will converge to a uniform value.
This effect is more pronounced over larger structures since the pad will distort more easily in that case. The removal rate on top and next to the structures is shown as a function of the time in figure 3.16. Next to the structures the removal rate is uniform in time and amounts approximately 165 nm/min. On top of the structures the removal rate converges from 280 nm/min after 60 seconds towards the flat removal rate next to the structures.

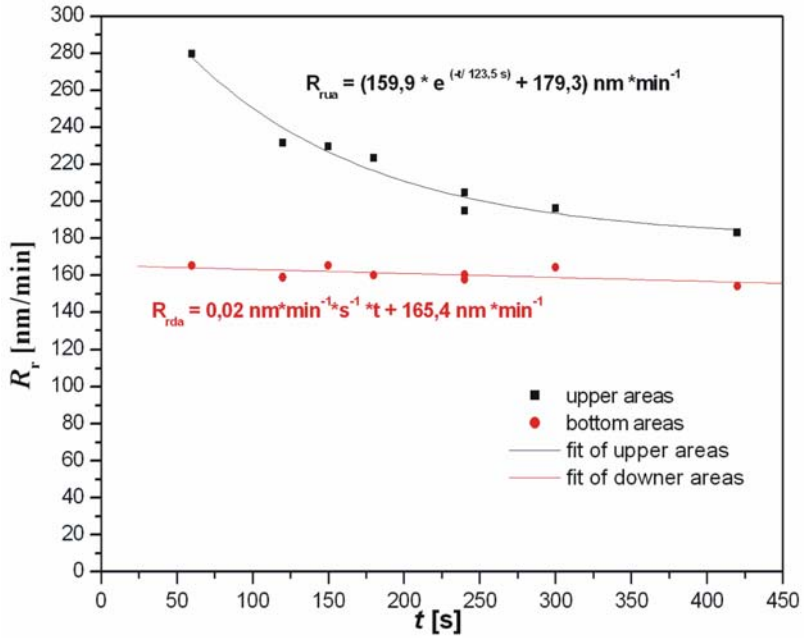

Fig.3.16: *Removal rate as a function of the time on top of and next to the structures.*

5.4.2 Surface roughness

A main function of the CMP process is to reduce the surface roughness to allow thermal bonding. A description of the reduction of the surface roughness with CMP is provided in chapter 4.

5.5 Dielectric breakdown of silica thin films

Figure 3.17 gives a schematic overview of the setup for the silica breakdown experiments. PECVD silica films were deposited on p-type silicon wafers. On the back site of the wafer an aluminum film was deposited to make electrical contact. To mimic the experimental conditions in which a silica electrolyte interface is present, reservoirs were glued on top of the silica films. 100 mM KNO_3 was used as an electrolyte since this electrolyte is known to undergo low preferential adsorption in the hydrated silica interface. The relatively high concentration leads to a high EDL capacitance and thus a low influence of the EDL on the potential distribution. In the breakdown measurements the positive/negative bias was connected to the aluminum contact while the ground electrode was connected to the electrolyte reservoir with a platinum electrode.

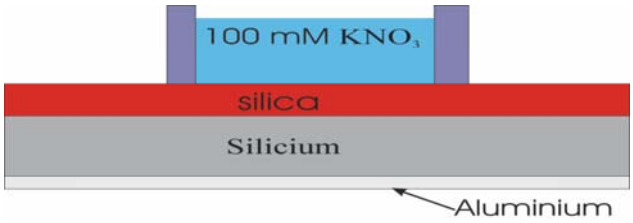

Fig. 3.17: *Schematic overview breakdown measurement setup.*

Table 1 gives an overview of the different PECVD recipes that were applied and the resulting breakdown values for positive and negative bias potentials. During deposition of PECVD silica a mixture of Silane (SiH_4) and Nitrous Oxide (N_2O) is used; the flow rate for both gases is given respectively in the first and second column. Furthermore, the deposition temperature (T_{dep}) and pressure during deposition where varied and are given in columns 3 and 5. In the fourth column the plasma deposition frequency is given, in which LF refers to low frequency (187.5 kHz) and HF to high frequency (13.56 MHz). The breakdown value was measured before and after an anneal step at 450 ˚C for 23 h.

The measured breakdown potentials show that LF processes result in a high breakdown value for positive bias potentials compared to the HF processes. However, for negative bias the breakdown potential is significantly lower. This effect is probably caused due to trapping of ions in the PECVD silica film in LF processed. In a lower frequency deposition, ions in the plasma are still able to follow the alternating electric field and can be trapped in the silica film, which can introduce additional energy levels in the bandgaps of the oxide. This effect can cause the breakdown value to strongly depend on the polarity of the applied potential depending on the valance of the trapped ions. Efficient control in FEFC structures requires a high breakdown potential towards positive and negative applied bias which makes the LF process less suitable.

Furthermore, all wafers that are deposited at 400 Pa show a high leakage current. Due to the high leakage current the silica film doesn't act as a pure capacitance, which can explain the high breakdown potential for positive bias potentials in series 4. The measurements show that deposition at 1000 Pa and 400 ˚C after an anneal step, as shown in series 7b, gives the best results. A high breakdown value is obtained for positive and negative bias with a low leakage current (in the sub nA range) at potentials which are below the electrical breakdown regime.

Series	SiH_4	N_2O	T_{dep} (C°)	LF/HF	Pressure (Pa.)	E_d pos. Bias MV/cm	E_d neg.bias MV/cm
1a	50	950	300	HF	1000	11,6	-7,8
2a	50	950	300	HF	400	16,4	-15,0
4a	50	950	300	LF	1000	13,6	-1,1
5a	50	950	300	LF	400	14,7	-0,5
6a	425	710	300	LF	1000	9,1	-1,0
7a	425	710	400	HF	1000	10,3	-7,2
Annealed 450 C° 23 h							
1b	50	950	300	HF	1000	9,8	-0,4
2b	50	950	300	HF	400	16,4	-0,9
3b	425	710	300	HF	1000	16,4	-1,2
4b	50	950	300	LF	1000	35,2	-3,5
5b	50	950	300	LF	400	13,6	-4,9
6b	425	710	300	LF	1000	8,4	-0,4
7b	425	710	400	HF	1000	9,5	-8,6

Table 1: *Settings PECVD* silica *deposition and breakdown values for positive and negative* bias *potentials.*

5.6 Gate electrode material

The gate electrode material should fulfill the requirements that it does not deteriorate during an anneal step that is required for wafer bonding. Possible mechanisms that cause problems are hillock formation, oxidation of the electrode or phase transitions. A discussion of the tested electrode materials is provided in chapter 4.

6 Applied materials and technologies

An overview of the fabrication process and the applied materials and technologies is provided in chapter 4.

7 Discussion and conclusions

It this chapter it has been illustrated that with the concept of a meandering channel structure in which the subsequent branches are electrically parallel and hydrodynamic serial, a flow can be generated at low absolute potentials. For this concept AC-modulation of the gate zeta potential and the longitudinal electrical field that drives the EOF is required. In order to allow a sufficiently large frequency to avoid bubble formation and still maintain a high hydraulic resistance, large channel aspect ration are required. With channel heights of approximately 5 µm and a channel width of a few millimeters both requirements can be met.

Furthermore, it was illustrated that for maximum flow control, gate insulation with both, a high dielectric constant and a high breakdown value is required. Since glass possesses both properties and is furthermore optically transparent and chemically inert, it has good characteristics for implications in a FEFC structure.

Silica PECVD films have been optimized to obtain high dielectric breakdown strength towards both positive and negative polarization. It is shown that optimal results are obtained during high frequency depositions at elevated temperatures.

To obtain uniform surface charge at the channel walls, which is favorable in studying the characteristics of FEFC, a complete glass device can be fabricated.

To allow bonding of channel and electrode wafers, a CMP process is optimized and characterized. It is shown that with CMP the surface topography can be reduced sufficiently to obtain high bond strength with an annealing step.

8 References

1. van der Wouden, E.J., T. Heuser, D.C. Hermes, R.E. Oosterbroek, J.G.E. Gardeniers and A. van den Berg, *Field-effect control of electro-osmotic flow in microfluidic networks.* Colloids and Surfaces a-Physicochemical and Engineering Aspects, 2005. **267**(1-3): p. 110-116.
2. Lemoff, A.V. and A.P. Lee, *An AC magnetohydrodynamic micropump.* Sensors and Actuators B-Chemical, 2000. **63**(3): p. 178-185.
3. Qin, D., Y.N. Xia and G.M. Whitesides, *Rapid prototyping of complex structures with feature sizes larger than 20 μm.* Advanced Materials, 1996. **8**(11): p. 917-&.
4. Duffy, D.C., J.C. McDonald, O.J.A. Schueller and G.M. Whitesides, *Rapid prototyping of microfluidic systems in poly(dimethylsiloxane).* Analytical Chemistry, 1998. **70**(23): p. 4974-4984.
5. Ng, J.M.K., I. Gitlin, A.D. Stroock and G.M. Whitesides, *Components for integrated poly(dimethylsiloxane) microfluidic systems.* Electrophoresis, 2002. **23**(20): p. 3461-3473.
6. Choi, E.S. and S.S. Yang, *Improvement of Electroosmotic Flow Characteristic in Poly(dimethylsiloxane) channels via a Long Life Chemical Surface Modification.* Micro Total Analysis Systems, 2003. Transducers Research Foundation, Cleveland Heights,OH, USA p. 1121–1124.
7. Makamba, H., Y.Y. Hsieh, W.C. Sung and S.H. Chen, *Stable permanently hydrophilic protein-resistant thin-film coatings on poly(dimethylsiloxane) substrates by electrostatic self-assembly and chemical cross-linking.* Analytical Chemistry, 2005. **77**(13): p. 3971-3978.
8. Buckel, W., *Internal stresses.* Journal of Vacuum Science & Technology,, 1969(6): p. 606-609.
9. Jung, W.W., S.K. Choi, S.Y. Kweon and S.J. Yeom, *Platinum(100) hillock growth in a Pt/Ti electrode stack for ferroelectric random access memory.* Applied Physics Letters, 2003. **83**(11): p. 2160-2162.
10. Gui, C.Q., *Direct Wafer Bonding with Chemical Mechanical Polishing.* Universiteit Twente, Enschede, 1998: p. 3/4, p. 21, pp.19-61, pp.66-69,.
11. Berthold, A., *Low-Temperature wafer-to-wafer bonding for microchemical systems.* Technische Universiteit Delft, 2001: p. p.7/8 and p. 18-23, p.32, p.62, .

12. M. Blom *On-chip separation and sensing systems for hydrodynamic chromatography.* Twente University, Enschede, 2002.: p. p.77.
13. Tong, Q.-Y. and U. Goesele, *Semiconductor Wafer Bonding.* John Wiley & sons, inc., New York, 1999: p. pp. 1-7.
14. Madou, M., *Fundamentals of microfabrication, Roca Baton.* CRC Press LLC, 1997: p. 487.

4

Fabrication of microfluidic networks with integrated electrodes

1 Abstract

In this paper a method is presented for the fabrication of micro-channel networks in glass with integrated and insulated gate electrodes to control the zeta-potential at the insulator surface and therewith the electro-osmotic flow (EOF). The fabrication of the electrodes is a sequence of photolithography, etching and thin film deposition steps on a glass substrate, followed by chemical mechanical polishing (CMP) and subsequently direct thermal bonding to a second glass plate to form closed micro-channels. Plasma enhanced chemical vapor deposition (PECVD) SiO2-layers as insulating material between the electrodes and micro-channels and different electrode materials are examined with respect to a high bonding temperature to obtain an optimal insulating result. A CMP process for the reduction of the SiO2 topography and roughness is studied and optimized in order to obtain a surface that is smooth enough to be directly bondable to a second glass plate.

2 Introduction

In microfluidic devices, the pumping mechanism plays an important role in the transportation of small liquid volumes, such as electro-osmotic flow (EOF). To create EOF, electrodes are placed at both ends of a channel and a voltage is applied resulting in an electric field in the channel. The charge in the double layer at the channel wall will move and consequently drag the liquid. By adjusting an additional electric field across an insulator, which is integrated in the channel wall, the charge distribution close to the insulator's surface can be controlled and in this way also the dynamics of electro-osmotic flow can be modified[1] . Such modified EOF is also an important component of electro kinetic separation techniques as it influences the efficiency, resolution and reproducibility [2, 3]. Hayes et al. realized devices using fused silica capillaries as channel and insulator, which were covered with a conductor to apply the external voltage [3, 4]. Tens of kilovolts were applied to modify the EOF. Later research showed that the potential could be decreased to 120 V by integrating the channel and electrodes on a glass substrate using micro fabrication: parallel to an etched channel, embedded electrodes were fabricated so that the insulator's thickness in between was reduced to 50 µm [5].

In this paper the fabrication of a microfluidic device is described, which has electrodes integrated in a glass substrate. The electrodes are covered with a 400 nm plasma enhanced chemical vapor deposition (PECVD) SiO_2-layer as insulator. On top of this substrate another glass substrate is bonded, in which channels are etched. Chemical mechanical polishing (CMP) is used to obtain a surface that is suitable for glass-to-SiO_2 direct wafer bonding.

3 Fabrication

As schematically shown in figure 4.1, the microfluidic device consists of two wafers: a bottom wafer with electrodes, contact pads and an insulating layer, and a top channel wafer with in and outlet holes. The size of the electrodes is 1.00 by 5.6 mm^2 and the dimension of the channels is 45 µm × 15 µm × 1.5 cm (w × h × l). The channels were etched with 25 % hydro fluoric acid (HF) using a chromium/gold mask, and access holes were powder blasted through the 1.1 mm thick 4-inch Borofloat (Schott Borofloat 33) substrate.

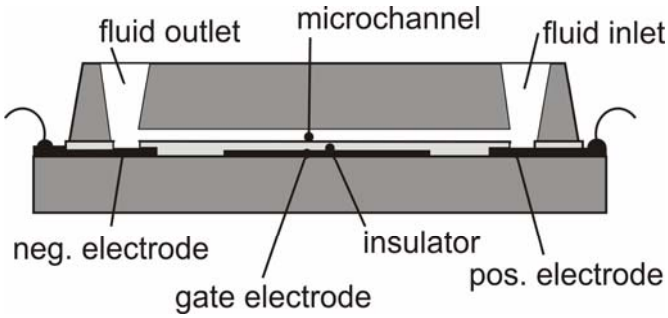

Fig. 4.1: *Schematic drawing of the device structure.*

In Figure 4.2, the process scheme of the bottom wafer is illustrated. First photolithography was performed on a 512 nm thick 4-inch Pyrex substrate to form an etch-mask for 200 nm deep gaps, which were etched with BHF. Next, a 15 nm thick tantalum (Ta) adhesion layer and 180 nm thick platinum (Pt) layer are sputtered on top. Then, the still present lithographic resist mask was used to form electrodes in the gaps by lift-off technique. Embedding the electrodes has two advantages: to ensure that the height difference between the Pyrex and electrode surface is small, and to prevent metal peak formation (lift-off ears) originating from metal deposited at the resist sidewalls that remains connected with the electrodes after lift-off. After resist lift-off, an 800 nm SiO_2 layer is deposited at 300 °C by PECVD. Next, the oxide layer is planarized by CMP and the surface roughness is reduced

by an additional CMP step to allow direct thermal bonding. The result is a 400 nm thick insulating layer.

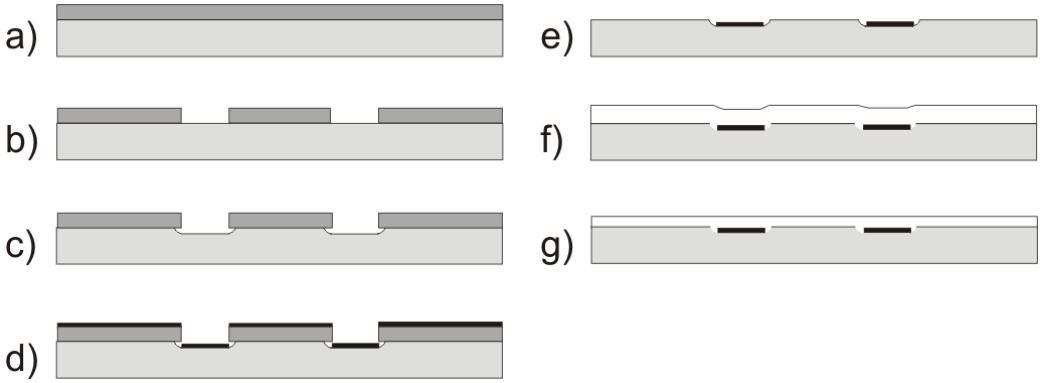

Fig. 4.2: *Fabrication process of* the *electrode wafer consisting of photolithographic steps on a glass substrate (a, b), etching (c), sputtering of the electrode material and lift-off process (d, e), and deposition of SiO_2-layer and step polishing via CMP (f, g).*

Following, the substrates are directly bonded and annealed at 550 °C for one hour and finally diced into individual devices shown in figure 4.3. As the bottom electrode wafer contains the critical process steps, its processing is described in detail below.

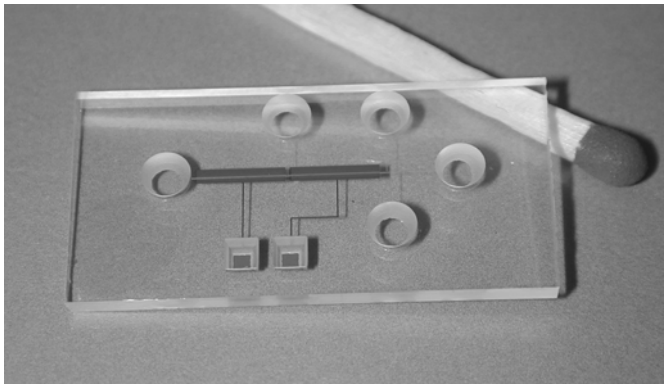

Fig 4.3: *Photograph of a microfluidic chip with two gate-electrodes.*

3.1 Electrodes

The electrode material should have strong adhesion to the Pyrex substrate and the SiO_2 layer since the CMP process will introduce great shear forces

on the electrode. Furthermore, it should withstand high annealing temperatures of at least 550 °C without deforming or creating hillocks, which potentially could cause cracking of the oxide layer. A combination of tantalum (Ta) and platinum (Pt) was found to be the optimal material compared to aluminum and chromium/gold combinations. Aluminum shows excellent adhesion to SiO_2 and Pyrex. However, it deforms dramatically above temperatures of 350 °C. Chromium/gold electrodes do not deform at these temperatures, though adhesion is not sufficient to the SiO_2 layer and consequently the oxide above the electrodes rips off or cracks during CMP. With a Ta/Pt combination, working devices could be obtained. However hillock formation on the Pt surface during the annealing process appears to deteriorate the SiO_2 layer, leading to high leakage current and dielectric breakdown of the SiO_2. Applying a high temperature step (e.g. at 600 ºC) before depositing the oxide helps to prevent cracking due to metal deformation during bonding. Pt does not deform further when in the bonding process the temperature is kept lower than in the first annealing step [6].

3.2 PECVD SiO_2

The PECVD deposition process was optimized to fulfill the requirements of SiO_2 as insulating as well as bonding layer. These requirements are low stress, good electrical insulation and good uniformity.
Vacuum deposited films generally exhibit remarkable internal stresses. Mechanisms that may be responsible for stress are incorporation of atoms, lattice mismatch, re-crystallization processes, microscopic voids and/or phase transformations [7]. Residual stress in oxide films leads to overall wafer bow, which makes polishing or bonding difficult. Furthermore, if the stress is too high, cracks, displacement and buckling of the oxide can be created and its function as an insulating layer will not be fulfilled. So, the radius of curvature of a silicon substrate was investigated before and after depositing the oxide, using a DekTak profilometer scanning in 0, 45, 90 and 135º direction. Then, the stress was calculated applying the Stoney equation [8], which was related to the substrate curvature.

$$\sigma_0 = \frac{1}{(R_1 - R_2)} \cdot \frac{E_S}{6 \cdot (1 - \nu_S)} \cdot \frac{t_S^2}{d}, \qquad \text{(Eq. 3.1)}$$

where R_1 and R_2 are the radii of curvature of the silicon substrate with and without film, respectively, E_s the Young's modulus, ν_S the Poisson's ratio, t_S the thickness of the substrate and d the thickness of the deposited film. A stress limit below 300 MPa is required. Recipes were investigated to minimize stress taking the other requirements into account. From the DekTak scans, a compressive stress of 236 MPa was calculated, which falls in the required range.
To study the insulation of the oxide layer, its breakdown voltage was investigated. Insulation can also be linked to the layer's refractive index (RI), which can be measured ellipsometrically. If the RI is higher than 1.458, there is too low oxygen content, which could mean that the oxide layer is not insulating enough. Also hydrogen atoms incorporated in the layer may deteriorate insulation. As hydrogen is very mobile, it will migrate towards the surface, which leaves small holes in the lattice structure of the oxide. Generally, annealing above the transition temperature of the film (approx. 1000 ºC) can help to remove hydrogen and ultimately increase the density of the film, which results in a much higher breakdown voltage, however compressive stress also increases [9]. Nevertheless, such high temperatures are not feasible for the current device, since the melting point of Pyrex lies at approx. 680 ºC. Cao et al. demonstrated that already at 500 ºC, plastic flow and density changes are taking place. During the thermal cycling, seams and voids are reduced, resulting in lower compressive stress and a more ordered SiO_2 network [10]. Electrical breakdown occurred at 9.6 ($\pm$ 0.3) MV/cm, which is sufficient for device operation.

Film uniformity over the wafer is essential for obtaining a good bonding result and to guarantee comparable insulating properties for each device. Therefore, the Within-Wafer Non-Uniformity (WIWNU) can quantify the performance of the PECVD and later the CMP process. The general definition of WIWNU is:

$$WIWNU = \frac{\sigma_{RR}}{RR_{average}} \times 100 \qquad \text{(Eq. 3.2)}$$

where σ_{RR} represents the standard deviation of thickness of either remaining or removed oxide [11, 12]. $RR_{average}$ represents the mean value of the measured thickness or of the removal. For the current process WIWNU of less than 5% is required. Therefore, the thickness of a SiO_2 layer was

scanned at 81 points with a Plasmos Ellipsometer. Subsequently, from these values a WIWNU of 3 % was determined.

4 Results

4.1 CMP

CMP is the key process in this work to obtain a flat SiO_2-layer with an enhanced surface smoothness to allow direct wafer bonding to the Borofloat plate. The samples were polished with a Mecapol E460 polishing machine (Presi). Semi-Sperse® 25 colloidal fumed silica slurry (Cabot Microelectronics) was used in different dilution ratios. There are many other process variables that influence the quality of polishing, such as rotation speed of the wafer carrier and polishing pad, polishing pressures, type of the pad, flow rate of the slurry, as well as the temperature. A CMP procedure for uniform removal was optimized and divided into two polishing runs. The first run was carried out with a CR IC 1000–A2 K-Groove pad to remove the oxide-steps originating from the height difference between the electrodes and the Pyrex surface. The second run was done with a UR 100 pad to reduce the surface roughness to sub-nanometer range. Prior to each run, pad pre-conditioning was performed using a diamond brush for the IC 1000 and a nylon brush for the UR 100 pad. This is required to obtain reproducible, uniform and consistent results. Parameters for both polishing processes are presented in table 3.1.

	Settings	Settings
Pad	CR IC 1000-A2 K-Groove	UR 100
Slurry		
Name	Semi-Sperse 25	Semi-Sperse 25
Dilution ratio	1:1	1:2
Flow speed /ml/min	60	125
Head		
Rpm	42	55
Rotation direction	Right	Right
Table		
Rpm	30	50
Rotation direction	Right	Right
Initial run		
Pressure p_1 / bar	0.0	0.0
Time t_1 / s	5	5
Working step		
Pressure p_2 / bar	0.75	1.00
Time t_2 / s	240	60
Backpressure / bar	0.20	0.15
Flushing step		
Pressure p_3 / bar	0.0	0.0
Time t_3 / s	60	60
Temperature / °C	20	20

Table 4.1: *Settings of the CMP processes.*

Resulting from CMP test runs, a removal rate of 153,5 nm/min for the IC 1000 pad and 160 nm/min for the UR 100 pad were obtained. Polishing times for the IC 1000 pad were then adjusted for different step heights up to 200 nm. In figure 4.4, DekTak scans are presented that were performed at the same spot before and after polishing 1 µm SiO_2 back to 400 nm. It is obvious that the 200 nm step was completely removed.

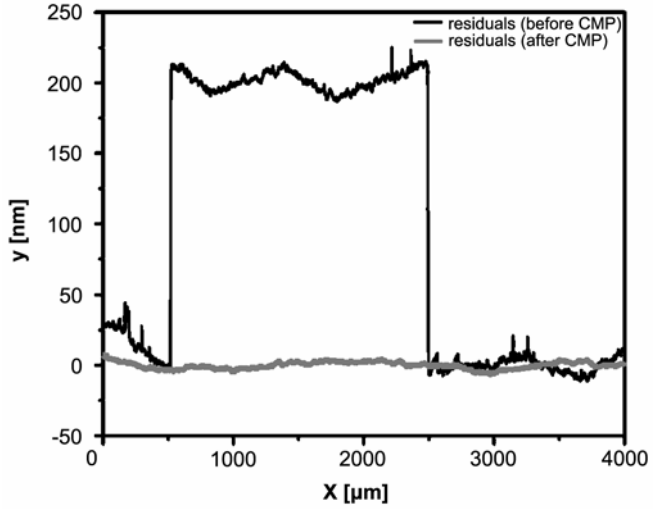

Fig. 4.4: *DekTak scan of step height before (black) and after polishing (gray).*

The other aspect of planarization that influences the bonding is the surface roughness of which a value less than 1 nm is required. Polishing 60 seconds with the UR 100 pad was sufficient. In figure 4.5, two AFM scans are shown, representing the roughness of unpolished SiO_2 with a value of 5.9 nm and polished SiO_2 with a roughness of only 0.7 nm.

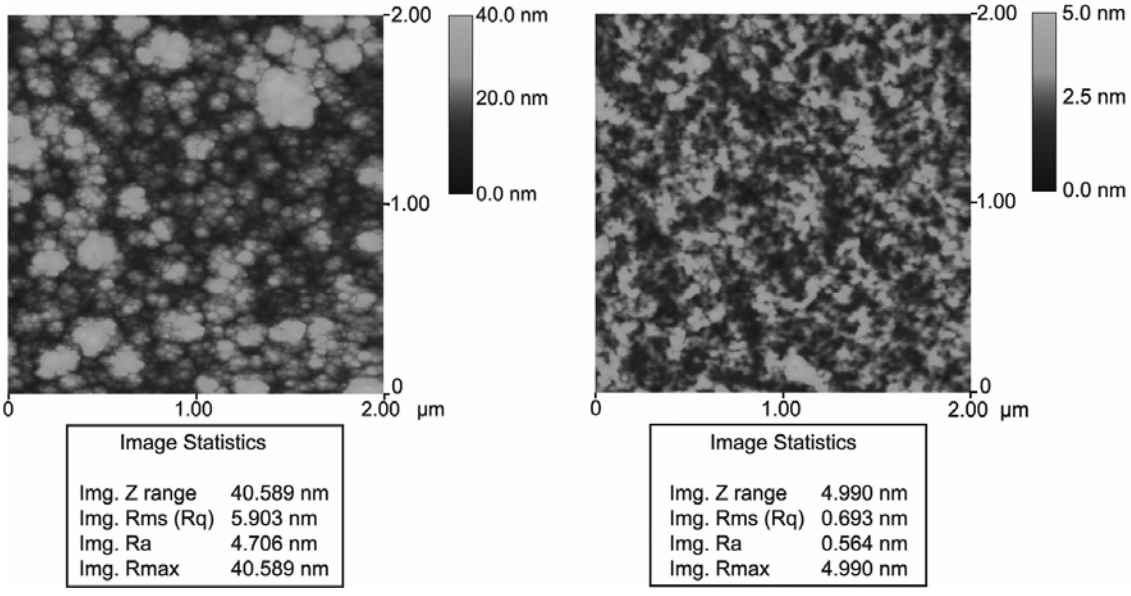

Fig. 4.5: *AFM measurement of the oxide roughness at a spot of 2 x 2 µm^2. Left: unpolished wafer, right: polished wafer.*

4.2 Cleaning and direct bonding

Apart from flatness and smoothness, direct bonding requires surfaces free of contaminants. Contaminations that play an important role in bonding can be classified as particle contamination and organic contamination [13]. Particles can act as spacers and inhibit the interaction between the opposing surfaces. Organic contaminants do not result in un-bonded areas at room temperature. However, they adhere only weakly to the substrate and may limit the ultimate bonding strength. Furthermore, they are responsible for the appearance of voids and bubbles in the interface during annealing.

A CMP post-cleaning step is essential, as residue slurry particles are very difficult to remove once the slurry is dried out. Several cleaning steps were applied to remove the contaminants but not affect the surface roughness. After polishing, first a roller brush was used that rotates over the wafer and with addition of de-ionized (DI) water, removes slurry from the surface. Additional ultrasonic cleaning in DI water for 60 min enhanced the removal of residue particles. Subsequently, the wafers were cleaned in fuming nitric acid for 20 min in order to remove organic films, followed by rinsing in DI water. The top-channel wafer was treated in the same way, though starting with ultrasonic cleaning, to remove residues from powder blasting. After spin-drying, both wafers were aligned and brought into contact immediately so that a pre-bond was formed at their interfaces. To enhance bond strength, the wafer stack was annealed at 550 ºC for 1 hour. Ramping up was set to 6 hours to prevent high stress formations originating from thermal mismatch of the applied materials. For ramping down, no active cooling was used, so that after approximately 12 hours a temperature of 100 ºC was reached, at the moment, when the wafers were removed from the furnace. Bonding results were excellent and no un-bonded areas or voids could be determined. The wafers could not be separated again by knife afterwards and dicing into individual chips was possible without delaminating the substrates.

5 Conclusions

A technique for integrating insulated electrodes in a channel wall is presented by using CMP and glass-to-SiO_2 direct bonding. A PECVD recipe was optimized to provide a low stress, good insulation and good uniformity

of the SiO_2-layer. Furthermore a CMP procedure was optimized that allows planarizing and smoothening of the oxide layer. Consequently, a good bonding between both wafers was obtained. Microfluidic testing of the devices was performed with success [14].

6 Acknowledgements

The authors gratefully acknowledge the Dutch technology foundation STW for financial support (project nr. 5384).

7 References

1. Schasfoort, R.B.M., S. Schlautmann, L. Hendrikse and A. van den Berg, *Field-effect flow control for microfabricated fluidic networks.* Science, 1999. **286**(5441): p. 942-945.
2. Giddings, J.C., *Unified Separation Science. 1st ed.* John Wiley & Sons, New York, 1991.
3. Hayes, M.A. and A.G. Ewing, *Electroosmotic Flow-Control and Monitoring with an Applied Radial Voltage for Capillary Zone Electrophoresis.* Analytical Chemistry, 1992. **64**(5): p. 512-516.
4. Hayes, M.A., I. Kheterpal and A.G. Ewing, *Electroosmotic Flow-Control and Surface Conductance in Capillary Zone Electrophoresis.* Analytical Chemistry, 1993. **65**(15): p. 2010-2013.
5. Polson, N.A. and M.A. Hayes, *Electroosmotic flow control of fluids on a capillary electrophoresis microdevice using an applied external voltage.* Analytical Chemistry, 2000. **72**(5): p. 1088-1092.
6. Tiggelaar, R.M., *Silicon-technology based microreactors for high-temperature heterogeneous partial oxidation reactions.* PhD Thesis, University of Twente, 2004.
7. Buckel, W., *Internal stresses.* Journal of Vacuum Science & Technology,, 1969(6): p. 606-609.
8. Stoney, G., *The tension of thin metallic films deposited by electrolysis.* Proc. R. Soc. Lond. A, 1909(82): p. 172.
9. Ghodssi, R., L.G. Fréchette, S.F.N. SF, X.Z. X, A.A. Ayon, S.D. Senturia and M.A. Smidt, *Thick bufied oxide in silicon (TBOS): An integrated fabrication technology for multi-stack wafer-bonded MEMS processes*

Proceedings of the 10th International Conference on Solid-State Sensors and Actuators, Technical Digest, Sendai, Japan, 1999: p. 1456-1460.
10. Cao, Z.Q. and X. Zhang, *Density change and viscous flow during structural relaxation of plasma-enhanced chemical-vapor-deposited silicon oxide films.* Journal of Applied Physics, 2004. **96**(8): p. 4273-4280.
11. Sorooshian, J., A. Philipossian, M. Goldstein, S. Beaudoin and W. Huber, *Impact of wafer geometry and thermal history on pressure and von Mises stress non-uniformity during chemical mechanical planarization.* Japanese Journal of Applied Physics Part 1-Regular Papers Short Notes & Review Papers, 2003. **42**(10): p. 6363-6370.
12. Sugimoto, F., Y. Arimoto and T. Ito, *Simultaneous temperature measurement of wafers in chemical mechanical polishing of silicon dioxide layer.* Japanese Journal of Applied Physics Part 1-Regular Papers Short Notes & Review Papers, 1995. **34**(12A): p. 6314-6320.
13. Ploβl, A. and G. Krauter, *Wafer direct bonding: tailoring adhesion between brittle materials.* Materials Science & Engineering R-Reports, 1999. **25**(1-2): p. 1-88.
14. van der Wouden, E.J., T. Heuser, D.C. Hermes, R.E. Oosterbroek, J.G.E. Gardeniers and A. van den Berg, *Field-effect control of electro-osmotic flow in microfluidic networks.* Colloids and Surfaces a-Physicochemical and Engineering Aspects, 2005. **267**(1-3): p. 110-116.

5

Simulation of Field Effect Flow Control of Electro-Osmotic Flow

1 Abstract

In this chapter, simulations of Field Effect Flow Control (FEFC) structures are presented. Simple structures that resemble fabricated devices are composed. The velocity profiles and the influence of the gate zeta potential on the net flow is analyzed and compared to experimental results with the aid of CFDRC. It is shown that the simulated velocity profiles agree qualitatively to the experimental results. The effect on the net flow of a FEFC device however, is drastically underestimated at low surface coverage of the gate electrode. The discrepancy between the results can be attributed to a spreading of the gate zeta potential to the non-gated areas due to surface conduction. More complex FEFC arrays are designed to investigate the ability for such networks for flow control in fluidic networks. It is shown that the flow can be directed. However, local recirculation effects occur in case of an offset value for the zeta potential.

2 Finite element modeling

Finite element simulations can provide a powerful tool for design, testing and realization of microfluidic structures. Especially in case the fabrication is complex and time consuming, it can be favourable to initially perform simulations to test the optimal geometries and dimensions to save money, time and materials in fabrication. Furthermore, they can provide a useful tool for validation or comparison to measurements.

3 Simulation model

Two different layouts have been investigated in the simulations to gain more insight in design parameters and behaviour of Field Effect Flow Control and to validate experimental data. An overview of the models that were used and the considerations for the choice of the shape and size are given below. The simulations were performed in the finite element program CFDRC (Computational Fluid Dynamics Research Corporation).

3.1 Half ellipse model

In chapter 3 and 4 the fabrication of FEFC structures with glass channels was discussed. The HF etching procedure leads to channel geometries with inclined side walls.

The chips are fabricated with several etching and thin film deposition steps, which finally results in 200 nm thick platina electrodes deposited on top of a Pyrex substrate. The electrodes are covered with a 350 nm or 210 nm silica insulation layer. On top of this, a second Pyrex wafer with an etched channel and access holes is bonded.
An example of a channel cross-section measured with a dektak scan is shown in figure 5.1. In figure 5.2, a simulation model based on the measured channel cross section is shown. Simulations have been carried out with a model of 19 mm length that represents the complete channel length and with a model for a 975 µm length, to save computing time. The channel depth amounts to 18 µm, the top and bottom width are respectively 70 and 30 µm.

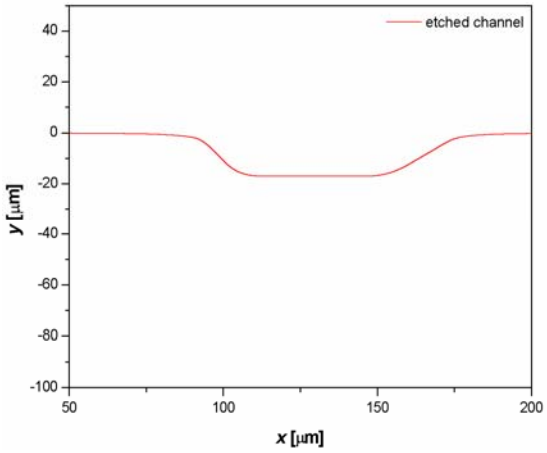

Fig. 5.1: *Profile of an HF etched channel cross-section.*

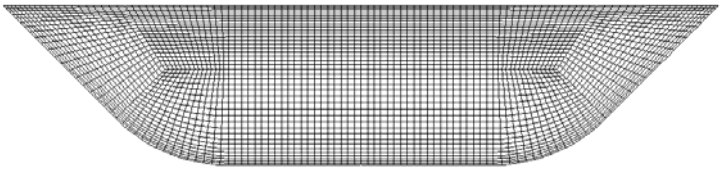

Fig. 5.2.: *Transverse grid structure consisting of 10 building blocks; with a total of 630,000 cells in the 3D domain.*

3.2 Square channel model

To simulate a channel geometry that resembles the channel structures fabricated in PDMS, as discussed in chapter 2, a square simulation model

was composed. Furthermore, the modelling of square geometries offers the advantage that a more effective mesh can be created which results in less computational demands than in the case of the half ellipse model.
The modeled channel consists of three parts, each 300 µm long. An illustration of the model is shown in figure 5.3. In the first and last section, a fixed zeta potential is applied while the top of the middle section is indicated as the gate area, in which a variable zeta potential is applied. The gate region is divided in 5 regions to allow the application of a gradient in the zeta potential in the length direction (i.e. x), which will also be present in the practical operation of a FEFC structure. The potential at the gate electrode will be uniform throughout the length of the channel, while the channel potential shows a gradient. Due to this, the potential difference between the gate and channel potential will show a gradient equally large as the potential gradient in the channel over the gate electrode length which will result in a non-uniform zeta potential over the gate electrode region.

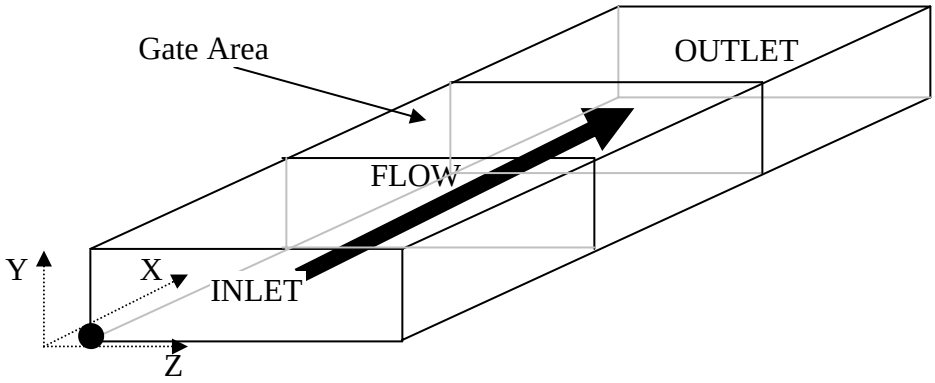

Fig. 5.3: *Schematic overview square geometry. With length: 900 µm, height: 15 µm and width 100 µm.*

3.3 Boundary conditions

The simulation of electroosmotic flow requires the implementation of the Helmholtz-Smoluchowski slip-velocity boundary condition along the side walls of the microchannel [1]:

$$v = \frac{\varepsilon_0 \varepsilon_r \zeta}{\eta} E_x \qquad \text{(Eq. 5.1)}$$

In equation 5.1, ε_r is the dielectric constant of the electrolyte solution, ε_0 is the permittivity of vacuum, ζ is the zeta potential, E_x is the externally applied electric field strength, and η is the viscosity. The slip boundary condition that is given in formula 5.1 requires knowledge of the zeta potential at the wall of the microchannel, which is dependent upon the gate voltage, *Vg*. As illustrated by Schasfoort *et al*. , the change in zeta potential in the vicinity of the gate electrode can be computed from the following equation [2]:

$$\Delta\varsigma = \frac{C_{wall}}{C_d}\left(V_g - V_{sol}\right) \qquad \text{(Eq. 5.2)}$$

Here C_{wall} is the capacitance of the channel wall and C_d is the capacitance of the electrical double layer. The capacitance (per unit area) of channel wall in the gate region is given by:

$$C_{wall} = \frac{\varepsilon_0 \varepsilon_r \mathrm{A}}{d} \qquad \text{(Eq. 5.3)}$$

were *d* is the thickness and ε_r is the dielectric constant of the oxide layer, while the capacitance (per unit area) of the electrical double layer can be estimated as [3]:

$$C_d = 228z\sqrt{c}\cosh\left(19.5z\varsigma\right) \qquad \text{(Eq. 5.4)}$$

Equations (5.2) and (5.4) can be solved using a simple iterative technique to estimate the change in zeta potential under the gate electrode. For a gate potential of +36 V, the change in zeta potential is estimated to be +35 mV leading to an absolute value of zeta potential of +21 mV (the unmodified zeta potential being −14 mV) for a gate insulation thickness of 210 nm with a dielectric constant of 4.
Conversely, for a gate potential of −36 V, the change in zeta potential is estimated to be −28 mV, leading to an absolute value of zeta potential of −42 mV. In a FEFC structure the operation is more efficient at a small offset value for the zeta potential [4]. Hence, in the simulations it is assumed that the aqueous electrolyte pH is close to the point of zero charge of the solid surface and an offset value for ζ_0 of -10 mV or -14 mV is chosen.

A fixed longitudinal electric field of 150 V/cm is applied in all simulations with atmospheric pressure conditions at the inlet and outlet of the channel.
When the channels are coupled to fluidic reservoirs, or field free side branches are present which is generally the case, induction of pressure driven flow has been observed [5, 6]. This effect is caused by expansion or contraction of the flow profile at the inlet and outlet. Consequently, viscous dissipation results in the formation of a pressure gradient [7-9]. However, these effects are manly to be considered at low hydraulic channel resistances or if plug velocity profiles are required, for instance in the case of electrophoretic separation. In FEFC, the generated pressures due to differences in zeta potential are generally much larger than those originating from entrance effects. In this case, the influence is limited to the flow development region that is roughly 0.6 times the channel diameter [10] so that an atmospheric pressure at the inlet and outlets can be assumed. An overview of the applied parameters and their values is given in table 5.1.

Parameter	Value
pH	3-4
Buffer concentration (c)	5 mM
Dielectric constant medium($\varepsilon_{r)}$	80
Dielectric constant insulation ($\varepsilon_{r)}$	4
Insulation thickness	210/350 nm
Viscosity (η)	0.001 Ns/m^2
Density (ρ)	1000 kg/m^3
Zeta potential offset ($\zeta_{0)}$	-10--14 mV
Electric field ($E_{x)}$	150 V/m
Inlet/outlet pressure (P)	$1*10^5$ Pa/m^2

Table 5.1: *Simulation variables.*

4 Heterogeneous surface charge

The velocity profiles in case of a heterogeneous zeta potential is shown in figure 5.4 for two different situations. In the left picture a zeta potential of 15 mV is assumed at the gate which is located only on 1/3 of the top of the channel. The natural zeta potential is set to -10 mV on the remaining channel wall. In the right picture the conditions are the same except that the gate zeta potential is also applied to 1/3 of the side channel walls. Both figures show the transition areas; with the gated area on the left side of the

square cross-section and on the right the non-gated area. It can be seen that the net velocity outside the gate region consists of two contributions: a plug EOF profile and a parabolic profile. The latter results from the pressure build up due to the differences in local flow rate, as was explained in chapter 2.5. In the gated areas a difference in velocity at the side walls is present due to the difference in local zeta potential.
The different zeta potential results in a linear gradient in the EOF. This gradient can be beneficial, it has for instance has been utilized to compensate for the race track effect that originates from velocity differences in channel turns and in this way minimize dispersion [11]. However in a straight channel the linear EOF results in locally complex flow profile due to the position dependent velocity of both hydrodynamic and EOF flow.

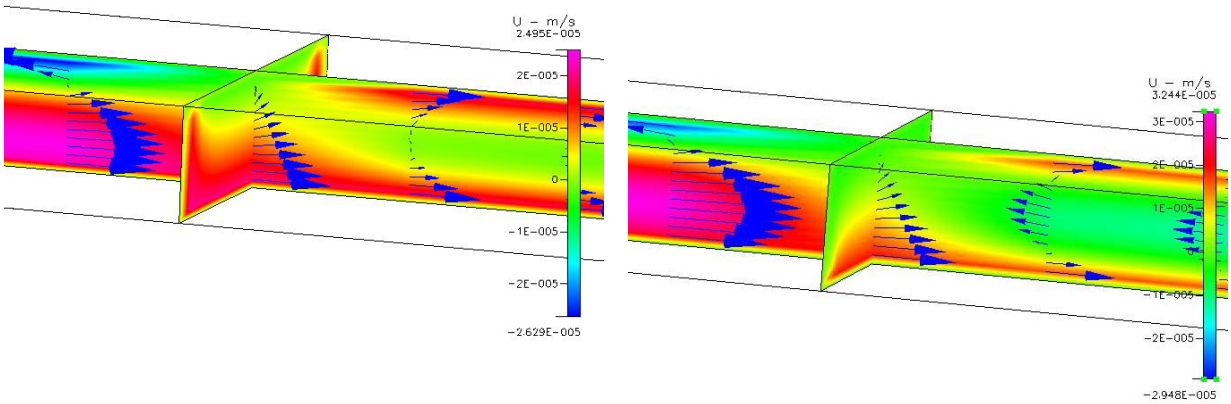

Fig.5.4: *Flow profiles for different gate electrode arrangements: left) one electrode located at the top of the channel that provides ζ = +15 mV; right) three electrodes located at the top of the channel and its two side walls that all provide ζ = +15 mV. Gate area is located upstream of indicated channel cross-section.*

At the interface between the gated and non-gated areas a transition area can be distinguished. In this region locally velocities in opposite direction are present so that a pressure difference emerges. It can be seen that the resulting flow is not confined to the horizontal direction but also a vertical component in the velocity vectors is present. This vertical flow results from the local pressure gradients that emerge to satisfy flow continuity in each section of the channel. From the difference in the left and right picture it can be clearly seen that the surface coverage affects the flow rate and flow profile. While in the left picture outside the gated region the natural EOF is

still dominant, in the left side the induced hydrodynamic component dominates and the flow velocity in the centre of the channel is reversed.
It is clear from the above pictures that with a heterogeneous zeta potential present at the surface, the typical plug flow profile associated with EOF is no longer present. The local differences in flow rate introduce a significant Taylor dispersion [12], which offers disadvantages when for instance the plug flow is favourable for electrophoretic separation techniques [13, 14].
However, this effect can also be utilized for mixing in microchannels. Typically flow in microchannels is laminar and has low Reynolds numbers associated with it. This implicates that for instance in chemical synthesis, reactions become diffusion limited. This can be time consuming, especially when for instance macromolecules with low diffusion constants are used.
In these cases, long channel lengths and long time scales are necessary. To reduce the mixing length and time, passive techniques have been applied, to induce transverse flows by creating complex geometries [15, 16], or the applications of coatings or surface patches to create heterogeneous surface charge [17-20]. However, these methods do not allow a dynamic control over the mixing rate in the channel. With the use of FEFC structures dynamic control of mixing can be obtained by the application of a suitable gate potential. The application of a controlled heterogeneous zeta potential has been shown to create eddies in the EOF that enhance the mixing rate [21, 22].
In figure 5.5 a simulation is shown for a channel geometry of 975 μm long. The channel resembles the half ellipse structure as was discussed in section 3.1.1. The simulation result shows that the local flow near the gated area wall is reversed. Before and after the gated area the flow consists of the typical plug EOF profile with a slight hydrodynamic profile due to the induced pressure flow. However, the influence on the net flow is limited.
A side view and cross-section of the simulated channel is shown in figure 5.6.

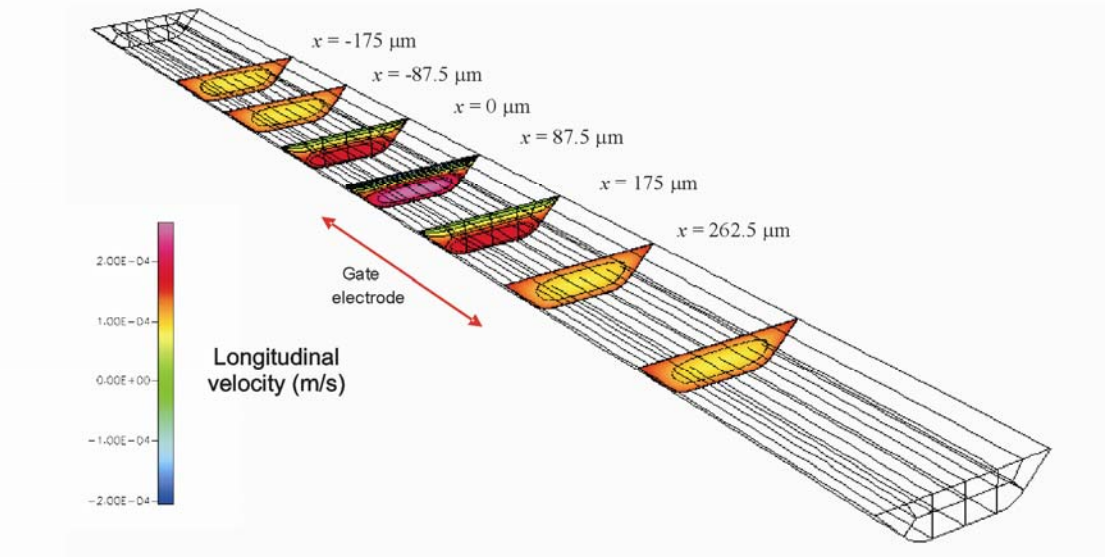

Fig. 5.5: *Modelled section 875 µm long: composed of a 350 µm long section with an unmodified zeta-potential, 175 µm long gate electrode at the top of the channel and a further 350 µm section with an unmodified zeta potential.* ζ_{normal} = -14 mV and ζ_{gate} =+ 21mV.

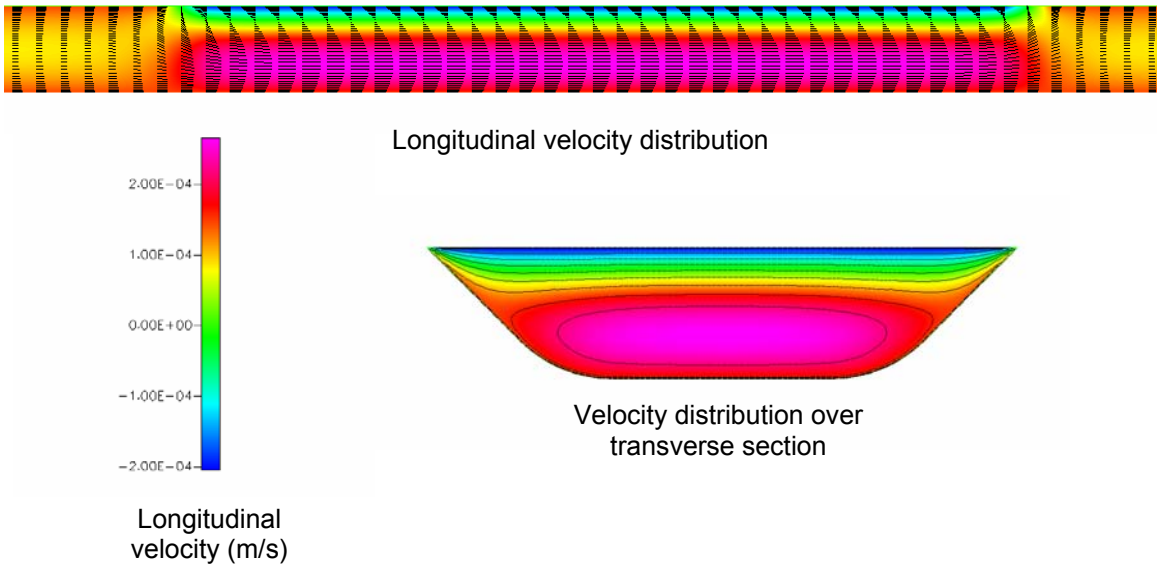

Fig. 5.6: Side view of the predicted velocity field in the vicinity of the gate electrode and a cross-section in the gate region with ζ_{normal} = -14 mV and ζ_{gate} = + 21 mV.

Figure 5.7 gives the velocity profiles in the gated area for different gate zeta potentials, for the channel geometry as described in figure 5.5. The simulations show that at the gate wall the flow is proportional to the gate zeta potential. However, as the gate zeta potential deviates more from the average zeta potential, also the counter hydrodynamic flow in the centre of the channel increases. This counter flow compensates to a large extend the change in flow obtained by the gate zeta potential.

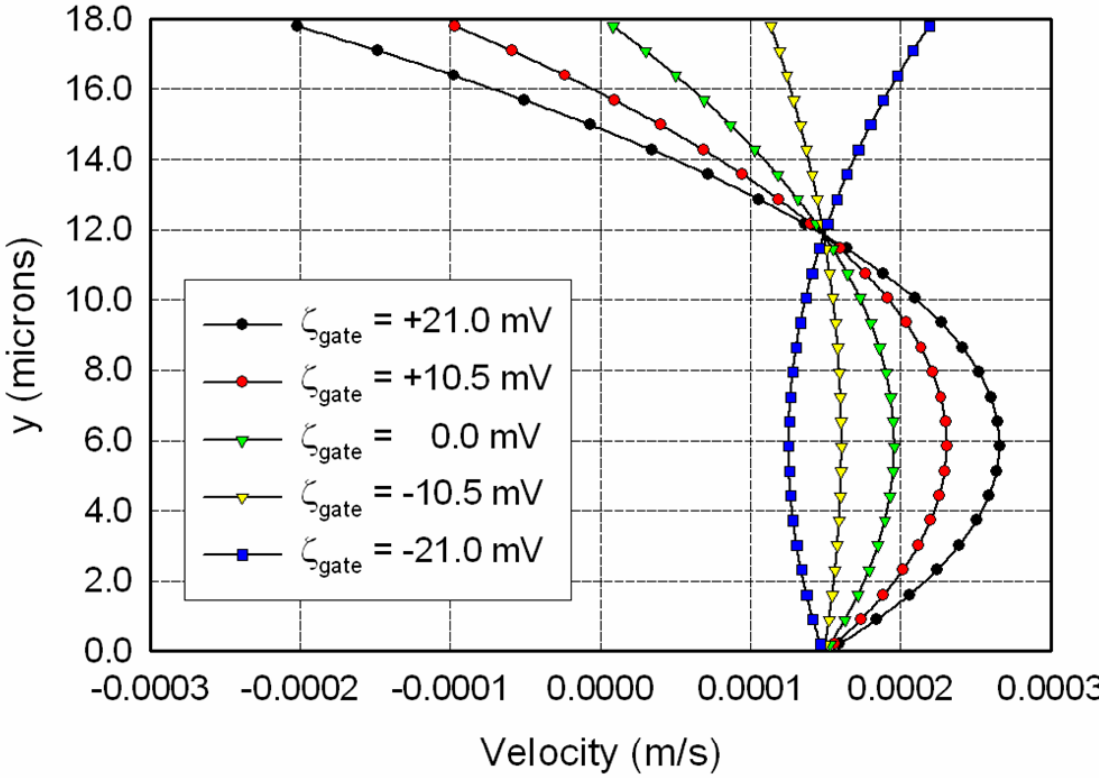

Fig. 5.7: Predicted velocity field in the vicinity of the gate electrode for different gate zeta potential with ζ_{normal} = -14 mV.

5 Influence gate area coverage

In figure 5.8 a transverse cross-section is shown for a 975 µm long section and the complete modelled channel of 19 mm, both with a fixed gate length of 175 µm long at the top of the channel. The cross-section is taken at the entrance of the gated area. It can be seen that in the gate region the velocity profile is equal over the entire channel height. However, away from the gated area, it can be seen that for the complete 19 mm channel a far

less influence on the velocity profile is induced. For the shorter 975 µm long section still an EOF profile with a hydrodynamic component can be distinguished, while for the complete simulated channel only a slight concave profile is visible.
This limited influence of the gate zeta potential can be understood by the influence of the gate zeta potential on the average flow. When the influence of the gate potential on the local zeta potential is assumed to be a purely capacitive effect, then it can be assumed that the influence of the gate potential is limited to the part of the channel wall that it is covering.
Since the gate area coverage of the channel is limited in this FEFC layout, its influence on the average zeta potential that is controlling the average flow will also be limited [23, 24]. This low modification of the average zeta potential will consequently lead to a low influence on the average flow.

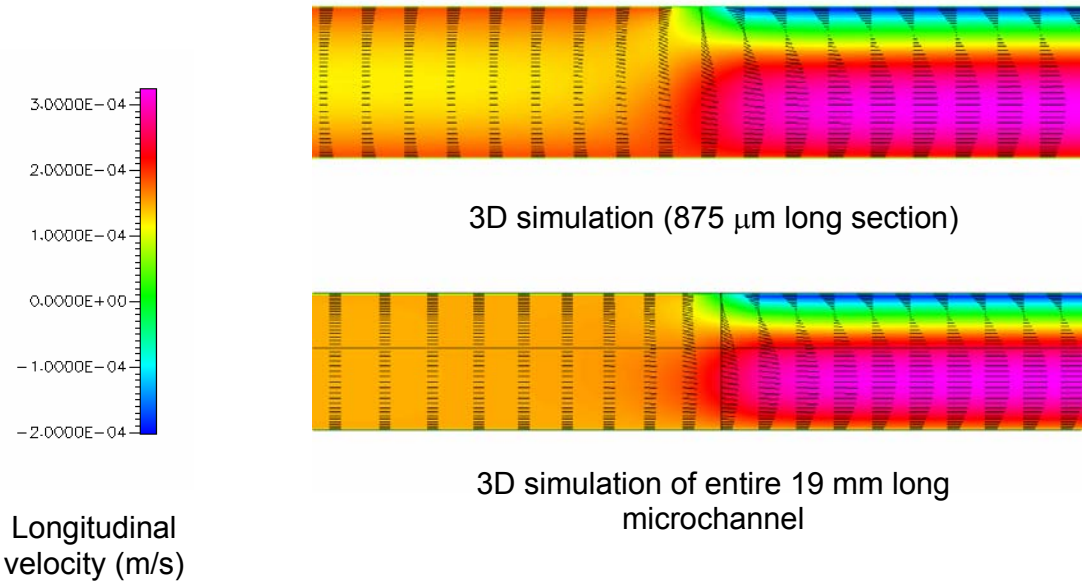

Fig.5.8: *Flow profiles for different channel length at a fixed gated area; with ζ_{normal} = -14 mV and ζ_{gatel} = +21 mV. The top figure shows a 975 µm modeled section, the bottom figure a complete modeled section of 19 mm.*

The influence of the average zeta potential is further illustrated by figure 5.9, where the mass flow is plotted as a function of the gate zeta potential for the model geometry of figure 5.3. A zeta potential offset of -10 mV was applied with a gate that covered 14.5% of the total channel surface. In the figure it

can be seen that the flow rate is a linear function of the gate zeta potential. When a trendline is fit to the data and extrapolated to zero flow, a gate zeta potential of approximately 60 mV is found. When the gate zeta potential is calculated to reach a zero average zeta potential, based on the model geometry, a value of 59 mV can be found.

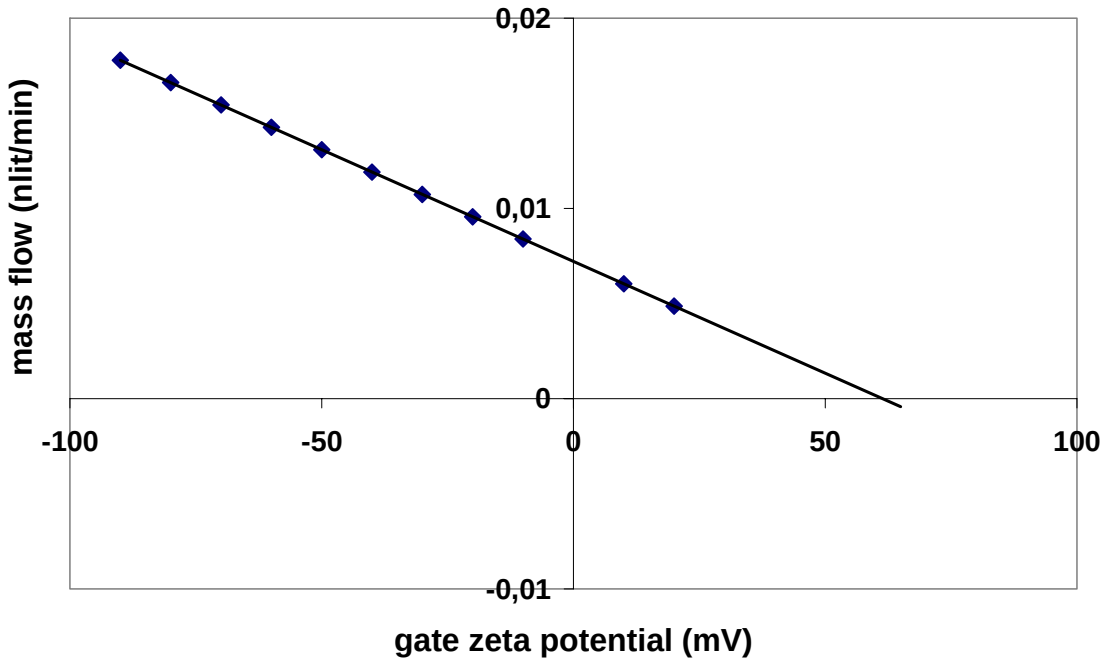

Fig. 5.9: *Relation between mass flow and the average zeta potential as simulated with the geometry illustrated in figure 2.3. A zeta potential of -10 mV was assumed in the non-gated channel walls.*

6 Comparison to experimental results

To measure the qualitative influence of a heterogeneous zeta potential on the velocity profile, Particle Image Velocimetry (PIV) has been applied. Polystyrene fluorescent beads of 0.91 µm were used as tracer particles. Displacement vectors were obtained with a Minimum Quadratic Difference Algorithm (MQD) in Matlab. With the MQD algorithm the quadratic difference in pixel intensity is evaluated when one Interrogation Region (IR) is displaced with respect to the second one. The displacement for a IR is calculated according to formula 2.5. Here, G and G' are respectively the first and second image with a size of M*N pixels.

$$\left| G - G' \right| = \sqrt{\sum_{k=0}^{M-1} \sum_{l=0}^{N-1} \left(G_{k,l} - G'_{k,l} \right)^2} \qquad \text{For. (2.5)}$$

The velocity vectors can be calculated when the displacement is known with formula 2.6, in which Δx is the displacement in a IR and Δt the time interval between the two images. A time interval of 40 msec was applied between image pairs with an IR width and length of 32 pixels.

$$v = \frac{\Delta x}{\Delta t} \qquad \text{For. (2.6)}$$

Figure 5.10a gives an example of a velocity profile without an applied gate potential. The figure shows a characteristic uniform velocity profile.
At a positive applied gate potential, as shown in figure 5.10b, a profile can be distinguished that consist of two contributions: the plug like EOF profile and a counter hydrodynamic flow that dominates in the center of the channel. This counter hydrodynamic flow originates from a difference in local flow rate, as explained previously.
When the gate potential is enhanced, as illustrated in figure 5.10c, it can be seen that in the center of the channel the EOF reverses. Integration of the velocity vectors over the channel cross-sections shows that also the average flow is reversed, which indicates a reversal of the average zeta potential. The figure shows some variation in the velocity profile, in the longitudinal direction of the channel due to clustering of nearby beads.
However, it can be seen that the velocity profiles as shown in figures 5.10 a) and b) are in qualitative agreement with the simulated profiles as presented in figure 5.4.

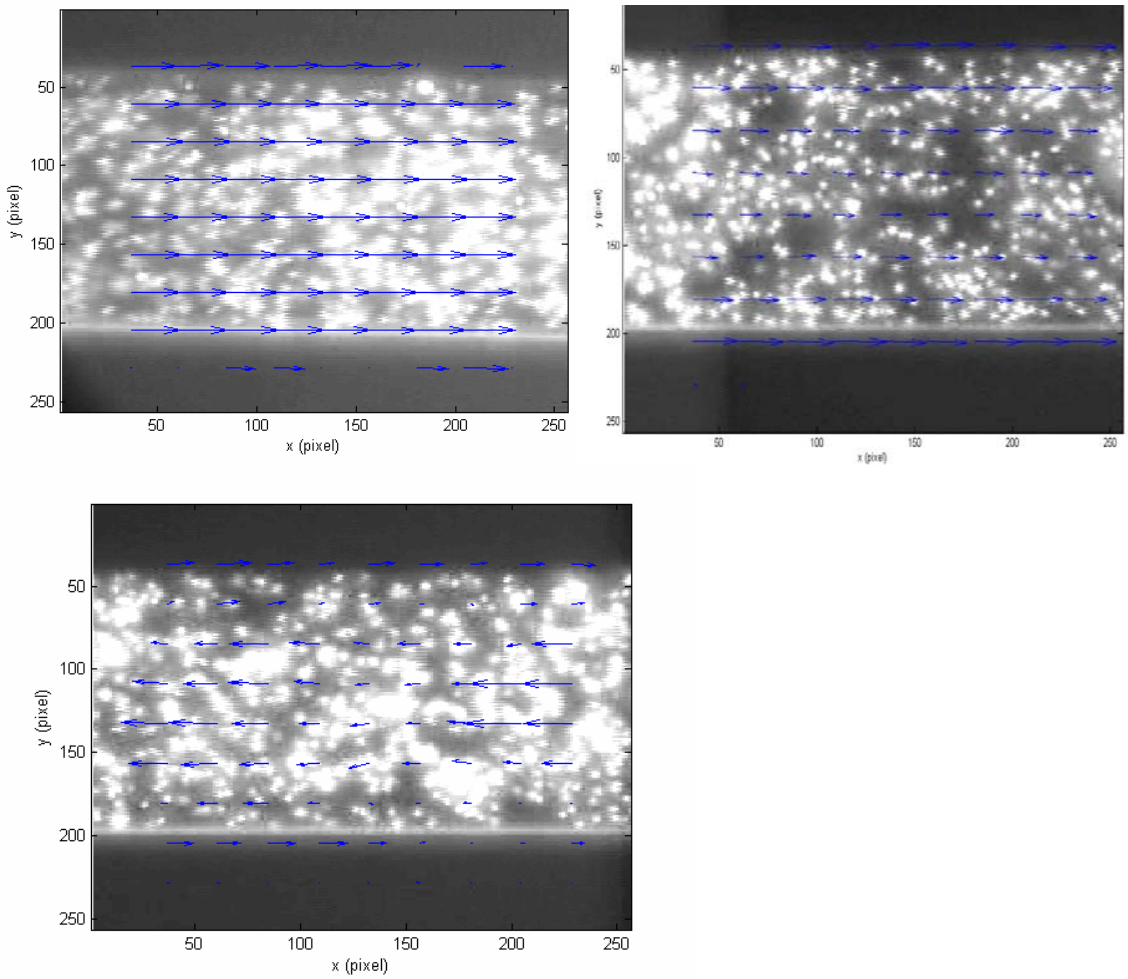

Fig. 5.10: a) *Velocity profile without gate potential.* ***b)*** *Velocity profile with positive gate Potential.* ***c)*** *Velocity profile with an enhanced positive gate potential. Electric field strength 150 V/cm. Time interval between image pairs amounts 40 msec.*

In figure 5.11 an experimental result is shown for a 19 mm long channel the cross-section dimensions are shown in figure 5.1. In the experiments
0.91 µm polystyrene beads were added to the solution to monitor the flow direction. The longitudinal field conditions and solution parameters were equal as applied in the simulations. A gate potential of 36 V with respect to the solution potential was applied.
In the figure a sequence of 3 images is shown, the normal EOF direction is towards the left. At t=0 the gate potential is applied and subsequently

removed after approximately 0.5 seconds. At t=1 sec a potential of 36 Volt is again applied at the gate electrode. It can be seen from the direction of the fluorescent tracer particles that the average flow in the channel is reversed upon application of a gate potential.
However, this result is in contradiction with the simulation results, as the simulations showed that only a limited influence on the net flow can be obtained with a limited surface coverage of the gate electrode.

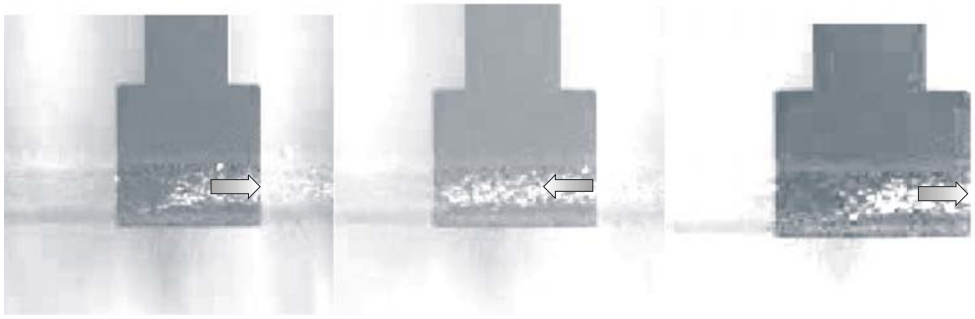

Fig.5.11: *Experimental result for a 19 mm long channel with a 175 µm long gated area. The dark arrow indicates the gate electrode, 0.9 µm beads* were used as tracer particles, the areas indicate the flow direction for **a)** t=0 **b)** t=0.6 and **c)** t=1.2 sec.

In previous publications discrepancies have been noticed between experimental results and analytical solutions. Polson and Hayes [25] obtained a large influence on local flow rates with just 120 Volt over 50 µm of gate insulation. Based on a capacitive effect, far less control would be expected. Furthermore, Hartley and Hayes compared several literature values of FEFC in capillaries with general theory. They concluded that a poor correlation between the theory and measurements exists [26].
A possible explanation for this lack of correlation and for the discrepancy in the simulated and measured result shown in figure 5.8 and 5.11 can be found by assuming a larger influenced region, than that covered by the gate electrode. Standard models initially proposed for External Voltage Control (EVC) assume a capacitive effect that is confined to part of the channel that is projected on the gate electrode [27-29]. An alternative model was presented by Horiuchi and Dutta. They include a leakage resistance through the gate insulation in their model. In this way, they were able to account for flow control with a very limited, capacitively obtained, change in zeta potential. However, when a large leakage current is present the flow control should be attributed to a change of the local channel potential, rather than a

field effect induced change in the zeta potential. In most publications, as well as the work presented in this thesis, the leakage current is in a range (sub nA) where only a capacitive effect needs to be considered.
Hayes *et.al.* measured flow rates in EVC for capillaries as a function of the surface coverage of the external gate electrode. Their results showed a dramatic underestimation of the induced flow according to theory at low surface coverage compared to the measurement results. To account for the poor correlation between theory and measurements they proposed an alternative model that included surface conduction through the Electrical Double Layer (EDL). They argued that due to an enhanced conductivity in the EDL the influence of the gate electrode can spread beyond the position of the gated area. Their adapted model assumed a linear decay in zeta potential form the gate zeta potential to the offset value at the entrance and outlet of the capillary. Although this model was able to provide a better match between theory and measurements, still an underestimation of the expected flow rate was present [30].
Although little direct experimental evidence and theoretical foundation is present for the role of surface conduction in FEFC several researchers have pointed out the possible role of a spreading of the gate zeta potential to the non-gated regions. Sniadecki *et al.* attributed a position dependent flow rate to surface conduction [31] and several reports showed no additional band broadening when FEFC was applied in capillary electrophoresis [26, 28, 32]. This would be expected in case of a heterogeneous surface charge.
Based on the latter, the origin of the poor correlation between the simulated channel structure of figure 5.7 and the measurement results of figure 5.8, can be attributed to an influence of the gate potential on the zeta potential outside the gated area. In the simulations, surface conduction effects or leakage current is not taken into account so that the gate zeta potential is confined to the position of the gate area.

7 Simulation of FEFC arrays for flow directioning

7.1 FEFC array layout

A FEFC array was composed of trapezoidal channels with the same dimensions as illustrated in figure 5.1.
A gate insulation thickness of 210 nm was assumed with applied gate potentials of either +36 V or −36 V, relative to the potential in the channel. The microchannel is assumed to be filled with an aqueous solution with properties as summarized in table 1.

7.2 Mesh generation

The channel intersection was modeled as 13 separate structured blocks and a total of 94,200 cells were used to represent the flow domain. The geometrical layout of the grid is illustrated in Figure 5.12. The gate regions are assumed to be 175 μm long and are separated from the central channel intersection by a clearance of 3.5 μm. The end (non-gated) sections of the FEFC array are assumed to be 50 μm long.

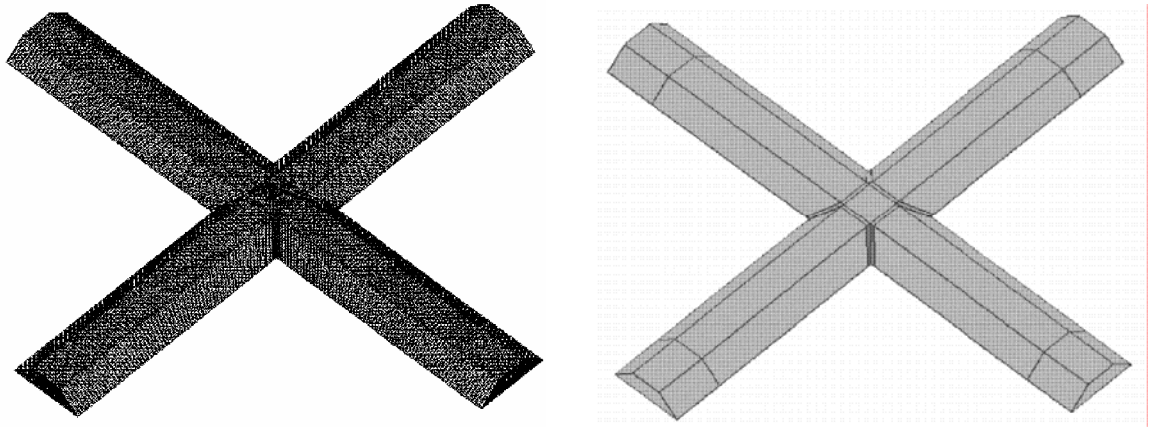

Fig. 5.12: *Grid structure (left) and structural building blocks (right) of the FEFC array model.*

7.3 CFD simulation parameters and boundary conditions

Simulations were performed with four different settings to assess the parameters for fluidic routing with FEFC structures.
To simplify the description, the gate electrodes associated with the inlet, outlet 1, outlet 2 and outlet 3 channels are referred to as left, right, bottom and top respectively, as illustrated in Figure 5.13.

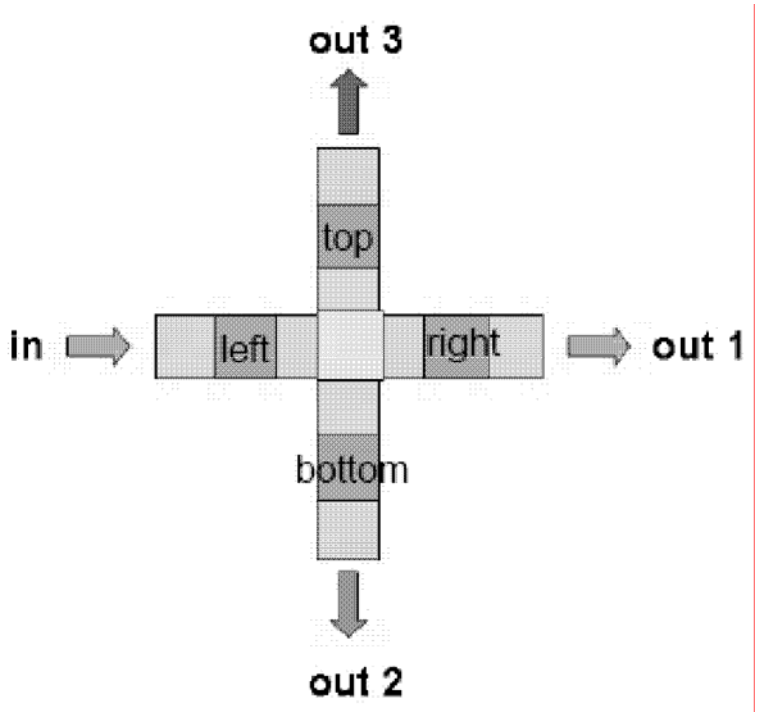

Fig. 5.13: Nomenclature of the gate electrodes for the CFD simulations.

The four flow cases considered are as follows:

Case 1

The top and bottom gate electrodes are adjusted to obtain a no-flow condition through outlets 2 and 3, whilst the other two electrodes (left and right) are set to their maximum flow condition (Vg = −36 V; ζ = −42 mV). This results in the flow traveling through the MEF array from the inlet to outlet 1. To obtain the required no-flow condition through outlets 2 and 3, a preliminary calibration study was performed. For the present geometry, it was found that the no-flow condition was obtained with a zeta potential of +31.3 mV.

Case 2

The top and right-hand gate electrodes are adjusted to obtain a no-flow condition through outlets 1 and 3, whilst the other two electrodes (left and bottom) are set to their maximum flow condition (Vg = −36 V; ζ = −42 mV). This results in the flow travelling through the MEF array from the inlet to outlet 2, with very little fluid lost to the top and right-hand channels.

Case 3
Similar to Case 1 but with an assumed surface treatment along the non-gated regions so that the zeta potential at the wall is zero. The gate voltages on the top and bottom electrodes are adjusted to give $\zeta = 0$ in order to obtain the no-flow condition through outlets 2 and 3. The other two gate electrodes (left and right) are set to their maximum flow condition (Vg = −36 V; ζ = −42 mV).

Case 4
Similar to Case 2, but again with an assumed surface treatment along the non-gated regions so that the zeta potential at the wall is zero. The gate voltages on the top and right-hand electrodes are adjusted to give $\zeta = 0$ in order to obtain the no-flow condition through outlets 1 and 3. The other two gate electrodes (left and bottom) are set to their maximum flow condition (Vg = −36 V; ζ = −42 mV). In all cases, a potential difference of 150 V/cm was maintained along each of the microchannels.

7.4 Blocking of flow

To obtain the required no-flow condition through the “blocked” channels for Cases 1 and 2, the zeta-potential at the gate electrodes must be carefully selected. This necessitates a preliminary calibration study of the MEF array intersection. Figure 5.14 demonstrates that the flow rate through the exit channel is linearly dependent on the zeta potential applied at the blocking electrodes. The zeta potential for the no-flow condition can thus be readily determined. For example, in the present study, application of a zeta potential of +31.3 mV to the gate electrodes will result in zero flow through the “blocked” channels. It should be noted, however, that the blocking zeta potential is problem dependent and is affected by many factors including channel length, intersection geometry, length and spacing of the gate electrodes, etc.

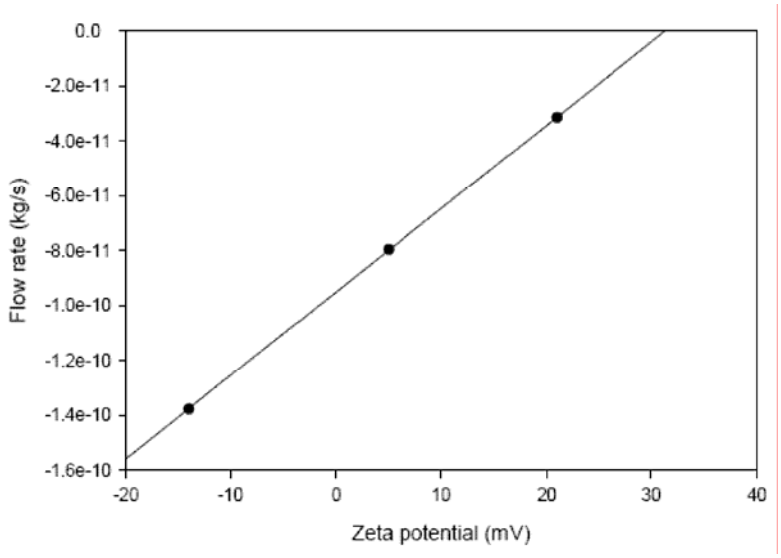

Fig. 5.14: *Flow rate as a function of the zeta potential*

7. 5 Analysis of results

The results from the 3D finite element simulations form the basis for evaluating the fluidic routing capabilities of the FEFC based MEF array. Figures 5.15-5.18 show the predicted velocity distributions and velocity vectors for each of the four simulated cases. The pictures show that by a proper set of zeta potential in the gated region the flow can be directed.
Figures 5.15-5.18 illustrate the velocity distribution along the central plane of the microchannels and show that the flow can be easily routed either straight ahead or through a 90° bend. It should be noted that the gate electrodes controlling the flow are located along the 70 µm wide edge of the channel, causing the highest velocities to occur in this region. Figure 5.19 demonstrates that the original design of MEF array (using microchannels with an unmodified zeta potential of −14 mV along the non-gated regions) gives rise to recirculating eddies at the channel intersection. These eddies can be detrimental to the operation of a FEFC array when mixing has to be prevented to avoid contamination between subsequent branches of the array.
However, the CFD simulations have shown that the recirculating eddies can be eliminated by application of a suitable coating to the non-gated wall regions to reduce the zeta potential. Figure 5.20 illustrates the effect of such a treatment for an idealized case where the zeta potential at the wall is reduced to zero. It can be seen that the eddies are completely eliminated and the routing of the fluid through the central intersection is more uniform.

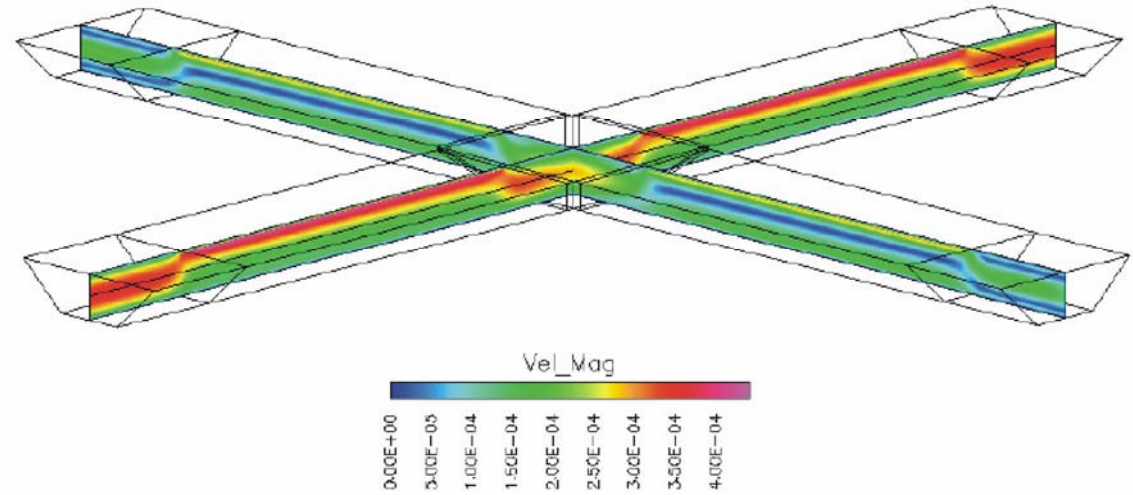

Fig. 5.15: *Flow velocities for settings of case 1.*

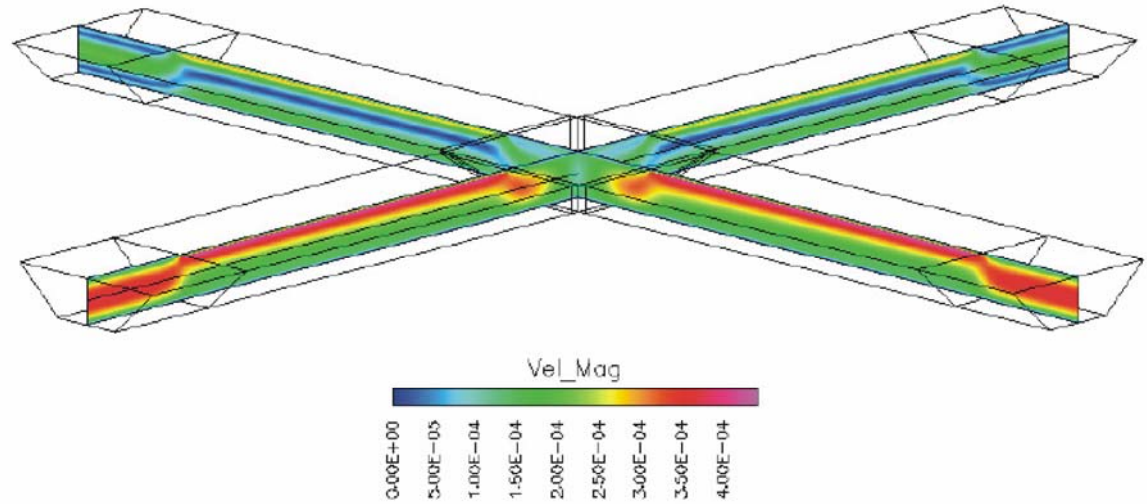

Fig. 5.16: *Flow velocities for settings of case 2.*

.

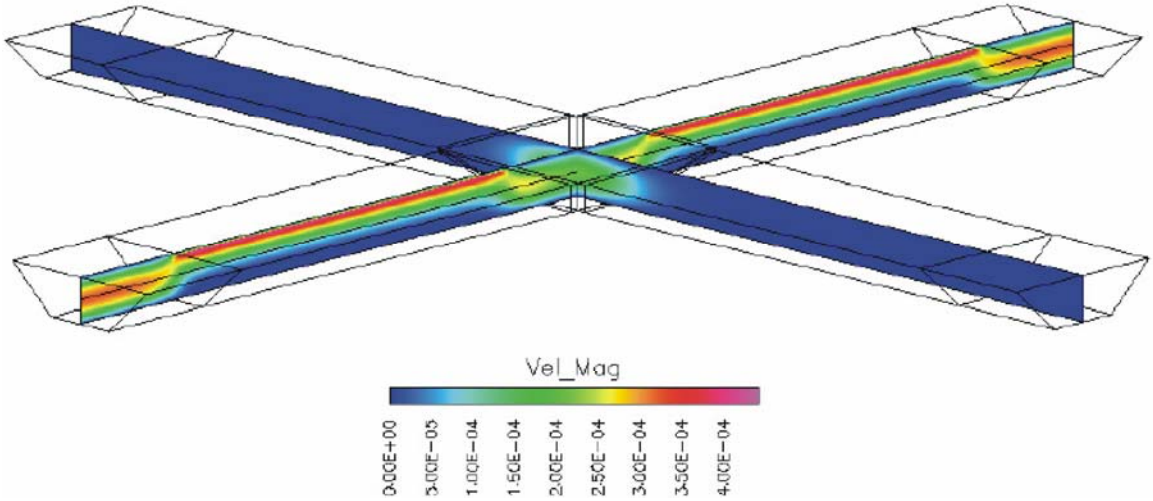

Fig. 5.17: *Flow velocities for settings of case 3.*

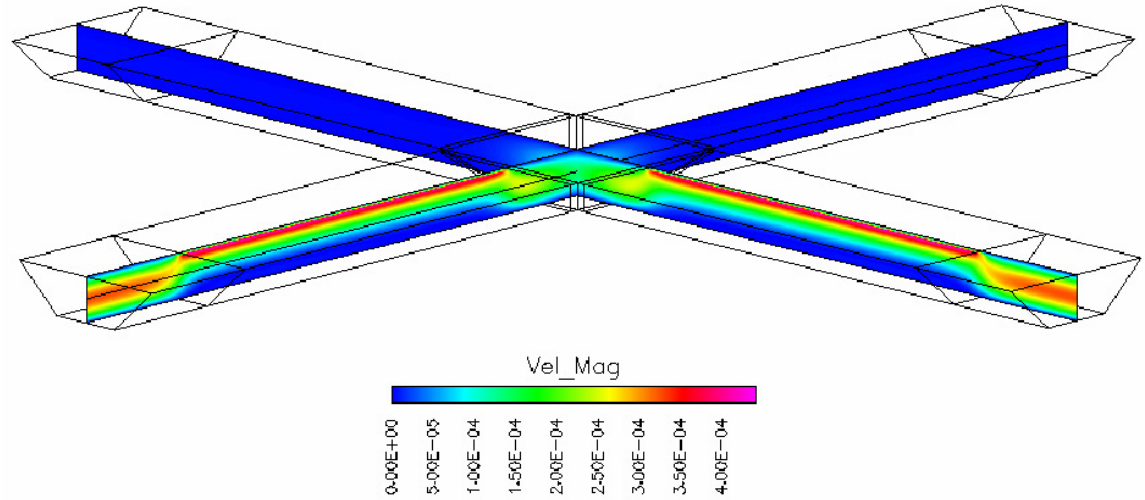

Fig. 5.18: *Flow velocities for settings of case 4.*

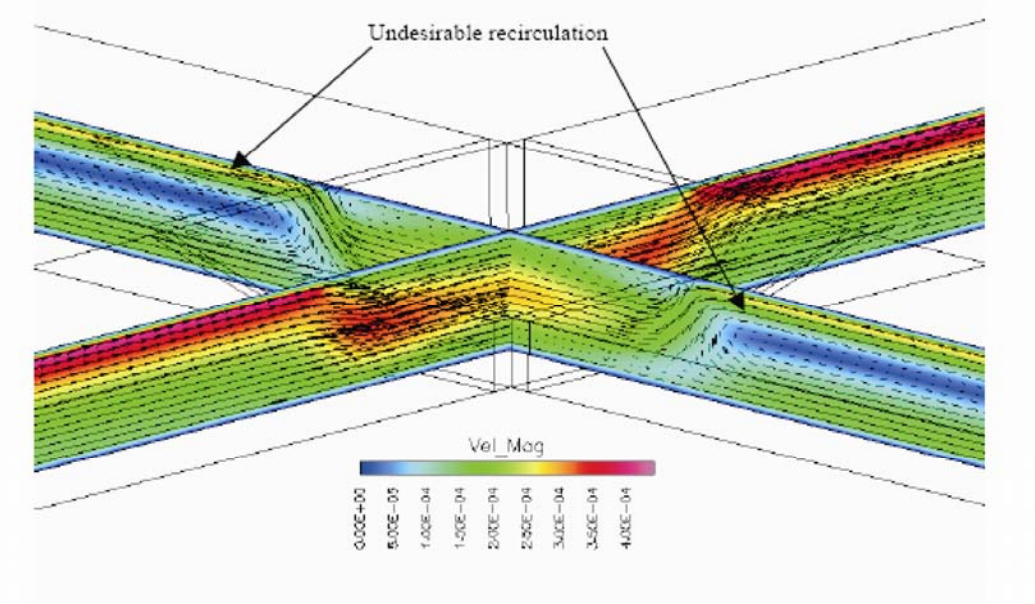

Fig. 5.19: *Recirculation of flow at non-zero zeta potential at the non-gated wall.*

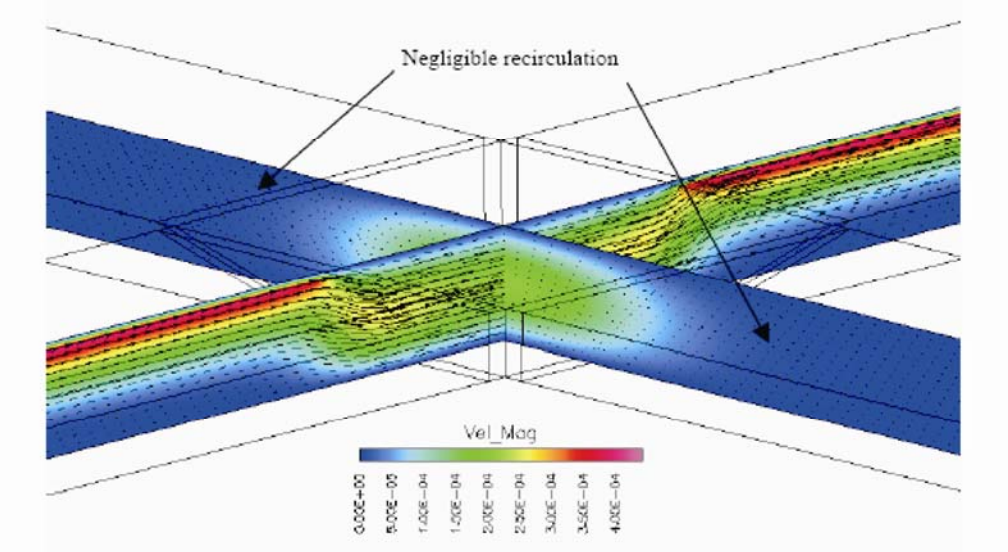

Fig. 5.20: *Recirculation of flow at zero zeta potential at the non-gated wall.*

8 Summary and conclusions

In this chapter finite element simulations of FEFC structures are presented. It is shown that under the conditions of heterogeneous surface charge the typical plug flow profile associated with EOF vanishes. Transverse and recirculating flow is observed at the gate electrode region. These flow profile can be beneficial to enhance mixing in microchannels, which under normal conditions is diffusion limited. The effect of the gate electrode coverage is investigated; simulations show that a small coverage leads to a limited influence on the net flow and flow profile, while experimental results indicate a far more effective influence. The discrepancy between the simulations and experiments could be explained by an influence of surface conduction. An enhanced conductivity in the EDL can lead to a spreading of the gate zeta potential beyond the location of the electrode in the channel.
PIV analysis of experimental results shows good qualitative agreement with the simulations, a reversal of the net flow is observed at a positive applied gate potential.
More complex FEFC arrays have been composed and simulated to investigate a FEFC structure for fluidic routing. It is shown that by a suitable choice of zeta potential in the gated regions, the flow can be directioned in fluidic networks. However, the offset value of the zeta potential on the non-gated wall results in recirculation of flow, which can be unwanted when mixing of flow streams should be avoided. Reduction of the zeta potential offset by, for instance application of a coating, can significantly reduce such recirculation.

9 References

1. Probstein, R.F., *Physicochemical Hydrodynamics.* 2nd Ed., John Wiley & Sons, 1995.
2. Schasfoort, R.B.M., S. Schlautmann, L. Hendrikse and A. van den Berg, *Field-effect flow control for microfabricated fluidic networks.* Science, 1999. **286**(5441): p. 942-945.
3. Hunter, R.J., *Zeta Potential in Colloid Science: Principles and Applications.* Academic Press, London, 1981.
4. van der Wouden, E.J., T. Heuser, D.C. Hermes, R.E. Oosterbroek, J.G.E. Gardeniers and A. van den Berg, *Field-effect control of electro-osmotic flow in microfluidic networks.* Colloids and Surfaces a-

Physicochemical and Engineering Aspects, 2005. **267**(1-3): p. 110-116.
5. Harrison, D.J., K. Fluri, K. Seiler, Z.H. Fan, C.S. Effenhauser and A. Manz, *Micromachining a Miniaturized Capillary Electrophoresis-Based Chemical-Analysis System on a Chip.* Science, 1993. **261**(5123): p. 895-897.
6. Harrison, D.J., A. Manz, Z.H. Fan, H. Ludi and H.M. Widmer, *Capillary Electrophoresis and Sample Injection Systems Integrated on a Planar Glass Chip.* Analytical Chemistry, 1992. **64**(17): p. 1926-1932.
7. Yang, R.J., T.I. Tseng and C.C. Chang, *End effects on electro-osmotic flows in micro-channels.* Journal of Micromechanics and Microengineering, 2005. **15**(2): p. 254-262.
8. Zhang, Y.H., X.J. Gu, R.W. Barber and D.R. Emerson, *An analysis of induced pressure fields in electroosmotic flows through microchannels.* Journal of Colloid and Interface Science, 2004. **275**(2): p. 670-678.
9. Zhang, Y.H., X.J. Gu, R.W. Barber and D.R. Emerson, *Influence of the electric double layer on induced pressure fields and development lengths in electro-osmotic flows.* Modern Physics Letters B, 2005. **19**(28-29): p. 1655-1658.
10. Chen, R.Y., *Flow in entrance region at low Reynolds-numbers.* Journal of Fluids Engineering, 1973. **95**: p. 153.
11. Lee, C.Y., C.H. Lin and L.M. Fu, *Band spreading control in electrophoresis microchips by localized zeta-potential variation using field-effect.* Analyst, 2004. **129**(10): p. 931-937.
12. Taylor, G.I., *Dispersion of soluble matter in solvent flowing slowly through a tube* Proceedings of the Royal Society of London series A-Mathematical and Physical Sciences, 1953. **219**: p. 186-203.
13. Chien, R.L. and J.C. Helmer, *Electroosmotic Properties and Peak Broadening in Field-Amplified Capillary Electrophoresis.* Analytical Chemistry, 1991. **63**(14): p. 1354-1361.
14. Keely, C.A., T.A.A.M. Vandegoor and D. McManigill, *Modeling Flow Profiles and Dispersion in Capillary Electrophoresis with Nonuniform Zeta-Potential.* Analytical Chemistry, 1994. **66**(23): p. 4236-4242.
15. Liu, R.H., M.A. Stremler, K.V. Sharp, M.G. Olsen, J.G. Santiago, R.J. Adrian, H. Aref and D.J. Beebe, *Passive mixing in a three-dimensional serpentine microchannel.* Journal of Microelectromechanical Systems, 2000. **9**(2): p. 190-197.

16. Stroock, A.D., S.K.W. Dertinger, A. Ajdari, I. Mezic, H.A. Stone and G.M. Whitesides, *Chaotic mixer for microchannels.* Science, 2002. **295**(5555): p. 647-651.
17. Biddiss, E., D. Erickson and D.Q. Li, *Heterogeneous surface charge enhanced micromixing for electrokinetic flows.* Analytical Chemistry, 2004. **76**(11): p. 3208-3213.
18. Erickson, D. and D.Q. Li, *Microchannel flow with patchwise and periodic surface heterogeneity.* Langmuir, 2002. **18**(23): p. 8949-8959.
19. Erickson, D. and D.Q. Li, *Influence of surface heterogeneity on electrokinetically driven microfluidic mixing.* Langmuir, 2002. **18**(5): p. 1883-1892.
20. Lee, J.S.H., C.L. Ren and D.Q. Li, *Effects of surface heterogeneity on flow circulation in electroosmotic flow in microchannels.* Analytica Chimica Acta, 2005. **530**(2): p. 273-282.
21. Lee, C.Y., G.B. Lee, L.M. Fu, K.H. Lee and R.J. Yang, *Electrokinetically driven active micro-mixers utilizing zeta potential variation induced by field effect.* Journal of Micromechanics and Microengineering, 2004. **14**(10): p. 1390-1398.
22. Lin, J.L., K.H. Lee and G.B. Lee, *Active micro-mixers utilizing a gradient zeta potential induced by inclined buried shielding electrodes.* Journal of Micromechanics and Microengineering, 2006. **16**(4): p. 757-768.
23. Anderson, J.L. and W.K. Idol, *Electroosmosis through pores with nonuniformly charged walls.* Chem. Eng. Commun., 1985. **28**: p. 93-106.
24. Herr, A.E., J.I. Molho, J.G. Santiago, M.G. Mungal, T.W. Kenny and M.G. Garguilo, *Electroosmotic capillary flow with nonuniform zeta potential.* Analytical Chemistry, 2000. **72**(5): p. 1053-1057.
25. Polson, N.A. and M.A. Hayes, *Electroosmotic flow control of fluids on a capillary electrophoresis microdevice using an applied external voltage.* Analytical Chemistry, 2000. **72**(5): p. 1088-1092.
26. Hartley, N.K. and M.A. Hayes, *Examination of theoretical models in external voltage control of capillary electrophoresis.* Analytical Chemistry, 2002. **74**(6): p. 1249-1255.
27. Poppe, H., A. Cifuentes and W.T. Kok, *Theoretical description of the influence of external radial fields on the electroosmotic flow in capillary electrophoresis.* Analytical Chemistry, 1996. **68**(5): p. 888-893.

28. Lee, C.S., C.T. Wu, T. Lopes and B. Patel, *Analysis of Separation Efficiency in Capillary Electrophoresis with Direct Control of Electroosmosis by Using an External Electric-Field.* Journal of Chromatography, 1991. **559**(1-2): p. 133-140.
29. Hayes, M.A., I. Kheterpal and A.G. Ewing, *Effects of Buffer Ph on Electroosmotic Flow-Control by an Applied Radial Voltage for Capillary Zone Electrophoresis.* Analytical Chemistry, 1993. **65**(1): p. 27-31.
30. Hayes, M.A., I. Kheterpal and A.G. Ewing, *Electroosmotic Flow-Control and Surface Conductance in Capillary Zone Electrophoresis.* Analytical Chemistry, 1993. **65**(15): p. 2010-2013.
31. Sniadecki, N.J., C.S. Lee, P. Sivanesan and D.L. DeVoe, *Induced pressure pumping in polymer microchannels via field-effect flow control.* Analytical Chemistry, 2004. **76**(7): p. 1942-1947.
32. Wu, C.T., T.L. Huang, C.S. Lee and C.J. Miller, *Dispersion Studies of Capillary Electrophoresis with Direct Control of Electroosmosis.* Analytical Chemistry, 1993. **65**(5): p. 568-571.
33. Biernacki, J.J., P.M. Mellacheruvu and S.M. Mahajan, *Electric circuit model for electrical field flow fractionation.* Analytical Chemistry, 2006. **78**(14): p. 4998-5005.
34. van Hal, R.E.G., J.C.T. Eijkel and P. Bergveld, *A Novel Description of ISFET Sensitivity with the Buffer Capacity and Double-Layer Capacitance as Key Parameters.* Sensors and Actuators B-Chemical, 1995. **24**(1-3): p. 201-205.
35. van Kirchhoff, J.C., J.C.T. Eijkel and P. Bergveld, *ISFET Responses on a Stepwise Change in Electrolyte Concentration at Constant Ph.* Sensors and Actuators B-Chemical, 1994. **18**(1-3): p. 56-59.

6

Field effect control of electro-osmotic flow in microfluidic networks

1 Abstract

This chapter describes microfluidic networks based on glass microchannels with integrated insulated gate electrodes that are used to modify the zeta potential at specific locations on the wall surface of the microchannels. This modification is used to control direction and size of the electroosmotic flow (EOF) in the microchannels. A new microfabrication process was developed that leads to mechanically more robust structures and better flow visualization in the gate region, compared to earlier work in our institute [1]. In the new process sequence, the microfluidic chips were fabricated using deposition on a Pyrex glass substrate of a thin film metal electrode, which was covered with a thin insulating film of silicon dioxide, followed by chemical mechanical polishing prior to bonding to a second glass plate to form closed micro channels. Electrical breakdown of the metal-insulator structures was measured and occurred at 9.6 ± 0.3 MV/cm. Experiments using fluorescent beads to visualize the flow patterns in the microchannel showed that the EOF is linearly dependent on the applied gate voltage. The average EOF could be stopped completely for longitudinal fields of 150 V/cm by applying a gate field of 1.7 MV/cm.

2 Introduction

Integrated microfluidic devices containing micromachined channels are currently being studied for automated and high-throughput synthesis and analysis of chemical compounds or for the study of biological processes in (single) cell cultures [2-5]. In these microchannel networks pumping and valving is an important issue. Although traditionally these functions have been performed by mechanical means [6], during recent years other ways of liquid transport and control have been introduced, e.g. using capillary forces to drive and hydrophobic patches to stop the flow at specific locations [7]. In a large number of microfluidic circuits, especially those that use electrophoretic separations, liquid is driven and directed by electrokinetic principles (see e.g.[8]), which offer some advantages over pressure-driven methods, like ease of fabrication, absence of moving parts, and low dispersion of sample plugs due to the almost uniform velocity profile across the microchannel width. Electrokinetic pumps are usually controlled by manipulating voltages applied to the ends of microchannels. In this paper, we will discuss the control of electrokinetic flow by applying a principle that resembles the field-effect that is well-known in electronic transistor circuits,

and which for the fluidic case was named "flow-FET" (FET for field effect transistor) [1] or Field-Effect Flow Control, FEFC [9] in previous publications. The paper will describe the design, fabrication, modeling and testing of a new microfluidic device that has integrated electrodes covered with an insulating layer, of which the zeta-potential will be modified by a voltage applied to the electrodes. Compared to previous work at our institute [1], in which very thin and therefore fragile micromachined silicon nitride tube structures, locally covered with thick silicon gate electrodes were used, which obstructed flow visualization in the gate region, in the present study a microfabrication process is used that leads to robust structures and allows flow analysis in the gate region.

3 Theoretical background and FEFC simulations

3.1. Principle of field-effect flow control

It is well-known that, especially in aqueous systems, an electrical double layer (EDL) forms spontaneously at the phase boundary of the liquid with a solid, due to preferential adsorption or desorption of certain ions [10]. For example, when fused silica is immersed in an aqueous solution with a pH above the pK_a value of silica, 2.8, it will acquire a negative surface charge due to deprotonation of surface silanol groups. Because of the resulting surface charge, co-ions from the solution will be repelled and counter-ions will be attracted in order to screen the surface charge, creating a charged region close to the surface forming the EDL. Due to strong electrostatic interaction, the layer of counter-ions closest to the surface will be immobilized, a region referred to as the Stern-layer. Further away from the surface the counter-ions will have more freedom to move, this layer is called the diffuse layer. The potential at the interface of these two layers is the so called zeta potential, ζ.

When an electric field is applied along the surface as described above, ions in de EDL will move due to the forces exerted on them by the electric field. Due to viscous coupling between the ions in the EDL and the bulk liquid electroosmotic flow, EOF, will develop. EOF has been used to pump liquids in microfluidic networks and has been well-studied in the field of capillary electrophoresis [11-14]. The linear velocity v_{EOF} corresponding to the EOF is given by:

$$v_{eof} = \frac{\varepsilon_o \varepsilon_r \zeta}{\eta} E \qquad \text{(Eq. 6.1)}$$

with ε_0 and ε_r the dielectric constant of vacuum and of the liquid, respectively, E the electric field and η the viscosity of the liquid.
Eq. 6.1 shows that the EOF in a specific liquid can be controlled by both the electric field and the zeta potential. It was demonstrated that in a microchannel network liquid flows can be switched between different branches by changing the electric fields along the different channels, via switching of the voltages at electrodes at the outlets of the microchannels [13]. A drawback of this method is that in more complex networks, with many crossing microchannels, independent control of the flow in the different branches becomes difficult, due to the fact that the electrical voltages in the channels are all resistively linked. Thus, switching the voltage at one outlet of the network changes the voltages and therewith the EOF throughout the network. Local control of the voltages by introducing electrodes inside the channels is generally not feasible due to the generation of gas bubbles by electrolysis at these electrodes, which bubbles may disrupt the electrical network or block the channels.
A more subtle control over liquid flow can be obtained by introducing local changes in the ζ-potential, keeping the main electric fields along the channels constant. This can be done e.g. by applying a transverse electric field over the thickness of a thin insulator that is integrated in the walls of a microfluidic channel.
The principle was demonstrated already in the beginning of the nineties [15-20]. In these early studies, fused silica capillaries were used, with electrodes on the outside wall of the capillary to change the ζ-potential on the inside wall. The purpose of that work was the enhancement of electrophoretic separation efficiency, rather than flow control. Because of the thickness of the capillary walls relatively high voltages (several kilovolts) were required to establish a significant effect on ζ. Since modern microfabrication and thin-film deposition techniques allow the fabrication of channels with extremely thin walls, the required radial electrical fields can now be achieved with more acceptable voltages, like a few tens of Volts, as was demonstrated in recent work [1, 21]. We will refer to this principle as “Field-Effect Flow Control” (FEFC) [9].
The change in ζ that can be achieved in FEFC depends on the potential distribution across the different capacitors that can be identified in an electrical circuit description of the channel wall-electrolyte system, as shown in Fig.6.1. The EDL can be modeled as a series of two capacitances [22], i.e. that corresponding to the Stern layer, C_{Stern}, and that of the diffuse layer, C_d. For dilute aqueous solutions at 25^{o}C the diffuse layer capacitance per unit surface area in μF/cm^2 has the value [23]:

$$C_d = 228z\sqrt{c}\cosh(19.5z\varsigma) \qquad \text{(Eq. 6.2)}$$

with z the ion valance, c the electrolyte concentration in mol/L and ζ the zeta potential (here expressed in mV). The capacitance C_{Stern} only contributes to the electrical circuit at large electrolyte concentrations, or at large polarizations in dilute media. Therefore, like in most publications on EOF, we neglect it in the present work. The wall capacitance C_{wall} (per unit surface area) is given by:

$$C_{wall} = \frac{\varepsilon_0 \varepsilon_r}{d} \qquad \text{(Eq. 6.3)}$$

The change in zeta potential due to a voltage V_g applied on the electrode at the outer side of the wall is given by:

$$\Delta\varsigma = \frac{C_{wall}}{C_d}\left(V_g - V_{sol}\right) \qquad \text{(Eq. 6.4)}$$

with V_{sol} the electrical potential in the bulk of the solution far away from the surface (i.e. outside of the double layer). Note that according to Eq. 6.2, C_d depends on ζ so that the final zeta potential after the application of a voltage has to be calculated by iteration.

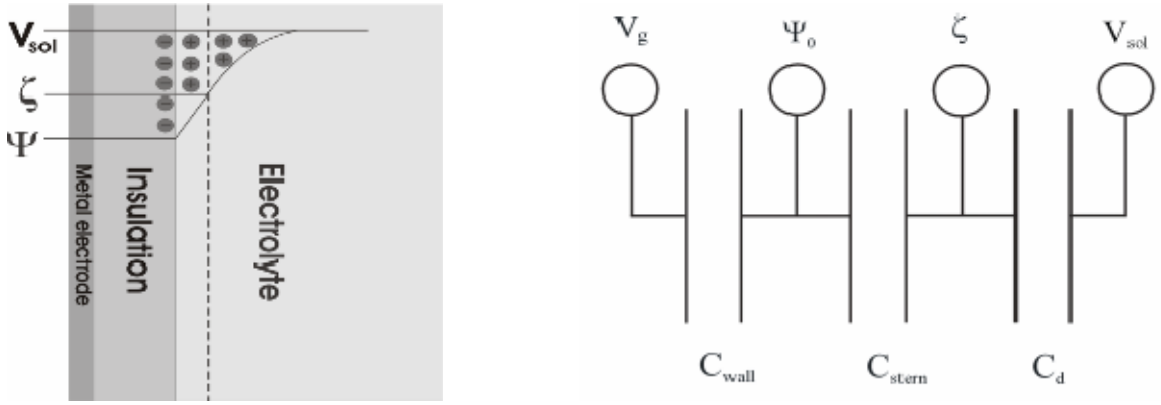

Fig. 6.1: *Left: simplified drawing of the electric double layer close to an insulator-covered electrode; right: three-capacitor model for the solid/liquid interface, where V_g is the gate potential applied on the electrode and ψ_0 the surface potential.*

Since the change in EOF as a result of the gate voltage *Vg* is proportional to the capacitance of the wall, a wall material with a high dielectric constant is preferred. Furthermore, the material should have high electrical breakdown strength, allowing the use of a thin wall so that the voltage over the channel wall can be kept as low as possible. A low unmodified ζ at the pH of interest is required to keep the voltages for switching of the direction of the EOF low. Materials used for FEFC purposes described in recent literature are: silicon nitride (thickness 390 nm [1]), Corning 0211 glass (50 µm thick [21]), unspecified glass (130 µm [24] and 40 µm thick [25]), Polydimethylsiloxane, PDMS (thickness 2 µm [26]) and parylene (0.5 µm [27]] or 1.22 µm thick [9].). Older work has used fused silica capillaries with a wall thickness in the range of 124 to 360 µm (see e.g.[17, 28]). In this work we have used silica layers with a thickness ranging from 200 to 400 nm deposited with a Plasma-Enhanced Chemical Vapor Deposition (PECVD) process (for details see below).

3.2. Design of microfluidic chips

The microfluidic FEFC chip design is shown in a side view in Fig.6.2 and consists of 1,2, or 4 patterned metal "gate" electrodes on a Pyrex or Borofloat glass plate, covered with an insulating silica layer. This plate is bonded to a second plate which contains inlets and outlets for the liquid, and a channel which runs over the insulated electrodes. Multiple electrodes are applied to be able to establish a potential gradient along the microchannel wall that matches the electric field gradient in the channel, in order to obtain a uniform change in zeta potential in the entire gate region. It is unclear over what length of the fluid channel one should apply the gate voltage V_g, to obtain the desired influence on the EOF. In the early work on EOF controlled by radial electrical fields either a capillary-in-capillary structure with an electrolyte in the annulus between inner and outer capillary [19] was used, or a thin, ionic-conducting polymer coating was applied on the outside of a single capillary [16], to obtain a voltage gradient along the capillary wall in conformity with the longitudinal electrical field in the liquid inside of the capillary. In these previous studies the main purpose of the gradient was to prevent vortex formation, which leads to extra peak dispersion during electrophoretic separations.

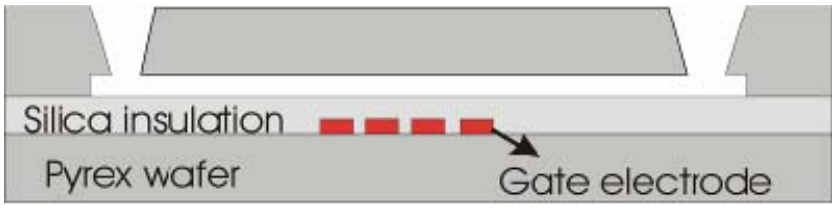

Fig. 6.2: *Schematic representation of a FEFC structure.*

Despite the fact that the early experiments showed that the applied radial voltage (the voltage over the channel wall) affects the ζ-potential only in those portions of the capillary directly under the gate electrode, experimental data were presented by Hayes et al. [17] that even if only a small portion of a capillary is covered with a conductive silver paint, EOF was controlled to a similar extent as with the other systems mentioned above. The explanation that these authors present for this unexpected result is conductance along the inside surface of the capillary, leading to spreading of the field-induced double-layer potential to areas outside of the gate-covered region. This effect is relevant for flow control and may be studied relatively easily by the introduction of the patterned and insulator-covered metal electrodes in a microchannel network. We are currently studying this problem of surface conduction in more detail; here we will focus on the effects of a single gate electrode on EOF.

4 Experimental

4.1. Fabrication of microfluidic chips

Details of the microfabrication procedure will be described elsewhere [29], here we give only a brief outline of the methods, see Fig. 6.3.
In step 1, a 20 nm thick Ta adhesion layer covered with a 200 nm thick Pt layer were deposited on a Pyrex (or Borofloat) substrate and patterned using a photolithographic lift-off process. In step 2, approximately 1 µm of PECVD silica was deposited, which acts as the gate insulation layer. In order to be able to bond this substrate to a micro channel plate (see below) both the surface topography and surface roughness of this substrate have to be reduced, which was done with a Chemical Mechanical Polishing (CMP) procedure (step 3 in Fig. 6.3). After this polishing step, a silica layer with a thickness of 200-300 nm results. Microchannels are etched in a second substrate, and holes are powder blasted through it to establish access to these channels from the backside (step 4 in Fig. 6.3). Both substrates are then brought together and annealed for 1 hour at 650 °C,

after which the substrates are diced into individual chips, leading to the completed device shown in step 5 of Fig. 6.3. Fig. 6.4 shows a photograph of the final device.

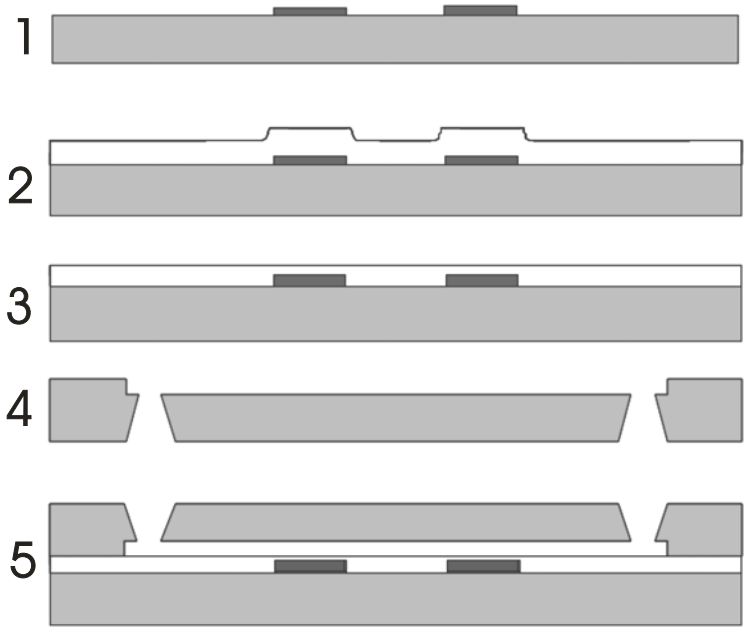

Fig. 6.3: *Schematic overview of the process steps*

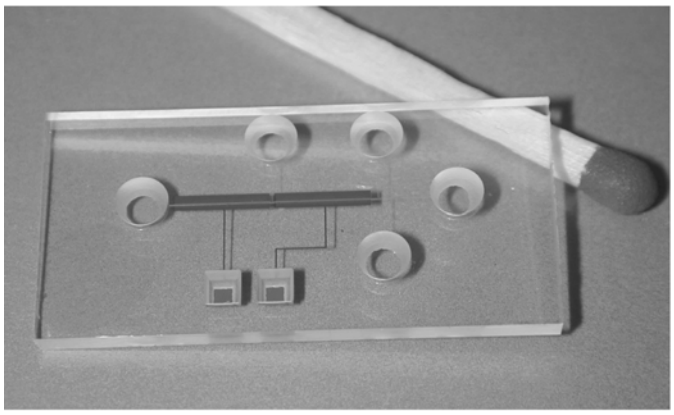

Fig. 6.4: *FEFC microstructure with 2 gate electrodes. Channel width 45 µm, height 15 µm, length 1.5 cm. Dimensions of the gate electrodes are 1.0×5.6 mm. The electrodes are covered with 350 nm PECVD silica.*

4.2. Measurement of EOF and FEFC

The measurements of the EOF and FEFC were performed on a probe station (Probe System PM8 Manual Probe System User Manual, Karl Süss, 2001). Power supply and current monitoring was performed with Keithley 2910 1100 V source meters. The probe station was equipped with a Leica DMLM metallurgical microscope equipped for fluorescence imaging, images where taken with a WAT 902B CCD camera (Watec Co. Ltd. Taiwan) at 25 frames/sec and recorded with a Sony RDRGX7 DVD recorder.

FEFC measurements were performed with 5mM sodium acetate buffers at pH 3.6 and 4. In the fabricated chips the change in zeta potential was measured as a function of the applied electric field over the gate isolation using 2% P (S/V-COOH)*(425, 480) fluorescent beads from Bangs Laboratories, Inc. with a mean diameter of 0.91 μm added to the buffer to monitor flow. All chemicals were used as received without further purification.

In order to measure the ζ-potential of silica films as a function of solution pH, current monitoring measurements [30] where performed in straight microchannels as follows: The channels where initially filled with a solution of a certain conductivity. Next, at the inlet of the channel a solution with a lower conductivity is applied and a field along the length of the microchannel is applied using needle electrodes inserted in the vials present at the ends of this channel. The field leads to EOF which gives a replacement of the electrolyte solution in the channel. The resulting change in conductivity leads to a current variation, and from the changes in the slop of the current-time graph, the EOF is calculated. Sodium acetate (pH below 6) and sodium phosphate (pH 6 and higher) where used for these measurements. Data acquisition was performed in LabView software (National Instruments, Austin, TX).

Breakdown of the silica insulation layers was measured at a solid/liquid interface. Silica films where deposited on a silicon substrate with aluminum contacts at the backside. On the front side fluid reservoirs filled with 100 mM KNO_3 were formed. Dielectric breakdown was measured at both positive and negative bias, using a voltage ramp from zero until breakdown occurred. Voltage control and data acquisition was performed in HPVee (Hewlett-Packard Development Company, L.P.).

5. Results and discussion

5.1. Measurement of properties of PECVD silica film

The electric field over the silica film at which electric breakdown occurred was measured to be (9.6 ± 0.3) MV/cm.

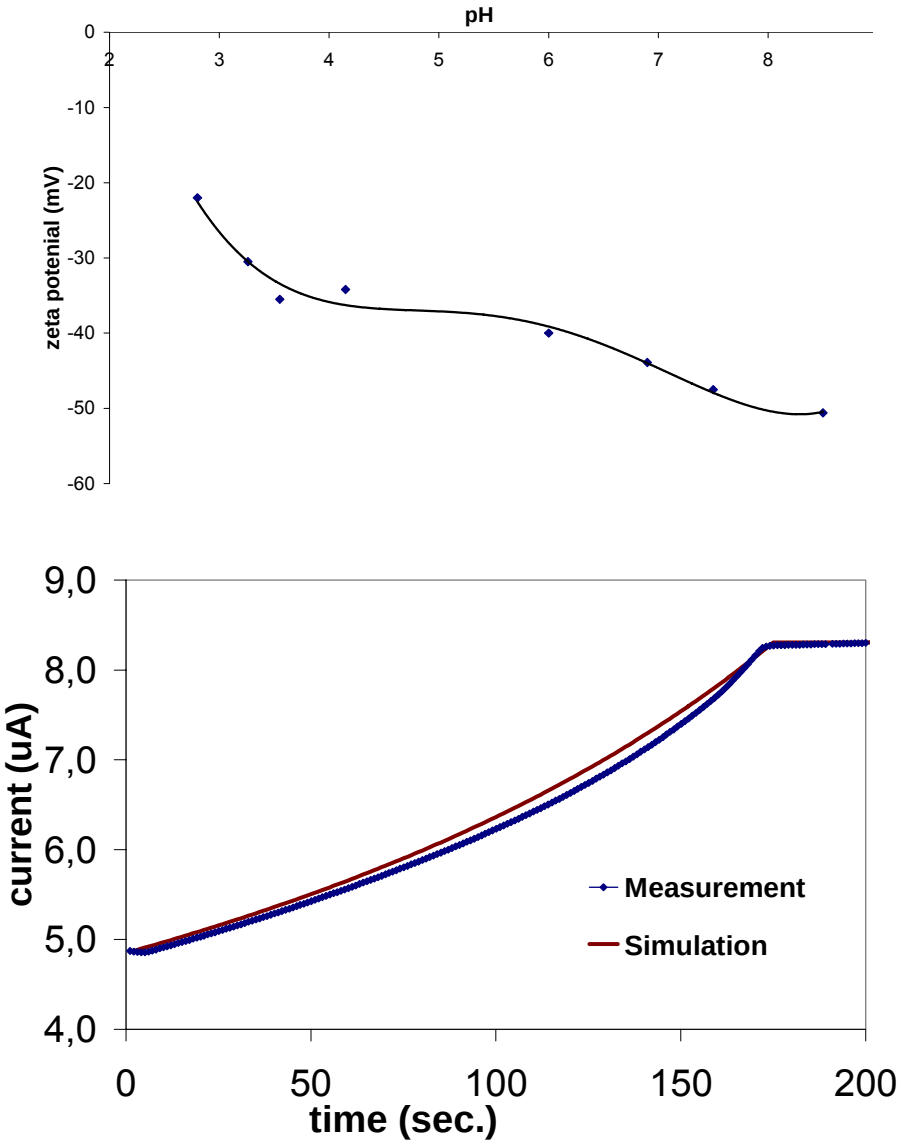

Fig. 6.5: *Measured zeta potential of PECVD silicon dioxide films as a function of pH (top) and a typical result of a current vs. time measurement (see experimental section) with a simulation of the current time relation based on known conductivity values and a constant flow rate (bottom).*

The choice of a pH close to the Point-of-Zero-Charge (PZC) of the wall material is crucial to be able to control and more particularly reverse the EOF with a reasonably low voltage over the channel wall. For a silica layer obtained by thermal oxidation of silicon the PZC is ca. 2 [31]. For the PECVD silica films used in our work we have measured the pH influence on the ζ-potential with the aid of current-time measurements as described in the previous section, for channels with no external voltage applied to the gate electrodes (i.e. gate electrodes are electrically floating). The results are shown in Fig. 6.5 (top). The bottom graph of Fig. 6.5 shows a typical current-time measurement. It was checked experimentally that in the longitudinal voltage range of 20-200 Volts the variation in channel resistance for the used buffers was less than 5 % (taking a voltage drop of 1.2 V due to electrolysis reactions at the electrodes into account).
A point of concern in the current-time measurements is that if the buffer in the microchannel is replaced (in Fig. 6.5, bottom, by a buffer with two times higher conductivity), the electric field distribution in the microchannel will change, such that in the part of the channel with the higher conductivity the electric field will become lower than the original field, while in the lower conductivity region the electric field will become higher. The average electric field in the channel will remain the same as long as the longitudinal voltage is not changed, and thus the average EOF will also not change. The interface between the regions of different conductivity, however, will move with non-linear velocity through the channel, as can clearly be seen in the bottom part of Fig. 6.5. This effect can easily be calculated if the conductivities of the two buffers are known, as the simulated curve in Fig. 6.5 (bottom) shows. A second point of concern is that in general ζ depends on ionic strength and thus on the concentration of the buffer solution, however buffer concentrations were chosen such that this effect is negligibly small.

5.2. FEFC in a microfluidic chip with integrated electrodes

FEFC was measured on a number of microfluidic devices, according to the procedures described above. The dimensions of the investigated microdevice were: channel width 45 μm, height 45 μm, and length 15 mm; 4 gate electrodes each with a size of 2.75 mm by 1.00 mm, located halfway the length of the microchannel. Since the diffuse layer capacitance is proportional to the square root of the ionic concentration, at the relatively low salt concentration of 5 mM this capacitance is still rather small

(ca. 0.16 F), so the zeta potential can be influenced effectively, while there is still enough buffering capacity of the solution to keep the pH constant.
The EOF for different gate voltages was determined by the addition of 0.9 µm diameter fluorescent beads to the running buffer. By adjusting the focus of the optical equipment and in this way monitoring the local flow above the gate electrode, the EOF that relates to the gate-region ζ can be determined. From these EOF data, the zeta potential was calculated, using Eq. 6.1. The longitudinal voltage in the channel was kept constant during these measurements in order to avoid a change in electrophoretic movement of the beads, which movement originates from the charging of the carboxyl surface groups on the beads for the pH conditions used. In case this electrophoretic movement is kept constant, a change in flow velocity corresponds only to a change in ζ of the gate region. Fig. 6.6 shows the relation between the change in ζ-potential and the applied electric field over the insulation layer at the gate region.
The maximum change in zeta potential that could be achieved was limited by electrical breakdown of the silica layers. The plot shows an almost linear trend, which is expected in this electric field regime.

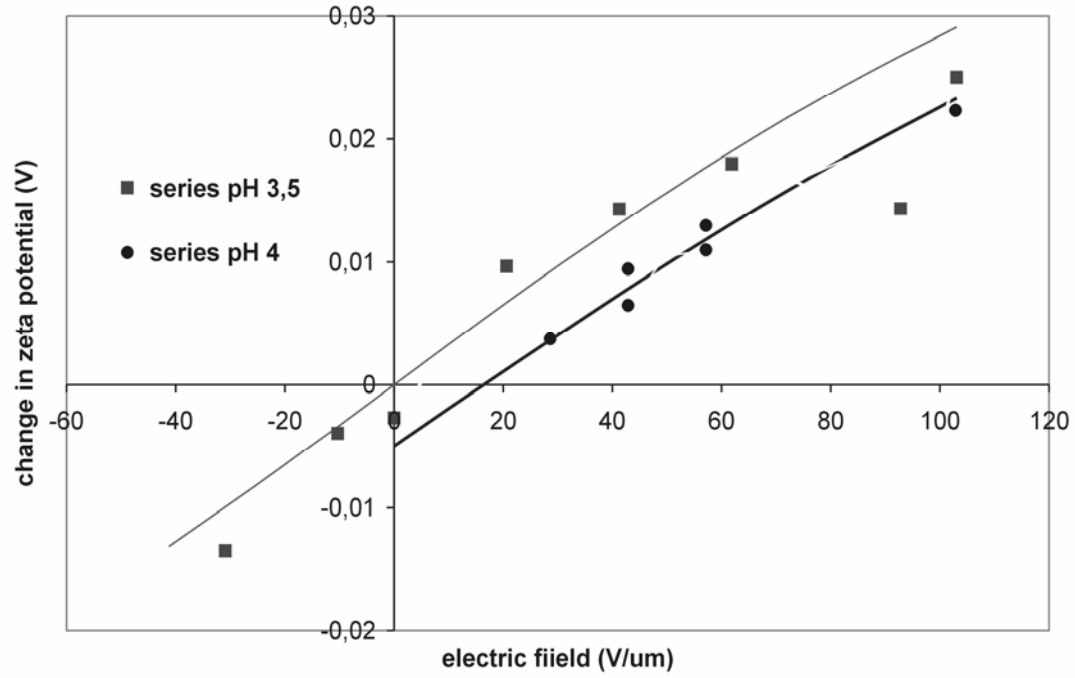

Fig. 6.6: *Change in zeta potential as a function of the applied electric field over the PECVD silica insulation. Buffer: 5 mM sodium acetate, pH 3.5/4.0. The lines indicate fitted curves.*

The slope of the zeta potential vs. V_g curve, $d\zeta/dV_g$, which is a useful parameter describing the effectiveness of flow control, is proportional to the ratio between the capacitance of the silica insulation layer and that of the diffuse layer, as follows from Eq. 6.4. From Fig. 6.6 we derive a value of 0.57 mV/V for this parameter using Eq. 6.4, for both pH 3.5 and 4.0. The solid lines in Fig. 6.6 describe the trend expected from theory. The lower line indicates the trend expected for an off-set in ζ of -5 mV and a 350 nm thick silicon dioxide insulation layer. For the pH 3.5 experiment, the precise gate insulation thickness was not known, the upper line is a fit to the measurement data, and corresponds to an oxide thickness of 320 nm using a dielectric constant of 4.
It has to be mentioned that due to vortex formation at the edge of the gate region (an effect that has been modeled and experimentally observed for surfaces with a heterogeneous composition, which therefore have a varying ζ-potential along the surface [32-35], just like in our case), the measurements presented above are not very accurate. By changing the focus of the microscope lenses in the studies with the fluorescent beads, different flow directions in different vertical planes (i.e. in the height direction of the microchannel) could clearly be observed, however a quantitative evaluation of this phenomenon (e.g. by particle image velocimetry, PIV[36]) has not yet been performed and will be the topic of our future work. In our future work we will also combine such PIV measurements with detailed computer simulations.
Using the data in Fig. 6.6 it is possible to calculate the efficiency factor Γ according to Polson and Hayes [21]:

$$\Gamma = \frac{\Delta\mu_{EOF}}{V_g} \qquad \text{(Eq. 6.5)}$$

where $\Delta\mu_{EOF}$ can be calculated from the change in ζ-potential at which flow reversal occurs, using Eq. 6.1 and the equation:

$$v_{EOF} = \mu_{EOF} E \qquad \text{(Eq. 6.6)}$$

We have observed that it is possible to stop the average flow by applying a field over the insulation layer at the gate region of 1.7 MV/cm, while it is known from Fig. 6.5 that the unmodified ζ-potential at the pH used is ca. -35

mV. The resulting Γ-value is $1.46 \cdot 10^{-6}$ (cm^2/Vs)/ (V/μm), which compares well with values given in literature [21].
It may seem that the actual value of the EOF in the unmodified parts of the microchannel is not important for the effectiveness by which the EOF can be reversed or stopped by FEFC, the relevant parameter being the efficiency by which the ζ-potential at the electrode can be made 0 or made to change sign, which is the Γ-factor calculated above. In principle, no EOF should be possible at a wall which has zero ζ-potential, provided that ζ is zero all around the channel wall (which was not the case in our experiments, only 25% of the wall was covered with a gate electrode). However, changes in ζ-potential along a channel wall may result in pressure build-up, as was experimentally observed by Herr et al. for EOF in capillaries with a heterogeneous surface [37]. The pressure gradient is known to be confined to a small region near the discontinuity in zeta potential [38]. This pressure modifies the flow as well. The complete device design should be taken into account to have the precise effect on direction and size of the resulting flow. This makes a calculation of the effectiveness of FEFC difficult, and a comparison between different configurations based on the Γ-factor alone doubtful.

6 Summary and Conclusions

Microfluidic networks based on glass microchannels with integrated insulated gate electrodes that are used to modify the ζ-potential at specific locations on the wall surface of the microchannels were fabricated and tested. The ζ-potential modification was used to control the direction of the EOF in the microchannels. The average EOF could be stopped completely for longitudinal fields of 150 V/cm by applying a field over the gate insulation layer of 1.7 MV/cm, for conditions where the unmodified ζ-potential was ca. -35 mV. The measurements show that at moderate values of the ζ-potential an almost linear relation between the applied gate field and ζ-potential exists, which agrees with theory for the conditions investigated.
Without chemical modification, the silica films used in this work at pH 7 have a ζ-potential of -44 mV. Since our future application of FEFC will be in the biomedical field, where solutions with a near-neutral pH are most common, such a high off-set value of the ζ-potential is unwanted. In order to shift ζ_0 at pH 7 to a lower value, EOF-suppressing coatings or dynamic coatings may be applied [28], which will be the topic of our future work. [39]

7 Acknowledgements

The authors thank the Dutch Technology Foundation, STW, for financial support (project nr. 5384).

8 References

1. Schasfoort, R.B.M., S. Schlautmann, L. Hendrikse and A. van den Berg, *Field-effect flow control for microfabricated fluidic networks.* Science, 1999. **286**(5441): p. 942-945.
2. Kikutani, Y., T. Horiuchi, K. Uchiyama, H. Hisamoto, M. Tokeshi and T. Kitamori, *Glass microchip with three-dimensional microchannel network for 2 x 2 parallel synthesis.* Lab on a Chip, 2002. **2**(4): p. 188-192.
3. Mastrangelo, C.H., M.A. Burns and D.T. Burke, *Microfabricated devices for genetic diagnostics.* Proceedings of the Ieee, 1998. **86**(8): p. 1769-1787.
4. Neils, C., Z. Tyree, B. Finlayson and A. Folch, *Combinatorial mixing of microfluidic streams.* Lab on a Chip, 2004. **4**(4): p. 342-350.
5. Thorsen, T., S.J. Maerkl and S.R. Quake, *Microfluidic large-scale integration.* Science, 2002. **298**(5593): p. 580-584.
6. Elwenspoek, M., T.S.J. Lammerink, R. Miyake and J.H.J. Fluitman, *Towards Integrated Microliquid Handling Systems.* Journal of Micromechanics and Microengineering, 1994. **4**(4): p. 227-245.
7. Duffy, D.C., H.L. Gillis, J. Lin, N.F. Sheppard and G.J. Kellogg, *Microfabricated centrifugal microfluidic systems: Characterization and multiple enzymatic assays.* Analytical Chemistry, 1999. **71**(20): p. 4669-4678.
8. Gau, H., S. Herminghaus, P. Lenz and R. Lipowsky, *Liquid morphologies on structured surfaces: From microchannels to microchips.* Science, 1999. **283**(5398): p. 46-49.
9. Sniadecki, N.J., C.S. Lee, P. Sivanesan and D.L. DeVoe, *Induced pressure pumping in polymer microchannels via field-effect flow control.* Analytical Chemistry, 2004. **76**(7): p. 1942-1947.
10. Lyklema, J., *Fundamentals of Interface and colloid Science: Volume II: solid-liuid interfaces.* Academic Press, London, 1995.
11. Harrison, D.J., K. Fluri, K. Seiler, Z.H. Fan, C.S. Effenhauser and A. Manz, *Micromachining a Miniaturized Capillary Electrophoresis-Based Chemical-Analysis System on a Chip.* Science, 1993. **261**(5123): p. 895-897.

12. Jacobson, S.C., R. Hergenroder, L.B. Koutny and J.M. Ramsey, *High-Speed Separations on a Microchip.* Analytical Chemistry, 1994. **66**(7): p. 1114-1118.
13. Jacobson, S.C., T.E. McKnight and J.M. Ramsey, *Microfluidic devices for electrokinetically driven parallel and serial mixing.* Analytical Chemistry, 1999. **71**(20): p. 4455-4459.
14. Manz, A., C.S. Effenhauser, N. Burggraf, D.J. Harrison, K. Seiler and K. Fluri, *Electroosmotic Pumping and Electrophoretic Separations for Miniaturized Chemical-Analysis Systems.* Journal of Micromechanics and Microengineering, 1994. **4**(4): p. 257-265.
15. Ghowsi, K. and R.J. Gale, *Field-Effect Electroosmosis.* Journal of Chromatography, 1991. **559**(1-2): p. 95-101.
16. Hayes, M.A. and A.G. Ewing, *Electroosmotic Flow-Control and Monitoring with an Applied Radial Voltage for Capillary Zone Electrophoresis.* Analytical Chemistry, 1992. **64**(5): p. 512-516.
17. Hayes, M.A., I. Kheterpal and A.G. Ewing, *Electroosmotic Flow-Control and Surface Conductance in Capillary Zone Electrophoresis.* Analytical Chemistry, 1993. **65**(15): p. 2010-2013.
18. Hayes, M.A., I. Kheterpal and A.G. Ewing, *Effects of Buffer Ph on Electroosmotic Flow-Control by an Applied Radial Voltage for Capillary Zone Electrophoresis.* Analytical Chemistry, 1993. **65**(1): p. 27-31.
19. Lee, C.S., W.C. Blanchard and C.T. Wu, *Direct Control of the Electroosmosis in Capillary Zone Electrophoresis by Using an External Electric-Field.* Analytical Chemistry, 1990. **62**(14): p. 1550-1552.
20. Wu, C.T., T. Lopes, B. Patel and C.S. Lee, *Effect of Direct Control of Electroosmosis on Peptide and Protein Separations in Capillary Electrophoresis.* Analytical Chemistry, 1992. **64**(8): p. 886-891.
21. Polson, N.A. and M.A. Hayes, *Electroosmotic flow control of fluids on a capillary electrophoresis microdevice using an applied external voltage.* Analytical Chemistry, 2000. **72**(5): p. 1088-1092.
22. Hunter, R.J., *Zeta Potential in Colloid Science: Principles and Applications.* Academic Press, London, 1981.
23. Bard, A.J. and L.R. Raulkner, *Electrochemical Methods, Fundamentals and Applications.* J. Wiley & Sons: New York, 1980; Chapter 12, 1980.
24. Lee, C.Y., G.B. Lee, L.M. Fu, K.H. Lee and R.J. Yang, *Electrokinetically driven active micro-mixers utilizing zeta potential*

variation induced by field effect. Journal of Micromechanics and Microengineering, 2004. **14**(10): p. 1390-1398.
25. Lee, C.Y., C.H. Lin and L.M. Fu, *Band spreading control in electrophoresis microchips by localized zeta-potential variation using field-effect.* Analyst, 2004. **129**(10): p. 931-937.
26. Buch, J.S., P.C. Wang, D.L. DeVoe and C.S. Lee, *Field-effect flow control in a polydimethylsiloxane-based microfluidic system.* Electrophoresis, 2001. **22**(18): p. 3902-3907.
27. Mutlu, S., F. Svec, C.H. Mastrangelo, J.M.J. Fréchet and Y.B. Gianchandani, *Enhanced Electro-Osmotic pumping with liquid bridge and Field Effect Flow rectification.* Proceedings of the IEEE Workshop on MEMS, January 25–29,Maastricht, The Netherlands,, 2004: p. 850-853.
28. Hayes, M.A., *Extension of external voltage control of electroosmosis to high-pH buffers.* Analytical Chemistry, 1999. **71**(17): p. 3793-3798.
29. Hermes, D.C., T. Heuser, E.J. van der Wouden, J.G.E. Gardeniers and A. van den Berg, *Fabrication of microfluidic networks with integrated electrodes.* Microsystem Technologies-Micro-and Nanosystems-Information Storage and Processing Systems, 2006. **12**(5): p. 436-440.
30. Huang, X.H., M.J. Gordon and R.N. Zare, *Current-Monitoring Method for Measuring the Electroosmotic Flow-Rate in Capillary Zone Electrophoresis.* Analytical Chemistry, 1988. **60**(17): p. 1837-1838.
31. Bousse, L.J., N.F. de Rooij and P. Bergveld, *Operation of chemically sensitive field-effect sensors as a function of the insulattor-electrolyte interface.* IEEE Transactions on Electron Devices, 1983. **30**: p. 1263.
32. Ajdari, A., *Elctroosmosis on Inhomogeneously Charged Surfaces.* Physical Review Letters, 1995. **75**(4): p. 755-758.
33. Ajdari, A., *Transverse electrokinetic and microfluidic effects in micropatterned channels: Lubrication analysis for slab geometries.* Physical Review E, 2001. **65**(1): p. 016301.
34. Erickson, D. and D.Q. Li, *Three-dimensional structure of electroosmotic flow over heterogeneous surfaces.* Journal of Physical Chemistry B, 2003. **107**(44): p. 12212-12220.
35. Stroock, A.D., M. Weck, D.T. Chiu, W.T.S. Huck, P.J.A. Kenis, R.F. Ismagilov and G.M. Whitesides, *Patterning electro-osmotic flow with patterned surface charge.* Physical Review Letters, 2000. **84**(15): p. 3314-3317.
36. meinhart, C.D., S.T. Wereley and J.G. Santiago, *Micron-resolution velocimetry techniques.* Developments in Laser Techniques and

Applications to Fluid Mechanics, R. J. Adrian et al. (Eds.), Springer-Verlag, Berlin, 1998., 1998.
37. Herr, A.E., J.I. Molho, J.G. Santiago, M.G. Mungal, T.W. Kenny and M.G. Garguilo, *Electroosmotic capillary flow with nonuniform zeta potential.* Analytical Chemistry, 2000. **72**(5): p. 1053-1057.
38. Long, D., H.A. Stone and A. Ajdari, *Electroosmotic flows created by surface defects in capillary electrophoresis.* Journal of Colloid and Interface Science, 1999. **212**(2): p. 338-349.
39. Bazant, M.Z. and T.M. Squires, *Induced-charge electrokinetic phenomena: Theory and microfluidic applications.* Physical Review Letters, 2004. **92**(6).

7

Directional flow induced by synchronized longitudinal and zeta-potential controlling AC-electrical fields

1 Abstract

Electroosmotic flow (EOF) in a microchannel can be controlled by electronic control of the surface charge using an electrode embedded in the wall of the channel. By setting a voltage to the electrode, the zeta-potential at the wall can be changed locally. Thus, the electrode acts as a "gate" for liquid flow, in analogy with a gate in a field-effect transistor. In this paper we will show three aspects of a Field Effect Flow Control (FEFC) structure. We demonstrate the induction of directional flow by the synchronized switching of the gate potential with the channel axial potential. The advantage of this procedure is that potential gas formation by electrolysis at the electrodes that provide the axial electric field is suppressed at sufficiently large switching frequencies, while the direction and magnitude of the EOF can be maintained. Furthermore we will give an analysis of the time constants involved in the charging of the insulator, and thus the switching of the zeta potential, in order to predict the maximum operating frequency. For this purpose an equivalent electrical circuit is presented and analyzed. It is shown that in order to accurately describe the charging dynamics and pH dependency the traditionally used three capacitor model should be expanded with an element describing the buffer capacitance of the silica wall surface.

2 Introduction

Pumping and valving in microchannels is an important issue in for instance cell trapping, drug delivery and chemical synthesis and analysis. Traditionally these functions are performed by mechanical means. Electro kinetic pumping offers several advantages over conventional pressure driven pumping like ease of fabrication and absence of moving parts. The possibility of external control of the zeta potential offers the possibility to pump in complex micro fluidic networks. Modification of the zeta potential has been demonstrated by both electrical and chemical means. Compared to chemical control the electronic method has the advantage that it allows dynamic control of the surface charge, and thus a dynamic control of the zeta potential Electronic control of the surface charge can be performed by embedding a gate electrode in the micro channel wall. The application of a gate potential will then modify the surface potential through capacitive coupling. This method of flow control has been referred to as Field Effect Flow Control (FEFC) [1] or flowFET [2] because of the analogy to a MOSFET.

Conventional electrokinetic pumping makes use of a dc potential to generate an Electro-Osmotic Flow (EOF), using metal electrodes at the ends of microchannels. A major problem with this set-up is potential gas bubble formation by electrolysis at these electrodes that are in direct contact with an electrolyte. For aqueous electrolytes, electrolysis is already present at potentials as small as 1.2 V. Bubble formation may lead to blocking of the conducting path between the channel electrodes and in this way stops the EOF.
A possible way to prevent bubble formation is the application of AC-signals of sufficiently high frequency to ratchet-type arrays of open electrodes inside the channel [3-5], the modulation of non-zero average AC-potential with zero average current [6], or the synchronized AC-switching of the zeta potential at the solid/liquid interface and the channel potential [7].
This paper will present FEFC pumping with AC-signals applied at both the channel and gate electrodes and present an analysis of the timescales that are involved in the switching of both zeta potential and EOF.

3 AC-FEFC AND TRANSIENT BEHAVIOR

At the interface between a solid and a polar liquid, most materials will develop a surface potential due to pH dependent deprotonation or association of surface groups. Consequently co-ions will be repelled and counter ions will be attracted to the surface and form the so called electrical double layer (EDL)[8]. Close to the surface a layer of immobilized counter ions will form due the electrostatic interaction with the surface, this layer is referred to as the Stern layer. Further away from the surface the counter ions will have more freedom to move until the point where equilibrium in the electrostatic interaction and thermal energy of the ions exists. This layer is referred to as the diffuse layer; the potential at the interface with the Stern layer is called the zeta potential ζ.
When an axial potential is applied along the channel the ions in the EDL will move with the electric field E. Due to viscous coupling between the EDL and the bulk fluid a flow with an almost uniform velocity profile over the channel width will develop, under the condition that the viscous coupling is fast enough to establish stationary EOF profiles or when $\omega < \omega_{viscous}$. The flow velocity v_{EOF} as a result of a sinusoidal applied E-field is given by equation 1.1, where ε_0 and ε_r, are respectively the dielectric constant of vacuum and the fluid, η is the viscosity, ω the angular frequency of the applied potential and t the time [7].

$$v_{EOF} = \frac{\varepsilon_0 \varepsilon_r \varsigma}{\eta} E \sin(\varpi t) \qquad \text{(Eq. 7.1)}$$

When a gate electrode is covered with an insulator that acts as a wall (see below), the zeta potential in the gate region can be modified by the application of a gate potential. The insulator, the Stern and diffuse double layer can be described by capacitors. The influence of the gate potential on the local zeta potential can then be illustrated by a three capacitor model [2] as is shown in Figure 7.1.

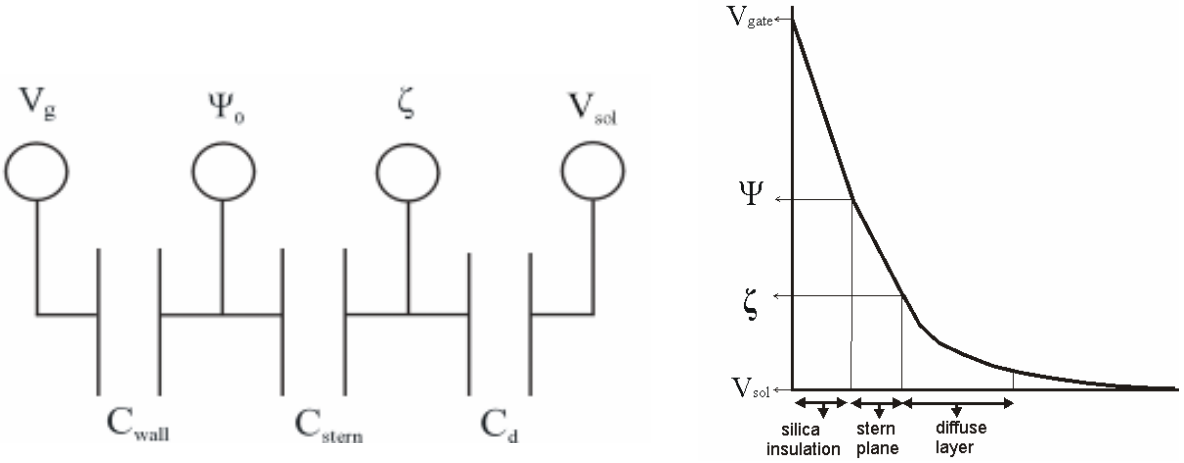

Fig. 7.1: *Three-capacitor model of a FEFC structure (a) and its potential distribution (b) (not to scale).*

At moderate and low ionic concentrations the capacitance of the Stern capacitance is very large compared to the diffuse layer capacitance and can thus be neglected.
The capacitance of the wall is given by equation 7.2. Here 0 and r are the dielectric constant of vacuum and the gate insulation, d is the thickness and A the area. The capacitance of the diffuse layer is give n by equation 7.3 [9], here c is the ionic concentration in mol, ζ_0 the natural zeta potential and $\Delta\zeta$ the induced change in zeta potential.

$$C_{wall} = \frac{\varepsilon_0 \varepsilon_r}{d} A \qquad \text{(Eq. 7.2)}$$

$$C_d = 228\sqrt{c} A \cosh(19.5(\varsigma_0 + \Delta\varsigma)) \qquad \text{(Eq. 7.3)}$$

The influence of the gate potential on the local zeta potential can then be described by equation 7.4, in case the same frequency is used for the gate and channel potentials.

$$\Delta\varsigma = \frac{C_{wall}}{C_d}\left(V_g \sin(\varpi t) - V_{sol} \sin(\varpi t + \varphi)\right) \qquad \text{(Eq. 7.4)}$$

In equation 7.2, C_{wall} and C_d are respectively the capacitance of the gate insulator and the diffuse double layer, V_g and V_{sol} are respectively the amplitude of the applied gate and channel potential, $\Delta\zeta$ the induced difference in the zeta potential and φ the phase difference between the gate and channel potential.

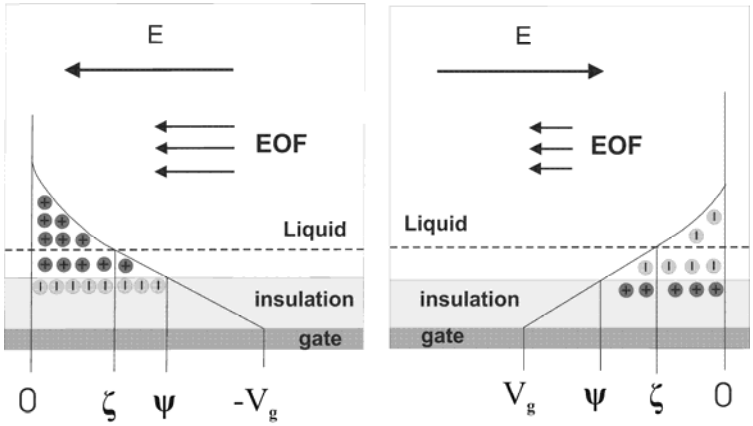

Fig. 7.2: *Schematic overview of directional AC-pumping*

Figure 7.2 shows a schematic overview of the concept. The first drawing shows the situation where both channel and gate potential are negative. The negative gate will lead to a more negative zeta potential and thus an enhanced flow in the direction of the anode. The second image shows the situation for both a positive gate and channel potential. The positive gate potential will lead to a reversal of the zeta potential; since also the channel potential is reversed the EOF will maintain the same direction. This synchronized switching scheme is analog to the concept of AC magnetohydrodynamic pumping where both the current and magnetic field are synchronized to create a unidirectional Lorentz force on the ions in a microchannel [10, 11].

The maximum operating frequency that can be achieved depends on the charging dynamics of the EDL and the time needed for the EOF to establish. The charging of the EDL upon application of a gate potential is limited by the current, which depends on the series impedances of the gate insulation capacitance and the channel electrolyte resistance. The time τ for the EOF to develop in a microchannel with diameter d filled with a liquid with density ρ is given by equation 7.5 [12].

$$\tau = \frac{d^2}{\eta / \rho} \qquad \text{(Eq. 7.5)}$$

From equation 7.5 it can be seen that for water based solutions in microchannels (d ~ 10 μm) the time needed for the EOF to develop will be in the sub millisecond range [13].

3.1 Influence of the buffer capacitance

When a potential is applied at the gate electrode the zeta potential in the gate region will be modified according to equation 7.2. However the validity of this equation is limited to the case where the pH of the channel electrolyte is close to the point of zero charge (p.z.c.) of the gate insulation surface groups. In our case this will be the p.z.c. value of silica which is known to be around pH 2 [14].
This limitation is caused by the influence of the buffer capacitance of the silanol surface groups.
If a potential is applied at the gate electrode, the induced surface charge and the proportional change in surface potential will lead to a change in pH of the silica surface as is illustrated by the Boltzmann equation
(Eq. 7.6) [15].

$$\left[H^+\right]_s = \left[H^+\right]_b \exp\left(\frac{-q\Psi_0}{\kappa T}\right) \qquad \text{(Eq. 7.6)}$$

Here [H+]s and [H+]b are respectively the proton concentration at the surface and in the bulk, q is the elementary charge, κ is the Boltzmann constant, T is the temperature and ψ0 is the surface potential. However silica acts as a good buffer for protons and will react with dissociation or

association of SiOH surface groups to keep the proton concentration constant (eq. 7.7 and 7.8) [16].

$$SiOH \xleftrightarrow{Ka} SiO^- + H^+ \qquad \text{(Ka=6)} \qquad \text{(Eq. 7.7)}$$

$$SiOH_2^+ \xleftrightarrow{Kb} SiOH + H^+ \qquad \text{(Kb=-2)} \qquad \text{(Eq. 7.8)}$$

The counter change in surface potential that is induced can be calculated by the equivalent circuit of figure 2. A difference in pH will lead to a change in chemical potential for a proton of -59 mV per unit pH. This potential will be divided over the buffer capacitance of the silica surface and the EDL capacitance.
Equation 7.9 gives the magnitude of the buffer capacitance in case only the dissociation reaction of Equation 7.7 is taken into account which is valid in the case that the electrolyte pH is far from the pKb value and protonation of the silanol groups is negligible [17].

$$\beta = \frac{d\sigma_0}{dpH_s} = N_s \frac{K_a}{(K_a + a_{H_S^+})^2} 2.3 a_{H_S^+} \qquad \text{(Eq. 7.9)}$$

In equation 7.9 N_s is the number of charged surface groups, K_a is an equilibrium constant and $a_{H_s^+}$ is the proton activity at the surface which is related to the bulk pH by the Boltzmann equation. It can be seen that the magnitude of the buffer capacitance is proportional to the number of surface sites that are charged and thus will increase with increasing pH.

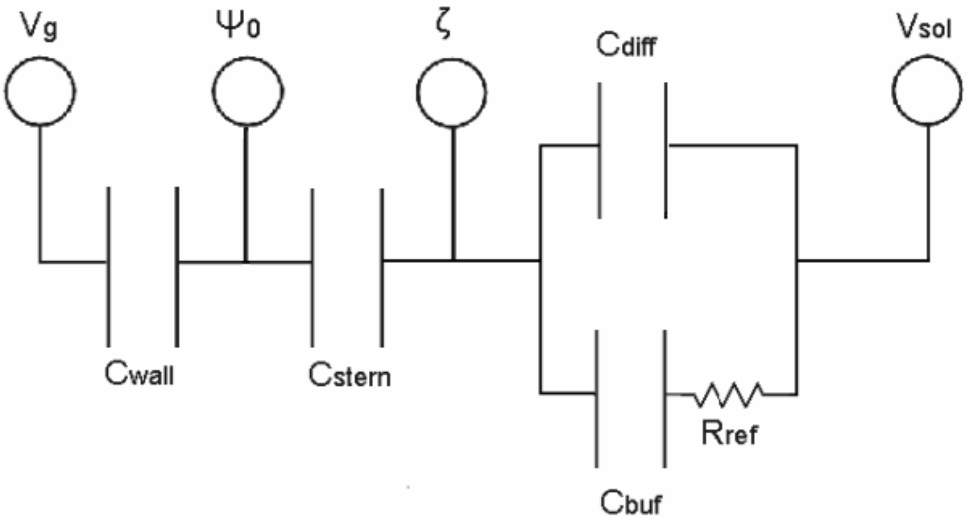

Fig. 7.3: *schematic view influence buffer capacitance*

Figure 7.3 shows the equivalent electrical circuit of figure 1 extended with the buffer capacitance Cbuf to model the surface response to a gate potential and a resistance Rref that represents a proton diffusion resistance [18].
Since proton diffusion occurs over the EDL thickness and has a time constant in the nanosecond range associated with it, Rref can be neglected.
Based on figure 2 the pH dependent change in surface potential can then be calculated according to equation 7.10.

$$\frac{d\psi}{dpH} = -0.059\,\frac{C_{buf}}{C_{buf} + C_{edl}} \qquad \text{(Eq. 7.10)}$$

It can be seen that when Cbuf >> Cedl the potential drop is over the buffer capacitance and the surface potential will change with -59 mV per unit pH. In the case that Cedl >> Cbuf as is the case close to the p.z.c. the largest potential drop is over the diffuse double layer.

4 MATERIALS AND METHODS

4.1 Fabrication

EOF with synchronized gate and channel potentials was measured in glass chips with integrated electrodes. An overview of the fabrication process is shown in Figure 7.4.

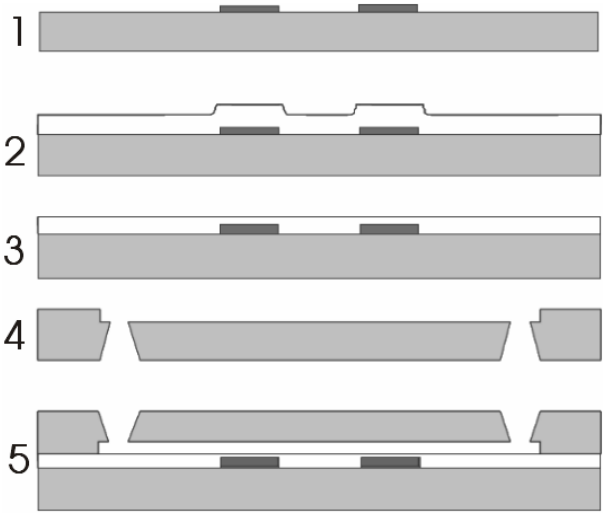

Fig. 7.4: *Schematic overview of the fabrication process*

In the first step of the fabrication process the electrodes are deposited onto a Pyrex substrate. They are covered with a PECVD silica insulating layer of approximately 1 µm in a subsequent step. The silica layer is planarized and polished using Chemical Mechanical Polishing (CMP). In a second Pyrex or Borofloat substrate microchannels are etched, and holes are powder blasted through the substrate to provide in- and outlets with liquid reservoirs and electrical contacts to the gate electrodes. In a last step the two substrates are aligned, brought together and annealed at 600 °C for 1 hour [19]. Figure 7.5 shows an example of a fabricated structure.

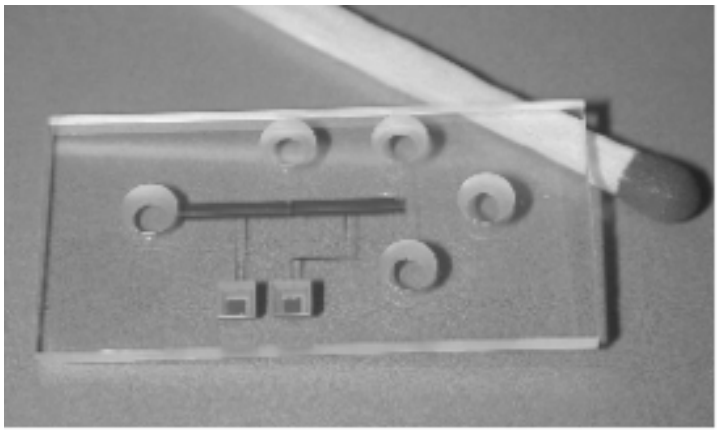

Fig. 7.5: *FEFC microstructure with two gate electrodes; channel width 150 µm, height 20 µm, length 1.5 cm*

4.2 Measurement of EOF

The EOF was measured by the addition of a 2% solution of fluorescent polystyrene beads with a size of 0.9 µm to a 5 mM potassium acetate buffer of pH 3.6. Velocities were determined using optical particle tracking with the aid of a microscope. By changing the focus of the optical microscope, flow velocities at different height in the channel could be determined.
For the application of gate and channel potentials and the measurement of currents two Keithley 2410 source meters where used and controlled with LabView software, the AC signals where modulated with discrete steps where each sine-wave signal was composed of at least 10 data points. The flow velocities were determined by monitoring the flow over at least 20 periods.

5 RESULTS AND DISCUSSION

Upon application of an AC-potential at both the gate electrode and the channel electrodes, the observed movement can consist of three components: EOF due to the natural zeta potential, EOF due to the modified zeta potential in the gate region, and electrophoretic movement due to charging of the fluorescent beads. It was verified that upon application of only an axial AC-potential, only oscillation of the beads occurs with no net component. However, with both a gate and an axial channel potential applied, a net movement of the beads and thus a net flow was observed in

those cases where both AC-signals had the same amplitude and phase, and in the case where two independent power supplies where used to allow a phase difference between the potentials. Close to the gate electrode oscillational flow with a component in only one direction could be observed when the gate potential exceeded 100V, which indicates a complete sign reversal of the local zeta potential.
Figure 7.6 shows the mobility of fluorescent beads at a frequency of 15 Hz as a function of the applied gate potential. Series 1 indicates measurements that where performed with the same signal applied at the gate and channel electrodes. Because the electrophoretic movement of the beads and the EOF due to the unmodified zeta potential has no net component, the observed net flow is directly related to the gate zeta potential.

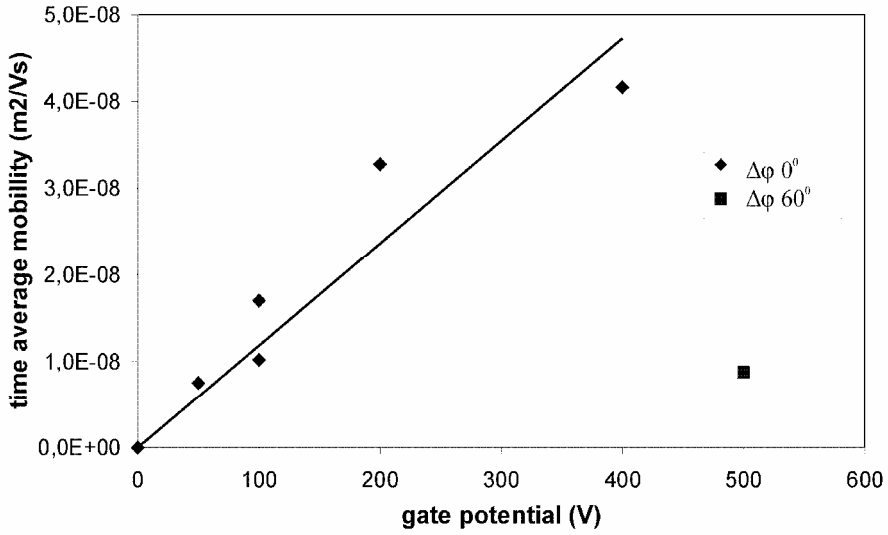

Fig. 7.6: *Measured average net bead mobility as a function of the gate potential. The trend line indicates a linear fit through the measurement point with 0˚ phase difference. The individual point at 500 V was measured with a phase difference of 60˚ between the gate and channel potential.*

Because the electrophoretic movement of the beads and the EOF due to the unmodified zeta potential has no net component, the observed net flow is directly related to the gate zeta potential. Since the change in zeta potential is a linear function of the gate potential as follows from equation 4 also a linear relation between the net flow and the gate potential is expected.
However the linear trend line shows some deviation especially at larger gate potentials, this effect can be explained by the effect of the zeta potential on

the diffuse double layer capacitance. As can be seen from equation 3 C_d increases as a cosines hyperbolicus function with ζ. So at larger values for the zeta potential the effect of the gate potential on Δζ will decrease as can be seen from equation 4. This effect can explain the flattening of the average mobility with the gate potential in figure 7.6.
The individual point at a gate potential of 500 V shows a measurement performed with a phase difference in the gate and channel potential of approximately 60°. It can be seen that the observed average mobility is significantly smaller than in the case of the same applied potential due to the less effective coupling between the effective zeta potential and the channel potential.
The maximum induced average mobility was approximately $4 * 10^{-8}$ m^2/Vs which is more than a factor 100 larger than reported by Mutlu *et al*. [7]. The larger influence on the flow might be due to the larger area covered by the gate electrode in our case, which leads to a more effective FEFC.
In case of a heterogeneous surface charge a pressure difference will build up at the interface between the areas with different zeta potentials to compensate for the differences in flow rate in the subsequent sections.
Thus the flow in each cross-section will be composed of EOF component due to local zeta potential and a pressure driven component due to the induced pressure difference [20].
The generated pressure can be calculated by an analysis of the induced net flow. The maximum induced average mobility was approximately $4 *10^{-8}$ μm/Vs. The cross-section of the HF etched channels resembles roughly the shape of a half ellipse with a width, height and length of respectively 150 μm, 20 μm and 1.5 cm. The cross-section area of a half ellipse is given by: $A_{cross}=1/2\pi ah$, where *a* is half the width and *h* the height of the channel. From this a net induced flow rate of 2.4 nl/sec can be calculated. The flow rate and induced pressure are related by: Q=P*R, where Q is the flow rate in m^3/sec. P is the pressure in Pa and R is the hydraulic resistance which is given by equation 10, where η is the viscosity and l the length of the channel. With the aid of equation 10 a hydraulic resistance of $2.6*10^{14}$ can be calculated. Based on the former mentioned relation between resistance and flow rate this results in a calculated pressure of $6*10^2$ Pascal. However it should be mentioned that the generated pressure scales with the hydraulic resistance of the channel, by optimizing the design towards small dimensions larger pressures can be generated as has been demonstrated in the case of porous silica plugs [21].

$$R = \frac{32\eta l}{\pi} \frac{3a^2 + b^2}{3a^3 b^3} \qquad \text{(Eq 10)}$$

The pressure build up in each section will be such that the sum of the pressure driven flow and the EOF in each section is equal to the average EOF which is determined by the average zeta potential of the total channel. This implies that a large surface coverage is desired for the applied gate potential to have as large a possible influence on the average zeta potential and thus on the average flow [22] . However in some publications it was suggested that the influence of surface conduction could lead to an influence of the gate potential outside of the gate area and that instead of a model that assumes discrete changes in the zeta potential at the interface between influenced and non-influenced region a linear decay model which assumes a gradient in zeta potential from the gate to the inlet/outlet reservoir could provide a better match with the measurements [23, 24].

5.1 Analysis of charging dynamics

RC charging characteristics of the EDL were determined by measuring the potential decay over a reference resistor in series with the channel resistance and gate capacitance. Upon application of a gate potential the potential drop will first be over the channel resistance, after which the gate and double layer capacitance will be charged until the point where the entire potential drop is over the capacitances. The 90 % charging time is defined as the point where the gate current has dropped to 10 % of the initial value which is equivalent to a potential drop of 90 % over the reference resistor. This 90% RC charging time is shown in Figures 7.7 and 7.8 for respectively positive and negative bias potentials, as a function of the electrolyte resistance with sodium acetate buffers of pH 3.6 over a range of 1-100 mM. Note that the vertical scale in the two plots is different.

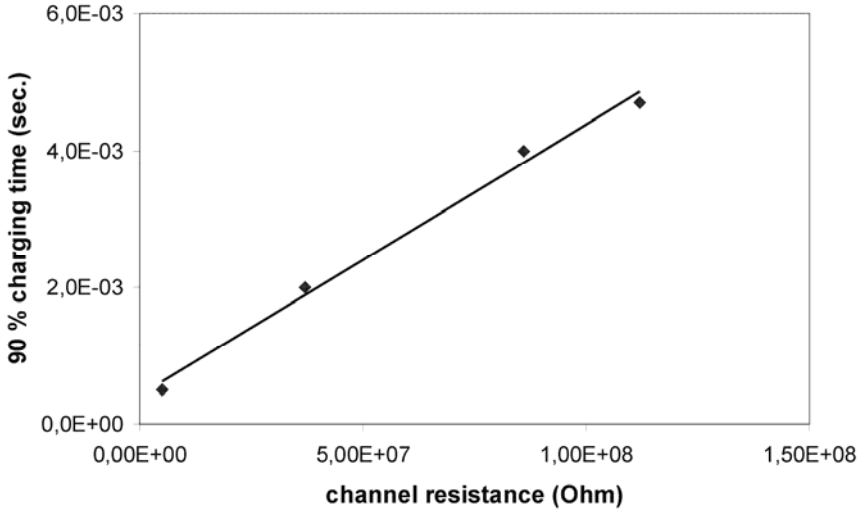

Fig. 7.7: *90% charging time for the double layer capacitance as a function of channel resistance for a gate oxide capacitance of 25 pF for a positive gate bias*

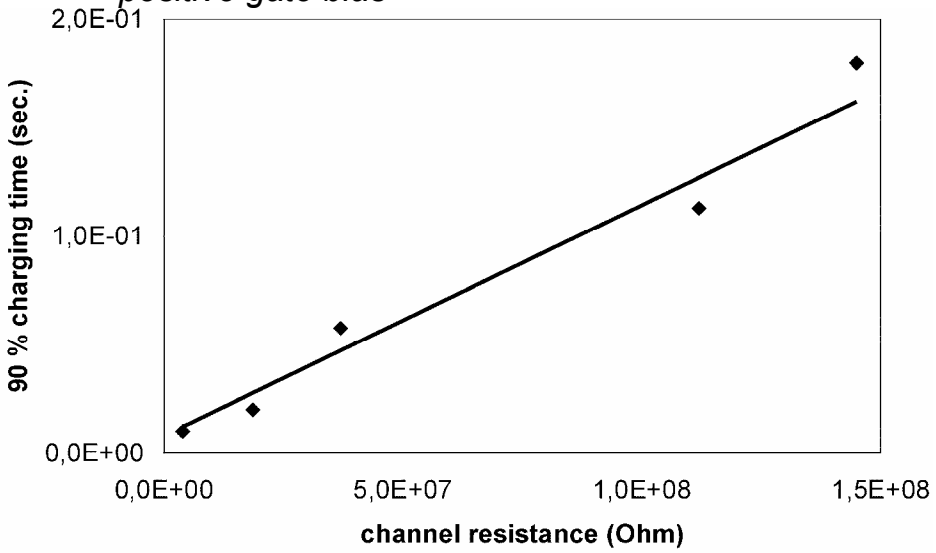

Fig. 7.8: *90% charging time for the double layer capacitance as a function of channel resistance, for a gate oxide capacitance of 25 pF and for a negative gate bias.*

It becomes clear from Figures 7 and 8 that there is a large difference in charging time for positive and negative bias potentials. In case of a positive bias potential the 90 % charging time is close to the value expected when the charging is determined by the series impedance of the channel resistance and the gate oxide capacitance. However in the case of a

negative gate potential the observed charging times are more than an order of magnitude larger.
In Figures 7.9 and 7.10 we show a typical potential decay plot, for a positive and negative bias, respectively. Note that the time scale on the horizontal axis in the two plots is different.
Figure 7.9 indicates that in case of a positive bias the curve is linear on a logarithmic scale, i.e. the potential is exponentially decaying with time. This is expected for a simple electronic series circuit composed of a single resistor R and a single capacitor C [25].
However in case of a negative bias potential the potential decay seems to consist of a fast and a slow response. The initial fast response is still determined by the simple series circuit of channel resistance and gate capacitance. The second slower response can probably be explained by the response of the silica surface to the applied gate potential.
The application of a negative gate potential will lead to a more negative surface potential, as can be seen in equation 7.6 this will shift the surface pH to a higher value and lead to a consequent higher buffer capacitance. This in turn will lead to larger diffusion driven current and longer timescales for re- establishment of equilibrium.

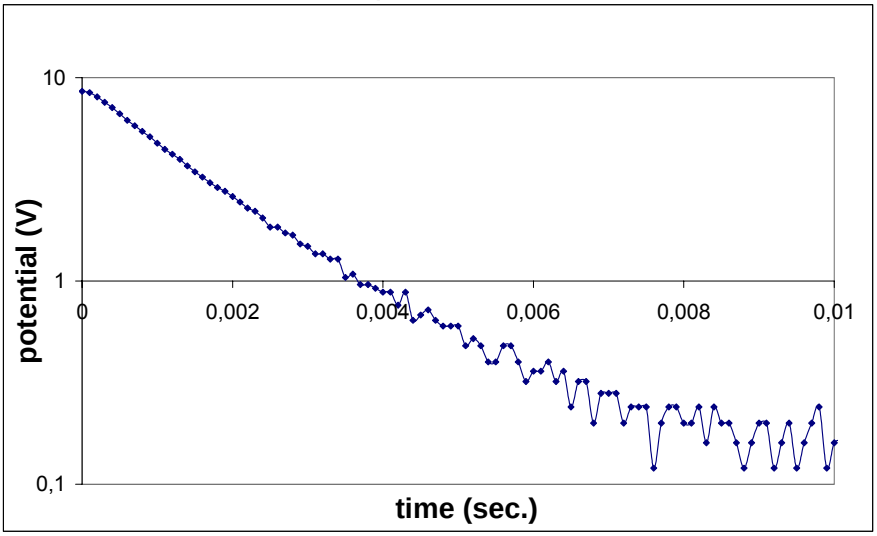

Fig. 7.9: *Potential decay over a reference resistance in series with the channel resistance for a positive bias potential. Rref = 1 MΩ*

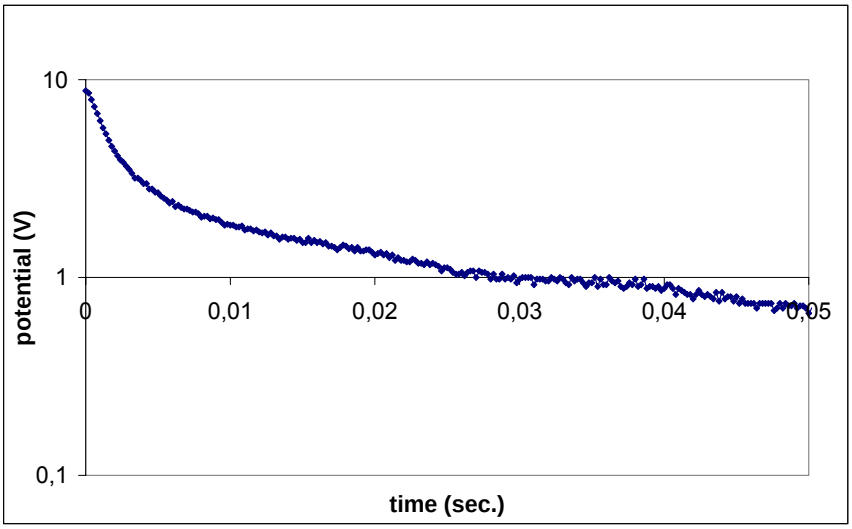

Fig. 7.10: *Potential decay over a reference resistance (1 MΩ) in series with the channel resistance, for a negative bias potential.*

Figures 7 and 8 indicate that the maximum frequency that can be applied for AC-switching is determined by the charging characteristics at negative bias potential. For an electrolyte resistance of approximately 50 MΩ Figure 7.8 gives an RC time of 60 msec, which would allow a maximum switching frequency of 16 Hz.
The time for the EOF to develop is given by equation 7.5. In case of a channel diameter of 20 μm this time τ = 0.4 msec, which indicates that in the FEFC-device developed in this study, the time response is limited by RC charging of the EDL.

5.2 Influence of the buffer capacitance

The influence of the buffer pH on the window in which the zeta potential can be switched in the gate region was calculated and is shown in Figure 7.11.
The calculated curves are based on measured values for the zeta potential at zero gate potential [26], values for the buffer capacitance as a function of pH where taken from [27]. It can be seen that the offset value of the zeta potential decreases with increasing pH, and that the effective change in zeta potential at a certain gate potential reduces with increasing pH because of the increasing buffer capacitance.
The increasing buffer pH affects the change in zeta potential in two ways. First, as can be seen in figure 7.3, a larger portion of the potential drop that

is induced by the gate potential will be over the buffer capacitance if the ratio Cbuf / Cedl increases.
Secondly, the effective potential drop over the substitution impedance of the parallel capacitances will decrease if Cbuf increases.

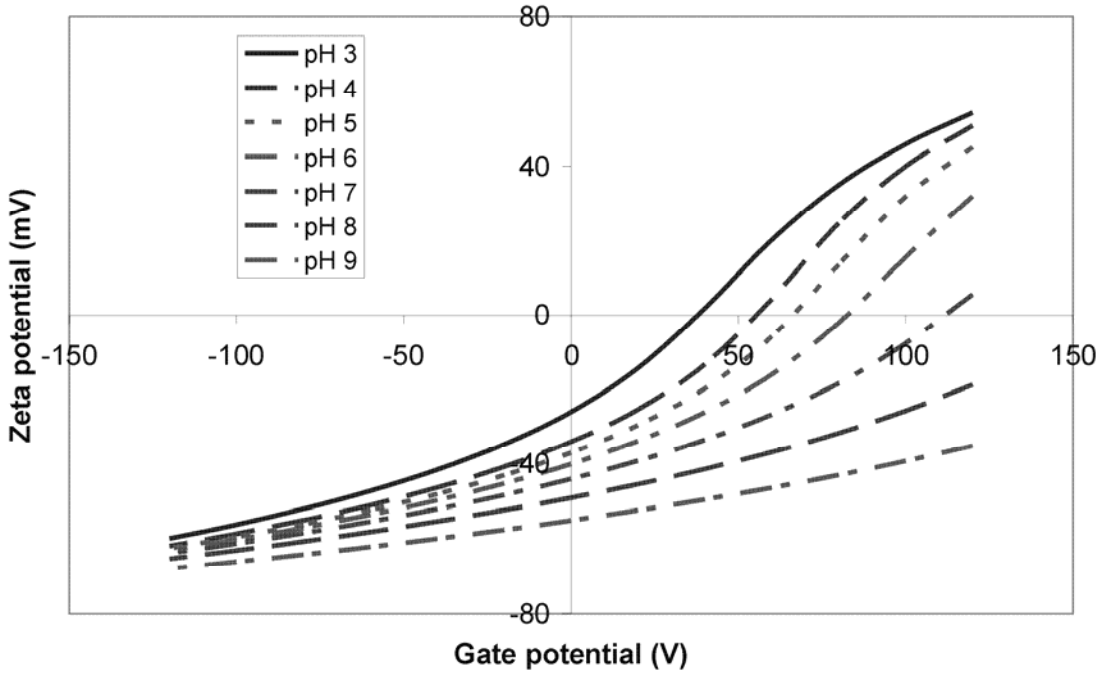

Fig. 7.11: *Change in zeta potential as a function of the gate potential for various pH as calculated for 10 mM electrolyte concentration and 200 nm silica gate insulation with a dielectric constant of 4*

The above figure shows that for reversal of the zeta potential the electrolyte pH should remain below pH 7. At larger pH the gate potential for reversal exceeds the breakdown voltage of the silica insulating layer. For flow control in a wider pH window, surfaces with a limited pH response are desired. This can be obtained by the application of surface coatings [28] which decrease the buffer capacitance over a wide pH window and still benefit of the favorable properties of the silica insulation. If switching at higher pH values is desired, alternatively a gate insulation material with a higher p.z.c. may be chosen, e.g. Al2O3.

6 *Electrical modeling of a FEFC device*

To gain more insight in the expected charging dynamics the transient behaviour of a FEFC structure, an equivalent electrical model has been

composed and analyzed in transient mode. Simple models that have been composed to describe the charging dynamics of a FEFC structure assume a RC time based on the series of the channel electrolyte resistance and the wall capacitance [2]. However, analysis of the charging dynamics in Electrical Field Flow Fractioning (EFFF) has shown that the charging dynamics does not show a simple logarithmic decay as expected but exists of a more complex double exponential response [29]. Analysis of the response time of ISFET's has shown that the influence of the surface buffer capacitance can play a significant role in the dynamic operation [16, 17].
An equivalent circuit based on the 3 capacitor model as proposed by Schasfoort *et al.* has been composed and expanded with a leakage resistance to model current leakage through the silica gate oxide and a buffer capacitance in series with a diffusion resistance (figure 7.12), to model proton diffusion resulting from the buffer capacitance at an applied gate potential as explained in section 4.3.1. Values for the channel resistance and gate insulation were experimentally determined. The EDL capacitance was determined according to equation 5.4 assuming an electrolyte concentration of 5 mM. The capacitance is simulated as a constant phase element to account for its non ideal capacitive behaviour. The value for the buffer capacitance was taken from [17], assuming a pH of 7 for a silica surface. A gate of 1 cm length and 100 µm with was assumed. The diffusion resistance was chosen such that the diffusion length was equal to the channel height. An overview of the parameters and their values is provided in table 7.1.

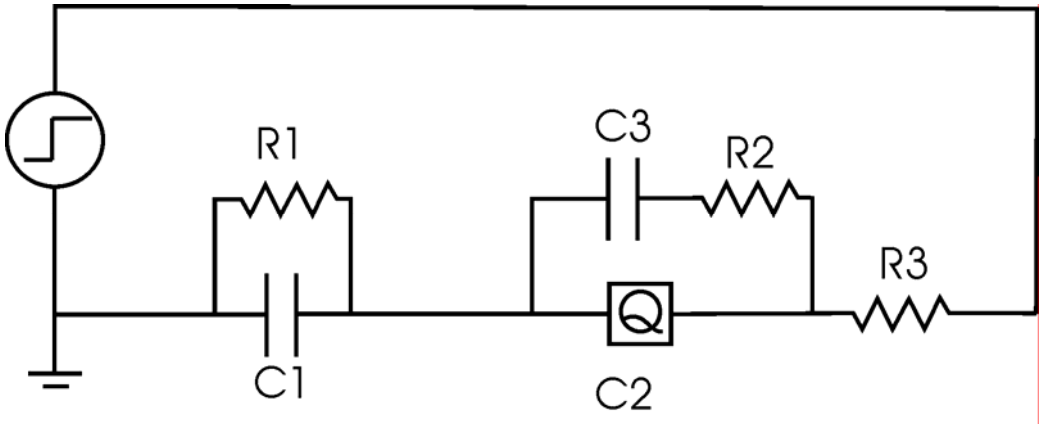

Fig.7.12: *Equivalent electrical circuit for a FEFC structure.*

Abbreviation	Parameter	value
C1	Wall capacitance	60 pF
R_1	Leakage resistance wall	$1*10^{16}\ \Omega$
C2	EDL capacitance	50 nF
C3	Buffer capacitance	1 µF
R2	Diffusion resistance	$5*10^{4}\Omega$
R3	Channel electrolyte resistance	$1*10^{7}\ \Omega$

Table.7.1: *Overview of the parameters used in figure 5.18.*

The validity of the model was verified by a fit of measured impedance data to the composed model using the electrochemical data analysis software Zsimpwin. Figure 7.13 shows the measured impedance and phase over a frequency range of 100 – 100 MHz, indicated by the dotted lines. The solid lines indicate a fit to the measurement data according to the model of figure 7.12. The fit results in a chi^2 which indicates the correlation between measurements and fit, with a maximum correlation at 0 and a minimum at 1 the resulting value of $8.9*10^{-3}$ indicates a good fit and thus a valid description of the model for a FEFC device.

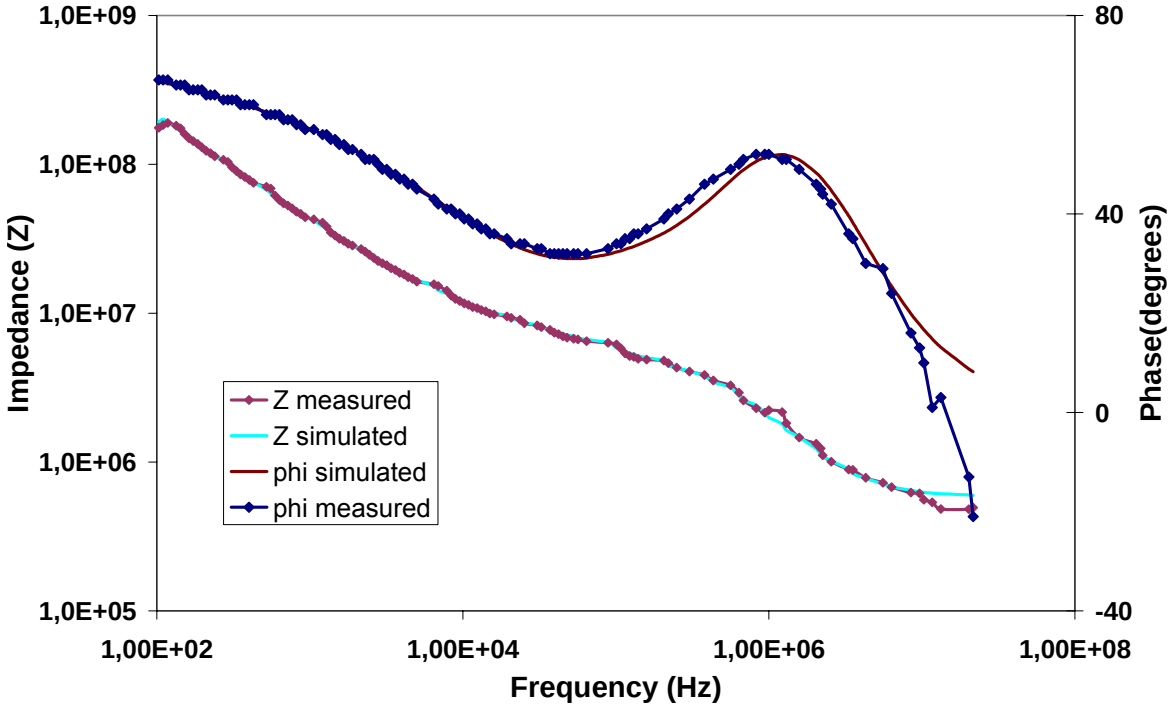

Fig.7.13: *measured impedance and simulated impedance data according to the circuit of figure 5.18.*

Figure 7.14 shows the transient response of a FEFC structure after the application of a gate potential of 5 V. The potential of the channel resistance is plotted as a function of the time.
It can be seen that initially after application of a gate potential the time response is dominated by a relatively fast process dominated by the RC charging of the gate insulation through the channel resistance. After approximately 4 msec the slower relaxation of the series of the buffer capacitance and the diffusion resistance dominates the dynamics.
It should be mentioned however that the role of the buffer capacitance is dependent on several parameters and its behaviour is modeled here in a simplified way. Under the conditions that the buffer capacitance is low and a high concentration buffer is present in the channel, the diffusion length of protons will be limited to the EDL thickness. This will result in a much shorter time response. While under the reverse conditions of a large surface buffer capacitance and a small electrolyte buffer concentration, proton diffusion might not be limited to the radial channel direction, but spread into the longitudinal direction. Under these conditions the consequent relaxation time would be significantly increased.

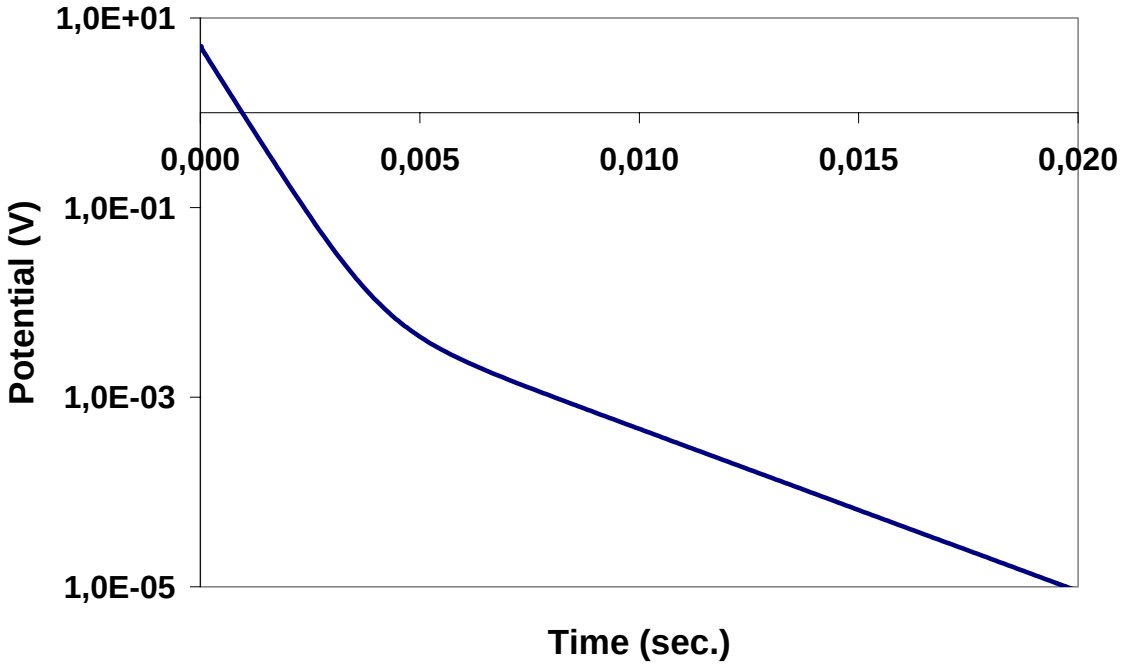

Fig.7.14: *Simulated transient response of a FEFC device on a applied gate potential*

7 Summary and conclusions

It has been shown that a net flow can be induced by the synchronized switching of axial channel voltage and gate potential. Directional flow was observed above the gate electrode, with an oscillating (AC) component due to the electrophoretic movement of the beads and the asymmetry in the zeta potential in the positive and negative half of the gate potential period. This concept offers high potential for the use of EOF in fully integrated systems.

From an analysis of the time scales involved in the dynamic behavior of a FEFC structure it follows that the maximum operating frequency is limited by the charging of the EDL, which is controlled by the series impedance of the channel resistance and the gate capacitance.

Since the performance of the device is optimal at moderate and low ionic concentration, for fast FEFC the concentration of the electrolyte is limited to the mM range which gives an RC time limited by switching at negative bias potentials, with a typical time constant of approximately 60 milliseconds. This value allows a maximum operating frequency of 16 Hz. However, this value may be increased by decreasing the gate electrode area or using shorter channels.

From an analysis of the pH dependency of a FEFC structure it follows that the 3 capacitor model that is traditionally used to describe FEFC is only valid at low buffer capacitances. At larger surface charge the model should be expanded to account for the influence of the buffer pH. It follows that the practical pH range for AC-operation is below pH 5. Above this value the gate potential needed for switching the sign of the zeta potential are in the range of the breakdown values of the silica insulating layer. This limitation is caused by the influence of the buffer capacitance of the silanol surface groups. However a complete reversal of the zeta potential in the gate region is not necessary for the generation of a net flow with an applied AC-channel potential, but the range in which the flow can be controlled will be narrowed.

Electrical modeling of a FEFC structure shows that the dynamic behaviour is dominated by a double relaxation process. Initially the response is determined by a charging of the wall capacitance through the channel electrolyte resistance. After the initial fast response a smaller relaxation resulting from proton diffusion, initiated by the influence of the buffer capacitance of the solid surface dominates the time response.

However, the influence of the buffer capacitance on the time response can vary largely dependent on various parameters.

8 Acknowledgements

This research is supported by the Dutch Technology Foundation STW, applied science division of NWO and the technology program of the Ministry of Economic Affairs.

9 References

1. Sniadecki, N.J., C.S. Lee, P. Sivanesan and D.L. DeVoe, *Induced pressure pumping in polymer microchannels via field-effect flow control.* Analytical Chemistry, 2004. **76**(7): p. 1942-1947.
2. Schasfoort, R.B.M., S. Schlautmann, L. Hendrikse and A. van den Berg, *Field-effect flow control for microfabricated fluidic networks.* Science, 1999. **286**(5441): p. 942-945.
3. Ajdari, A., *Pumping liquids using asymmetric electrode arrays.* Physical Review E, 2000. **61**(1): p. 45-48.
4. Cahill, B.P., L.J. Heyderman, J. Gobrecht and A. Stemmer, *Electro-osmotic pumping on application of phase-shifted signals to interdigitated electrodes.* Sensors and Actuators B-Chemical, 2005. **110**(1): p. 157-163.
5. Ramos, A., H. Morgan, N.G. Green and A. Castellanos, *Ac electrokinetics: a review of forces in microelectrode structures.* Journal of Physics D-Applied Physics, 1998. **31**(18): p. 2338-2353.
6. Selvaganapathy, P., Y.S.L. Ki, P. Renaud and C.H. Mastrangelo, *Bubble-free electrokinetic pumping.* Journal of Microelectromechanical Systems, 2002. **11**(5): p. 448-453.
7. Mutlu, S., F. Svec, C.H. Mastrangelo, J.M.J. Fréchet and Y.B. Gianchandani, *Enhanced Electro-Osmotic pumping with liquid bridge and Field Effect Flow rectification.* Proceedings of the IEEE Workshop on MEMS, January 25–29,Maastricht, The Netherlands,, 2004: p. 850-853.
8. Lyklema, J., *Fundamentals of Interface and colloid Science: Volume II: solid-liuid interfaces.* Academic Press, London, 1995.
9. Hunter, R.J., *Zeta Potential in Colloid Science: Principles and Applications.* Academic Press, London, 1981.
10. Eijkel, J.C.T., C. Dalton, C.J. Hayden, J.P. Burt and A. Manz, *A circular ac magnetohydrodynamic micropump for chromatographic applications.* Sensors and Actuators B-Chemical, 2003. **92**(1-2): p. 215-221.

11. Lemoff, A.V. and A.P. Lee, *An AC magnetohydrodynamic micropump.* Sensors and Actuators B-Chemical, 2000. **63**(3): p. 178-185.
12. Dose, E.V. and G. Guiochon, *Timescales of Transient Processes in Capillary Electrophoresis.* Journal of Chromatography A, 1993. **652**(1): p. 263-275.
13. Yan, D., N.T. Hguyen, C. Yang and X. Huang, *Visualizing the transient electroosmotic flow and measuring the zeta potential of microchannels with a micro-PIV technique.* Journal of Chemical physics, 2006. **124**: p. 021103.
14. Bousse, L.J., N.F. de Rooij and P. Bergveld, *Operation of chemically sensitive field-effect sensors as a function of the insulattor-electrolyte interface.* IEEE Transactions on Electron Devices, 1983. **30**: p. 1263.
15. Bousse, L.J., *The chemical sensitivity of electrolyte/insulator/silicon structures : fundamentals of ISFET operation.* PhD Thesis, University of Twente, the Netherlands, 1982.
16. van kerkhof, J.C., J.C.T. Eijkel and P. Bergveld, *Isfet Responses on a Stepwise Change in Electrolyte Concentration at Constant Ph.* Sensors and Actuators B-Chemical, 1994. **18**(1-3): p. 56-59.
17. van Hal, R.E.G., J.C.T. Eijkel and P. Bergveld, *A Novel Description of Isfet Sensitivity with the Buffer Capacity and Double-Layer Capacitance as Key Parameters.* Sensors and Actuators B-Chemical, 1995. **24**(1-3): p. 201-205.
18. Conway, B.E., *Transition from Supercapacitor to Battery Behavior in Electrochemical Energy-Storage.* Journal of the Electrochemical Society, 1991. **138**(6): p. 1539-1548.
19. Hermes, D.C., T. Heuser, E.J. van der Wouden, J.G.E. Gardeniers and A. van den Berg, *Fabrication of microfluidic networks with integrated electrodes.* Microsystem Technologies-Micro-and Nanosystems-Information Storage and Processing Systems, 2006. **12**(5): p. 436-440.
20. Herr, A.E., J.I. Molho, J.G. Santiago, M.G. Mungal, T.W. Kenny and M.G. Garguilo, *Electroosmotic capillary flow with nonuniform zeta potential.* Analytical Chemistry, 2000. **72**(5): p. 1053-1057.
21. Zeng, S.L., C.H. Chen, J.C. Mikkelsen and J.G. Santiago, *Fabrication and characterization of electroosmotic micropumps.* Sensors and Actuators B-Chemical, 2001. **79**(2-3): p. 107-114.
22. Anderson, J.L. and W.K. Idol, *Electroosmosis through pores with nonuniformly charged walls,.* Chem. Eng. Commun., 1985. **28**: p. 93-106.

23. Hayes, M.A., I. Kheterpal and A.G. Ewing, *Electroosmotic Flow-Control and Surface Conductance in Capillary Zone Electrophoresis.* Analytical Chemistry, 1993. **65**(15): p. 2010-2013.
24. Sniadecki, N.J., R. Chang, M. Beamesderfer, C.S. LEe and D.L. Devoe, *Field Effect Flow Control in a polymer T-intersection microfluidic networkI.* Proceedings 7th lnternational Conference on Miniaturized Chemical and Blochemlcal Analysts Systems, 2003

25. Gajar, S.A. and M.W. Geis, *An Ionic Liquid-Channel Field-Effect Transistor.* Journal of the Electrochemical Society, 1992. **139**(10): p. 2833-2840.
26. van der Wouden, E.J., T. Heuser, D.C. Hermes, R.E. Oosterbroek, J.G.E. Gardeniers and A. van den Berg, *Field-effect control of electro-osmotic flow in microfluidic networks.* Colloids and Surfaces a-Physicochemical and Engineering Aspects, 2005. **267**(1-3): p. 110-116.
27. van Hal, R.E.G., J.C.T. Eijkel and P. Bergveld, *A general model to describe the electrostatic potential at electrolyte oxide interfaces.* Advances in Colloid and Interface Science, 1996. **69**: p. 31-62.
28. Hayes, M.A., *Extension of external voltage control of electroosmosis to high-pH buffers.* Analytical Chemistry, 1999. **71**(17): p. 3793-3798.
29. Biernacki, J.J., P.M. Mellacheruvu and S.M. Mahajan, *Electric circuit model for electrical field flow fractionation.* Analytical Chemistry, 2006. **78**(14): p. 4998-5005.

8

Particle Image Velocimetry and Particle Tracking Velocimetry for electrokinetic flow in microchannels

1 Abstract

In this chapter, Particle Tracking Velocimetry (PTV) and Particle Image Velocimetry (PIV) measurements are presented in Field Effect Flow Control (FEFC) systems with a floating gate electrode. It is shown that at large channel potentials an induced gradient between the gate and channel potential contributes significantly to the flow profile and a strong deviation from a typical plug EOF profile is observed. PTV measurements show an increase in velocity variation with in increase in channel potential, which indicates a stronger local flow variation. In PIV measurements a velocity component normal to the channel length is observed, which indicates recirculation effects.

2 Tracer particles

2.1 Surface properties of fluorescent tracer particles

When PIV or PTV is applied in EOF systems the fluid motion is deduced by monitoring the motion of individual or ensembles of tracer particles. In order to achieve accurate results, tracer particles should fulfill the following properties [1] :

- The particles exactly follow the fluid motion.
- They do not influence the fluid motion
- The particles do not interact with each other.

If these requirements are met, the particles can be considered as ideal tracer particles. However, when PIV or PTV is applied in systems with an electrical field present this is generally not the case; an important aspect that needs to taken into consideration is that tracer particles will show an electrophoretic (EP) component due to the formation of charge on the solid particles. Under the condition that the particle diameter is large compared to the double layer thickness, or $\kappa a >> 1$, with κ the inverse Electrical Double Layer (EDL) length and a the particle radius, the electrophoretic velocity of a particle v_{EP} in an applied electrical field is similar to the Smoluchowski equation for EOF as is shown in equation 8.1.

$$v_{EP} = \frac{\varepsilon_0 \varepsilon_r \zeta}{\eta} E_x \qquad \text{(Eq. 8.1)}$$

In this equation, $\varepsilon_{o \text{ and}}$ ε_r are respectively the dielectric constant of vacuum and that of the solution, ζ the zeta potential of the particle, η the viscosity of the solution and E_x the electrical field strength. Under the opposite extreme condition that $\kappa a << 1$, the electrical field lines around the particle are unaffected by the particle, opposite to the previous case. In this situation, equation 8.1 has to be multiplied with a factor of 2/3 to compute the EP velocity of the particle.
Generally, the zeta potential of the tracer particle will have the same order of magnitude as the solid surface.
So in order to accurately measure EOF, the electrophoretic component of the tracer particles should be subtracted from the measured flow field. Minor *et al.* [2] showed that the electrophoretic mobility can be separated from the electroosmotic mobility by the application of a sufficiently large frequency. Oddy and Santiago applied this method in microchannels by a combination of DC and AC signals to determine the DC EOF component with PIV [3], while Yan *et al.* looked at the transient response after an applied potential at a time scale where the EOF component was not fully developed [4].
Devasenathipathy and Santiago used a different approach where the current monitoring method was used in combination with particle tracking to determine the contribution of EOF and EP [5]. With the use of one of the latter techniques the EP velocity component can be determined and subtracted from the flow field, so the real velocity profile can be obtained.

2.2 Brownian movement

When fluorescent particles are seeded in a solution to measure the flow field an error in the determined velocity vectors will be present due to the Brownian motion of the tracer particles. The Brownian movement of a particle can be expressed by its diffusion constant that is given by equation 8.2:

$$D = \frac{\kappa T}{3\pi\eta D_p} \qquad \text{(Eq. 8.2)}$$

Here κ is the Boltzmann constant, η the dynamic viscosity, T the temperature and D_p the particle diameter. The relative error determined in a velocity vector for a displacement $\Delta x = v^*\Delta t$ due to Brownian movement can be estimated by the ratio in displacement due to random movement and due to the velocity as shown in equation 8.3 [6].

$$\varepsilon_b = \frac{\left\langle s^2 \right\rangle^{\frac{1}{2}}}{\Delta x} = \frac{1}{v}\sqrt{\frac{2D}{\Delta t}} \qquad \text{(Eq. 8.3)}$$

Since Brownian motion is a random process, averaging over several images can reduce the error due to the random movement and increase the accuracy of the measurements [7]. The error due to random motion decreases with $\frac{1}{\sqrt{N}}$, where N is the total number of particles in the averaged images [8].

3 Materials and methods

3.1 Setup

FEFC measurements were performed with 5mM sodium acetate buffers at pH 3 seeded with 1 µm (PTV) and 300 nm (PIV) polystyrene fluorescent microspheres obtained from Duke Scientific with excitation wavelength 542 nm (green) and emission wavelength 612 nm (red). Control of the channel and gate potential with simultaneous monitoring of the current was acquired with two Keithley 2410 1100 V source meters controlled in HPVee. Image recording was performed with a Carl Zeiss microscope Axiovert 40 CFL with a 63X magnification objective, water immersion with a numerical aperture (NA) of 1.0 (Water Plan-Apochromat objective) and a working distance of 2mm for the PTV experiments. In the PIV experiments a 100X objective with a NA of 1.4 and a working distance of 170 µm was used. Illumination was performed with a New Wave Solo PIV III-15, dual cavity laser light sources, flashlamp-pomped ND:YAG at 532 nm, with a maximum repetition rate of 2X15 Hz and a PCO sensicam double shutter, resolution 1376X1040. A laser intensity of typically 1 mJ/pulse was applied.
Focusing in the microchannel was obtained with a piezosystem: Jena Piezoelectric Micro Lens Positioning System, with a reproducibility below 100 nm. Velocity profiles were obtained with the aid of a home made MatLab program.
FEFC systems were obtained from Micronit Microfluidics Bv. An example of a structure is shown in figure 8.1. In the experiments, the Interrogation Region (IR) was chosen in the middle of the left gate electrode and focused in the middle of the channel. The ground and positive potential were respectively applied to the right and left reservoir.

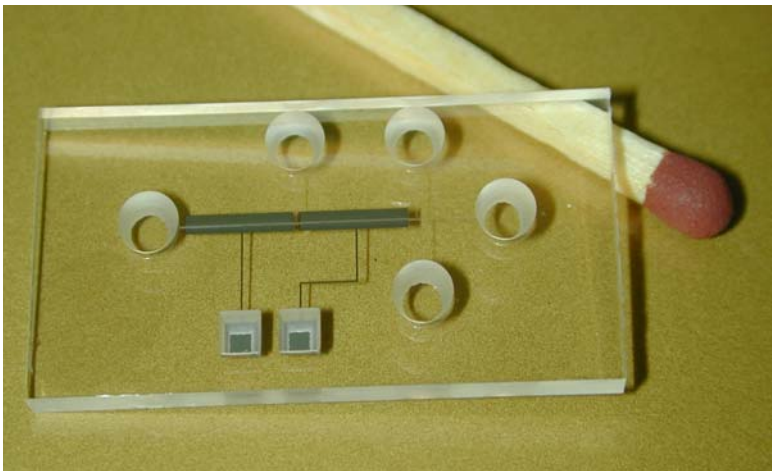

Fig. 8.1:*FEFC microstructure with 2 gate electrodes. Channel width 100 µm, height 20 µm, length 1.5 cm. Dimensions of the gate electrodes are 1.0×5.6 mm. Channel cover thickness 170 µm.*

3.2 Surface coating

To reduce sticking of beads to the channel surface, which is detrimental to PIV or PTV measurement, chips have been treated with a Hexa Methyl Di Silazane (HMDS) coating prior to the measurements. Chips were placed overnight in a solution of toluene with 0.1 vol. % HMDS. The methyl surface groups of the HMDS lead to a hydrophobic channel surface and in this way reduce the adsorption of fluorescent tracer particles to the channel surface.
In order to be able to separate the EOF and the electrophoretic velocity component of the tracer particles in an applied electric field, the zeta potential was measured in a separate experiment. The current monitoring method was applied with sodium acetate buffers of 5 and 2.5 mM with a pH of 3. The zeta potential of the HMDS coated glass wall was determined to be approximately -10 mV.

3.3 Measurement principle

Figure 8.2 shows an overview of the experimental setup and measurement principle. On the left side the setup is shown with a piezo controlled z-stage to focus in the desired plane of the microchannel. The channel is illuminated with a double pulsed Nd-YAG laser and imaged with a high sensitivity

2 frame camera. In this way image pairs with a maximum of 15 Hz can be obtained. A time interval of 0.3 sec between each frame pair was applied for both the PIV and PTV measurements.

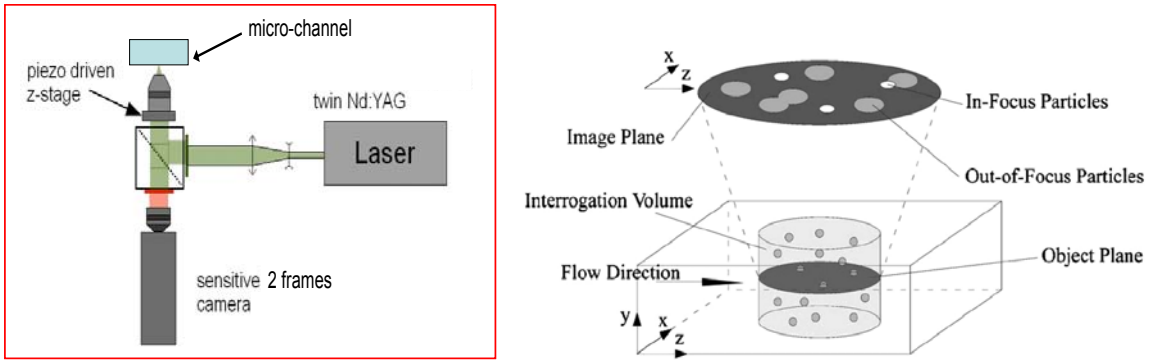

Fig. 8.2: *Schematic overview of the measurement setup.*

The right side of figure 8.2 shows the focusing principle. By adjusting the piezo driven z-stage, an image plane in the channel can be selected. Particles outside of the image plane are out of focus and will be displayed in the image with a deviating diameter and intensity compared to the in focus particles. In an image recording of particles with a diameter d_p, the particle image will differ from the real particle diameter due to the magnification M and an influence of the optical equipment.
The influence of the optical equipment can be represented by a point spread function that dependents on the numerical aperture (NA), magnification M and the wavelength of the light λ as shown in equation 8.4 [9].

$$d_s = 1.22(1+M)\lambda NA^{-1} \qquad \text{(Eq. 8.4)}$$

The particle size appearing in the recording can be expressed by equation 8.5 when it is assumed that both the point spread function d_s and the magnification Md_p are Gaussian functions [6].

$$d_e = \left(M^2 d_p + d_s^2\right)^{\frac{1}{2}} \qquad \text{(Eq. 8.5)}$$

After acquisition, the images are subjected to a threshold mask to remove the out of focus particles as shown in the example of figure 8.4.

Subsequently, the filtered image pairs are cross-correlated to yield the displacement and velocity.

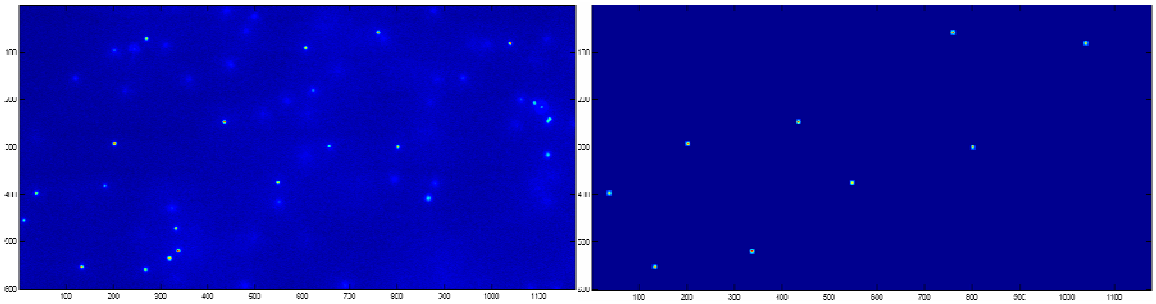

Fig. 8.4: *Example of a raw image (left) and an image after filtering to clear out of focus particles (right).*

The cross-correlation principle for the PTV is illustrated in figure 8.5. The particle position in the first image is set as a reference position. Based on a pre-assumption of the maximum flow velocity and direction, a rectangular box is drawn around the particle. Subsequently, the cross-correlation in the IR box is determined between the image pairs, which yield the displacement. By dividing the displacement by the time interval the local velocity can be determined. The correlation algorithm assumes only a flow direction parallel to the channel and requires a low probability of tracer particle overlap in the IR boxes. The last requirement puts some restrictions on maximum particle concentrations especially at high velocities. So, to be able to obtain an accurate and complete velocity profile over the entire channel cross-section at low particle concentration, averaging over several frames is necessary.

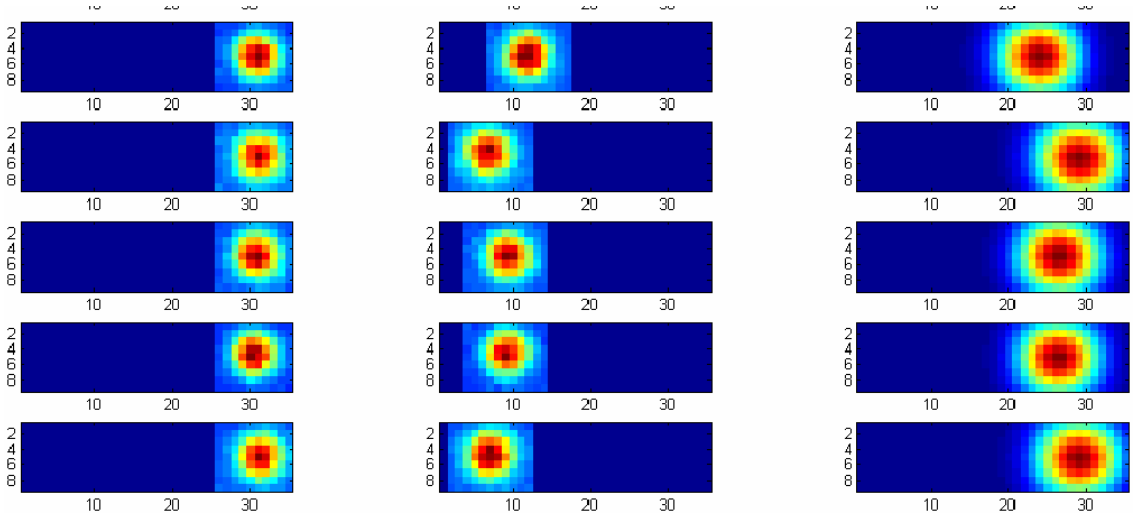

Fig. 8.5: *Calculation of displacement: Left and middle column shows respectively the first and second image, the right column gives the displacement calculated by cross-correlation.*

4 Velocity distribution as a function of the channel potential with a floating gate electrode

4.1 Particle Tracking Velocimetry

In figure 8.6a-f, the velocity profile is shown as a function of the channel potential from 100-350 V. In the chip, as shown in figure 8.1, both gate electrodes were left floating. The measurements are composed of an average over the entire channel length of 200 frames. The fitted curve indicates an average of the individual data points. It can be seen in the figures that at low potentials, a flow profile with a maximum in the center of the channel is present. At higher potentials, a dip in the center is present and a recirculating flow can be observed.

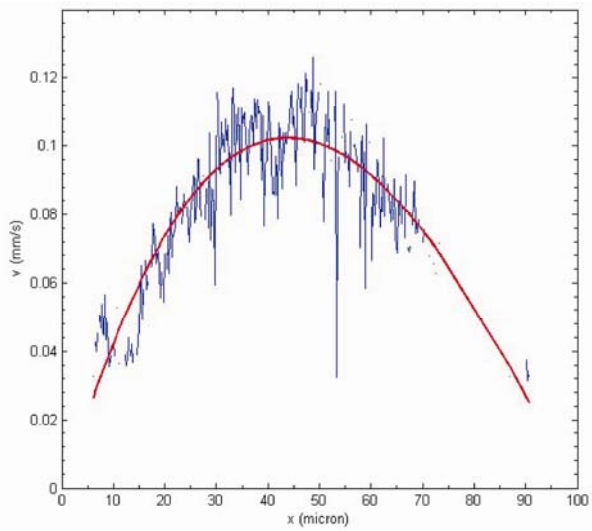

Fig. 8.6a: *Velocity profile for 100 V*

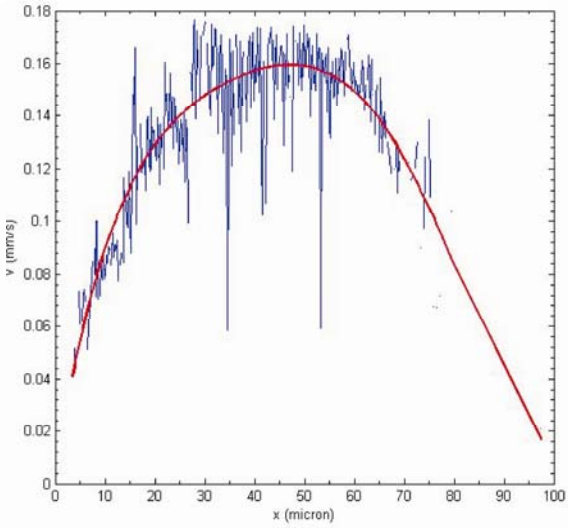

Fig. 8.6b: *Velocity profile for 150 V*

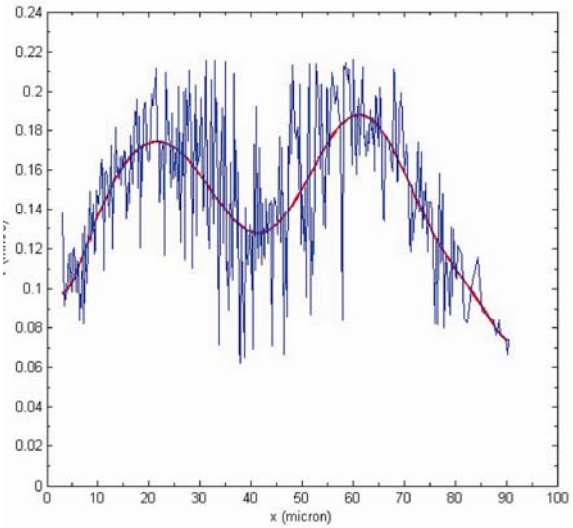

Fig. 8.6c: *Velocity profile for 200 V*

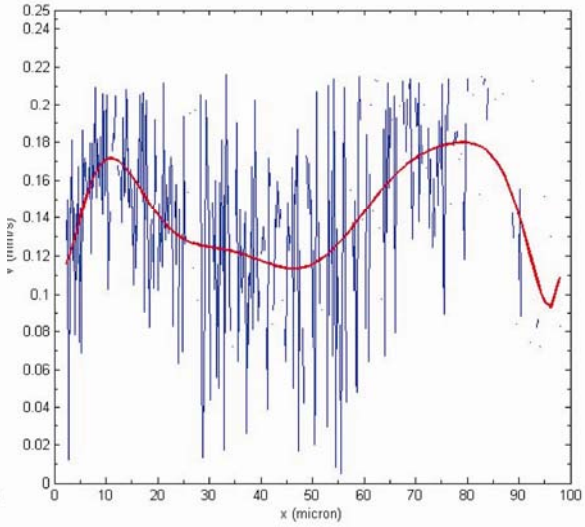

Fig. 8.6d: *Velocity profile for 250 V*

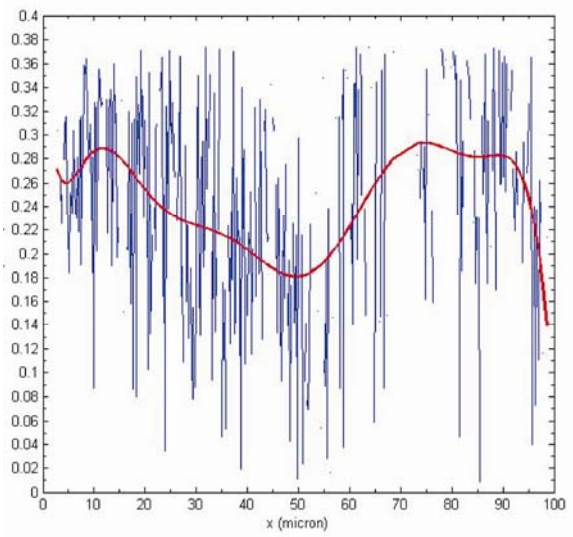

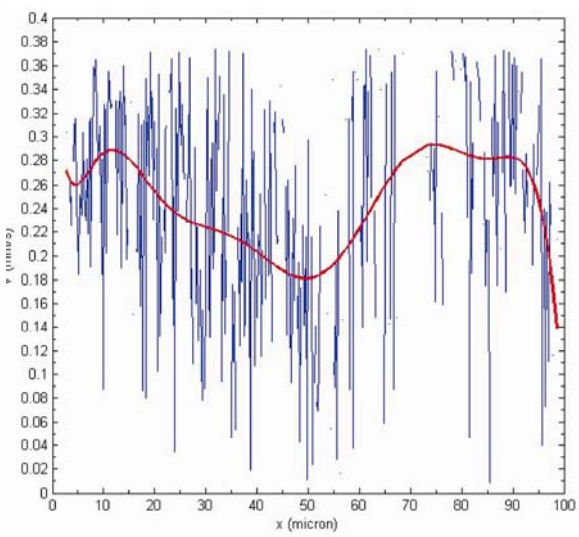

Fig. 8.6e: *Velocity profile for 300 V*

Fig. 8.6f: *Velocity profile for 350 V*

The effect of the non-uniform flow profile can be understood by looking at the potential distribution of the gate electrode with respect to the channel potential in the IR window.

When a longitudinal potential is applied over a microfluidic channel to create an EOF, the potential in the channel will show a gradient, so the electric potential will be a function of the position in the channel.

When the gate electrode is left floating, it will acquire a potential that is the average of the gradient at its position in the channel. In the experiments we look at the center of the gate. Left from this point the gate potential will be negative with respect to the channel potential, while on the right it will be positive. This implicates that locally different zeta potentials and thus different flow rates are present. Since the differences in zeta potentials and flow rate increase with the channel potential, this effect can explain the increased variation in velocity for individual data points at larger potentials.

The influence of the potential gradient over the channel is illustrated in figure 8.7. The slope of the ζ-potential originates from the superposition of the potential difference resulting from the applied electrical field E and the applied gate voltage V_g. Depending on the applied potentials and the offset value for the zeta potential, at a particular position in the channel the condition that $\Delta\zeta = \zeta$ might occur. So that at this position in the channel the flow will be zero, while beyond this position the flow is reversed. In this region vortices may occur as illustrated in figure 8.7d. These recirculating flow profiles were indeed observed at large channel potentials, at a position in the gate where a large positive potential difference between the gate and

the channel was present and thus a reversal of the zeta potential is expected.
In the older work on FEFC in capillaries this effect of a zeta potential gradient was held responsible for the introduction of extra band broadening in electrophoretic separation.
Lee *et al.* [10] and Hayes and Ewing [11] matched the gate and channel potentials respectively by the use of two capillaries with in-between a electrolyte that acted as the gate and the application of a resistive polymer on the outside of a capillary to apply a gate potential gradient.
To prevent the occurrence of a gradient between the gate and channel potential and achieve a stable flow situation either several gate electrodes or a resistive gate electrode can be created to match the gradient in the channel potential.

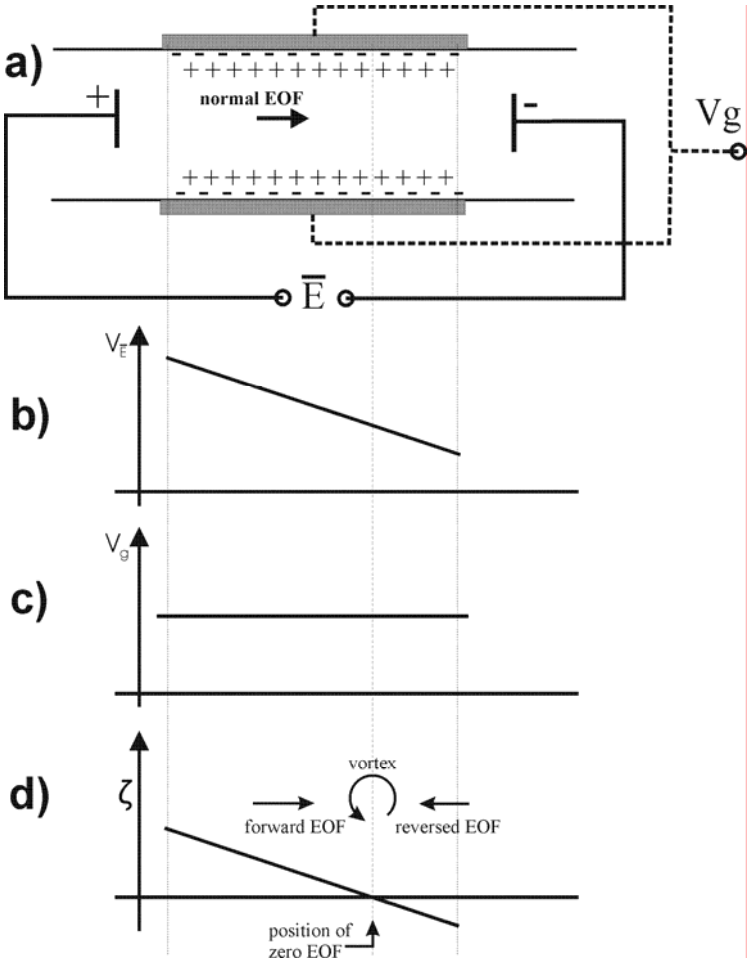

Fig. 8.7: *Schematic illustration of the origin and influence of zeta potential gradients.*

4.2 Particle Image Velocimetry

In figure 8.8 the velocity as a function of the horizontal channel position is shown as obtained with PIV. In the analysis, the total window size was 960X864 pixels with 1 pixel=0.1244 μm. The IR size was 64X32 pixels with a spacing of 16X16 pixels for overlap. Calculation of the velocity was performed in 3 steps. Initially, a threshold value was applied and a sum over 5 frames was determined. Subsequently, cross correlation was performed to obtain the mean displacement for each IR. Step one and two were repeated 20 times and the average value was determined, so that the velocity component was determined over a total of 100 frames.

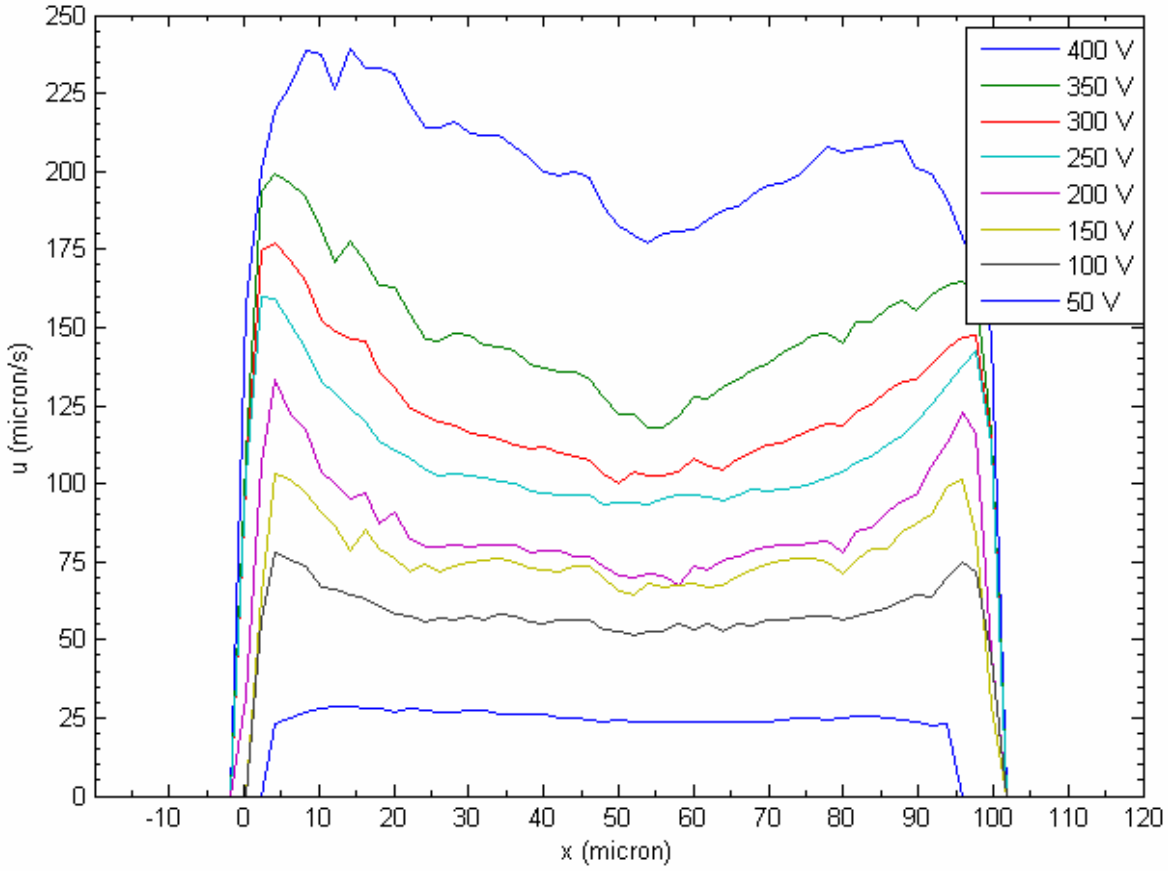

Fig. 8.8: *PIV profiles of the velocity component parallel to the channel as a function of the channel potential (50-400 V.)*

The results presented in figure 8.8 show a plug velocity profile at low channel potential, as the potential increases a plug flow with a concave character can be distinguished. This effect can be attributed as discussed

before, to an increasing gradient in zeta potential in the gate region with an increase in channel potential. The resulting differences in local flow rate induce a pressure gradient and a resulting hydrodynamic flow [12, 13]. The net flow profile will thus consist of the sum of a plug EOF profile and a pressure driven component. Depending on the longitudinal and radial position in the channel the induced pressure driven flow can either be in the same, or the reverse direction as the local EOF.
Furthermore, it can be noticed in he graph that at low potentials the flow near the walls seems to be zero. This is, however, a result of an applied threshold mask. Figure 8.9 shows an example of a calculated velocity profile. It can be seen that apart from 300 nm beads present in the channel, also a few 1 µm beads from the PTV measurements adsorbed to the wall are present. In order to remove the resulting erroneous velocity vectors, a threshold mask was applied. At low potentials the velocity near the wall comes below this threshold value and consequently the velocity is displayed as zero.

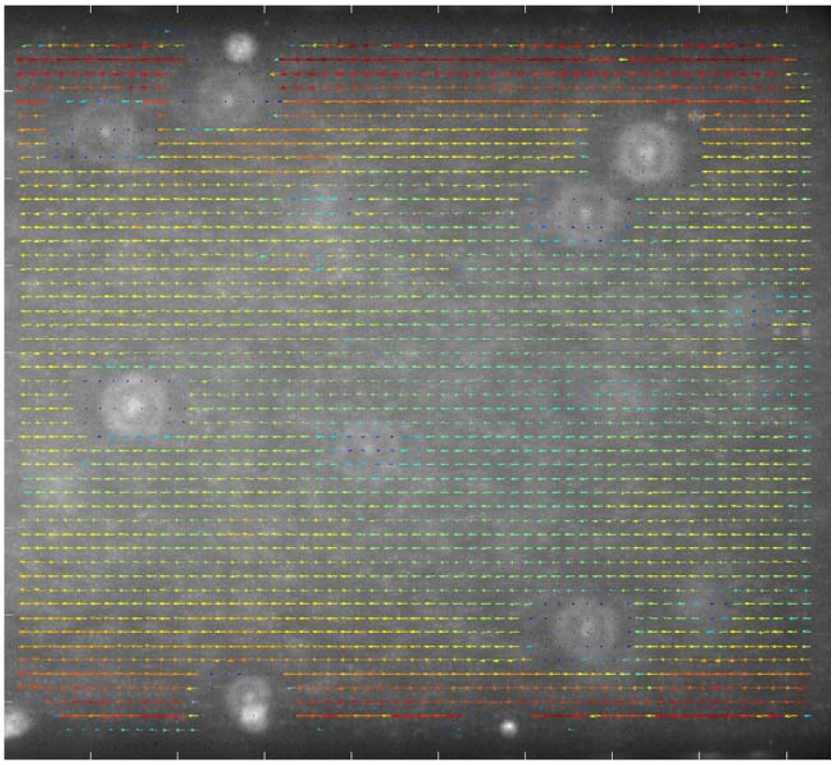

Fig. 8.9: *PIV profile for a channel potential of 200 V Blurred areas indicate adsorbed 1 µm tracer particles.*

In figure 8.10 the velocity component normal to the channel length is shown as a function of the horizontal channel position. Although the measured velocities are in the limiting range of the PIV setup, it can be seen that with an increase in potential a flow towards the center of the channel occurs. This indicates that recirculation effects in the channel occur and also a velocity component in the height direction of the channel is present.

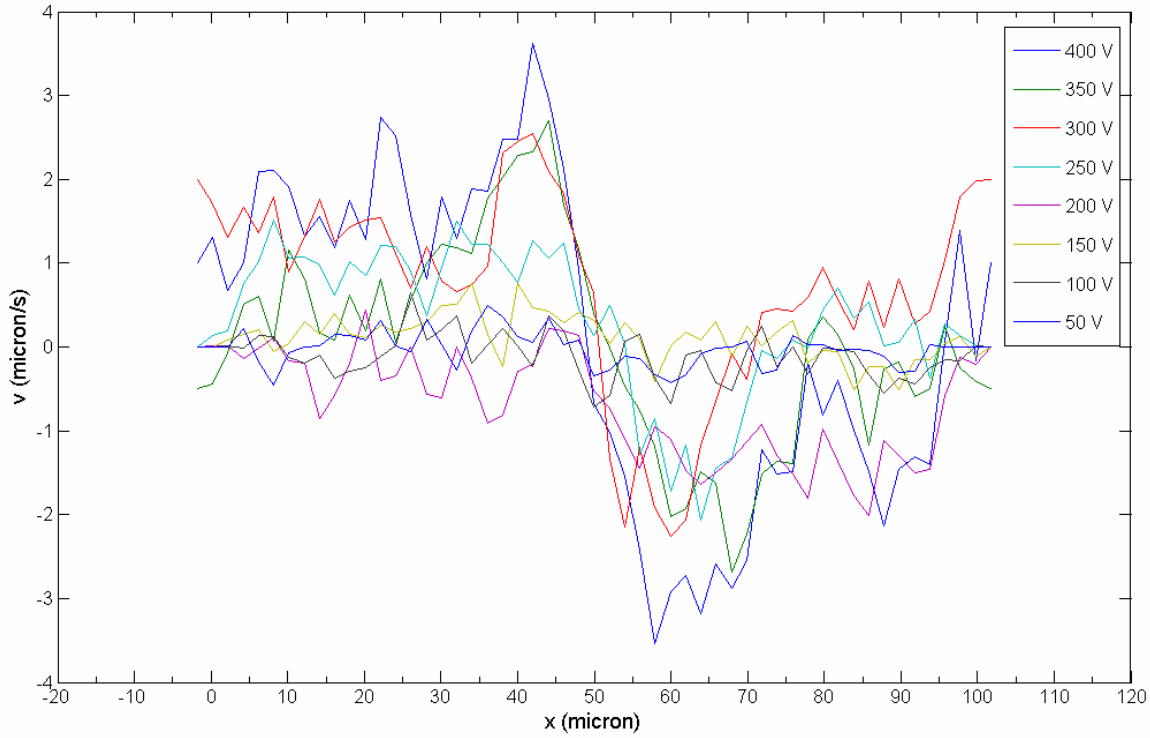

Fig. 8.10: *PIV profiles of the velocity component normal to the channel as a function of the channel potential (50-400 V).*

5 Discussion and conclusions

It is shown with the aid of Particle Tracking Velocimetry (PTV) and Particle Image Velocimetry (PIV) that in a FEFC system with a floating gate electrode the gradient in zeta potential resulting from the channel potential gradient, significantly influences the flow distribution. PIV measurements show that with increasing channel potential the typical plug EOF profile disappears and a concave profile with a minimum in the channel centre is present. The first results indicate that PIV seems to provide more accurate results than the PTV measurements. This is probably mainly due to a more sensitive objective and the use of smaller beads. The PTV experiments do

not provide very conclusive results and further experiments will be necessary. Especially the observed influence on the flow needs to be looked at in more detail, since it is expected that the flow profile will have a strong dependence on the radial and longitudinal position in the channel. This effect should be investigated in more detail to check the reliability of the measurements.

6 References

1. Westerweel, J., *Fundamentals of digital particle image velocimetry.* Measurement Science & Technology, 1997. **8**(12): p. 1379-1392.
2. Minor, M., A.J. van der Linde, H.P. van Leeuwen and J. Lyklema, *Dynamic aspects of electrophoresis and electroosmosis: A new fast method for measuring particle mobilities.* Journal of Colloid and Interface Science, 1997. **189**(2): p. 370-375.
3. Oddy, M.H. and J.G. Santiago, *A method for determining electrophoretic and electroosmotic mobilities using AC and DC electric field particle displacements.* Journal of Colloid and Interface Science, 2004. **269**(1): p. 192-204.
4. Yan, D.G., N.T. Nguyen, C. Yang and X.Y. Huang, *Visualizing the transient electroosmotic flow and measuring the zeta potential of microchannels with a micro-PIV technique.* Journal of Chemical Physics, 2006. **124**(2): p. -.
5. Devasenathipathy, S., J.G. Santiago and K. Takehara, *Particle tracking techniques for electrokinetic microchannel flows.* Analytical Chemistry, 2002. **74**(15): p. 3704-3713.
6. Santiago, J.G., S.T. Wereley, C.D. Meinhart, D.J. Beebe and R.J. Adrian, *A particle image velocimetry system for microfluidics.* Experiments in Fluids, 1998. **25**(4): p. 316-319.
7. Olsen, M.G. and R.J. Adrian, *Brownian motion and correlation in particle image velocimetry.* Optics and Laser Technology, 2000. **32**(7-8): p. 621-627.
8. Bendat, J.S. and A.G. Piersol, *Random data : Analysis and measurement procedures.* 2nd , rev. and expand ed. New York: Wiley, 1986.
9. Born, M. and E. Wolf, *Principles of Optics.* Pergamon Press, Oxford, 1991.
10. Lee, C.S., W.C. Blanchard and C.T. Wu, *Direct Control of the Electroosmosis in Capillary Zone Electrophoresis by Using an*

External Electric-Field. Analytical Chemistry, 1990. **62**(14): p. 1550-1552.
11. Hayes, M.A. and A.G. Ewing, *Electroosmotic Flow-Control and Monitoring with an Applied Radial Voltage for Capillary Zone Electrophoresis.* Analytical Chemistry, 1992. **64**(5): p. 512-516.
12. Herr, A.E., J.I. Molho, J.G. Santiago, M.G. Mungal, T.W. Kenny and M.G. Garguilo, *Electroosmotic capillary flow with nonuniform zeta potential.* Analytical Chemistry, 2000. **72**(5): p. 1053-1057.
13. Long, D., H.A. Stone and A. Ajdari, *Electroosmotic flows created by surface defects in capillary electrophoresis.* Journal of Colloid and Interface Science, 1999. **212**(2): p. 338-349.

9

Summary & conclusions

This thesis describes the development of a Field Effect Flow Control (FEFC) system for the control of Electro Osmotic Flow (EOF) in microfluidic networks. For this several aspects of FEFC have been reviewed and a process to fabricate microfluidic channels with integrated electrodes has been developed.

In chapter 2, an overview of various detection and characterization techniques for EOF are summarized and discussed. For flow characterization of FEFC, PIV seems to over the best characteristic since it couple the ability to obtain local flow information with high accuracy. However, the method requires an elaborate and extensive setup. So, when only information of the EOF velocity is required the current monitoring technique is a more suitable one, since it allows fast and easy measurement without the need of an elaborate setup.
The zeta potential of bare silica is measured with the current monitoring. For efficient manipulation of the flow with FEFC, low offsets in zeta potential are required. It is shown that with bare silica, low buffer pH's are necessary to obtain such a low offset. To allow efficient actuation at neutral pH, which is required in biomedical applications, several dynamic and fixed coatings have been applied. Best results are obtained for APS coatings when coating at 60 ˚C for 1 hour, an offset value for the zeta potential of 5 mV is found at pH 7.
Furthermore, the three capacitor model is discussed that is classically used in FEFC. It is shown that in order to account for the response of active surface groups, the influence of the surface buffer capacitance should be included in the model.

The development for a process to fabricate microfluidic channels with integrated electrodes and its layout is described in chapters 3 and 4.
It is has been illustrated that with the concept of a meandering channel structure in which the subsequent branches are electrically parallel and hydrodynamic serial, a flow can be generated at low absolute potentials. For this concept, AC-modulation of the gate zeta potential and the longitudinal electrical field that drives the EOF is required. In order to allow a sufficiently large frequency to avoid bubble formation and still maintain a high hydraulic resistance, large channel aspect ration are required. With channel heights of approximately 5 μm and a channel width of a few millimeters, both requirements can be met.
Furthermore, it was illustrated that for maximum flow control gate insulation with both, a high dielectric constant and a high breakdown value, is

required. Since glass possesses both properties and is furthermore optically transparent and chemically inert, it has good characteristics for implications in a FEFC structure. Silica PECVD films have been optimized to obtain high dielectric breakdown strength towards both positive and negative polarization. It is shown that optimal results are obtained during high frequency depositions at elevated temperatures.
To obtain uniform surface charge at the channel walls, which is favorable in studying the characteristics of FEFC a complete glass device can be fabricated.
A technique for integrating insulated electrodes in a channel wall is presented by using CMP and glass-to-SiO_2 direct bonding. A PECVD recipe was optimized to provide a low stress, good insulation and good uniformity of the SiO_2-layer. Furthermore, a CMP procedure was optimized that allows planarizing and smoothening of the oxide layer. Consequently, a good bonding between both wafers was obtained.

In chapter 5 finite element simulations of FEFC structures are presented for validation of experimental results and to test FEFC structure designs.
It is shown that under the conditions of heterogeneous surface charge the typical plug flow profile associated with EOF vanishes. Transverse and recirculating flow is observed at the gate electrode region. These flow profile can be beneficial to enhance mixing in microchannels, which under normal conditions is diffusion limited. The effect of the gate electrode coverage is investigated; simulations show that a small coverage leads to a limited influence on the net flow and flow profile, while experimental results indicate a far more effective influence. The discrepancy between the simulations and experiments could be explained by an influence of surface conduction. An enhanced conductivity in the EDL, can lead to a spreading of the gate zeta potential beyond the location of the electrode in the channel.
PIV analysis of experimental results shows good qualitative agreement with the simulations, a reversal of the net flow is observed at a positive applied gate potential.
More complex FEFC arrays have been composed and simulated to investigate a FEFC structure for fluidic routing. It is shown that by a suitable choice of zeta potential in the gate regions the flow can be directioned in fluidic networks. However, the offset value of the zeta potential on the non-gated wall results in recirculation of flow, which can be unwanted when mixing of flow streams should be avoided. Reduction of the zeta potential offset by for instance application of a coating can significantly reduce such recirculation.

In chapter 6 microfluidic networks based on glass microchannels with integrated insulated gate electrodes that are used to modify the ζ-potential at specific locations on the wall surface of the microchannels were fabricated and tested. The ζ-potential modification was used to control the direction of the EOF in the microchannels. It is shown that the EOF could be stopped completely for longitudinal fields of 150 V/cm by applying a field over the gate insulation layer of 1.7 MV/cm, for conditions where the unmodified ζ-potential was ca. -35 mV. The measurements showed that at moderate values of the ζ-potential an almost linear relation between the applied gate field and ζ-potential exists, which agreed with theory for the conditions investigated.

In chapter 7 it was shown that a net flow can be induced by the synchronized switching of axial channel voltage and gate potential. Directional flow was observed above the gate electrode, with an oscillating (AC) component due to the electrophoretic movement of the beads and the asymmetry in the zeta potential in the positive and negative half of the gate potential period. This concept offers high potential for the use of EOF in fully integrated systems.
From an analysis of the time scales involved in the dynamic behavior of a FEFC structure it follows that the maximum operating frequency is limited by the charging of the EDL, which is controlled by the series impedance of the channel resistance and the gate capacitance.
Since the performance of the device is optimal at moderate and low ionic concentration, for fast FEFC the concentration of the electrolyte is limited to the mM range, which gives an RC time limited by switching at negative bias potentials, with a typical time constant of approximately 60 milliseconds. This value allows a maximum operating frequency of 16 Hz. However, this value may be increased by decreasing the gate electrode area or using shorter channels.
From an analysis of the pH dependency of a FEFC structure it follows that the three capacitor model that is traditionally used to describe FEFC is only valid at low buffer capacitances. At larger surface charge the model should be expanded to account for the influence of the buffer pH. It follows that the practical pH range for AC-operation is below pH 5. Above this value the gate potential needed for switching the sign of the zeta potential is in the range of the breakdown values of the silica insulating layer. This limitation is caused by the influence of the buffer capacitance of the silanol surface

groups. However, a complete reversal of the zeta potential in the gate region is not necessary for the generation of a net flow with an applied AC-channel potential, but the range in which the flow can be controlled will be narrowed.

In chapter 8 it was shown with the aid of Particle Tracking Velocimetry (PTV) and Particle Image Velocimetry (PIV) that in a FEFC system with a floating gate electrode, the gradient in zeta potential resulting from the channel potential gradient, significantly influences the flow distribution. PIV measurements showed that with increasing channel potential the typical plug EOF profile disappears and a concave profile with a minimum in the channel centre is present. The first results indicate that PIV seems to provide more accurate results than the PTV measurements. This is probably mainly due to a more sensitive objective and the use of smaller beads. The PTV experiments do not provide very conclusive results and further experiments will be necessary. Especially the observed influence on the flow needs to be looked at in more detail, since it is expected that the flow profile will have a strong dependence on the radial and longitudinal position in the channel. This effect should be investigated in more detail to check the reliability of the measurements.

Samenvatting

Dit proefschrift beschrijft de ontwikkeling van een flow controle systeem voor microkanalen. In het systeem wordt de Electro Osmotische Flow (EOF) beïnvloed door manipulatie van de lading op een vaste stof/vloeistof interface middels een radiaal elektrisch veld. Deze wijze van flow controle wordt ook wel aangeduid als Field Effect Flow Control (FEFC).

Om tot een optimaal ontwerp te komen voor een FEFC device zijn de verschillende theoretische aspecten van FEFC in kaart gebracht.
The opbouw van een Elektrische Dubbel Laag (EDL) op een vaste stof/vloeistof interface is besproken en de formatie van een oppervlakte lading op verschillende typen oppervlakken is behandeld.
Voor het berekenen van een snelheids profiel met een heterogene oppervlaktelading op de kanaal wand, is een analytische oplossing gepresenteerd voor half ellips L-vormige kanaal geometrie.

Voor het fabriceren van FEFC structuren zijn verschillende microfabricage technieken geëvalueerd. Voor het verkrijgen van een device met een uniforme wandlading is fabricage in glas gekozen. Voor het vervaardigen van microkanalen met geïntegreerde elektroden is een fabricage proces ontwikkeld dat gebruikt maakt van Chemisch Mechanisch Polijsten (CMP), het CMP proces is geoptimaliseerd om de oppervlakte topografie te reduceren en lijdt tot een oppervlakte ruwheid van minder dan 1 nm.

Het is aangetoond dat het drie capaciteiten model, dat traditioneel word gebruikt voor de controle van de zeta potentiaal in FEFC, is gelimiteerd tot een vloeistof pH die dicht bij het “point of zero charge” (p.z.c.) van het oppervlak licht. Voor de gefabriceerde structuren houdt dit in dat toepassing van het systeem is gelimiteerd tot het zure pH regime. Verschillende coatings zijn getest om de silanol oppervlakte groepen van het silica oppervlak te inactiveren en het p.z.c. te verschuiven naar meer neutrale pH. De beste resultaten zijn bereikt voor een aminopropylsiloxane (APS) coating, waarbij een offset waarde voor de zeta potentiaal bij pH 7 van 5 mV werd gemeten.

Teneinde belformatie aan de open kanaal elektroden te reduceren is gekeken naar het gesynchroniseerd schakelen van de zeta potentiaal

contolerende gate potentiaal met de kanaal potentiaal. Er is aangetoond dat een netto flow kan worden geïnduceerd met een frequentie van 15 Hz. Uit een analyse van de dynamische respons van het systeem blijkt dat frequentie limiterende relaxatie tijd wordt bepaald door de buffer capaciteit van de silanol oppervlakte groepen.

Voor het bepalen van de vloeistof stroom in een FEFC device en de daarbij optredende snelheidsprofielen zijn “ Particle Image Velocimetry” (PIV) en “ Particle Tracking Velocimetry” (PTV) metingen uitgevoerd. Vooralsnog lijkt de PIV techniek de meest betrouwbare resultaten op te leveren. De gemeten snelheidsprofielen vertonen een goede correlatie met eindige elementen simulaties uitgevoerd in CFDRC.

Dankwoord

Met dit dankwoord komt er een eind aan dit proefschrift en een periode van vier jaar onderzoek. Verschillende mensen hebben hier op verschillende manieren een belangrijke bijdrage aan geleverd. Vanaf deze plek wil ik dan ook een poging doen deze mensen hiervoor mijn waardering te laten blijken. Tijdens vier jaar promoveren leer je ook jezelf ook een stuk beter kennen, vandaar dat ik maar begin met het bedanken van alle mensen die ik het vervolg vergeet te noemen, bij deze.

In eerste instantie wil ik Albert van den berg bedanken voor de mogelijkheid om mijn promotie onderzoek in de BIOS groep te doen. Ook bedankt voor je motiverende input aan ideeën tijdens onze meetings.
Han Gardeniers bedankt voor je dagelijkse begeleiding. Zonder jouw heldere feedback en commentaar was het afronden van dit proefschrift een stuk lastiger geweest.

Throughout the last years several cooperation's have lead to valuable results described in this thesis.
I would like to acknowledge Robert Barber, David Emerson, Raluca Muller, Oana Nedelcu and Hans Kerkhof for their cooperation in the Patent project, of which some results are presented in chapter 5.
The measurements presented in chapter 8 wouldn't have been possible without the enthusiastic cooperation of Christophe Pirat.
Also several students have contributed to the work presented in this thesis. Especially Thorsten I would like to thank for the work he performed for his graduation assignment. Furthermore, Dong Liang, Arjen de Waal and Rein Hoekema are acknowledged for their contributions.

Voor de fabricage van mijn chips wil ik Dorothee en Gabriel bedanken.
Het fabriceren van werkende chips in glas bleek toch wat lastiger als verwacht. Dorothee, bedankt dat er uiteindelijk toch werkende exemplaren uit de cleanroom kwamen rollen.
Hermine bedankt voor het regelen van alle administratieve dingen.

Het werken in de Bios groep de afgelopen periode was een erg leuke ervaring, naast de vele nuttige werkgerelateerde discussies en gesprekken was er ook veel ruimte voor wat socialere gesprekken. Bedankt voor de leuke tijd, Erik K, Wim, Paul, Wouter S., Jacob, Woitek, Jan N., Floor, Han,

Regina, Steven, Johan, Arjan, Svetlana, Anil, Ana, Hermine, Jan E., Piet, Wouter O., Jurjen, Erik F., Roald, Severine, Lingling, Joke Georgette, Kevin, Eddy, Daniel, Ad, Ton, Hien, Gabriel Edwin and Vincent.

Verder moet ik vooral Jurjen, Ana en Floor bedanken voor hun pogingen het 4 jaar lang met me op een kamer uit te houden. Ana ook bedankt voor de leuke tijd naast het werk. Bedankt ook voor het doorlezen van mijn proefschrift. Floor, heel veel succes met je proefschrift straks. Jurjen, dat geld ook voor jou en ik hoop dat je er ooit nog eens achterkomt dat die motoren zwaar overschat worden en dat voetbal echt de enige bijzaak is die er echt toe doet.
Wat voetbal betreft wil ik het BioMEMS team bedanken voor de ontspannende potjes zaalvoetbal. Roald, Rob, Han en Patrick, ook bedankt dat jullie met me een poging hebben willen doen om voetbal een gespreksonderwerp in de BIOS groep te maken.

Tot slot wil ik vooral iedereen bedanken die me op wat voor manier dan ook buiten het werk om heeft gesteund.